N°d'ordre NNT : 2017LYSEI067

THESE de DOCTORAT DE L'UNIVERSITE DE LYON
opérée au sein de
l'INSA LYON

École Doctorale ED 162 MEGA
Mécanique, Énergétique, Génie Civil, Acoustique

Spécialité de doctorat :
GÉNIE MÉCANIQUE

Soutenue publiquement le 01/09/2017, par :
José Luis GOMEZ CHIRINOS

ANGLE MODELING OF A ROTATING MACHINE. APPLICATION TO WIND TURBINE SURVEILLANCE

Devant le jury composé de

VELEX, PHILIPPE	Professeur	INSA de Lyon	Président
SERRA, ROGER	Maître de Conférences, HDR	INSA Centre Val de Loire	Rapporteur
DION, JEAN-LUC	Professeur	CNAM	Rapporteur
AUBRY, EVELYNE	Professeur	ENSISA	Examinatrice
RÉMOND, DIDIER	Professeur	INSA Lyon	Directeur
BOURDON, ADELINE	Maître de Conférences	INSA Lyon	Co-Directeur
ANDRÉ, HUGO	Maître de Conférences	Université Jean MONNET	Invité
GIRARD, NICOLAS	Ingénieur	Engie Green	Invité

Département FEDORA – INSA Lyon - Ecoles Doctorales – Quinquennal 2016-2020

SIGLE	ECOLE DOCTORALE	NOM ET COORDONNEES DU RESPONSABLE
CHIMIE	**CHIMIE DE LYON** **http://www.edchimie-lyon.fr** Sec : Renée EL MELHEM Bat Blaise Pascal 3e etage secretariat@edchimie-lyon.fr Insa : R. GOURDON	M. Stéphane DANIELE Institut de Recherches sur la Catalyse et l'Environnement de Lyon IRCELYON-UMR 5256 Équipe CDFA 2 avenue Albert Einstein 69626 Villeurbanne cedex directeur@edchimie-lyon.fr
E.E.A.	**ELECTRONIQUE, ELECTROTECHNIQUE, AUTOMATIQUE** **http://edeea.ec-lyon.fr** Sec : M.C. HAVGOUDOUKIAN Ecole-Doctorale.eea@ec-lyon.fr	M. Gérard SCORLETTI Ecole Centrale de Lyon 36 avenue Guy de Collongue 69134 ECULLY Tél : 04.72.18 60.97 Fax : 04 78 43 37 17 Gerard.scorletti@ec-lyon.fr
E2M2	**EVOLUTION, ECOSYSTEME, MICROBIOLOGIE, MODELISATION** **http://e2m2.universite-lyon.fr** Sec : Sylvie ROBERJOT Bât Atrium - UCB Lyon 1 04.72.44.83.62 Insa : H. CHARLES secretariat.e2m2@univ-lyon1.fr	M. Fabrice CORDEY CNRS UMR 5276 Lab. de géologie de Lyon Université Claude Bernard Lyon 1 Bât Géode 2 rue Raphaël Dubois 69622 VILLEURBANNE Cédex Tél : 06.07.53.89.13 cordey@ univ-lyon1.fr
EDISS	**INTERDISCIPLINAIRE SCIENCES-SANTE** **http://www.ediss-lyon.fr** Sec : Sylvie ROBERJOT Bât Atrium - UCB Lyon 1 04.72.44.83.62 Insa : M. LAGARDE secretariat.ediss@univ-lyon1.fr	Mme Emmanuelle CANET-SOULAS INSERM U1060, CarMeN lab, Univ. Lyon 1 Bâtiment IMBL 11 avenue Jean Capelle INSA de Lyon 696621 Villeurbanne Tél : 04.72.68.49.09 Fax :04 72 68 49 16 Emmanuelle.canet@univ-lyon1.fr
INFOMATHS	**INFORMATIQUE ET MATHEMATIQUES** **http://infomaths.univ-lyon1.fr** Sec :Renée EL MELHEM Bat Blaise Pascal, 3e étage Tél : 04.72. 43. 80. 46 Fax : 04.72.43.16.87 infomaths@univ-lyon1.fr	M. Luca ZAMBONI Bâtiment Braconnier 43 Boulevard du 11 novembre 1918 69622 VILLEURBANNE Cedex Tél :04 26 23 45 52 zamboni@maths.univ-lyon1.fr
Matériaux	**MATERIAUX DE LYON** **http://ed34.universite-lyon.fr** Sec : Marion COMBE Tél:04-72-43-71-70 –Fax : 87.12 Bat. Direction ed.materiaux@insa-lyon.fr	M. Jean-Yves BUFFIERE INSA de Lyon MATEIS Bâtiment Saint Exupéry 7 avenue Jean Capelle 69621 VILLEURBANNE Cedex Tél : 04.72.43 71.70 Fax 04 72 43 85 28 Ed.materiaux@insa-lyon.fr
MEGA	**MECANIQUE, ENERGETIQUE, GENIE CIVIL, ACOUSTIQUE** **http://mega.universite-lyon.fr** Sec : Marion COMBE Tél:04-72-43-71-70 –Fax : 87.12 Bat. Direction mega@insa-lyon.fr	M. Philippe BOISSE INSA de Lyon Laboratoire LAMCOS Bâtiment Jacquard 25 bis avenue Jean Capelle 69621 VILLEURBANNE Cedex Tél : 04.72 .43.71.70 Fax : 04 72 43 72 37 Philippe.boisse@insa-lyon.fr
ScSo	**ScSo*** **http://recherche.univ-lyon2.fr/scso/** Sec : Viviane POLSINELLI Brigitte DUBOIS Insa : J.Y. TOUSSAINT Tél : 04 78 69 72 76 viviane.polsinelli@univ-lyon2.fr	M. Christian MONTES Université Lyon 2 86 rue Pasteur 69365 LYON Cedex 07 Christian.montes@univ-lyon2.fr

*ScSo : Histoire, Géographie, Aménagement, Urbanisme, Archéologie, Science politique, Sociologie, Anthropologie

Abstract

This work has been developed within the framework of non-stationary rotating machinery surveillance with emphasis on the detection of roller bearing defects. It focuses on the modeling and analysis of instantaneous angular speed variations. The numerical models developed are based on an “angular” approach which introduces explicitly the machine’s free body rotation degrees of freedom allowing simulations in non stationary operating conditions. A deep groove ball bearing model has been developed coupling tangential and normal forces by taking into account the rolling resistance phenomenon. This coupling allows to explain the origin of angular speed fluctuations in the presence of outer race roller bearing defects, phenomena that has been observed experimentally: a roller bearing defect periodically modifies the friction torque. The description of the gear mesh has been performed by means of a classic approach where the scientific issue has been to verify the compatibility with the angular modeling, cornerstone of this dissertation. Integration of the roller bearing and the gear modeling approaches into a simple mechanical architecture has shown that the presence of bearing defects provoking variations in the rolling element-races normal forces, modifies the gear mesh forces leading to perturbations of the angular speed. A simplified wind turbine model has been used for the test and validation of non stationary surveillance spectral indicators. The robustness of the model has been shown by means of a comparison with measurements performed on a wind turbine. It has allowed to show the importance of the operating conditions (load and speed), on the level of indicators used. This means the model may be used as a tool for phenomenological analyses as well as a device to test surveillance indicators. If needed, the approaches presented may be easily extended into more complex models of bearings, gears, casings and foundations.

KEYWORDS: Bearing and gear modeling, Instantanous Angular Speed, angular approach, non stationary rotating machinery surveilance

Résumé

Ce travail de recherche s'inscrit dans le cadre de la surveillance des machines tournantes en régime non stationnaire et plus particulièrement la détection des défauts de roulement. Il se focalise sur la modélisation et l'analyse des variations de la vitesse de rotation instantanée. Les modèles numériques développés s'appuient sur une approche originale dite "angulaire" qui introduit explicitement les degrés de rotation libres de la machine et permet de s'affranchir de condition de fonctionnement en régime stationnaire. Un modèle de roulement à billes à gorge profonde a été développé couplant les efforts de contact normaux et tangentiels grâce à l'introduction du phénomène de résistance au roulement. Ce couplage permet d'expliquer l'origine des fluctuations de vitesse de rotation en présence de défaut de bague extérieure, phénomènes constatés expérimentalement : la présence d'un défaut sur une bague modifie périodiquement le couple de frottement. La modélisation de la liaison par engrenages est plus classique, la problématique a été de s'assurer qu'elle était compatible avec l'approche angulaire utilisée dans ces travaux. Le couplage des éléments de roulement et d'engrenage dans un modèle simple a montré que la présence de défauts de roulement provoque des variations des efforts radiaux ce qui modifie les efforts d'engrènement et en conséquence perturbe également la vitesse de rotation. Un modèle simplifié d'une éolienne a été réalisé et utilisé pour tester et valider des indicateurs spectraux de surveillance en conditions de fonctionnement non stationnaires. La comparaison avec des mesures expérimentales issues d'une éolienne a montré la robustesse du modèle. Il peut donc être exploité comme un outil d'analyse phénoménologique et de test d'indicateurs de surveillance. Il a par exemple permis de montrer l'importance des conditions de fonctionnement (charge et vitesse) sur le niveau des indicateurs utilisés en surveillance. Si besoin, les développements proposés peuvent être étendus sans difficulté à des modèles plus complexes de roulements, d'engrènements et de structures d'accueil de ces éléments technologiques.

MOTS CLÉS: Modélisation de roulements et engrenages, Variation de la Vitesse Instantanée, approche angulaire, surveillance de machines tournantes en conditions de fonctionnement non stationnaires

Contents

List of Figures

List of Tables

General Introduction

The development of renewable energies is a worldwide priority for the energy transition and for the execution of the Paris Agreement signed the 12 of December 2015 as a result of the COP21 (Conference of Parties part of the United Nations Framework Convention on Climate Change) meeting. According to Ségolène Royal, French minister for the environment, the energy, the seas, in charge of international relations for the climate, the objectives of renewable energies foresee between 21800 and 26000 MW of installed onshore wind turbine generation capability in 2023. Within this framework, on December 1st 2016, Engie Green has been born from the fusion between MAIA Eolis and Futures Energies, becoming a major actor in the domain of renewable energies. Among the different domains where Engie Green develop its business, the expertise of the new company comprises the development, the construction, the operation and the maintenance of onshore wind farms.

Regarding the domain of the maintenance, the surveillance of the machines by non intrusive methods represents an angular stone to minimize the downtime increasing reliability and availability of the wind farms. This kind of technique is based on measuring one or several variables, in which a statistical threshold is estimated in normal conditions, allowing to set fault alarms based on the values of the surveyed variables.

The maintenance department of Engie Green, bases its Condition Monitoring System on the following technologies: oil temperature, oil analysis, the measurement of the active power and the measurement of the radial vibrations. Among these techniques, only the radial vibration allows the identification of the faulted components of the machine by means of advanced signal processing techniques. This feature permits the planning of the maintenance interventions for the replacement of the damaged components.

There are several critical details regarding radial vibration surveillance. A sensor (piezoelectric accelerometer) have to be installed near to almost every roller bearing of the machine to be able to perform the surveillance of the whole machine's shaft-line which makes the system very expensive. Besides, the sensors are attached to the casings which means that the response is largely filtered by the transfer ways of the mechanical system's supports. Another issue is that the measurements are sampled in time which makes almost impossible the analysis of the signals due to the large speed variations of a wind turbine in operation. This problem is solved by performing angular resampling of the signals which adds extra instrumentation and processing techniques increasing the costs of this technique.

In the framework of a CIFRE thesis under a partnership between MAIA Eolis (current Engie Green) and the LaMCoS of INSA de Lyon, a novel surveillance tool was proposed based on the analysis of the Instantaneous Angular Speed (IAS) measured with encoders by means of direct angular methods. Several processing techniques were studied and adapted in analogy of the radial vibration methods to be used for the study of the IAS and it was proved that a maximum of two encoders are needed for the surveillance of the whole shaft line of the wind turbines. Also, a long measurement campaign was performed and a method to treat non stationary spectral indicators was developed and improved after the thesis on a research and development project executed on the Expertise department of the company [3, 4].

While developing these projects different research perspectives were identified regarding the construction of mechanical models. The origin of the angular perturbations leading to speed variations related to cyclic mechanical phenomena was proposed to be explored to answer the question: Is the tangential perturbation and its transfer way independent of the radial excitations? The answer to this question is important to establish the complexity and the sizes in terms of degrees of freedom needed in a model to accurately describe the IAS response of a mechanical system. Once this question is answered, the construction of a mechanical model is intended to be used as a tool to develop and test complex surveillance indicators in a controlled environment in which the severity of the defect may be analyzed related to the operating conditions of the machine. With the interest of developing this research opportunities, Engie Green and the LaMCoS decided to propose the current thesis subject with a funding of the ANRT in a CIFRE framework.

Scheme of the report

The first chapter presents to the reader an introduction of the state of the art of the IAS as a machinery surveillance tool by performing a review of the literature versing about this technology. In this context, the measuring and analysis techniques concerning this research are expanded. Then, the introduction to the modeling approach considering the angular degree of freedom is presented by putting emphasis on the construction of the angle-time function as a tool to the analysis of the models under non stationary conditions.

A modeling approach for deep groove roller bearings is presented in the second chapter in which the origin of the angular perturbations is taken into account by means of the rolling resistance phenomenon which couples the radial and the tangential forces on the rolling elements - cages interaction. The model is then tested on two different mechanical architectures in which the potential of the model for handling non stationary conditions is shown. Additionally, the characteristics of the IAS response on the physical domain in presence of a defect is compared to an equivalent experimental measurement resulting from a research development presented in [5].

The third chapter presents an adjustment of the assumptions of a classic gear mesh model to validate its utilization considering rigid body angular rotations. In this framework, the roller bearing model is integrated to explore the transfer ways between the shaft as well as the impact of the gear mesh onto the IAS response. Next, A brief analysis of the impact of the support flexibilities of the system is performed showing the influence it has on the IAS in the physical as well as in the frequency domain.

Finally, the last chapter presents the construction of a wind turbine shaft line model, based on the modeling approaches introduced in the previous chapters. A model of the automated control was developed to manage the angular speed response of the system and the power generation under experimentally measured wind speeds. Then, a set of wind speed measurements were used to generate the IAS responses considering a roller bearing defect evolution to estimate different surveillance indicators. The IAS were obtained by simulating the quantification method performed in reality to the encoder signals. The indicators were normalized by means of the methodology used by Engie Green and the results are compared with an experimental campaign in which a roller bearing defect appeared in the machine. These results show the potential of the model to be used as a tool for testing and developing complex surveillance indicators.

Chapter 1

IAS as a tool for machinery surveillance: from measuring to modeling

Contents

1.1 Introduction

Being the analysis of the instantaneous angular speed signal as a preventive maintenance tool and the modeling of the attached phenomena the center of this dissertation, this chapter focuses on the state of the art as well as on presenting the principles in which this technology is based which will serve as a theoretical background developed and deepened throughout the ensemble of the different chapters comprising this work.

The first part will be committed to present the state of the art of the IAS technique by evoking the research dedicated to measuring the phenomenon and describing the type of instrumentation and the measuring technique that has been pointed as the more advantageous to measure the IAS signal. In addition, even if not a lot of work has been published regarding the analysis tools for the IAS technique, an overview of the few published work will be presented as it represents the basics for the tools that will be explored further.

Finally, as modeling of the IAS phenomena represents the main core of this dissertation, published work in addition to the concept of the angular approach will be presented and discussed to give a reference frame and a point of departure to the current research.

1.2 The angular domain and the IAS

It has been widely proven that the dynamics of rotating machines is perturbed when mechanical defects develop in the rotating parts [6]. The events causing the dynamic perturbations occur recursively and are inherently periodic if the machine is under a stationary regime. Standard machinery vibration surveillance equipment is developed mostly for frequency observation which is directly linked to cyclic phenomena such as unbalance, mechanical looseness, bearing component defects and gear defects among others. However, the increasing number of industrial applications demanding for non stationary machines (e.g. wind turbines, airplanes, automotive transmissions, etc.), has been a catalyst for the improvement and the development of condition monitoring techniques. The difficulty with the typical vibration analysis in presence of non stationary regimes, which also implies variable load, is that it causes frequency modulation and also spectral smearing which hide the defects on the spectral domain complicating detection, analysis and prognosis of faults [7].

Most of the developed techniques for tracking defects in non stationary conditions take advantage of the cyclic characteristics of the system dynamics by taking the analysis to the angular domain instead of the time domain [8]. In the angular domain, all cyclic phenomena are directly related to the rotation of the shafts of the inspected machine and the dependency with time and ergo with speed is no longer an issue. Nevertheless, as it was mentioned before, the variation of the operating speed has a straight impact on the load applied to the mechanical components changing the amount of energy variation induced by the defect and thus the surveillance indicators. Different techniques have been developed to perform the angle domain conversion, and they are grouped in what is called order tracking techniques.

The principle of order tracking analysis is to sample the dynamic signals in equal angle intervals. Among the different techniques to perform order tracking, the most popular involves the estimation of the IAS as a reference signal permitting to obtain the angle/time function, allowing to pass from time sampling to constant angle sampling. In this framework the use of the cyclostationary processing tools [9] and further extension to cyclononstationary has extended the use of the order tracking analysis to rotative equipment signals of type deterministic (e.g gears) and nondeterministic (e.g. roller bearings) [10], making IAS estimation a fundamental issue.

In the last fifteen years, it has been proven that the IAS may be used not only as a reference signal to perform order tracking and cyclostationarity [11], the methods for measuring gear transmission error with optical encoders combined with the use of angular sampling led to the interest of the analysis of IAS as an original technique for the condition monitoring of variable operating condition machinery. Through the next section the state of the art of the use of the IAS as a machinery surveillance tool is presented.

1.2.1 State of the art of machinery surveillance by IAS

This section is dedicated to evoke the scientific research versing about the IAS as a tool for condition monitoring. The work may be divided into a group analyzing and describing estimation methods and another group focusing on applications in machinery diagnosis. The work corresponding to diagnostic is divided into Reciprocating and rotating machines applications, being the last the one in which this dissertation is focused.

A review of the techniques for measuring the IAS is presented by Li et al. [12]. The author stands out that the published IAS measurement techniques could be divided into time/counter-based methods and analog-to-digital converter based methods. The IAS is estimated by the system whether by counting the number of pulses in a given time duration or by measuring the elapsed time for a single cycle of encoder signal. In this sense, a more general classification has been proposed recently by André et al. [4] in which the first technique samples the data in the time domain and the second in the angular domain.

For some applications, the possibility of the installation of angular sensors is not possible or simply the surveillance system is not suitable for this kind of technology. In this cases the IAS is obtained from other measurements, usually radial vibrations signals. This kind of application is developed typically when the IAS is used as reference to resample vibration signals in the angular domain. One first proposition was developed based on complex envelope demodulation by Bonnardot et al. [13] from radial acceleration signals measured on a gearbox. Other methods are based on complex shifted Morlet Wavelets [14], the instantaneous frequency estimation [15], and harmonic signal decomposition methods [16] among others. Very recently, Leclère et al.[11] presented a multi ordered probabilistic approach in the frame of CMMNO 2014 diagnostic contest. The IAS was extracted for many contestants with various methods from non stationary wind turbine radial vibration signals. The methodology presented by the authors was shown to be more accurate than the results presented by the contestants.

Regarding the use of IAS as a machinery surveillance tool in the domain of reciprocating machines, Yang et al. [17] explore the feasibility of using the IAS waveform for evaluating the performance of diesel engines. A simple model of a four-stroke single-cylinder was developed from which the IAS variations of the main shaft may be obtained. Experiments on a test rig were performed for a healthy condition and a fuel leakage affecting the gas pressure in the cylinder. Model results showed how the variations of the IAS can be correlated to the gas pressure while the experiments showed that the leakage condition affect the IAS due to the gas pressure variation, information that can be used for performing condition monitoring. More recently and in the same framework, Desbazeille et al [18] performed a model based diagnosis of a large diesel engine based on angular speed variations. In this case the model was a more complex one, in which the shaft was discretized on many lumped nodes. Only the angular degree of freedom (DOF) was considered. The modal response of the model was corrected with experimental measurements of the IAS. The measurements were carried out with a laser rotational vibrometer. Once tuned, the model was utilized with few experimental data to train a neuronal network with the objective of performing pattern recognition of signals of faulted and healthy stages. In this context, an experimental fuel leakage fault was correctly diagnosed and identification of the faulty cylinder as well as indication of the severity of the fault was achieved.

In the domain of rotating machines, in direct relation with this dissertation, it is found that the first application for the IAS was the analysis of the gear transmission error. Several works have been presented where, by using two encoders the IAS signal has been obtained by means of the Elapse Time Method allowing to reconstruct the angle evolution of the shafts and therefore the possibility of transmission error estimation [19–21].

Applications for the IAS analysis for condition monitoring of electric motors were presented by Ben Sasi et al [22]. The authors perfomed the extraction of the IAS by means of the Hilbert transform filter [23] and further time differentiation of an encoder signal sample at a resolution of 360 pulses per revolution (ppr). A test rig with an induction AC motor coupled to a DC generator was tested at constant speed. Two cases of study were analyzed: an artificial rotor bar defect and voltage phase asymmetry. The analysis of the IAS signals were executed on the frequency domain by means of Fast Fourier transforms (FFT) and power density spectra. The results from the broken rotor bar show that the power spectrum reveals the defect through the pole pass speed sidebands around the speed frequency. The phase asymmetry defect was also observe trough the IAS waveforms and the power spectra, even when no mechanical load is applied to the motor, which may be useful to perform manufacturing tests before selling. In the same context, Spagnol et al. [24] used a test rig to investigate the influence of the current supply effect on the IAS measurement. The authors have detected some manifestations coming from electrical and magnetic phenomena which by means of the construction of spectral indicators could be used for machinery surveillance.

A study to analyze IAS monitoring of gearboxes under non-cyclic stationary load conditions was performed by Stander and Heyns [25]. In this study a simplified model of a single stage transmission of 4 degrees of freedom showed that the dynamics of an interacting pair of gears modifies the signature of the angular speed of the system. A test rig was built to perform tests over three different degrees of teeth defects, the operating angular speed was maintained constant as the load was fluctuating by means of an alternator varying the driving torque. The signature of the IAS was shown modulated by the fluctuating load conditions. To manage this, authors applied rotation domain averaging proving to be effective for non-cyclic stationary loads. Thus, a load demodulation normalisation procedure was also implemented to deal with cyclic stationary load modulation. These techniques combined were proven to improve the fault detection.

In a completely different approach, Renaudin et al. [26] analyze IAS to detect a natural roller bearing fault in an automotive application. The experimental tests were conducted in two stages. Former tests were delivered on a gear transmission test rig equipped with two optical encoders under stationary and non-stationary operating conditions. Then, tests were performed on automotive wheels mounted on an industrial vehicle in real operating conditions. This study was primarily based on the assumption that the presence of local faults induce very small angular speed fluctuations by changes in the kinematics. The processing of the angular speed signal consisted of a standard Discrete Fourier Transform performed on the angular domain. This work represents the primary bases for the analysis of IAS for condition monitoring of roller bearings. It was stated for the first time that the interest of angular sampling lies on the angular periodicity of the rotating parts of the mechanical system (frequency in events per revolution) no matter the operating condition, making it suitable for the surveillance of non-stationary machines. Results confirmed that faulted bearings originate angular perturbations observed within the IAS spectra. Authors concluded that due to the evident relation between the bearing fault dynamics and the response of the machine in terms of angular speed variations, further studies were imperative to understand how the spectral amplitudes of the bearing components are related to the nature and severity of the bearing fault.

As it was mentioned in the general introduction, one of the most extended works dedicated to the IAS was developed by André in his thesis dissertation. This work, a CIFRE thesis within a partnership between Maïa Eolis (current Engie Green) and LaMCoS, was entirely dedicated to the evaluation and the development of different processing and analysis tools for wind turbine surveillance through the IAS signal. In this framework André et al. [1] carried out a one year and a half experiment on a 2 MW wind turbine to qualify the potential of the IAS analysis. The generator's optical encoder, normally use for the machine's performance control, was used to compute the IAS signal. The measurements were focused on the low speed shaft of the machine to test the capability of the methodology when the sensor is placed far (three gear meshes away) from the surveyed mechanical components. Several signal processing solutions were developed during this work. Application of Hanning Windowing was proven to be useful to reduce the broad band perturbation phenomenon resulting from applying the Fourier transform to a non stationary IAS measurement. Results showed that spectra without windowing presented a hyperbolic shape due to the background noise induced by the macroscopic speed non stationary behavior. Part of this analysis will be briefly expanded in the next section to provide the reader with the theoretical and conceptual basics in which the current dissertation is supported. In a consecutive work [3] the authors developed a normalization procedure for becoming IAS spectral indicators independent of the operating condition based on a multivariate statistical approach.

To take advantage of the angular periodicity of a roller bearing defect, Bourdon et al. [5] developed a signal treatment tool to estimate the size of a roller bearing outer ring defect through the IAS signal by reconstitution of the speed variations using inverse Fourier

Transforms. The methodology was validated with measurements taken on a faulted roller bearing of a generator's wind turbine as a part of the same research project of [1, 3]. Among the conclusions, authors stated that IAS perturbations due to the bearing dynamics are less than 0.1% of the macroscopic rotating speed. Another interest observation is that in some cases the presence of a defect leads to a decreasing of the IAS perturbation amplitude which may explain why the detectability of a defect can vary with the operating condition. In a more recent work, Moustafa et al [27] showed experimental results of size defect estimations performed in a test rig with different seeded defect sizes on cylindrical roller bearings turning at low speed conditions. The results are promising, however, no information is given about the signal processing performed on the raw IAS signal which is important to have a vision of the difficulty of the method as well as the strengths and weaknesses.

In the frame of surveillance indicators selection and classification methods based on artificial intelligence, two works explored IAS indicators for gear defects on the same test rig. The former is the PhD thesis of Khelf [28] in which combined, temporal and angular accelerometer indicators as well as IAS indicators were used to test artificial intelligence classification methods for gear faults in non stationary conditions. The second work is the one of Fedala et al. [29] whom by using the same test rig in stationary conditions tested a different group of surveillance indicators extracted also from accelerometer and encoder signals. Both works stand out that in general, indicators extracted from angular sampled methods from accelerometer and encoder signals are more convenient for gear fault detection and identification. In both works is also pointed out that the use of combined angular measurement extracted indicators make the classification methods to perform better for fault detection. Fedala et al. pointed out that IAS and transmission error indicators performed better for defect detection and they pointed out that IAS measurements are more easily implemented as only one encoder is needed to survey both shafts.

Compared to the amount of published work about signal processing and experimentation, only few works have been presented concerning the modeling of the IAS phenomena regarding rotative equipment surveillance. Bourdon et al [30], presented a novel method of writing the equations of motion of a mechanical system in the angular domain and tested the introduction of a periodic angular disturbance leading to IAS perturbations. The rotating mechanical system is described by a nonlinear system of two equations and can be solved by common numerical methods. In a subsequent work, Bourdon et al [2] introduced a parametric model of an angular periodic disturbance representative of a mechanical fault on moving parts. This disturbance is linked to the angular DOF representing the mechanical component having the defect introducing small angular speed variations. The parametric disturbance is introduced by the perturbation of the external force and the angular nature of the parameters make the equations more suitable to be solved in the angular domain. A test rig was developed to deepen the understanding of the relationship between a bearing defect and the IAS variations. The test rig consists in a shaft supported by two tapered roller bearings. Adjustable radial loads are introduced through a device composed of a spherical bearing and two springs. A torsional numerical model of the bench was built to test the angular disturbance approach. In this case the disturbance is introduced as a perturbation external torque applied to the DOF representing the defective bearing. Experimental tests were conducted in non stationary conditions allowing the tuning and validation of the model. Numerical results showed good agreement with the experimental behavior confirming the potential of the approach. This research is also discussed further in this chapter as it is considered as the main foundations of the modeling approach introduced throughout this dissertation.

IAS analysis terminology

Before going further on this work it is important to familiarize the reader to the terminology adopted in this dissertation regarding the angular domain and the IAS to establish a clear differentiation from the temporal one. The terminology adopted was introduced, explained and argued by Rémond et al. in the editorial for the especial issue on IAS processing and applications [31]. In this way, the term *angle frequency* will be used in the current work to make reference to the extension of periodicity in the angular domain. The unit of the angle frequency will be then *events per revolution (epr)*.

The next section is dedicated to explain how the IAS is measured by means of the Elapse Time Method which is the one used and improved by Engie Green and the LaMCoS on their path to develop this signal as a surveillance machinery tool. This, with the aim of contextualize the reader in the angular nature of the IAS measurement technique.

1.2.2 Measuring the IAS for machinery surveillance

As it was mentioned in the previous section, it exists different surveillance applications based on the analysis of the IAS. Obtaining such a signal is subject to the choice of a transducer capable of converting the rotation of the mechanical device into an electric signal to be conditioned, in most cases, by an analogical to digital converter. Once the sensor is selected the estimation of the IAS signal can be performed in different manners. The ways in which the IAS may be estimated have been deeply analyzed by André et al. [4]. André has presented a classification for the different IAS measurement methods by dividing them into angular and temporal methods. A method is labeled as *temporal* when the signal is sampled in time, and *angular* when the signal is sampled in the angular domain. As it is expected, the angular methods are best adapted to accomplish the objective of machinery surveillance under non-stationary conditions. The choice made by Engie Green as a result of their research work, is the use of angular encoders as the measurement sensor, and the Elapse Time Method to perform the IAS estimation. Thus, a brief description of the sensor measurement principle as well as the Elapse Time Method follows.

1.2.2.1 Angular Sensors, the transducers for the IAS

The most typical transducer used to measure the angular speed is the *encoder*. There are basically three types, they can be optical or magnetic and the third kind is typically called hall effect rotary sensor [32]. Regarding to the sensor components, no matter the type of encoder, the operating principle of the sensor is similar. There are basically two main parts in an encoder: the rotative part or rotor and the reading head or sensor. The main characteristics may be described as follows:

With or without contact

Often, with the objective of improving the conditioning or for industrial protection requirements a roller bearing links the rotor to the fixed part of the sensor. On the other hand, non contact sensors have less influence on the rotor flexibility.

Air Gap

Is the distance between the rotor and the sensor characterizing non contact sensors. This parameter is important regarding ease of installation and performance in terms of resolution as well as the sensor response in terms of the mobility of the rotor that, at being attached to the rotating device shaft, will be submitted to its dynamics.

Type of mounting

There are basically two types of mounting, at the end of the measured shaft or else where. the “end mounted” can be hollowed or solid shafted as the other type can be nothing but hollow shafted. It exists also flanged mounted encoders which are typically magnetic. In this kind of encoder, the flange fixes the rotative part while the sensor is a separated device having its own base. These features are shown on Figure 1.1

(a) End mounted solid shaft

(b) End mounted hollow shaft

(c) Through hollow shaft

(d) Encoder flanged ring

Figure 1.1: Encoders. Types of mounting

Encoder Resolution

The resolution is the number of electric impulses delivered by the transducer by revolution of the shaft. It is usually expressed in pulses per revolution. The resolution is whether related to the number of sensitive segments of the encoder or to an interpolation procedure (if is the case) integrated in the sensor.

Signal conditioning

The conditioning of the encoder comprehends the amplification, filtering and the interpolation (if necessary) of the impulses delivered by the sensor.

As a result of several experimental analyses as well as economic analyses, André et al. [1] made the choice of using optical and magnetic encoders for measuring the wind turbine shaft line. As it was mentioned before, there are different methods to estimate the angular speed performed in the temporal or in the angular domain. The choice of the angular method has been made by several authors to performed their analyses for condition monitoring [1, 19, 20, 26, 33] and is described in the following section.

1.2.2.2 The Elapse Time Method

The Elapse Time Method consists in counting the pulses of a high frequency clock between two rising edges of an encoder signal. The information recovered by the data acquisition system is then treated with equation 1.1 to estimate the angular speed.

$$\bar{\omega} = \frac{\Delta\theta}{\Delta t_i} = \frac{2\pi}{R} \cdot \frac{1}{N_i \delta t} = \frac{2\pi}{R} \frac{f_c}{N_i} \tag{1.1}$$

where Δt_i is the elapsed time between two consecutive encoder rising edges separated by the angular distance $\Delta\theta$, R is the resolution of the encoder and f_c is the clock frequency. N_i represents the inferior integer number of clock pulses between two consecutive rising edges. Figure 1.2 shows a scheme synthesizing the IAS signal estimation.

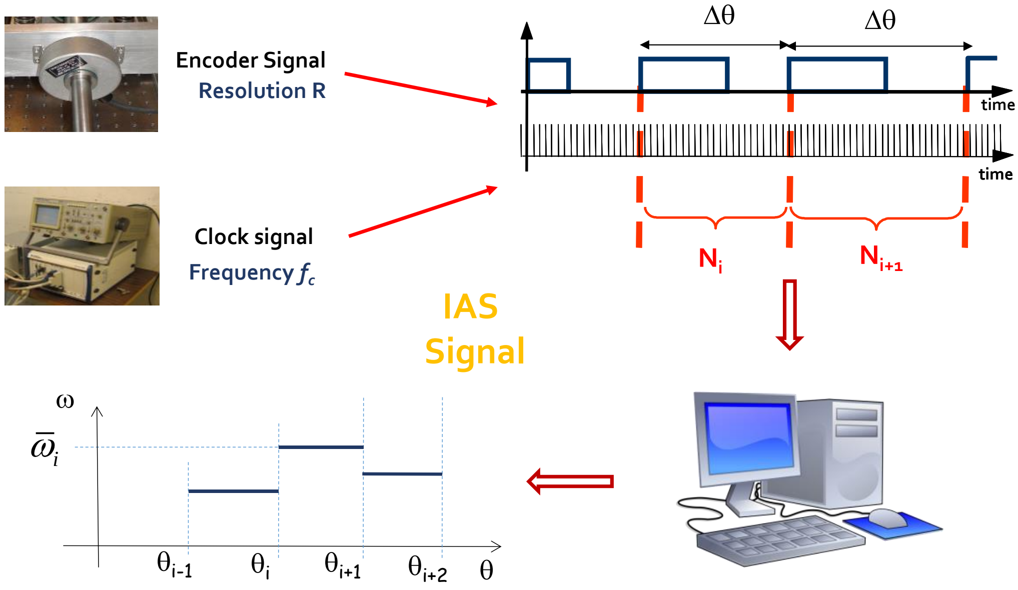

Figure 1.2: Schema of the IAS estimation by the Elapsed Time Method

When talking about machinery surveillance, the spectral analysis is a fundamental tool to observe the evolution of mechanical phenomena of periodic nature. The influence that the measurement method has over the IAS signal and its equivalent spectral behavior is then of enormous significance. As it can be observed from equation 1.1 the IAS obtained is averaged related to the elapsed time in each angular increment. Besides, the time difference is sampled according to the counter clock frequency. These two facts have influence over the IAS estimation. It was pointed out by André et al. [4] that this influence is manifested as a low-pass filtering effect as well as a quantization error directly linked to the counter clock frequency. In addition to the filtering and the quantization effects, it exists also another phenomena affecting the accuracy of the IAS: the geometrical error associated mostly to encoder manufacturing. Even if it is not on the focus of this work to deeply analyze the measurement errors, being aware of their effects into the IAS measured signal is important at the moment of analyzing it in the spectral domain. A brief description of the nature of theses errors and their consequences follows.

Filtering effect

As it was mentioned before, the measured IAS is a discretized average of the actual IAS meaning that the latter is low-pass filtered by the Elapsed Time Method. It was demonstrated analytically as well as experimentally by means of a test rig [4] that the measured spectrum of a IAS is attenuated by a cardinal sine shape.

Quantization error

The quantization error is originated by the estimation of the time occurring between two consecutive rising edges by means of the counting clock frequency. The number of clock ticks has to be rounded because of the non coincidences between the clock and the angle impulses due to the temporal and angular sampling. Therefore, the difference between the actual time between two rising edges and the clock ticks is what is called the quantization error. It was shown by André et al. [4] that the quantization phenomenon introduces spectral ghosts in the case of stationary signals or in the case of a very slow counting clock frequency. In the case of non stationary signals, the quantization phenomenon becomes a spread noise all over the frequency span and it depends on parameters as the counter frequency, the mean macroscopic speed and the angle frequency of the observed phenomena. It is important to consider this at the moment of setting up an IAS data acquisition system.

Geometric error

There are two main causes producing the geometric error [4]:

- The defects in the distribution of the sensitive segments or misalignment between the shaft and the sensor originating position errors of the rising edges during one revolution.
- The interpolation procedure generating position errors during a period.

One of the main characteristics of this error is that it is periodic in angle. In the spectral domain, this error will manifest itself in the shaft angle synchronous frequency of the angular speed variation and/or its harmonics. This represents a major inconvenient when a defect characteristic frequency coincide with an integer frequency, i.e. unbalance. Even though there has been some scientific and industrial efforts, a solution for this error has not been found, it is then an issue to take into account when IAS spectral analysis is performed.

1.3 Signal treatment techniques for IAS spectral observation

It was previously pointed out that in the research works where the IAS signal has been used as rotative equipment surveillance tool, the resource utilized for the analysis of the signals is the Fourier transform [1, 26, 27, 33] and/or the angular averaged signal for direct observation in the physical domain [19–21].

Besides the already mentioned research, the PhD dissertation of André [34] is the more comprehensive work (known by the author), about the treatment and analysis of the IAS signal measured with the Elapsed Time Method. As it was already pointed out, this dissertation oriented to wind turbine surveillance operating in non stationary conditions, is under confidential protection by interest of Engie Green. In this work, several signal treatment tools, as a logic extension of the vibratory analysis in temporal as well as in the angular domain has been presented and tested in experimental work performed over different test rigs and by means of an extensive measurement campaign (still running at the present day) deployed over different wind turbine machines. Two specific signal treatment techniques of the published work regarding the mentioned dissertation are presented as there are tools being used further in the current research.

1.3.1 Defect frequency localization and resolution

This development is closely related to the fact that in a wind turbine the great amount of mechanical elements under surveillance produce a bigger number of defect frequencies subjected to observation (57 for an Engie Green's Senvion MM82, Figure 1.3). This fact makes that a great number of observed defect angle frequencies be very close to each other which could demand increasing of spectral resolution to be able to differentiate the surveyed phenomena.

The technique of zero padding was proposed to artificially reduce the width of the angle frequency channels within an interval defining the vicinity of the angle frequency of interest. The size of this interval will depend on how the defect angle frequency may vary according to the mechanical features of the surveyed asset. It is well known, for example, that spectral channels in which the defect of a roller bearing manifests may change affected by the operating conditions and load, varying the contact angle and the slippage conditions which finally changes the bearing kinematics [35]. The technique was proved effective but computing expensive and difficult to apply. Also, parameterizing the

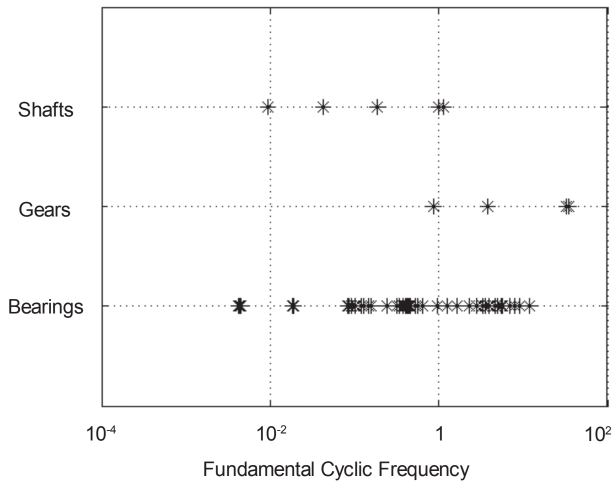

Figure 1.3: Angle Frequency distribution of the MM82 shaft line components [1]. Frequency in *epr*.

intervals which is mostly empirical work, would be complex due to the already mentioned number of observed angle frequencies.

1.3.2 Treatment of the macroscopic tendency

Treating a raw non-stationary signal introduces spectral noise over the entire frequency span being more pronounced in the range of the low frequencies. Figures 1.4(a) and 1.4(b) show these phenomena in a raw measured IAS signal from the High Speed Shaft of a Senvion MM82 wind turbine.

It was shown and proven by André et al. [1] that with the application of an apodization window such as the Hanning window the perturbation will be efficiently reduced permitting a better observation of the spectrum. The effect of a Hanning window applied over a wind turbine IAS High Speed Shaft signal is shown in Figures 1.4(c) and 1.4(d), where the broadband effect of the macroscopic behavior is efficiently reduced allowing the easy observation of a peak representing one of the machine's gear mesh angle frequencies.

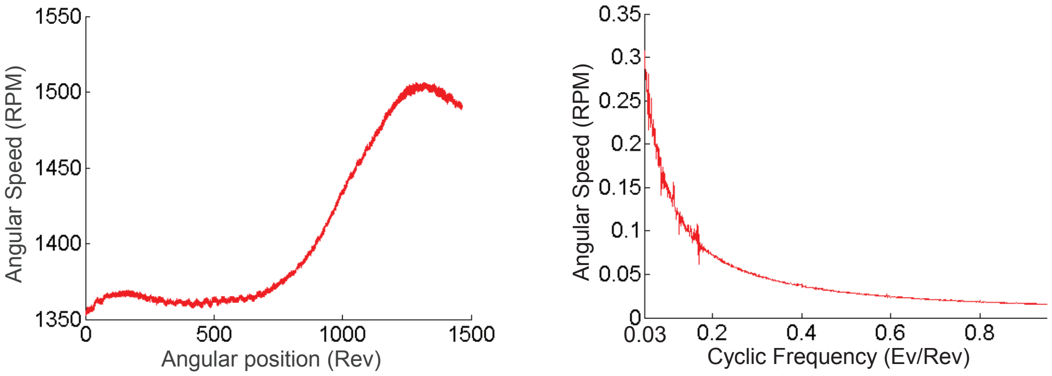

(a) Raw measured IAS signal

(b) Raw IAS Spectrum

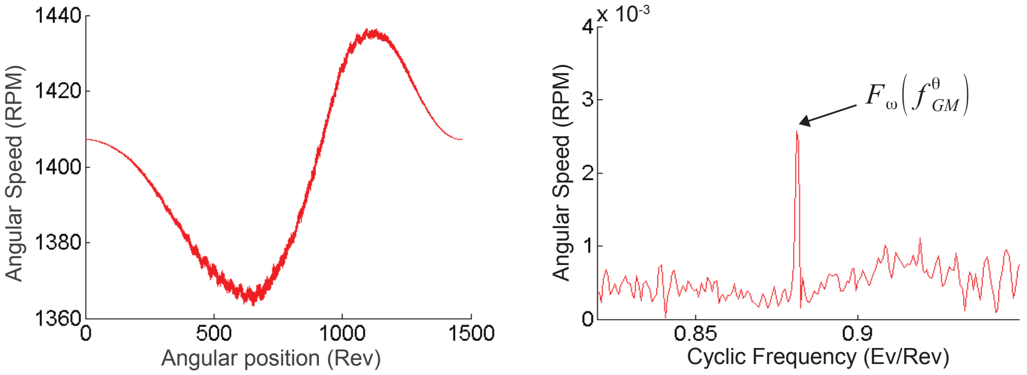

(c) Windowed raw measured IAS signal

(d) IAS Spectrum

Figure 1.4: IAS signals measured on the HSS of a MM82. Windowed and not windowed treated signals [1]

1.4 Modeling the IAS

In the previous sections, it was pointed out the potential that analysis of the IAS signal expressed in the angular domain has for detection of incipient faults in rotative equipment, even when operating in non stationary conditions. Mechanical modeling is considered to be an interesting mean to understand and test physical phenomena.

In this context, Bourdon et al. [2, 30] have given the first steps to explain how the dynamics of angle periodic mechanical devices lead to IAS variations. They have also proposed a method to express the equations describing the behavior of the system in the angular domain. In the next sections are described the more important contributions of this research in which the developments presented in the subsequent chapters find their foundation.

1.4.1 The angle time function as the basics for modeling angular perturbations

The point of departure to introduce the nature of the origin of the angular speed variations is the classical representation of the dynamics of a rotating flexible shaft with n degrees of freedom. This configuration is expressed by the matrix system of differential equations:

$$[M]_{nn} \cdot \{\ddot{X}\}_n + [C]_{nxn}\{\dot{X}\}_n + [K]_{nxn}\{X\}_n = \{F_{ext}(t)\}_n \tag{1.2}$$

A mechanical defect will change the ensemble of the dynamic parameters of a given system. Theses changes will subsequently generate among other consequences, very small angular speed variations. The solution of a system of equations described by Equation 1.2 is expressed by the vector $\{X\}$. To be able to described angular perturbations an approach was presented by Bourdon et al. [2] in which the angular DOF of the system needs to be considered explicitly in the resolution of the equations. The angular DOF $\theta(t)$, a component of the vector $\{X\}$, represents the angle-time function and it contains the information of the variable perturbations. This function could be described as:

$$\theta(t) = \theta_o(t) + \Delta\theta \tag{1.3}$$

Where the variable $\theta_o(t)$ represents the rigid body rotations and $\Delta\theta$ a set of angle periodic perturbations originated from the system's dynamics. It will be discussed further in this dissertation that most of the applications found in the literature are meant to treat systems operating in stationary conditions i.e. constant angular speeds. This consideration leads to replace the rigid body angular variable by (e.g. [36, 37]):

$$\theta_o(t) = \Omega_o \cdot t \tag{1.4}$$

In consequence, the angular rotations obtained in these models are those describing the small angle perturbations. In general, in the approach presented by Bourdon et al. the estimation of the angle time-function is intrinsically performed by the resolution of the equations considering the rigid body rotations and the angular perturbations. This last consideration allows not only to couple both phenomena but it leads to the possibility of dealing with non stationary conditions.

Another important question regarding the modeling of the IAS phenomena is the origin of the angular perturbations in the mechanical system. Bourdon et al. [2] proposed an approach in the frame of roller bearing dynamics, which is described hereafter.

1.4.2 Torque perturbations as the source of angular speed variations

By analogy with the radial vibrations where variation of the inner forces of the system generates variations in the radial response of the same nature (in terms of frequency), it is inferred that small torque variations would be the origin of the angular perturbations in the system's response. In a general form, the disturbance may be expressed as small variations of the external forces $\left\{\Delta F_p(\theta)\right\}$, as well as small variations of the stiffness $[\Delta K_p(\theta)]$ and damping $[\Delta C_p(\theta)]$ of the faulted component. In practice, the current work will only take into account the force perturbations. The general system becomes:

$$[M]\cdot\left\{\ddot{X}\right\} + [C]\left\{\dot{X}\right\} + [K]\left\{X\right\} = \left\{F_{ext}(t)\right\} + \left\{\Delta F_p(\theta)\right\} \tag{1.5}$$

With the objective of giving shape to the disturbance which is assumed to be impulsive in nature, the perturbed parameter is described by Bourdon et al. [2] as shown in Figure 1.5. Each of the non zero segments was defined with parametric sinuses to ease the handling of different amplitudes and angle periods.

The impulsive nature of the perturbation becomes the systems of Equation 1.5 non linear. The resolution is to be performed with numerical non linear methods. Note that the objective of the presented analysis is the modeling of mechanical systems operating in macroscopic non-stationary conditions. When looking close at the perturbation presented in Figure 1.5(b), we can observe that in the case of non-stationary conditions, it would

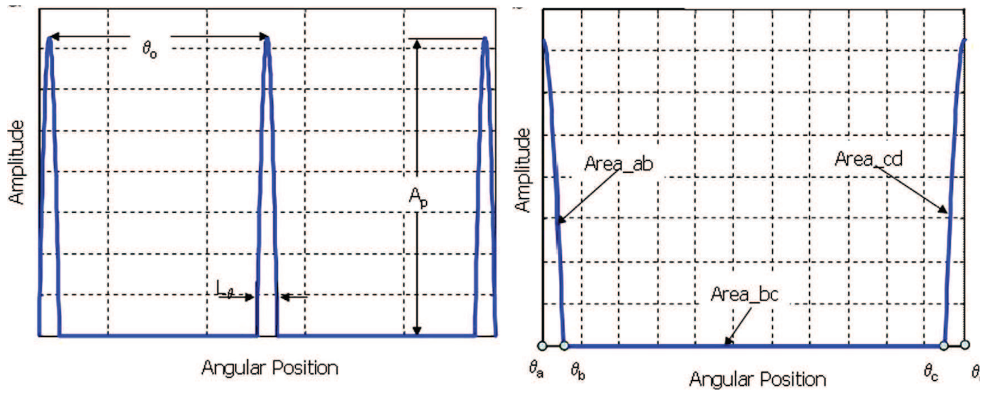

(a) Parametric perturbation definition (b) Angle period

Figure 1.5: General perturbation definition [2]

be difficult to determine the time in which the angles θ_a, θ_b, θ_c and θ_d are reached. This issue complicates the resolution algorithms and would be adding numerical errors that should be managed by limiting the size of the resolution time steps which would increase in consequent the calculation time. Bourdon et al. [2] proposed to handle the described situation by translating the problem into the angular domain, procedure described in the next section.

1.4.3 Expressing the general system of equations into the angular domain

First, the general system of equations 1.2 is expressed in the state form by setting:

$$\{Q\}_{2n} = \begin{Bmatrix} \{x\}_n \\ \{\dot{x}\}_n \end{Bmatrix} \tag{1.6}$$

Substitution of $\{Q\}_{2n}$ in equation (1.2) results in the following expression which now represents the general system:

$$\{\dot{Q}\}_{2n,1} = \begin{bmatrix} 0 & [I] \\ -[M]^{-1}\cdot[K] & -[M]^{-1}\cdot[C] \end{bmatrix}_{2n,2n} \cdot \{Q\}_{2n,1} + \begin{bmatrix} 0 \\ [M]^{-1} \end{bmatrix}_{2n,n} \cdot \{F_{ext}\}_{n,1} \tag{1.7}$$

We introduce matrices A and B as constants and defined by:

$$[A] = \begin{bmatrix} 0 & [I] \\ -[M]^{-1} \cdot [K] & -[M]^{-1} \cdot [C] \end{bmatrix} \tag{1.8}$$

$$[B] = \begin{bmatrix} 0 \\ [M]^{-1} \end{bmatrix} \tag{1.9}$$

By considering the defect perturbation $\left\{\Delta F_p(\theta)\right\}$ we have:

$$\left\{F_p\right\} = \left\{F_{ext}\right\} + \left\{\Delta F_p(\theta)\right\} \tag{1.10}$$

The perturbed general system becomes:

$$\left\{\dot{Q}\right\} = [A] \cdot \{Q\} + [B] \cdot \left\{F_p\right\} \tag{1.11}$$

We are focusing on the problem of modeling angle periodic perturbations representing mechanical defects. Once defined, the system of equations (equation 1.11) is translated into the angular domain [30]. To do so, the master DOF θ defining the angular position of the shaft supporting the defective element becomes the variable of integration.

Conventionally, the angular DOF θ is expressed by a function $\Theta(t)$, which may be invertible on its domain if:

$$\forall \quad t \in [0 \quad t_{max}], \quad \frac{d\Theta(t)}{dt} = \omega(t) \neq 0 \tag{1.12}$$

This mathematical condition for the inversion means that the angular speed of the system can not be equal to zero, which does not represent an issue on the operating conditions we are interested in this work. Then, we define the inverse of the angle-time function as:

$$t = \Theta(\theta)^{-1} = \Psi(\theta) \tag{1.13}$$

Let $\left\{\tilde{Q}(\theta)\right\}$ and $\tilde{\omega}(\theta)$ be defined by:

$$\begin{gathered} \left\{\tilde{Q}(\theta)\right\} = Q\left\{\Psi(\theta)\right\} \\ \tilde{\omega}(\theta) = \omega(\Psi(\theta)) \end{gathered} \tag{1.14}$$

Where "$\sim$" accounts for angle dependency. Substitution of these variables into equation 1.11 results:

$$\begin{cases} \dfrac{d\tilde{Q}(\theta)}{d\theta} = \dfrac{1}{\tilde{\omega}(\theta)} \cdot ([A_p] \cdot \tilde{Q}(\theta) + [B] \cdot \{F_p\}) \\ \dfrac{dt}{d\theta} = \dfrac{1}{\tilde{\omega}(\theta)} \end{cases} \tag{1.15}$$

The system of equations becomes an angular one, and it may be integrated by different non linear numerical methods. Notice that when the angular perturbations are considered only in the external forces, the mechanical parameters matrices are essentially the same.

Bourdon et al. [2] validated the angular resolution by comparing a non perturbed simple system solved in the time domain throwing exact results with equivalent resolution times. The perturbation approach was then tested by modeling an experimental bench designed especially for testing the IAS phenomena. This test rig was elaborated to test tapered roller bearings with the possibility of applying different external loads and non stationary conditions. Note that the loads applied are independent from the operating conditions. Experimental tests were performed for a healthy bearing and one with an outer race defect. At the same time, the test bench model was built considering only the torsional DOF. The model parameters were adjusted including the perturbations representing the defects. Only the torque components of the perturbation ($\{\Delta F_p(\theta)\}$) were considered. The angle period of these perturbations were set equal to the inverse of the angle ball pass frequency over the outer race (BPFO) to simulate the outer race defect. The authors reported good agreement between the experiments and the simulations. The comparisons were made for the IAS physical response as well as the spectral response. These results (experimental and numerical) validated the assumption made by the authors that in analogy with radial vibrations where radial forces induces radial acceleration variations, the angular speed microscopic changes linked to mechanical defects could be consequence of torque variations related to the component dynamics. The amplitude of the perturbations introduced were realistic regarding the experimental results. From the modeling point of view, the analysis also confirmed the importance of considering the angular DOF in the equations to be able to describe angular perturbations.

1.5 Conclusions

Throughout this chapter an introduction to the IAS signal, how is it measured and the existing tools for its analysis to perform rotating machinery surveillance has been presented with the aim of familiarizing the reader with the main subject of the current research work.

The last section dedicated to the state of the art of the modeling of the IAS phenomena represents the cornerstone of this dissertation. Construction of the Angle-time function by implicitly considering the angular DOF as an unknown variable couples the rigid body rotations with the small perturbations and allows handling of non stationary conditions. Also, the work of Bourdon et al. [2] has confirmed that by introducing angle periodical microscopic torque perturbations simulating a mechanical defect into the describing model of a given system, it is possible to successfully model the IAS signature obtained through experimental measurements.

The above statements opened the door to different possibilities of analysis. The evaluated test rig consisted in a single shaft with a roller bearing radially charged by an external device which leads to the following question: How is it possible that radial distributed loads on the rolling element bearing introduce torque perturbations leading to IAS variations. The answer to this question represents the core of the following chapter, where a roller bearing model is presented with the objective of understanding how the IAS variation phenomena is originated from the dynamics of the rotating mechanical components interacting with the loads applied to the system.

Chapter 2

Modeling Deep Groove Ball bearing dynamics introducing IAS variations

Contents

2.1 Introduction

In the last chapter, a general introduction of the IAS as a condition monitoring tool was presented by reviewing the state of the art and getting into the specifics of the nature of the signal and the mechanical origin of the phenomena. It was said that, by analogy with the corresponding radial vibration response having its origin in the variations of the interacting forces of the mechanism, the angular speed variations are originated by torque perturbations. What it is not clear is where these perturbations find their origin. Thus, through this chapter an approach is proposed to explain how torque variations are induced into the shaft of a mechanical system by means of the roller element bearing dynamics and radial load variations.

First, a short review of the literature of roller bearing modeling will be presented, oriented to existing models that are related to the approach that is going to be presented in this chapter. Then, the entire roller bearing model is described by going specifically in the origin of the perturbations leading to the angular speed variations.

The proposed approach is then tested by being integrated into simple shaft - support architectures and some simulations are compared with experimental results available on the literature. At the end of the chapter the discussion of the results will be presented leading to the integration of the model into more complex mechanical configurations.

2.2 Ball bearing modeling framework

The modeling of the dynamics of roller bearings has been in constant development since the first half of nineteenth century. Depending on the objective of the research, some works are dedicated to mathematically describing the experimental response of the bearing while others are based in the theoretical analysis of the mechanical components interaction. In the first group, the aim is to simply generate signals to be used as a tool for testing signal processing and detection methods. One comprehensive work in this context, was presented by Mc Faden and Smith [38] in which the bearing dynamics was described in terms of time frequency equations, taking into account the kinematics of the bearing leading to the characteristic frequencies. The model succeeded to simulate the amplitude spectrum of the demodulated vibration of a roller bearing under constant radial load with a defect in the inner race. In the same context Brie [39] proposes a different approach in which an analytical expression is presented modeling the bearing impulse with time-varying parameters. The model has been tested with different numerical simulations illustrating an inner race defect. One last example can be found in [40] where the authors model the defect as a series of short impulses occurring with a frequency inherent to the bearing characteristic frequency. The impulse was parameterized with the geometric characteristics of the bearing. These kind of approaches are only suitable to produce simulated signals that can be tuned to emulate specific dynamic behavior but they do not allow to describe the variation of magnitude in charge that occur in bearings, which is accentuated when the operating condition changes.

Regarding the approaches modeling the bearing's component interaction, the first extensive research about roller bearing dynamics was presented by Gupta [41] where the roller-races and roller-cages interactions were analyzed with consideration of elastohydrodynamic traction models for the lubricating film. Gupta presented several analytical formulations to estimate the normal forces and moments for deep groove ball and cylindrical bearings. More recent models use the theory of Hertz [42] for the estimation of the non linear normal force between the rolling elements and the races. In this context, Fukata et al. [43] introduced a two DOF model (displacements of the geometric center of the bearing) to connect the radial load of the system with the bearing raceways. The Hertz's non linear contact equation was used to estimate the normal forces of each roller bearing as a function of the race displacements. An extension of this analysis was presented by Feng et al. [44] whose added the bearing pedestals represented by two extra independent displacements. The model described, considers slippage by adding uncertainty to the rolling element location as well as mass unbalance and localized defects over the inner or outer races.

A more complex model was developed by Sawalhi and Randall [36]. This approach based on the model of Feng et al., comprehends 5 degrees of freedom. The extra degree of freedom, simulates a typical high frequency resonant response of the system where usually measurements with accelerometers are taken. The model takes into account the nonlinearity resulting from estimating the rolling element normal forces by means of the theory of Hertz which is translated into nonlinear varying stiffness related to the rolling element displacements. It also considers the bearing radial clearance. Localized defects may be added to the inner race (IR), the outer race (OR) and the rolling elements. Authors established the following assumptions: mass and inertia of the rolling elements are ignored, the rolling elements are in quasi static equilibrium and linear viscous damping is applicable. One of the limitations of this approach is that it was developed for a constant rotational speed of the inner race. The bearing model was tested and assembled to a lumped parameter model of a gear stage and shafts to build a numerical representation of a test rig.

Other approaches concentrate in the tribologic domain by improving the contact model whether by considering the bearing components as a 3D multibody interacting architecture [45] with the possibility of using the Finite Element method to estimate rolling element deformations [46], or by integrating elastohydrodynamic models taking into account the lubricant film interaction between the surfaces (rolling bearing - races) [47] or the wear of materials [48]. Models of this level of detail are difficult to be integrated into complex architectures due to the expensive calculation needed to obtain the body deformations and consequent forces. The deep groove bearing modeling approach to be presented in the next section is based on the analysis of Sawalhi and Randall [36], regarding the normal forces estimation. This choice was made to assure the possibility of coupling the model into more complex mechanical architectures. However some features were added to improve the coupling of the model into any mechanical structure and to describe the IAS phenomena. Among the novelties introduced, the model is suitable to manage variable operating conditions by considering the angular degree of freedom leading to the construction of the angle-time function and it is structured to be integrated into Finite Element shaft and casing models. Besides, the most important feature of the approach is the integration of the rolling resistance phenomenon describing the introduction of the perturbation leading to angular perturbations originated by the roller bearing dynamics.

2.3 Deep groove ball bearing model and the IAS perturbation approach

The roller bearing model is presented in the framework of a rotor-shaft-support system. The complete analytical description follows.

2.3.1 General shaft support model

We recall a general system's model with n DOF as it was presented in section 1.4.2 and described by equation 2.1:

$$[M]_{nxn} \cdot \left\{\ddot{X}\right\}_n + [C]_{nxn} \left\{\dot{X}\right\}_n + [K]_{nxn} \{X\}_n = \{F_{ext}(t)\}_n \tag{2.1}$$

The vector $\{X\}$ represents the generalized displacements. Matrices $[M]$, $[C]$ and $[K]$ are real, constant and symmetric and contain the ensemble of mass, damping and stiffnesses parameters of the mechanical system. The vector $\{F_{ext}(t)\}$ accounts for the external forces applied to the shaft.

The shafts and the supports are modeled in a classic way by a Finite Element configuration of beam elements with six DOF per node (three displacements and three rotations) organized as shown in equation (2.2). The component z represents the shaft rotation axis.

$$\{X\}_{nod} =^T \left\{x \quad y \quad z \quad \theta_x \quad \theta_y \quad \theta_z\right\}_{nod} \tag{2.2}$$

This approach allows supports to be modeled as simple elements of stiffness and damping or as reduced models obtained from FE codes. The assembly of the structural elements generates the system matrices $[M]$ and $[K]$ organized as described in equations (2.3) and (2.4).

$$[M]_{nXn} = \begin{bmatrix} [M_{shaft}] & 0 \\ 0 & [M_{Supp}] \end{bmatrix} \tag{2.3}$$

$$[K]_{nXn} = \begin{bmatrix} [K_{shaft}] & 0 \\ 0 & [K_{Supp}] \end{bmatrix} \tag{2.4}$$

n represents the number of DOF of the system. A modal approach is used for the structural damping. The modal damping matrix is obtained from the following expression:

$$[C_{mod}] = 2 \cdot \gamma_i \cdot \sqrt{[\Lambda]} \tag{2.5}$$

where $[\Lambda]$ is the eigenvalues matrix and the constant γ_i represents the modal damping coefficient. There is the possibility of choosing different values of the modal damping coefficient for each mode of vibration. If that is the case, γ becomes a diagonal matrix of size *nxn*. The damping matrix on the physical space is then obtained by:

$$[C] =^T [\Phi]^{-1} \cdot [C_{mod}] \cdot [\Phi] \tag{2.6}$$

in which $[\Phi]$ is defined as the modal matrix of the system.

2.3.1.1 The angular DOF or rigid body angular damping

Consideration of the angular DOF θ_z implies that viscoelastic damping in θ_z, or rigid angular damping ν has to be considered to reach the steady state condition. This parameter represents the set of mechanical losses of the system in rotation and it may be added to one of the rotational DOF of one node or it may be distributed into all the angular DOFs of the finite elements of the shaft. In Appendix A is illustrated the effect of this damping in a system of one degree of freedom. Notice that the steady state angular speed of the system is a function of this damping and it can be used to adjust the desired operating conditions of a given mechanical model. Throughout this work the rigid body angular damping is equally distributed through all the Finite elements.

2.3.2 Rolling element bearing model approach

To achieve the aim of making the model suitable to be assembled on classic Finite Element model configurations, roller bearings are considered as internal forces applied over two nodes representing the geometrical centers of the IR and the OR of the bearing. Theses forces describing the dynamic interactions between the shafts and the supports are expressed as a function of the IR and the OR displacements by means of the theory of Hertz. This model is shown on Figure 2.1. The nodes representing the IR and the OR have 6 DOF and they occupy the same geometric position when the system is unloaded. Therefore, depending on the configuration of the supports, the deep groove ball bearing model may have 12 DOF taking into account the IR and OR rotations.

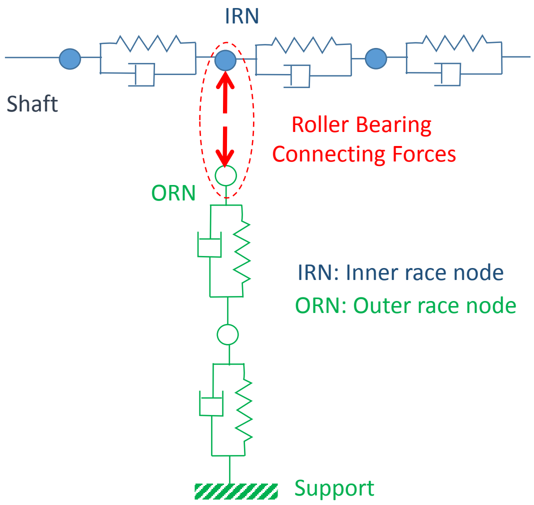

Figure 2.1: Bearing connecting element representation.

With this approach, the system of differential equations becomes:

$$[M]\ \{\ddot{X}\} + [C]\ \{\dot{X}\} + [K]\ \{X\} = \{F_{ext}(t)\} + \{F_{bea}(t)\} \tag{2.7}$$

where $\{F_{bea}(t)\}$ represents a vector assembled with the bearing connecting forces. The analysis that follows is based on the following assumptions:

1. There is no slippage between the OR, the IR and the rolling elements.
2. The rolling elements are in quasi static equilibrium, meaning that the normal contact force between the IR and a given rolling element is equal to the normal force between the OR and the mentioned rolling element.
3. The sole surface imperfections present on the races are the localized defects.

2.3.3 Roller bearing parameters

The main input parameters of the mechanical system represented by Equation 2.7 are the vector of external forces $\{F_{ext}(t)\}$ in which the torque applied over the shaft causing the system to turn is included. As it was already mentioned, the bearing connecting forces $\{F_{bea}(t)\}$ represent the interaction between the supports and the shaft. The output is the displacement vector $\{X\}$. The estimation of the bearing forces is based on the model of Sawalhi and Randall [36] adapted, as it will be shown in this section, to make it suitable for non-stationary input torques.

The bearing characteristics needed for the model description are: the number of rolling elements Z_b, the rolling element radius r, the rolling element mass m and inertia I, the inner and outer contact radius of the rolling element with the races (R_i and R_e), the clearance c, the defect frequency of the outer race $BPFO$, the rolling elements spin frequency BSF and the fundamental train frequency FTF. Figure 2.2 shows the initial position of the bearing and the coordinate system to describe the kinematics.

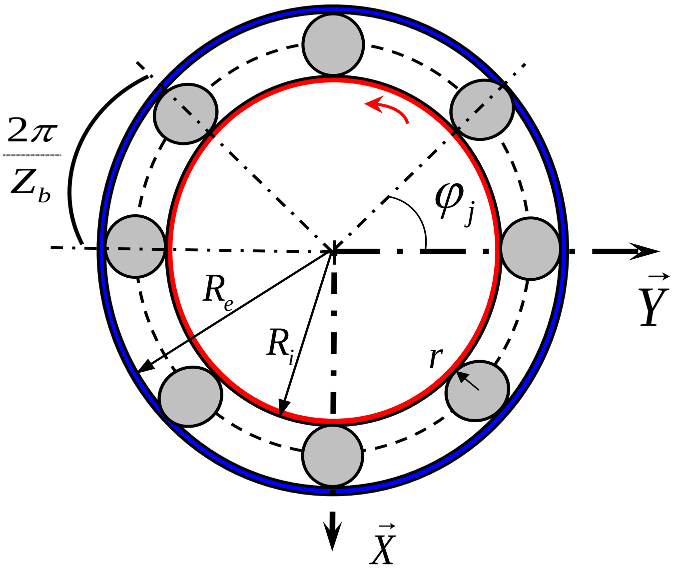

Figure 2.2: Representation of the deep groove roller bearing.

The rotation of all the components of the system is aligned with the shaft axis which is parallel to the coordinate Z. At an instant t the angular position of the j^{th} roller element is φ_j:

$$\varphi_j = \varphi_{jo} + \phi_c, \qquad j = 1,2...Z_b \tag{2.8}$$

where φ_{jo} represents the initial position of the j^{th} rolling element and ϕ_c is the angular position of the cage. At analyzing the kinematic bearing liaisons in presence of non-slippage we find that ϕ_c is a function of the angular position of the IR node θ_{IR}. For this analysis we have considered a fixed OR.

$$\varphi_{jo} = (j-1)\cdot\frac{2\cdot\pi}{Z_b} \tag{2.9}$$

$$\phi_c = \theta_{IR}\cdot FTF \tag{2.10}$$

The equation 2.10 is the key for the model to simulate non-stationary conditions because the rolling element angular position and the angle of rotation of the IR (θ_{IR}), are part of the unknown variables of the model as they form part of the response vector $\{X\}$, meaning that the system will interpret any torque perturbation as a variation of the angular displacements, speeds and accelerations.

2.3.4 The contact model

The contact model of Hertz is used for the estimation of the normal contact forces between the rolling elements and the races. For the j^{th} rolling element, these forces are described by the expression:

$$N_j = C_b \cdot \delta_j^{\frac{3}{2}} \tag{2.11}$$

where C_b represents the equivalent load deflection coefficient of the interaction between the rolling element and the bearing races. δ represents the overall contact deformation of the rolling element. The equivalent load deflection coefficient is obtained by the classical analysis of the Hertz's theory. Appendix B.1 deeps into the estimation of this coefficient.

The estimation of the overall contact deformation δ_j is performed as described by Sawalhi and Randall [36]:

$$\delta_j = (x_{IR} - x_{OR}) \cdot cos(\varphi_j) + (y_{IR} - y_{OR}) \cdot sin(\varphi_j) - c \tag{2.12}$$

The variables x_{IR}, y_{IR} and x_{OR}, y_{OR} describe the displacements of the IR and OR nodes in the plane defined by X and Y.

2.3.5 The modeling of localized faults

The introduction of the bearing defect is managed in the same way as in [36]. It is introduced by a modification of Equation 2.12 as follows:

$$\delta_j = (x_{IR} - x_{OR}) \cdot cos(\varphi_j) + (x_{OR} - y_{OR}) \cdot sin(\varphi_j) - c - \beta_j \cdot C_d \tag{2.13}$$

C_d describes the defect depth which angular leading edge is located at the angle ϕ_d and which length is the angular distance $\Delta\phi_d$. The defect is introduced as a variation of the bearing geometry managed by means of the fault switch β_j which is defined by the following expression:

$$\beta_j = \begin{cases} 1 & \text{if} \quad \phi_d < \phi_j < \phi_d + \Delta\phi_d \\ 0 & \text{otherwise} \end{cases} \tag{2.14}$$

2.3.6 Dynamics of the Deep Groove Ball Bearing considering normal and tangential roller element contact forces. Origin of the angular perturbation

The approach is based on the hypothesis that the rolling resistance phenomenon is occurring due to the interaction between the races and the rolling elements, which causes the coupling of normal and tangential forces. In a system as the one shown in figure 2.3, the local deformation of the solids in contact by action of the external forces is modeled by moving forward (direction of the mass center's rolling element speed u) the point of application of the normal force. The displacement of the normal force b is a function of the rolling resistance coefficient μ and the radius r of the rolling element as it is shown by Equation 2.15. The displacement of the normal force is instantly translated as a torque opposed to the direction of the angular speed of the rolling element. This torque may be associated to the frictional moment and in consequence, the rolling resistance coefficient is considered an analogy of the constant friction coefficient.

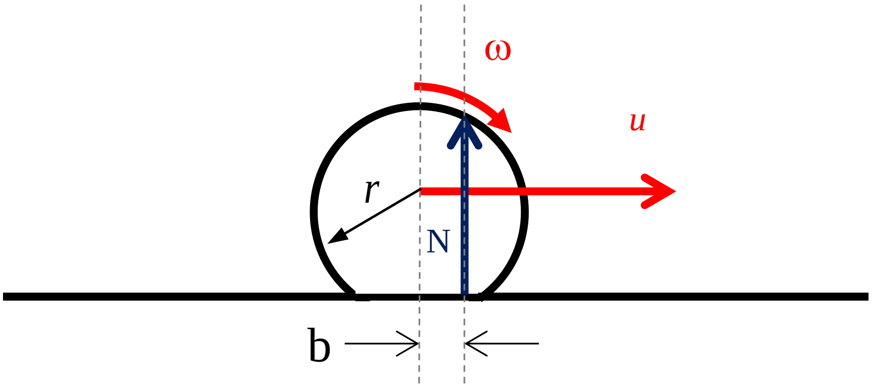

Figure 2.3: Rolling resistance phenomena.

$$b = \mu \cdot r \tag{2.15}$$

The dynamics of the bearing is analyzed considering the rolling resistance phenomenon. The free body diagrams of the j^{th} rolling element the inner and the outer races

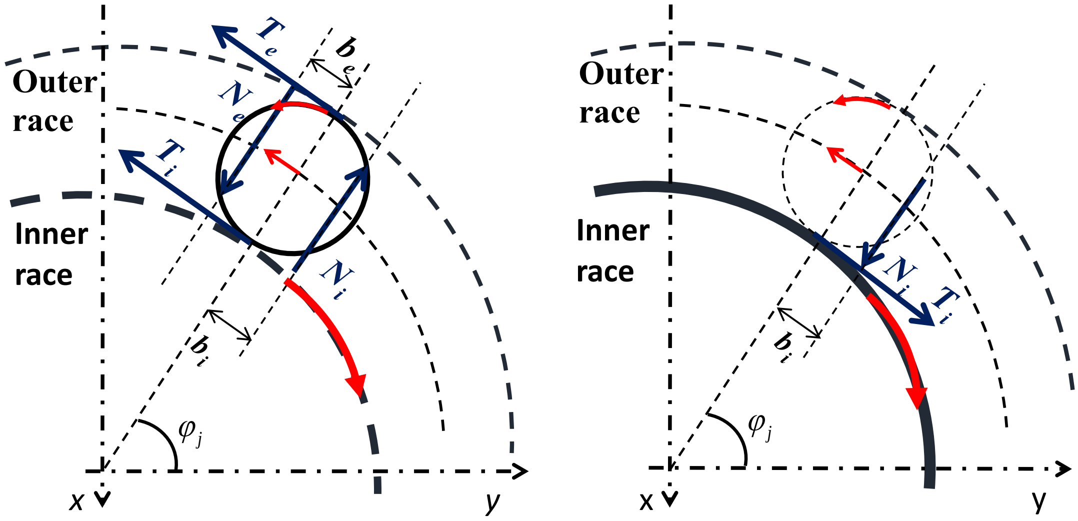

(a) Free body diagram of the j^{th} rolling element (b) Free body diagram of the inner race

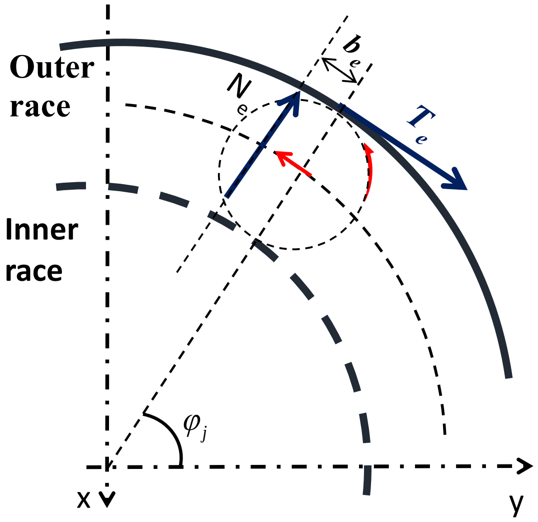

(c) Free body diagram of the outer race

Figure 2.4: Free body diagram of the rolling element-races interaction.

are shown in Figure 2.4. Considering the rolling element and the races as rigid bodies and applying the equilibrium of forces to the rolling element it is obtained:

$$m \cdot r \frac{d^2\theta_{b_j}}{dt^2} = T_{i_j} + T_{e_j} \tag{2.16}$$

Where θ_{b_j} represents the absolute rotation of the j^{th} rolling element in the XY plane; T_{i_j} and T_{e_j} represent the tangential forces between the rolling element and the bearing inner and outer races respectively. As the tangential forces are algebraic, the directions are established in an arbitrary manner in the same direction of the rolling element mass center displacement. All the analysis is performed neglecting the inner damping of the interacting bodies.

The equilibrium of moments of the j^{th} rolling element leads to the expression:

$$I \cdot \frac{d^2\theta_{b_j}}{dt^2} = r \cdot (T_{i_j} + T_{e_j}) + N_{i_j} \cdot b_{i_j} + N_{e_j} \cdot b_{e_j} \tag{2.17}$$

The quasi static assumption establishes the equality between the inner and outer race normal forces interacting with the rolling element:

$$N_i = N_e = N \tag{2.18}$$

The non-slippage assumption allows to set a kinematic liaison expressing the rotational DOF of the rolling elements θ_b as a function of the rotational DOF of the IR θ_{IR}:

$$\theta_{b_j} = \theta_{IR} \cdot BSF \tag{2.19}$$

Let γ_{IR} describe the angular acceleration of the IR which is not known at instant t. Then, operating Equations 2.16 and 2.17 leads to the general expressions of the tangential forces applied to the inner and outer race T_i and T_e, as a function of the bearing geometrical and physical parameters, the normal force between the rolling element and the races N_j and the angular acceleration of the inner race γ_{IR}:

$$T_{i_j} = D_{i\gamma_j} \cdot \gamma_{IR} + T_{iT_j} \tag{2.20}$$

$$T_{e_j} = D_{e\gamma_j} \cdot \gamma_{IR} + T_{eT_j} \tag{2.21}$$

$$\text{with} \quad \begin{cases} T_{iT} = \frac{1}{2 \cdot r} \cdot N \cdot (b_i + b_e) \\ D_{i\gamma} = \dfrac{1}{2 \cdot r} \cdot (I \cdot BSF + r \cdot m \cdot FTF \cdot R) \end{cases} \tag{2.22}$$

$$\text{and} \quad \begin{cases} T_{eT} = -T_{iT} \\ D_{e\gamma} = \dfrac{1}{2 \cdot r} \cdot (r \cdot m \cdot FTF \cdot R - I \cdot BSF) \end{cases} \tag{2.23}$$

Notice that at being the tangential forces a linear function of the normal force N, every change in the magnitude of this force, will induce tangential force perturbations which translate into angular perturbations. The next step is to find the resultant contact forces and moments over the roller bearing races. The resultant of forces and moments of the inner race by its interaction with the jth rolling element (See Figure 2.4(b)) is shown in the following expressions:

$$\begin{cases} \sum F_{IRx_j} = -N_j \cdot cos(\varphi_j) + T_{i_j} \cdot sin(\varphi_j) \\ \sum F_{IRy_j} = -N_j \cdot sin(\varphi_j) - T_{i_j} \cdot cos(\varphi_j) \\ \sum M_{xy_j} = -R_i \cdot T_{i_j} - N_j \cdot b_i \end{cases} \tag{2.24}$$

Expressing the inner race resultant forces and moments as a 6 degrees of freedom vectorial finite element arrangement it is obtained:

$$\{F_{IR}\}_j = \{F_{IRN}\}_j + \{F_{IRT}\}_j + \{F_{IR\gamma}\}_j \tag{2.25}$$

where,

$$\{F_{IRN}\}_j = \begin{Bmatrix} -N_j \cdot cos(\varphi_j) \\ -N_j \cdot sin(\varphi_j) \\ 0 \\ 0 \\ 0 \\ 0 \end{Bmatrix} \tag{2.26}$$

$$\{F_{IRT}\}_j = \begin{Bmatrix} T_{iT_j} \cdot sin(\varphi_j) \\ -T_{iT_j} \cdot cos(\varphi_j) \\ 0 \\ 0 \\ 0 \\ -R_i \cdot T_{iT_j} - N_j \cdot b_i \end{Bmatrix} \tag{2.27}$$

$$\{F_{IR\gamma}\}_j = \gamma_{IR} \cdot \begin{Bmatrix} D_{i\gamma} \cdot sin(\varphi_j) \\ -D_{i\gamma} \cdot cos(\varphi_j) \\ 0 \\ 0 \\ 0 \\ -R_i \cdot D_{i\gamma} \end{Bmatrix} \tag{2.28}$$

As it can be observed, the bearing connecting forces considering the rolling resistance phenomena have been decomposed in three main vectors. The former vector $\{F_{IRN}\}_j$

corresponds to the force bearing vector when no tangential forces are considered [36]. The second component vector $\{F_{IRT}\}_j$ represents the tangential forces directly related to the normal contact force N_j. Finally, the third vector $\left\{F_{IR\gamma}\right\}_j$ can be considered as the inertial component as it is assembled by expressions containing the inner race angular acceleration γ_{IR} as well as the rolling element mass and inertia.

Notice that consideration of the angular degree of freedom θ_z and the rolling resistance phenomena is what made the angular component of the force vector non equal to zero, which introduces torques into the different components of the system: rolling elements, outer and inner races and the shaft and represents the key of modeling the angular perturbations leading to angular speed variations.

Proceeding analogously the outer race bearing connecting forces vector and its components were obtained and are presented in equations (2.29) to (2.32); (See Figure D.10(c)).

$$\{F_{OR}\}_j = \{F_{ORN}\}_j + \{F_{ORT}\}_j + \left\{F_{OR\gamma}\right\}_j \tag{2.29}$$

Where,

$$\{F_{ORN}\}_j = \begin{Bmatrix} N_j \cdot cos(\varphi_j) \\ N_j \cdot sin(\varphi_j) \\ 0 \\ 0 \\ 0 \\ 0 \end{Bmatrix} \tag{2.30}$$

$$\{F_{ORT}\}_j = \begin{Bmatrix} T_{eT} \cdot sin(\varphi_j) \\ -T_{eT} \cdot cos(\varphi_j) \\ 0 \\ 0 \\ 0 \\ -R_e \cdot T_{eT} - N_e \cdot b_e \end{Bmatrix} \tag{2.31}$$

And,

$$\left\{F_{OR\gamma}\right\}_j = \gamma_{IR} \cdot \begin{Bmatrix} D_{e\gamma} \cdot sin(\varphi_j) \\ -D_{e\gamma} \cdot cos(\varphi_j) \\ 0 \\ 0 \\ 0 \\ -R_e \cdot D_{e\gamma} \end{Bmatrix} \tag{2.32}$$

The resultant forces for the kth bearing are composed by the sum of the forces of each rolling element over the inner and outer races as denoted in equation 2.33:

$$\begin{cases} \left\{F_{bea_{IR}}\right\}_k = \sum_{j=1}^{N_b} \left\{F_{IR}\right\}_j \\ \\ \left\{F_{bea_{OR}}\right\}_k = \sum_{j=1}^{N_b} \left\{F_{OR}\right\}_j \end{cases} \tag{2.33}$$

The general vector of bearing connecting forces is composed by the contribution of all the bearings comprised in the mechanical system. Its components have to be arranged following the finite element connectivity arrangement in which inner and outer race forces need to be carefully placed. Equation 2.34 shows the general expression for the bearing connecting forces vector (see Figure 2.1).

$$\left\{F_{bea}\right\} = \left\{F_{beaN}\right\} + \left\{F_{beaT}\right\} + \sum_{k=1}^{N_{bea}} \gamma_{IR_k} \cdot \left\{F_{bea\gamma}\right\}_k \tag{2.34}$$

where N_{bea} represents the total number of bearings being modeled in the mechanical system. Vectors $\left\{F_{beaN}\right\}$ and $\left\{F_{beaT}\right\}$ are composed by the normal and tangential rolling element bearing nodal force vectors properly assembled following the connectivity arrangement. The expressions $\gamma_{IR_k} \cdot \left\{F_{bea\gamma}\right\}_k$ are the k^{th} inner race inertial component, which are treated separately since in a multiple shaft system each inner race could have different angular accelerations.

2.3.7 General system rearrangement

Applying the procedure presented in section 1.4.3 the general system of n differential equations of order 2 (Eq. (2.7)) expressed in the state form is rewritten as a system of $2n$ equations of order 1 by setting:

$$\{Q\}_{2n} = \begin{Bmatrix} \{x\}_n \\ \{\dot{x}\}_n \end{Bmatrix} \tag{2.35}$$

Substitution of $\{Q\}_{2n}$ in equation (2.7) results in the following expression which now represents the general system:

$$\{\dot{Q}\}_{2n,1} = \begin{bmatrix} 0 & [I] \\ -[M]^{-1}\cdot[K] & -[M]^{-1}\cdot[C] \end{bmatrix}_{2n,2n} \cdot \{Q\} + \begin{bmatrix} 0 \\ [M]^{-1} \end{bmatrix}_{2n,n} \cdot (\{F_{ext}\} + \{F_{bea}\})_{n,1} \tag{2.36}$$

We recall the definition of matrices A and B:

$$[A] = \begin{bmatrix} 0 & [I] \\ -[M]^{-1}\cdot[K] & -[M]^{-1}\cdot[C] \end{bmatrix} \tag{2.37}$$

$$[B] = \begin{bmatrix} 0 \\ [M]^{-1} \end{bmatrix} \tag{2.38}$$

Substitution of equation (2.34) into (2.39) leads to:

$$\{\dot{Q}\} = [A]\cdot\{Q\} + [B]\cdot(\{F_{ext}\} + \{F_{beaN}\} + \{F_{beaT}\} + \sum_{k=1}^{N_{bea}} \gamma_{IR_k} \cdot \{F_{bea\gamma}\}_k) \tag{2.39}$$

The angular acceleration γ_{IR} may be expressed in vectorial form by:

$$\gamma_{IR_k} = \langle T \rangle_{1,2n_k} \cdot \{\dot{Q}\}_{2n,1} \tag{2.40}$$

Where $\langle T \rangle$ is a line vector whose components are zero except for the one corresponding to γ_{IR_k} which is equal to 1. Hence, equation (2.39) becomes:

$$\{\dot{Q}\} = [A]\cdot\{Q\} + [B]\cdot(\{F_{ext}\} + \{F_{beaN}\} + \{F_{beaT}\} + \sum_{k=1}^{N_{bea}} \{F_{bea\gamma}\}_k \cdot \langle T \rangle_k \cdot \{\dot{Q}\}) \tag{2.41}$$

The system is then rewritten to make it suitable for resolution:

$$\{\dot{Q}\} = [S]^{-1}\cdot([A] + [B]\cdot(\{F_{ext}\} + \{F_{beaN}\} + \{F_{beaT}\})) \tag{2.42}$$

Matrix [S] is the one allowing the accommodation of the unknown variables to prepare the system for resolution and is determined by:

$$[S]_{2n,2n} = [I]_{2n,2n} - [H]_{2n,2n} \tag{2.43}$$

Where $[H]$ is described as:

$$[H] = [B] \cdot \sum_{k=1}^{N_{bea}} \left\{F_{bea\gamma}\right\}_k \cdot \langle T \rangle_k \tag{2.44}$$

2.3.8 Resolution in the angular domain

Transformation of the system of equations into the angular domain has been performed by following the procedure described in section 1.4.3. The substitution of the angular variables defined in equation 1.14 into equation 2.42 results:

$$\begin{cases} \dfrac{d\tilde{Q}(\theta)}{d\theta} = \dfrac{1}{\tilde{\omega}(\theta)} \cdot [S]^{-1} \cdot \left([A] \cdot \tilde{Q}(\theta) + [B] \cdot \{U\}\right) \\ \dfrac{dt}{d\theta} = \dfrac{1}{\tilde{\omega}(\theta)} \end{cases} \tag{2.45}$$

with:

$$\{U\}_{2n,1} = \begin{Bmatrix} \{0\}_{n,1} \\ \{F_{ext}\} + \{F_{beaN} + \{F_{beaT}\}\} \end{Bmatrix} \tag{2.46}$$

The angular system may be solved with conventional non linear resolution methods. In particular, after testing different Matlab ODE methods, the ODE15s happens to be more effective in computation time for the systems tested.

2.4 Testing the roller bearing model under different mechanical architectures. Understanding the angular perturbations

In this section two mechanical configurations are tested comprising bearings modeled with the approach introduced in the previous sections. The aim is to take advantage of the different parameters that are possible to extract from the model results to look closer to the dynamics of the roller bearing and the nature of the perturbations introduced by OR defects.

2.4.1 Model of a single shaft supported by a deep groove ball bearing and a rigid support

The first model consists in a simple shaft supported by a deep groove ball bearing and a rigid support that works as a ball joint by restraining only the three displacements (x, y, and z equal to zero). A scheme of the mechanical system is shown in figure 2.5.

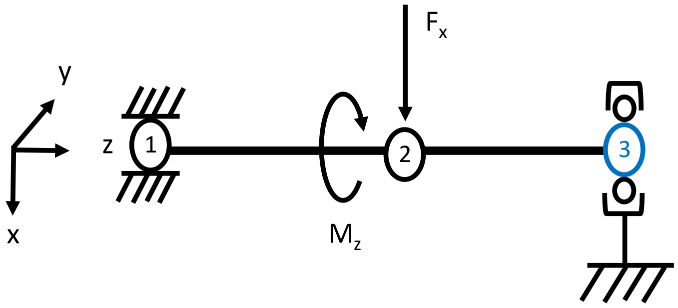

Figure 2.5: Single shaft supported by a DGBB and a rigid support.

The shaft's length is 600 mm, its diameter is 30 mm and it was discretized in two Finite Elements and three nodes. The external torque M_z is 15 Nm and the external static load F_x applied over the node 2 is 400 N. The bearing, which is a single row 6306/JIS deep groove ball bearing, is the same model as the one tested by Fukata et al. [43]. The value chosen for the rolling resistance coefficient was made equal to the constant friction coefficient for deep groove ball bearings which is 0.0015 [49]. Different runs were performed during 10 shaft revolutions simulation with and without defect. A spall with a length $\Delta\phi_d$ of 8° and a depth C_d of 100 μm was introduced at the outer race aligned with the bearing load zone as shown in figure 2.6.

Figure 2.7 shows the response of the “macroscopic” angular speed of the system. The steady state angular speed is a result of the relationship between the external torques and the rigid angular damping of the system (see Appendix A). It is recalled that the introduction of the rolling resistance phenomenon adds a resistant moment which depends

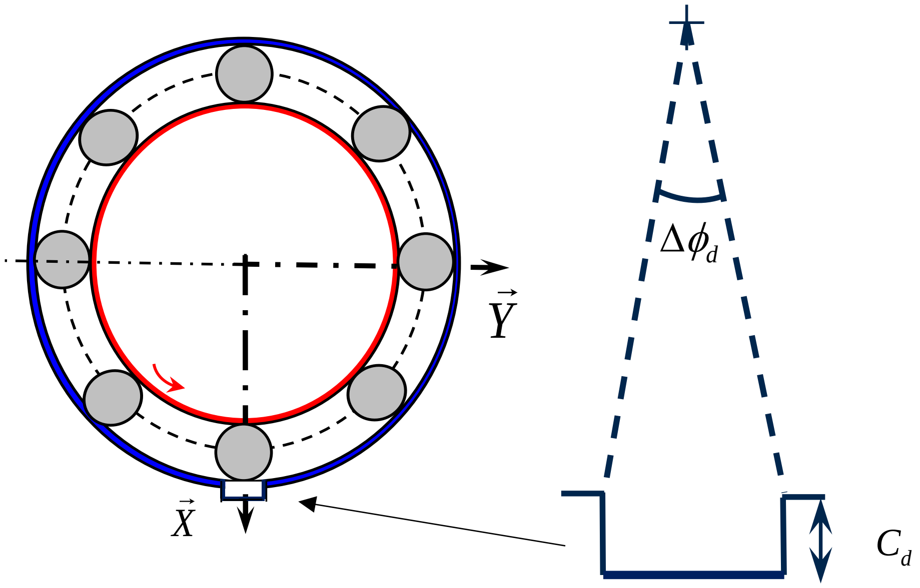

Figure 2.6: Defect representation, not scaled with the bearing’s geometry

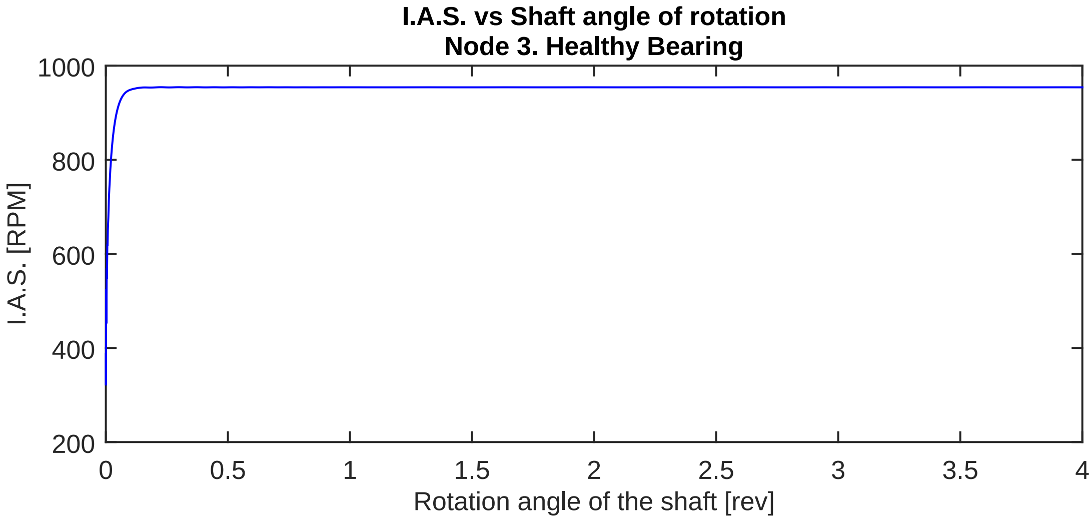

Figure 2.7: Single shaft supported by a DGBB and a rigid support.

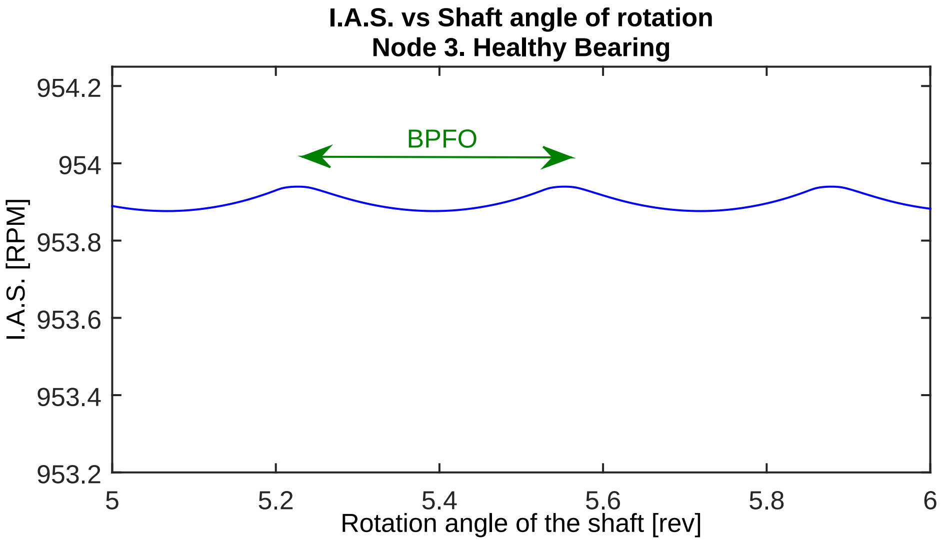

(a) Healthy bearing

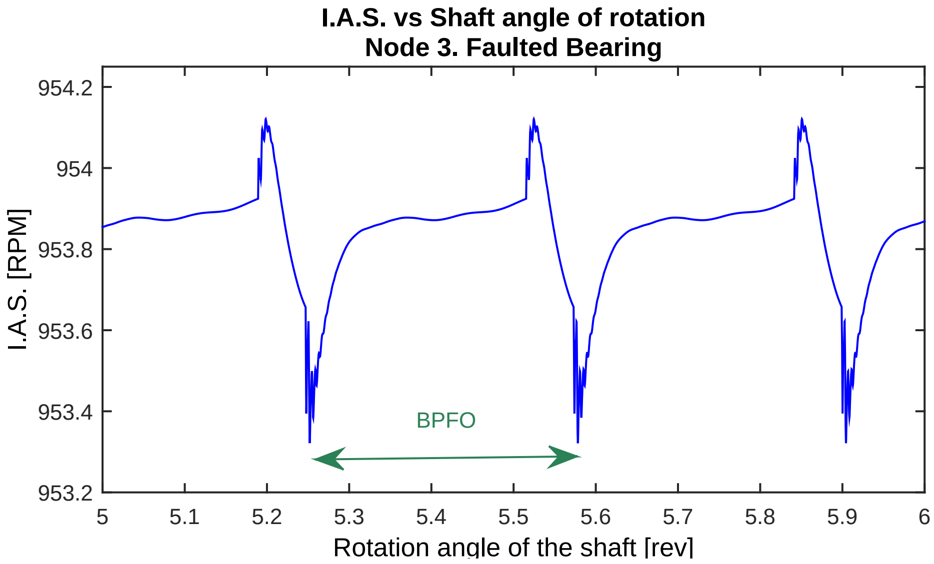

(b) Faulted Bearing

Figure 2.8: I.A.S. vs angle of rotation. Node 3. $\mu = 0.0015$

on the load applied to the bearing. This statement means that the rigid body solution described in the Appendix is altered by this moment making the obtained steady state angular speed lower than the expected value. When parameters of torque and speed are known or fixed, an iterative process is needed to adjust the value of the rigid damping ν leading to the expected response for a given resultant torque.

An amplification of the angular speed for the non-faulted and the faulted bearing is

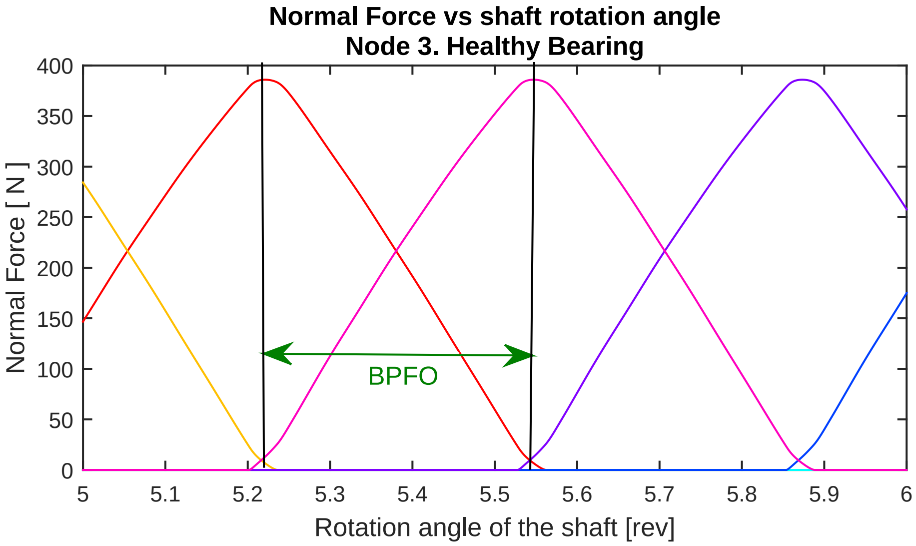

Figure 2.9: Rolling element normal force distribution

presented in figure 2.8 to observe the IAS phenomena on the node 3. First, it can be noticed that the "peak to peak" amplitude of the faulted bearing is around thirteen times bigger related to the healthy bearing curve. The angular frequency of the IAS perturbation is the BPFO expressed in the angular domain [26] which is 3.07 events per revolution. As it can be observed, the non-faulted bearing oscillation has also a frequency equals to the BPFO. This phenomena is related to the evolution of the normal force distribution between the rolling elements. Figure 2.9 shows this distribution for one revolution of the shaft. Each curve represents the normal effort evolution of one rolling element passing through the load zone. Here, we can appreciate how the angular frequency in which two rolling elements reach the maximum normal load is exactly the BPFO of the bearing. Thus, the perturbation observed in figure 2.8(a) has its origin on the torque induced by the rolling resistance phenomenon which is, as we have seen in the analysis, a direct function of the normal force. These phenomena have been found also experimentally by Bourdon et al [2].

Figure 2.10 shows the radial vibration speed and acceleration of the node 3 in the x direction for the faulted bearing. The observed event periodicity is related to the BPFO of the bearing. The "peak to peak" speed amplitude response around 250 mm/s, is coherent with the vibration amplitude of a faulted machine according to the ISO 10816-I for machines rotating between 600 to 12.000 rpm [50]. The shape of the response when the rolling element passes through the spall may be attributed to the spall squared shape and to the fact that the supports are rigid, however, this has not been confirmed.

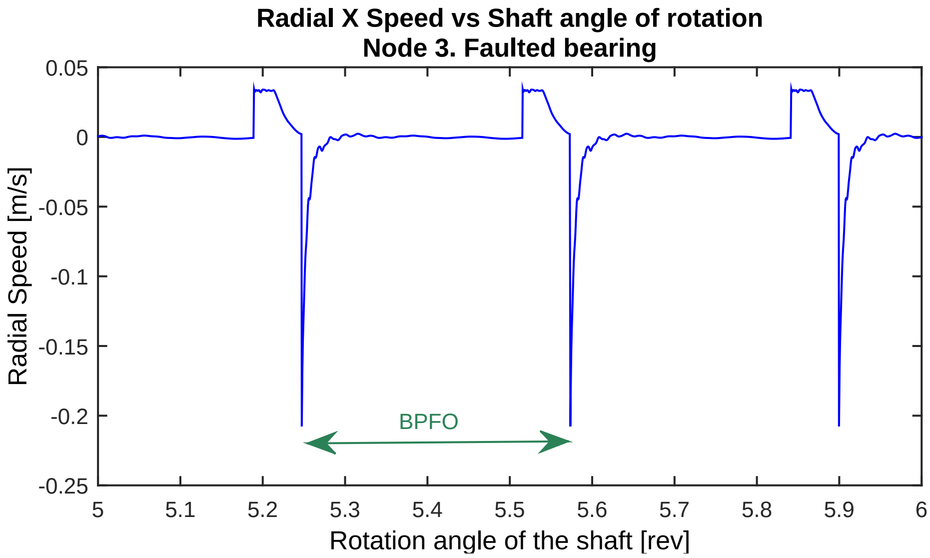

(a) Speed

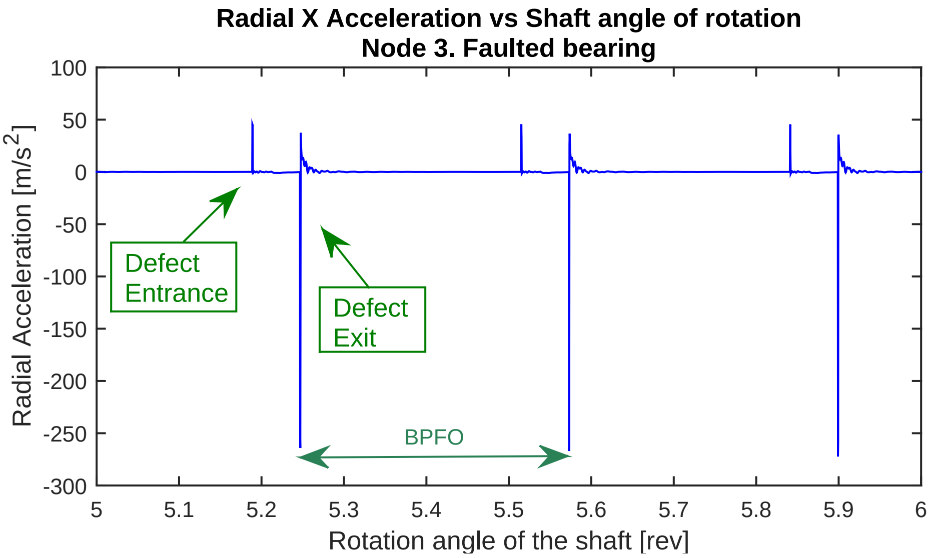

(b) Acceleration

Figure 2.10: Radial vibration, direction “X” vs angle of rotation. Node 3. $\mu = 0.0015$. Faulted Bearing

Finally, to test the potential of the model in non stationary conditions an input torque described with a ramp was set up between 1 to 10 Nm, leading to a linear response in the system’s angular speed. Figure 2.11 shows the IAS response of the faulted bearing with a rolling resistant coefficient μ of 0.060 to make the phenomenon observable on the plot. Notice that this choice was made knowing that the coefficient’s value was set without realistic basis but with the objective of showing the model’s capabilities. The perturbation representing the effect of the rolling elements passing through the defect has an angle frequency equals to the BPFO as it was observed on the previous figures. It is important to recall that the possibility of testing non stationary conditions, lies on the consideration of the angle DOF θ_z as an unknown variable, which is independent to the domain of integration (angular or temporal).

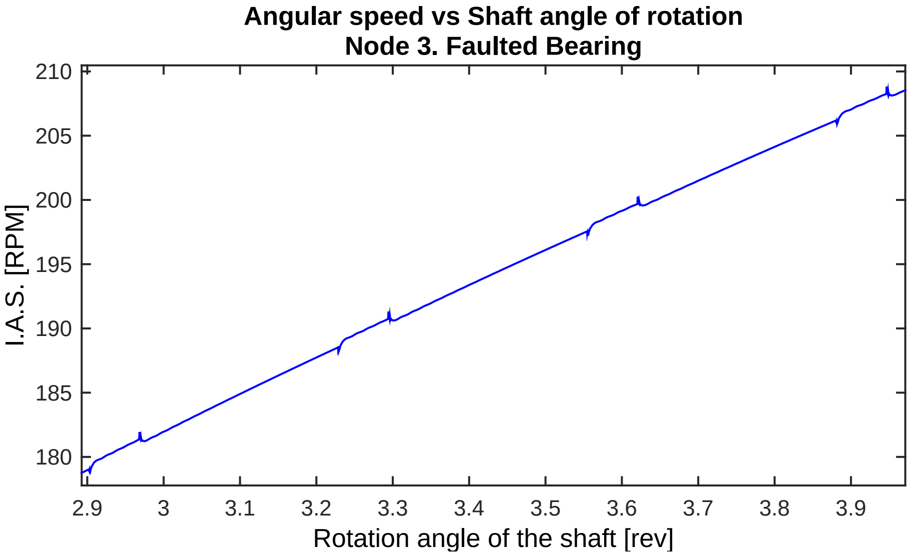

Figure 2.11: I.A.S. vs angle of rotation. Node 3. $\mu = 0.060$

To analyze the dynamic behavior of a system with two different bearings interacting, in the next section, one more bearing is added to the architecture.

2.4.2 Model of a single shaft supported by two deep groove ball bearings and rigid supports

The geometrical dimensions of the current mechanical configuration as well as the loads, torques and angular speeds were established inspired on a roller bearing test rig of the company SNR. As a part of a research project, they shared the bearing data used for the modeled bearings. Figure 2.12 shows the representation of the system discretized in three FE nodes plus two extra nodes representing the OR of the bearings which are resting on rigid supports. The shaft length is 400 mm and the diameter is 70 mm. The bearing in the node 1 is a 6214 bearing with 10 rolling elements and a BPFO expressed in the angular domain of 4.1045 ev/rev. This bearing will be for now on denoted as bearing 1. The bearing in node 3 is a 6314 with 8 rolling elements and an angular BPFO of 3.0760 ev/rev and will be identified as bearing 2. The external torque M_z was set up to 12.5

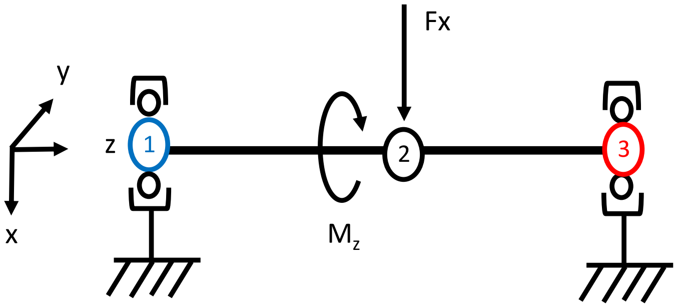

Figure 2.12: single shaft supported by two deep groove ball bearings

Nm and the external static force F_x equals to 45.90 kN. The perturbation torque leading to IAS perturbations was introduced by means of a rolling resistance coefficient μ of 0.0015 added to the bearing 1. To simplify the analysis in this section, a rolling resistance coefficient equal to zero was added on bearing 2, implying that no torque perturbation is introduced to the shaft from this bearing.

The methodology was first tested with healthy bearings. Then, a small defect characterized as a “pit” [51] was introduced into bearing 1. The angular length of the pit was $\Delta\phi_d$ of 8° with a depth C_d of 7 μm and it was located at the middle of the bearing load zone (see figure 2.6).

Figure 2.13 presents bearing 1 IAS and the induced perturbation torque versus the angle of rotation of the cage, which gives a different perspective referencing the plots to the rolling element translation. Notice that the torque applied over the inner race is calculated with equation (2.34) and is opposed in direction to the torque making the system turn (M_z). It represents an estimation of the actual frictional moment between the bearing rotating elements. Roller bearing commercial web packages give a value of the total frictional moment as a function of the load, the angular speed of the IR and the operation temperature of the bearing. This is the case of the bearing calculator provided by SKF [52] on its website, which was consulted to compare results with the current model for the operating conditions of Bearing 1. The friction torque found from SKF’s calculator was 1530 Nmm. From figure 2.13 we can observe that the average torque estimated with the bearing model is 1930 Nmm, which is in the same order of magnitude. This parameter may be used to calibrate the rolling resistance coefficient. More information about the friction torque estimation with the SKF calculator may be found in Appendix B.2.

Figure 2.14 shows the radial acceleration in presence of the defect of Node 1. In figure 2.14(a) we can observe the effect of two rolling elements going in and out of the

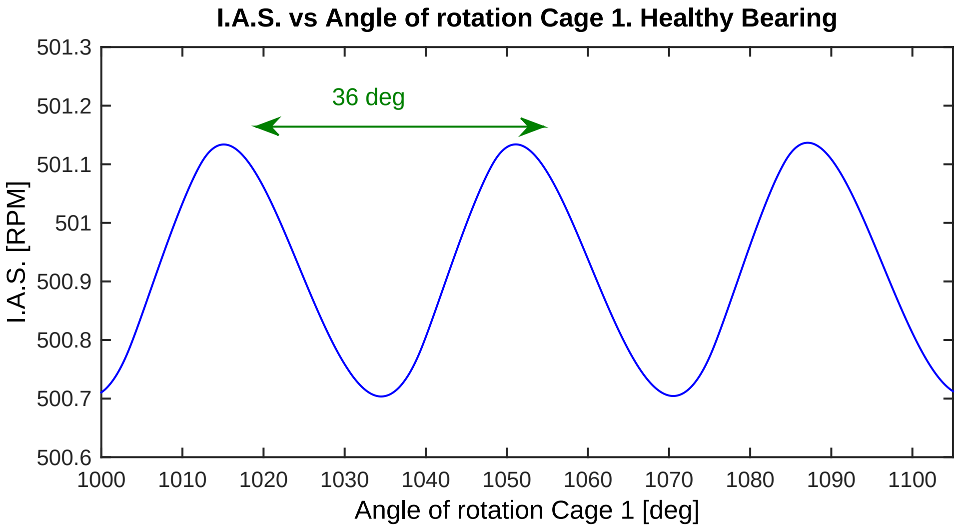

(a) I.A.S.

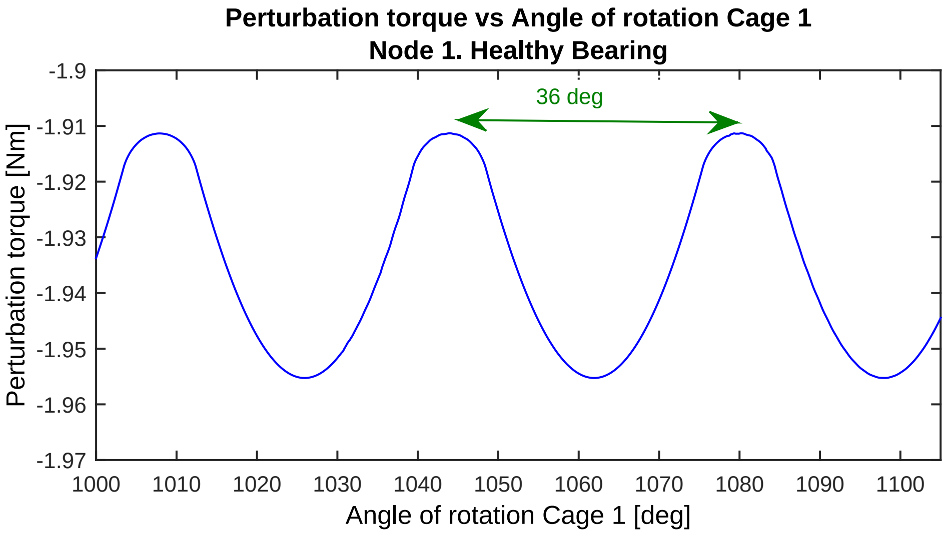

(b) Perturbation torque

Figure 2.13: I.A.S. and perturbation torque over the IR, Node 1 vs rotation of the cage. Healthy bearing

squared defect. The angle period of 36 degrees is equivalent to the angle between two rolling elements for a ten ball bearing. The angle of 8 degrees observed in figure 2.14(b) is the angular extension of the defect which, as it was mentioned, is one of the input variables of the model. This result is in agreement with published results concerning defects with squared profiles [5]. The IR resultant force X is presented in Figure 2.15(a).

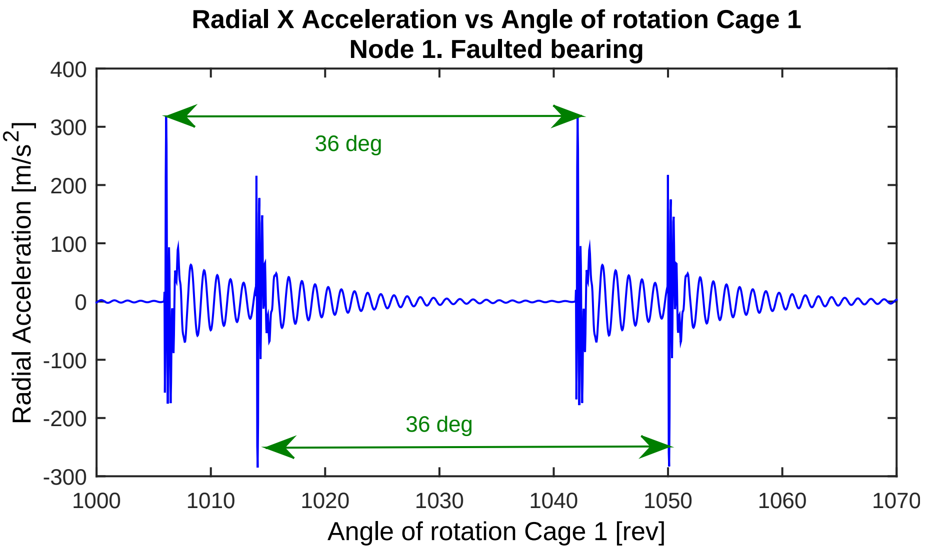

(a) Defect Angular period

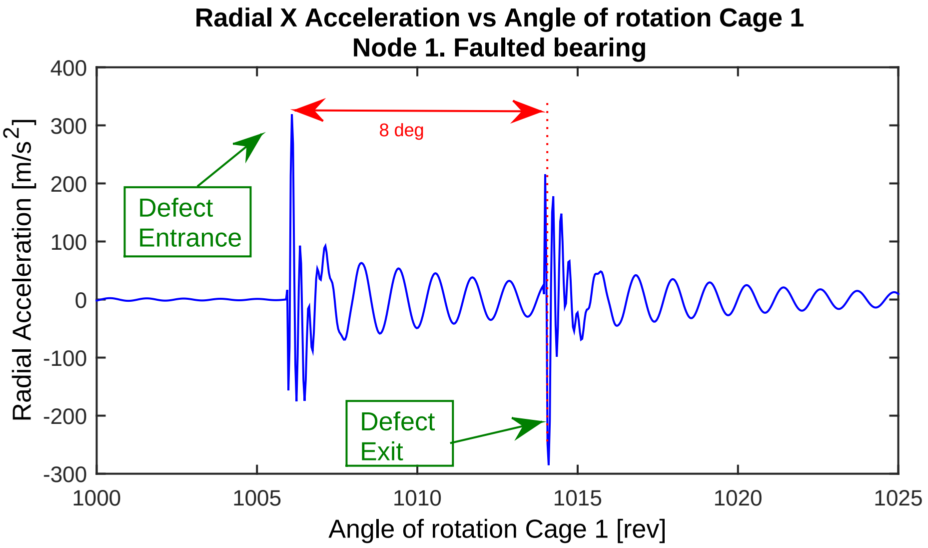

(b) Defect size

Figure 2.14: Radial acceleration of Node 1 vs rotation of the cage. Faulted bearing

Note that the force oscillates around the static charge of 22.95 kN which is, as expected, half of the force applied over the system ($F_x = 45.9kN$). A priori, we might be inclined to think that the response oscillations observed (Figures 2.14 and 2.15) are the ones of a regular free second order system. Actually, the system behaves as a closed loop non-linear system as shown in Figure 2.16. The defect provokes an impulsion which changes the position of the bearing races, thus, the bearing force reactions change. Figure 2.15(a) shows the variations occurring to the normal force distribution when a rolling element

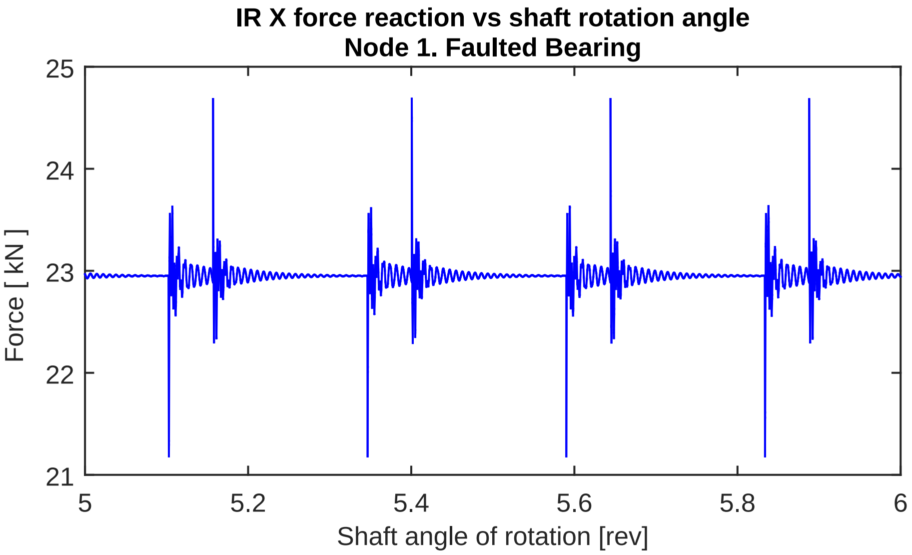

(a) Force reaction X over the inner race

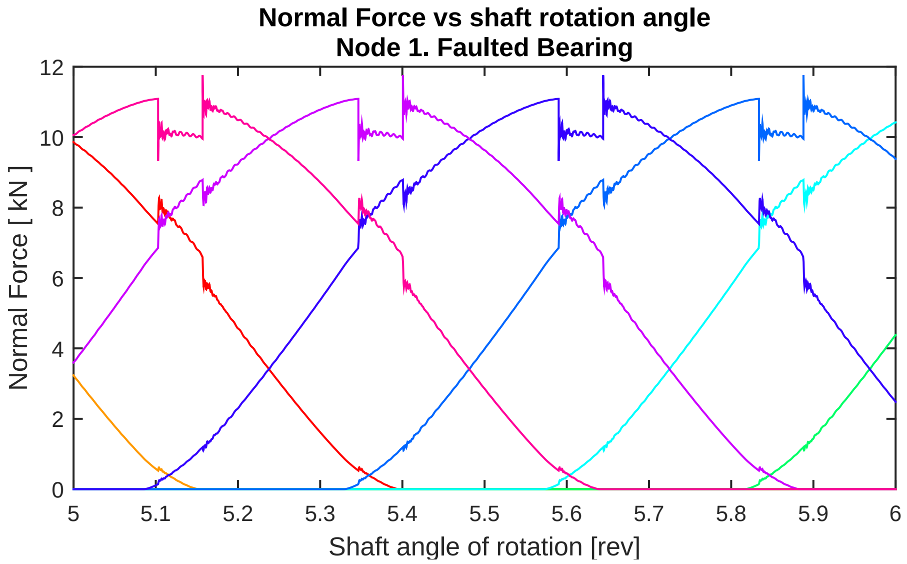

(b) Rolling element normal force distribution

Figure 2.15: Force reaction X and normal force distribution over the inner race vs rotation of the shaft. Node 1

passes through the defect. We can notice that the defect affects the value of the normal force not only for the rolling element passing through, but for all the elements inside the load zone. This result is expected because, as it is seen in the graph, when the ball is inside the defect loses charge, and the system compensates the load distribution by increasing the load into the other rolling elements.

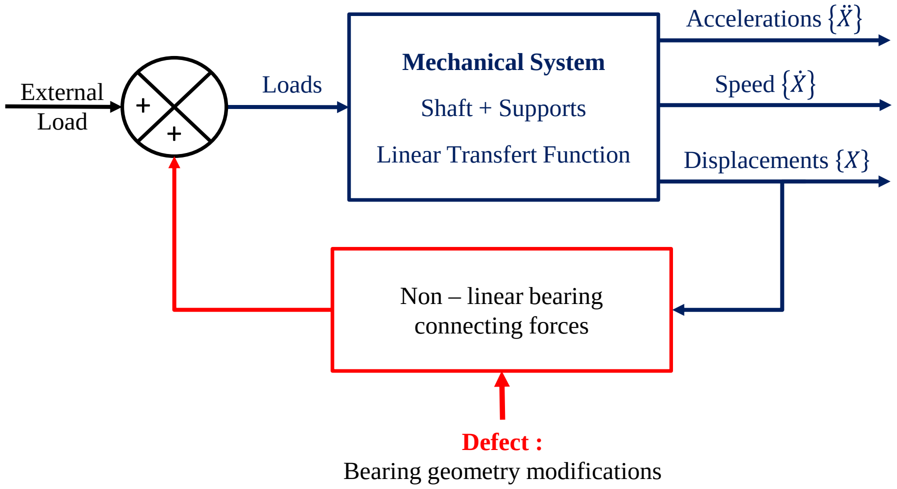

Figure 2.16: Representation of the non-linear loop system

Regarding the angular speed, figure 2.17 shows how the IAS and the perturbation torque are influenced by the bearing defect. In these plots we can also observe the perturbations of the responses related to the rolling element passing through the pit. As expected, these perturbations have a period equal to the angle between two rolling elements. As noticed on the radial vibration response, the angular duration of the rolling element "within" the pit is 8 degrees, which is the longitude of the defect. When comparing the IAS response of the faulted bearing in figure 2.8 to the one in figure 2.17(a) we can notice that in the former case the IAS amplitude becomes bigger in the presence of the defect while in the present case the amplitude is decreased in about 40%. The main difference between the two faulted bearing configurations are the size of the defect and the static load. A priori, it is difficult to directly analyze the two systems and explain in which conditions of angular speed, load and defect size the IAS response increases or decreases. Another aspect which may contribute with this behavior is the relationship between the defect angular longitude and the angle between two rolling elements. Further in this dissertation (Chapter 4), this phenomenon will be studied regarding the subject of IAS spectral indicators construction and analysis.

The shape of the perturbation torque (figure 2.17(b)) is particularly related to the one of the force reaction. As in the case of the force, the defect originates two impulsions with a "vibratory" behavior, but this phenomena is superposed to a low frequency one, similar to a step, with an angular "duration" equal to the longitude of the defect. We estimate that the oscillations are related to the evoked loop system.

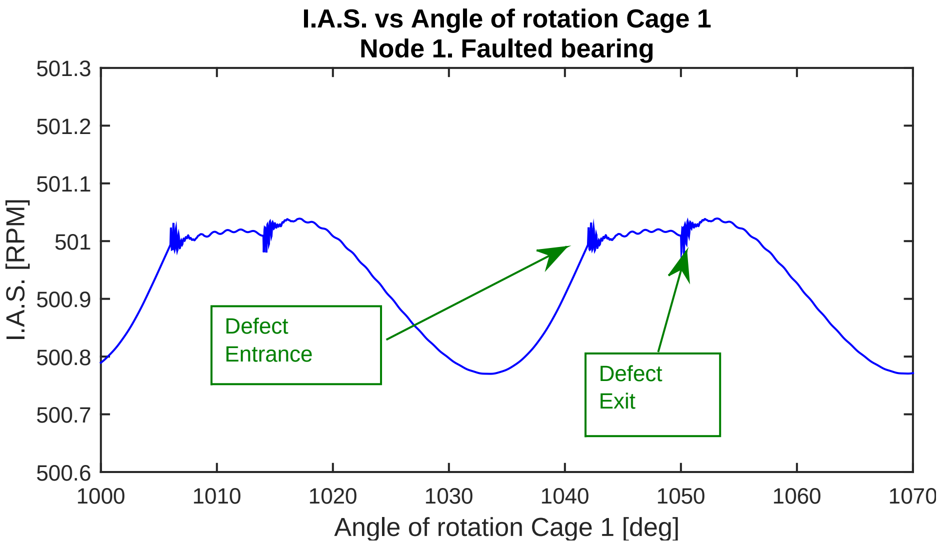

(a) I.A.S.

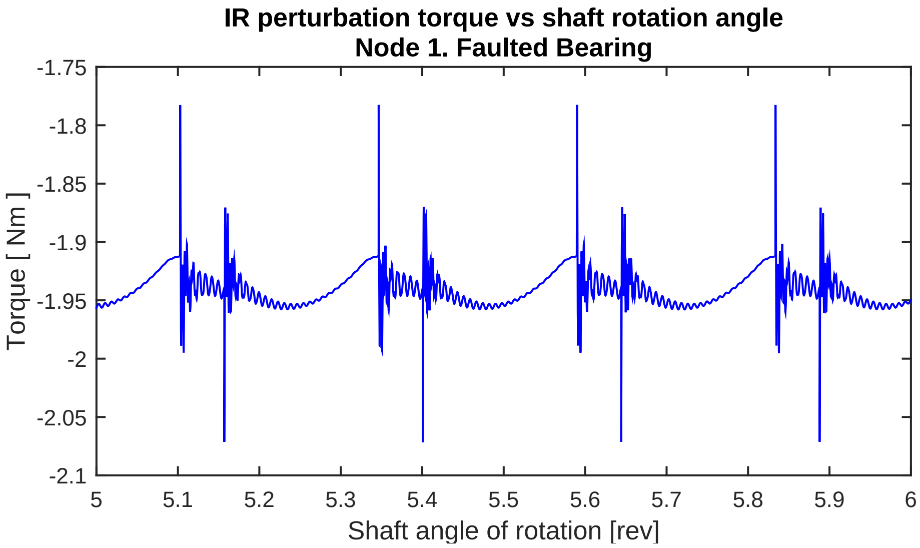

(b) Perturbation torque

Figure 2.17: IAS and Perturbation torque vs rotation of the cage. Node 1. Faulted bearing.

Figure 2.18 presents the IAS for the healthy and faulted bearing of the current model compared to an experimental IAS wind turbine's generator signal analyzed by Bourdon et al [5]. We can observe that the signals measured and those obtained from the model are similar. The IAS measured signals were presented normalized for sake of confidentiality. One of the differences between the model results and the measurements concerning the faulted bearings is the impulsiveness on the curve when the rolling element comes in

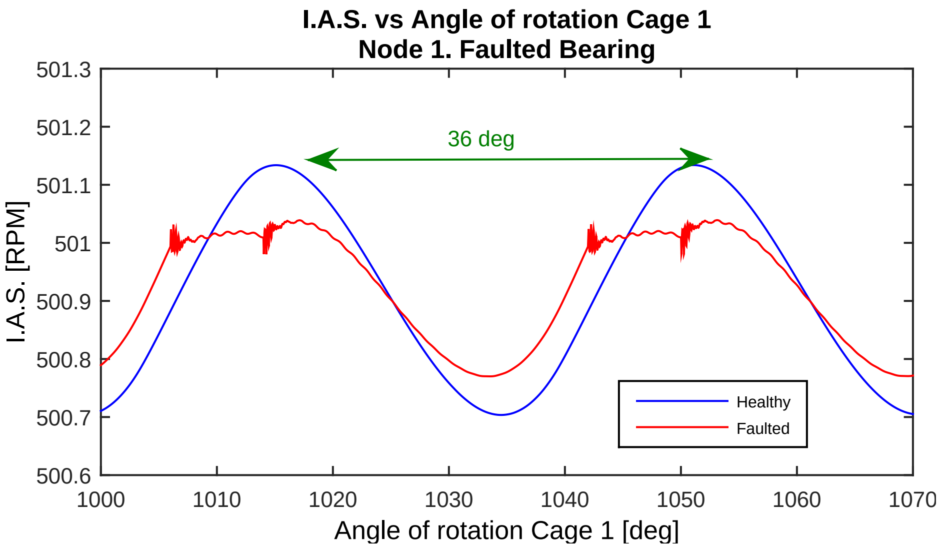

(a) I.A.S. Current model

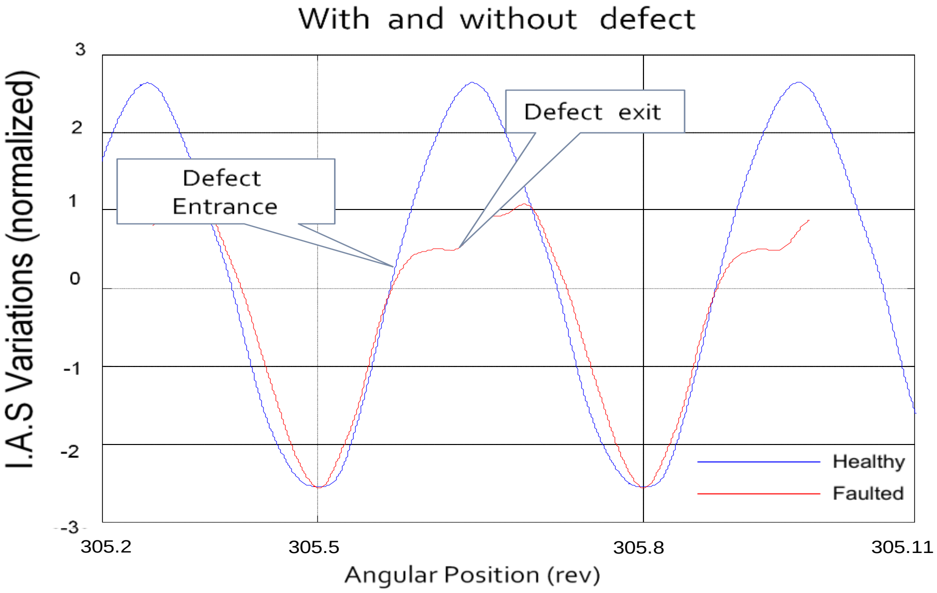

(b) I.A.S. Wind turbine generator. Bourdon et al. [5]

Figure 2.18: IAS comparison between the current model and a wind turbine generator with a faulted bearing.

and out of the defect. In the case of the measurements, the signal processing tools used for reconstruction of the rotational speed take only several harmonics into account which may be acting as a filter cutting the impulsiveness. However, experimental results in [5] show impulsiveness in the IAS measured on a test rig. In this case, the presence of the defect caused the increase of the IAS amplitude in presence of a defect which is the case of the simulation presented in figure 2.8. Further analysis is necessary in combination with experimental tests to find the relationship between load, angular speed and size-shape of the defect to explain this particular behavior of the IAS signal in presence of a bearing defect. What it may be inferred a priori is that in presence of high loads the IAS perturbation due to the variation of the normal load distribution might be more important than the perturbation of a small defect.

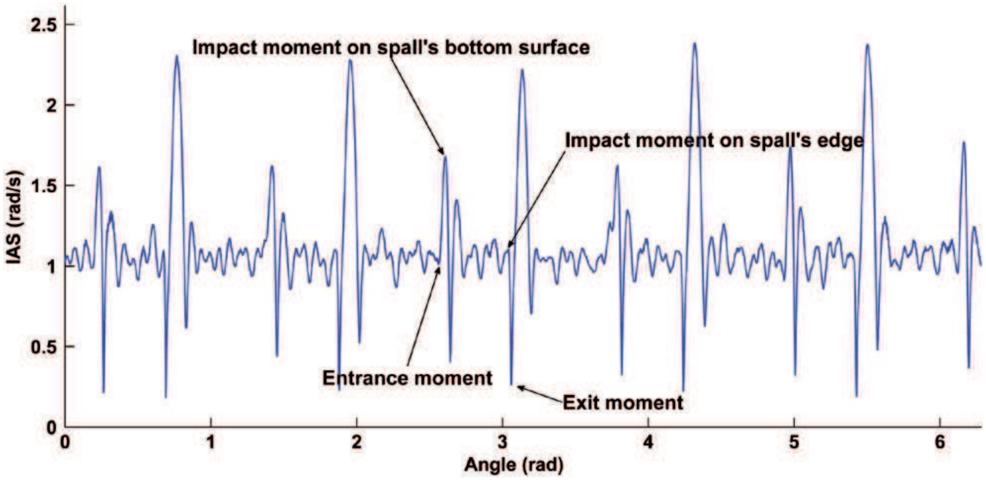

(a) I.A.S. vs angle at 10 rpm and 875 daN. Moustafa et al. [27]

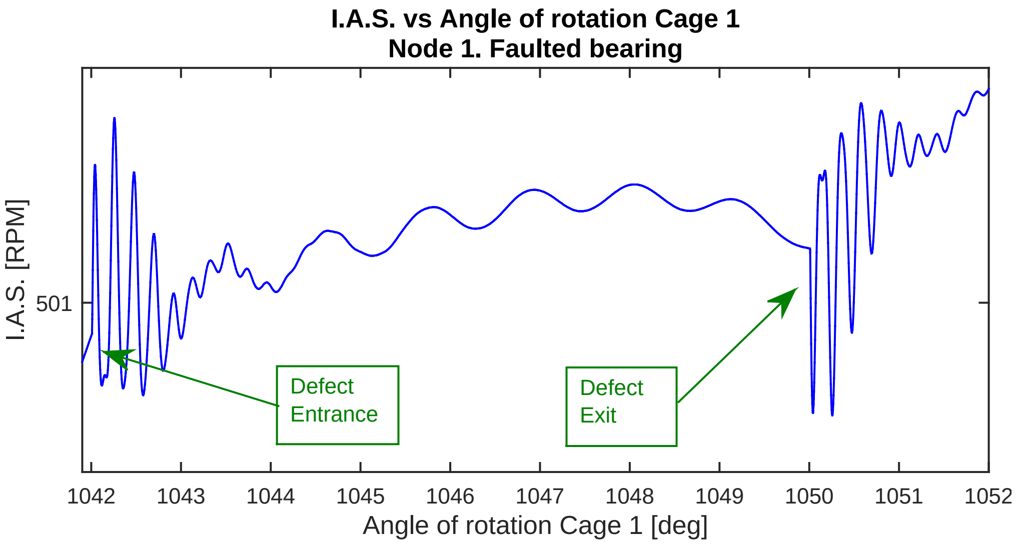

(b) I.A.S. vs rotation of the cage. Node 1. Faulted bearing

Figure 2.19: IAS Perturbation. Experimental vs Simulations

Finally, figure 2.19 shows a comparison between an experimental IAS measurement performed by Moustafa et al. [27] on a test rig with cylindrical bearings and simulated results with the current model, both in presence of a defect. The experimental work of Moustafa et al. to estimate the defect size was performed for very low speed applications and high loads. When presenting the methodology Moustafa et al. introduced the following hypothesis regarding the IAS variation while a rolling element passes trough a defect:

> “A speed increase due to the instantaneous loss of contact pressure when the rolling element’s center of mass passes the fault entrance edge. This contact pressure loss causes slippage of the rolling elements supporting the radial load that lead to a speed increase. This assumption is presumed based on the following facts: (i) the load is supported by the rolling elements passing through the loading zone; (ii) the fault is located in the load direction. Therefore, due to the contact loss when the rolling element enters the spall, the load pressure on this rolling element will be relieved, and distributed to the adjacent rolling element in the loading zone.”

When observing the results in figure 2.19, we find that the behavior of the speed variation is exactly as described by Moustafa et al. in both experimental and simulated results. The force distribution facts are also corroborated by the simulations in figure 2.15(b). However, even if the normal force decreases without inducing slippage, as in the simulated results, the speed increases when the rolling element enters the defect. Actually, the instantaneous normal force reduction, before being compensated by the other rolling elements within the load zone, causes the friction torque to instantly decrease which is translated into an instantaneous angular speed augmentation as seen in figure 2.17(b). As expected when the rolling elements exits the defect a reduction in angular speed is noticed as the element gets charged. The assumption made by Moustafa et al. of slippage is not necessarily what is occurring as it is the loss of normal load and not the slippage what causes the speed variation.

2.5 Conclusions

The analysis presented in this chapter extend previous work intending to describe the IAS perturbation due to roller bearing dynamics. An original approach to introduce IAS perturbations was developed based on the rolling resistance phenomena. The current analysis allows to explain how an outer race defect modifies the friction torque which leads to IAS perturbations.

The deep groove roller bearing model presented is based on the approach of Sawalhi and Randall, generalized to be integrated into finite element models and to manage non-stationary conditions. Considering the angular degree of freedom allowing to construct the angle time function introduces the term of the inner race angular acceleration as an unknown variable which led to a particular manipulation of the non linear system of differential equations to achieve resolution.

Simulations were performed for two different shaft bearing configurations. Interesting observations were made regarding the effect of an outer race bearing defect on the IAS phenomena. IAS perturbation related to the bearing dynamics with a frequency equal to the $BPFO$ is present even when the bearing is healthy, phenomena that is directly related to the rolling element normal force evolution. The IAS perturbation is modified in shape and amplitude in presence of a defect: the amplitude of the perturbation may increase or decrease which has to be considered when analyzing IAS signals. Results tend to show that high loads combined with small defects will tend to decrease the IAS signal amplitude.

From the analysis of the rolling element normal force distribution, the bearing force reaction and the perturbation torque, it was found that the defect originates instantaneous impulses over the static force reaction, that have their origin in the sudden normal load redistribution. In the case of the perturbation torque, this phenomenon is added to a low frequency perturbation with a “step” shape with longitude equal to the defect. Certainly, for real defects this longitude will be smaller than the defect size.

Numerical results of IAS variations in healthy and faulted conditions were compared to experimental measurements from a wind turbine generator. Several similarities were found related to the effect of the bearing’s defect over the system response.

Comparison between the simulations and the experimental results of Moustafa et al. [27] were valuable to understand the nature of the angular speed perturbation due to the behavior of the normal force distribution and the perturbation torque.

Further analyses with experimental validation would be of substantial value to study the relationship between the angular speed, the load and the defect size, the defect shape and the IAS perturbation. These analyses would contribute to deepen the understanding of the phenomena leading to the improvement of IAS surveillance indicators.

The next chapter is dedicated to the assembly of the current roller bearing model to architectures considering single gear stages. The aim is to analyze the nature of the IAS phenomena in gear transmissions leading to more complex mechanical systems.

Chapter 3

Modeling the IAS phenomenon on gear coupled systems

Contents

3.1 Introduction

Throughout this chapter the roller bearing model presented in this work is integrated to more complex mechanical architectures in presence of gear coupled systems. The aim is to analyze the behavior of the friction torque perturbation leading to IAS variations, knowing that it is the coupling between the tangential and the radial forces on the bearing which originates the torque variations.

The first section will verse about exploring the state of the art giving the necessary context to the modeling of the gear mesh. Then, the general approach for the gear model, taking into account rigid body rotations, is described presenting the assumptions and the limitations.

The approach is first tested by validating the rigid body pure rotative response in a single-stage transmission configuration by the application of external torques. A torque variation is then added to observe the transmissibility characteristics of the gear mesh model.

The Deep Groove Ball Bearing model is then integrated to the simulated architecture and simulation results are presented in the presence of a healthy and a faulted bearing.

Finally, a brief exploration of the dynamic parameters of the tested architecture is presented, by exploring the IAS response to a linear external torque and the bearing dynamics in different support configurations, to analyze the influence of the bearing casing modeling.

3.2 Brief review of modeling the gear mesh

The mechanical modeling of the gear interaction is about the description of the flexible coupling and the excitation sources introduced into the mechanical system by the interacting gears. Usually, the gear excitation is described as the non linear teeth mesh stiffness, the transmission error and the teeth imperfections [53]. The first lumped parameter mass-spring dynamic model was introduced by Tuplin in the fifties [54–56]. In this approach, an equivalent constant mesh stiffness was considered and gear errors were introduced by means of different surface variations of the spring support in a one DOF system. Almost two decades ago, a great number of research developed after Tupin's work was synthesized by Özgüven and Houser [57] in an extensive review (close to two hundred publications) of the different modeling approaches for gear coupled systems. Characterizing the number of work versing about gears in the literature is out of the scope of this dissertation.

The current section focuses in describing some recent publications with the objective of showing the variety of developments existing in the literature and to give context to the approach used in this chapter.

In [58], Bartelmus proposed an approach of multi-body modeling to represent one driving motor, one gear stage comprised by two gears and two shafts, and one driven machine as mechanical bodies. The approach for linking the multiple bodies is by external connecting forces considering: the driving moment, the gear tangential forces, the driven machine moment and the support forces. The equations of motion, obtained from the force diagrams (application of the second Newton's law) of each body consider three DOF: two radial displacements and the angular rotation which comprehends the rigid body motions. The supports are modeled as linear forces of stiffness and damping applied to the bodies. The gear interacting or connecting forces are obtained as the result of modeling the teeth mesh as a spring and a damper "attached" to both of the gear base circles. The dynamic gear mesh force of the gears is a function depending on several variables representing the interacting teeth stiffness, the teeth deformation and the transmission errors. The varying teeth stiffness depends on time, on the average teeth stiffness and on a squared function representing the distribution of the energy between the number of pairs in contact. The teeth deformation, estimated considering backlash, is the difference between the displacements of the base circles of the gears. The error function describes the maximum of the error value on the line of action and it models the gear excitations and defects based on parameters related to design, production technology and operating conditions.

In a further work, Bartelmus et al. [59, 60] tested the model described above in different configurations (two-stages, three-stages and a planetary transmission) under varying load configurations. The machines were considered to work in intervals of constant speed depending on the load to build defect simulated indicators that were compared to experimental ones. These analyses were performed by means of a two parameters regressive method resulting in the indicator statistical laws. Simulations and experiments confirmed the assumption of a two parameter regressive model for accelerometer measurements.

Another example of the modeling of a whole transmission is the work of Kubur et al. [61] where a general model for multi-stage parallel gear transmissions by finite elements was developed. According to the authors, the choice of modeling the shafts by finite elements requires simplifications in the dynamics of the casing and the supporting bearings. Also, the nonlinear effect of backlash and shaft separations are neglected as well as the time varying effects due to the alternating number of teeth in contact. Gears were considered to have rigid blanks, six DOF and they are connected by a linear gear mesh spring. The gear excitations were modeled as a dynamic transmission error described by an excitation aligned in the same plane of the spring introduced as a Fourier series harmonic perturbation representing the gear mesh frequency of each interacting pair. Experimental transmission error measurements were performed as a function of the angular speed of the motor shaft of a one-stage helical gear test rig. The model was tested by finding the modal response and estimating the excitation forces by means of a Modal Summation Technique [62] as a function of the excitation (gear mesh). Comparison of the model response with the experiments was considered consistent and validated the simplifications for the tested configurations. It was added by the authors that the assumptions may not be valid for spur gears.

With a different approach for the gearing excitations, Velex and Ajmi [37] performed the modeling in pure torsion and then considered three DOF of a one stage helical test rig to present an approach of gearing excitations by means of the combination of static and dynamic transmission errors. The static transmission error (or non loaded transmission error) concerning rigid body motions was superposed to the under load transmission error which is denoted by a dynamic perturbation of the angular DOF of the pinion and the gear. It is introduced into the term of conservative energy in the application of Lagrange equations. As the angular speed is considered constant the angular DOF θ is made equal to $\Omega \cdot t$ where Ω represents the speed of the driving shaft. These considerations allow the expression of the equations as a direct function of time but it would not permit the handling of non-stationary angular speed conditions as rotation will intrinsically be linear when related to time. The approach was validated by modeling a test rig of a single-stage with spur and helical gears, comparing simulations with different model approaches. An interesting fact is that the resisting rotational load in the model is a torsional stiffness, meaning that no free body angular rotation is allowed to the system.

Another work centered in the methods for the estimation of the gear coupling stiffness is the one of Eritenel and Parker [63], whose performed a lumped parameter model of a helical gear pair with six DOF per gear to analyze non linearities and partial contact loss between paired teeth. The approach is based on obtaining the distributed stiffness estimated by the local displacements of the contact line. A center of stiffness is found and the global mesh stiffness is composed by a translational and a spread twist stiffness. More recently, Wan et al. [64] used an approach of potential energy for an analytical estimation of the gear mesh stiffness. It considers the sum of potential energies from hertzian energy, bending energy, shear energy and axial compressive energy. Calculation of the mesh stiffness is compared to a finite element model where the FEM method estimates a slightly greater value than the proposed method. A crack is added to perform also comparison between the methods. The crack is along the contact line and, in the proposed model, modifies the estimation of the area moment of inertia and the area of the tooth section. The model is tested with a lumped mass parameter approach for the shafts in a single stage configuration showing good agreement with experiments.

The already explored model of Sawalhi and Randall [36] is revisited. They coupled the bearing and gearing interaction by modeling a single-stage gear test rig with lumped parameters with a total of 34 DOF taking into account the bearings and the casing. The pair of meshing gears are modeled as two cylindrical masses connected by an angular dependent stiffness and a damping coefficients combined with excitations taking into account the teeth deviations and misalignment. Gears have three DOF each: two translations plus the angular rotation. The angular-dependant stiffness was estimated by experimental static measurements. In this approach, the angular speed of the input shaft is considered constant thus, the angular DOF is linear related to time as it was also pointed in [37]. Different defects were introduced in the bearings of the test ring and were consequently modeled. The simulated accelerometer signals of the localized defects were found to have the same basic characteristics as the measured ones.

The brief modeling review described above is very different depending on the focus of each research. Based on the complexity of the mechanical architecture, different approaches are developed for the gear mesh. Very detailed models may be constructed by means of finite element analysis with usually high computational costs. This is why the research cited above focuses on creating smart ways to describe with enough detail the teeth contact and the gearing excitations regarding the application. The focus of this dissertation is the analysis of the IAS in geared mechanical systems as a tool for condition monitoring. This is why the approaches of Bartelmus et al. and Sawalhi and Randall are closest to our objectives. However, in the current analysis it is not the scope to study the perturbation of torque originated by the gear excitations as the roller bearings are the main subject of study. Thus, the approach developed hereafter focuses on the estimation of the forces originated within the gear mesh and their perturbation related to the dynamics of the whole architecture with origin in the roller bearings. Another important issue regarding the IAS and the wind turbine application is the non stationary nature of the angular speed. The author would like to stand out that in the consulted bibliography the majority of publications do not explicit the handling of the rotational rigid body DOF which, regarding the dissertation objective, is important to express the nature of the angle dependent forces and the modeling of non stationary conditions. Only the work of Bartelmus [58–60] describes the handling of the angular DOF and uses the model to explore non stationary conditions. However, no rigid body angular speed response is shown in the publication nor the handling of the rigid body angular damping is described (See Appendix A).

In the next section, the modeling approach used in the current work for the gear mesh is described. The focus is based on building a gear interaction allowing to study IAS variations introduced into the system by the bearing dynamics. The angle DOF is explicitly used in the approach which changes the assumptions and the basic formulation which have no repercussion in the resulting equations.

3.3 Gear modeling approach

The modeling strategy described hereafter is based on a very classic approach used widely on the literature . Being the interest, the analysis of the IAS response due to the bearing dynamics in non stationary conditions, explicit consideration of the angular DOF is necessary in order to build the angle time function. From a general point of view, gears are considered as rigid cylinders linked by restorative forces due to the paired gear stiffness representing the contribution of the ensemble of the deformable parts. Describing the gearing mesh as connecting forces is based on the same general concept presented in Chapter 2 for modeling the roller bearings and is similar to the approach of Bartelmus [58]. These forces are obtained by means of the following equation:

$$\left\{F_{gea}\right\} = \left[K_{gea}\right] \cdot \left\{X_{gea}\right\} \tag{3.1}$$

where the matrix $\left[K_{gea}\right]$ represents the gear mesh stiffness. Vectors $\left\{F_{gea}\right\}$ and $\left\{X_{gea}\right\}$ are the gear mesh connecting forces and the generalized displacements of the nodes representing the interacting gears. Figure 3.1 shows a schematic representation of this approach.

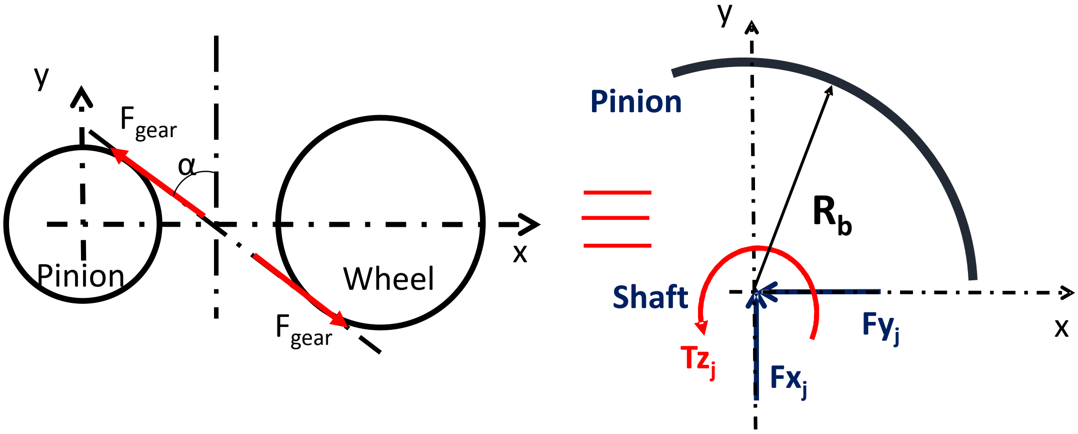

Figure 3.1: Representation of the gear connecting forces

Integrating the gear mesh to complex models considering shafts, bearings and supports means, adding the connecting forces to the general system shown in Equation 3.3 by following the finite element connectivity arrangement.

$$\begin{cases} \dfrac{d\tilde{Q}(\theta)}{d\theta} = \dfrac{1}{\tilde{\omega}(\theta)} \cdot [S]^{-1} \cdot ([A] \cdot \tilde{Q}(\theta) + [B] \cdot \{U\}) \\ \dfrac{dt}{d\theta} = \dfrac{1}{\tilde{\omega}(\theta)} \end{cases} \tag{3.2}$$

with:

$$\{U\}_{2n,1} = \begin{Bmatrix} \{0\}_{n,1} \\ \{F_{ext}\} + \{F_{beaN}\} + \{F_{gea}\} \end{Bmatrix} \tag{3.3}$$

All 6 DOF for each gear are considered, meaning that the gear coupling will have 12 DOF. The mass and inertia of the gears are lumped into the finite element nodes of the shaft to which each gear is attached. The formulation for the estimation of the gear mesh stiffness matrix $[K_{gea}]$ follows.

3.3.1 The gear stiffness estimation with a potential energy approach

The choice made is to consider one contact point between the two gears placed in a unique direction which are the gear pitch circles point of contact and the line of action. The analysis developed below is a classic approach in which the description has been done following the methodology of Bourdon [65]. However, the classic assumption pointed out by Bourdon based on the work of Velex [66] and Bard [67] of small rotations around the gear longitudinal axis is extended by an approach based on the static transmission error allowing, from a conceptual point of view, the consideration of “large” rigid body rotations. The main parameters of the gears used in the approach are the pressure angle α, the helix angle β_b and the base circle radius Rb.

The estimation of the gearing connecting forces, as it was mentioned before, allows the coupling between one node of the input shaft to a node of the exit shaft by means of the gear mesh stiffness matrix $[K_{gea}]$ and the general node displacements to estimate the teeth deformations. In Figure 3.2 a general disposition of the gear nodes is shown. The nodes $N1$ and $N2$ concentrate the lumped parameters of the gear. Their location related to the center of the gears ($d1$ and $d2$) is frequently equal to zero for sake of practicality.

Depending on the load, specially the external torque driving the shafts, two different gear configurations are possible corresponding to two different contact profiles as shown in Figure 3.3

Each of the configurations require the definition of a reference coordinate system as shown in Figure 3.4.

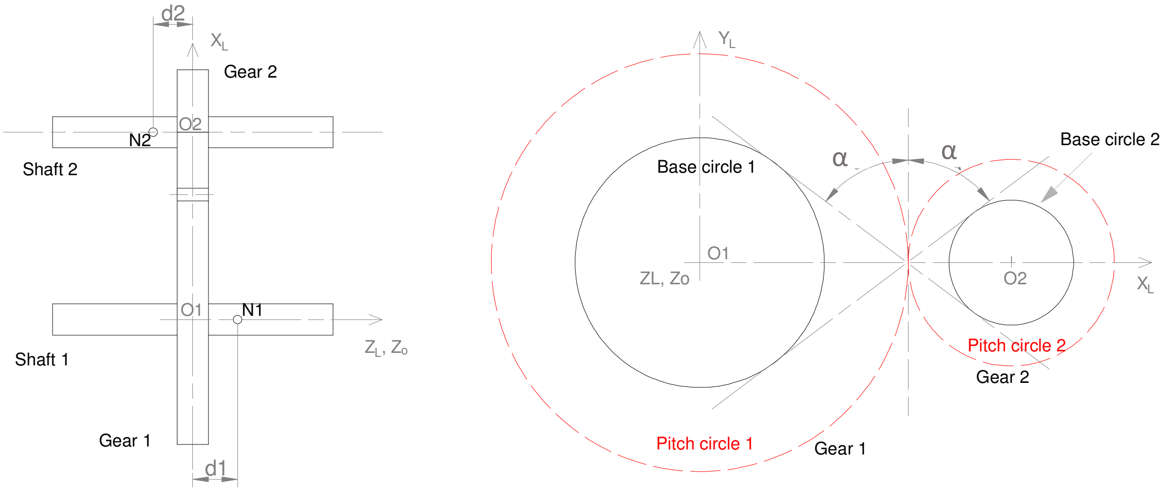

Figure 3.2: Representation of the gear nodes disposition

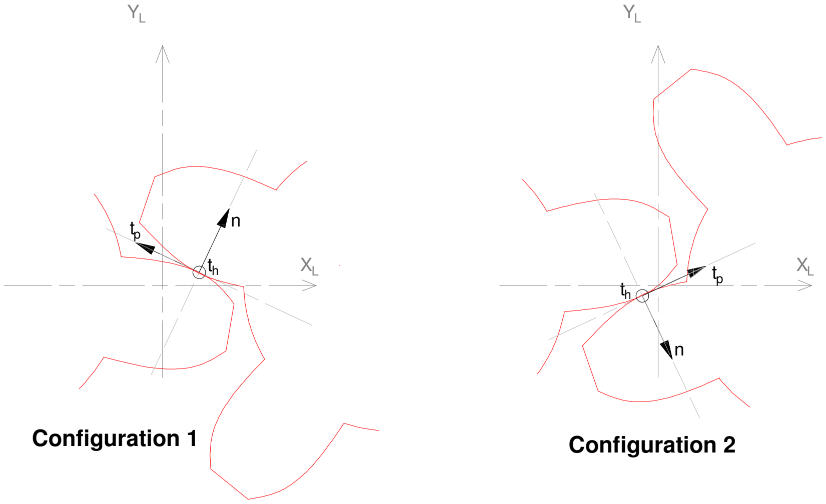

Figure 3.3: Gear contact profiles

The gear stiffness is modeled as a spring of stiffness K_o placed following the line of action which is normal to the contact plane. The potential energy cumulated in the mesh is expressed by:

$$E_p = \frac{1}{2} \cdot K_o(\theta_z) \cdot \Sigma^2 \tag{3.4}$$

In this expression, Σ refers to the teeth deformation by means of the teeth contact and is defined in Equation 3.5.

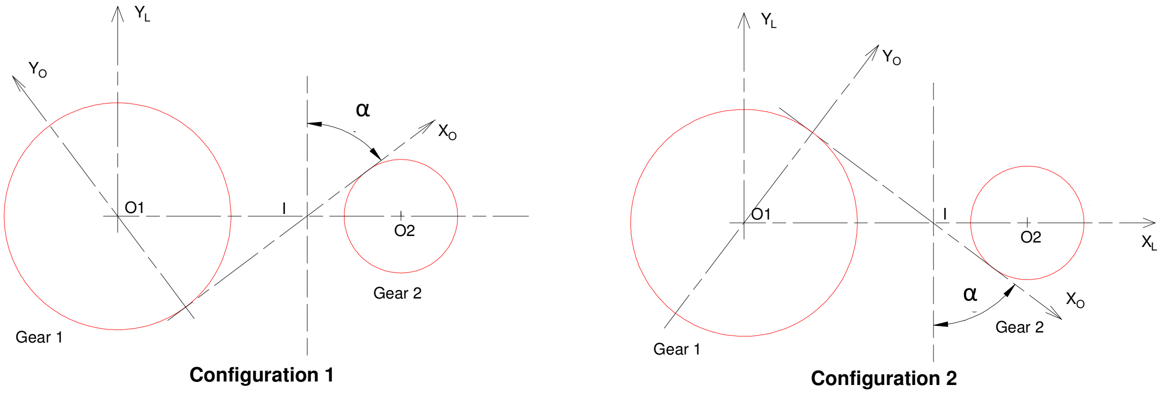

Figure 3.4: Gear configurations and Reference Gear coordinate system X_o, Y_o

$$\Sigma = \{disp(I \in S_1)\} \cdot \{n_1\} - \{disp(I \in S_2)\} \cdot \{n_1\} \tag{3.5}$$

where $\{disp(I \in S_i)\}$ is the projection of the displacement's vector of the gear i pitch circle contact point on the contact's normal direction.

3.3.1.1 Pitch point displacements

Knowing the generalized displacements of the nodes representing the gears (N_1 and N_2, Figure 3.2) referred to the elementary reference coordinate system CS_o (X_o, Y_o, Z_o), it is possible to estimate the displacements of the contact points of the gears.

First, let e_s represent the non loaded or rigid body transmission error [37, 65] defined by the following expression:

$$e_s = \theta z_2 + \frac{Rb_1}{Rb_2} \cdot \theta z_1 \tag{3.6}$$

The displacements and rotations of the node N_1 are defined by:

$$\{disp(N_1)\}_{CS_o} = U_1 \hat{i_o} + V_1 \hat{j_o} + W_1 \hat{k_o} \tag{3.7}$$

and

$$\{rot(N_1)\}_{CS_o} = \theta x_1 \hat{i_o} + \theta y_1 \hat{j_o} \tag{3.8}$$

For the node N_2 we have:

$$\{disp(N_2)\}_{CS_o} = U_2 \hat{i_o} + V_2 \hat{j_o} + W_2 \hat{k_o} \tag{3.9}$$

and

$$\{rot(N_2)\}_{CS_o} = \theta x_2 \hat{i_o} + \theta y_2 \hat{j_o} + e_s \hat{k_o} \tag{3.10}$$

where $\hat{i_o}$, $\hat{j_o}$ and $\hat{k_o}$ are the unit vectors of the axes X_o, Y_o, and Z_o. Variables U_i, V_i and W_i represent the displacements and θx_i, θy_i and θz_i are the rotations of the gear's node i in the directions X_o, Y_o, and Z_o.

Notice that the rotation in Z_o for the Node 1 is set as reference meaning that the whole displacement of rotations in this axe is contained in the non loaded error transmission expressing the rotation of Node 2.

The general pitch point displacement vector for the k^{th} gear is:

$$\{disp(I \in S_i)\}_{CS_o} = \{disp(N_i)\}_{CS_o} + \left\{\vec{IN_i}\right\} \times \left\{rot(\vec{N_i})\right\}_{CS_o} \tag{3.11}$$

with

$$\left\{\vec{IN_i})\right\}_{CS_o} = \mu_i \hat{i_o} + \lambda_i \hat{j_o} - d_i \hat{k_o} \tag{3.12}$$

where d_i is the algebraic distance $N_i\bar{O}_i$ measured along the axe Z_o (See Figure 3.2). Depending on the gear configuration the values for μ_i and λ_i are:

$$\text{Configuration 1:} \quad \begin{cases} \mu_1 = -Rb_1 \cdot tan(\alpha) \\ \mu_2 = Rb_2 \cdot tan(\alpha) \\ \lambda_1 = Rb_1 \\ \lambda_2 = -Rb_2 \end{cases} \tag{3.13}$$

$$\text{Configuration 2:} \quad \begin{cases} \mu_1 = -Rb_1 \cdot tan(\alpha) \\ \mu_2 = Rb_2 \cdot tan(\alpha) \\ \lambda_1 = -Rb_1 \\ \lambda_2 = Rb_2 \end{cases} \tag{3.14}$$

The general vector of pitch point displacements for the nodes N_1 and N_2 become:

$$\{disp(I \in S_1)\}_{CS_o} = (U_1 + d_1 \cdot ry_1)\hat{i_o} + (V_1 - d_1 \cdot \theta x_1)\hat{j_o} + (W_1 + \mu_1 \cdot \theta y_1 - \lambda_1 \cdot \theta x_1)\hat{k_o} \tag{3.15}$$

$$\begin{aligned}\{disp(I \in S_2)\}_{CS_o} = (U_2 + \lambda_2 \cdot e_s + d_2 \cdot \theta y_2)\hat{i_o} + (V_2 - \mu_2 \cdot e_s - d_2 \cdot \theta x_2)\hat{j_o} + ... \\ (W_2 + \mu_2 \cdot \theta y_2 - \lambda_2 \cdot \theta x_2)\hat{k_o}\end{aligned} \tag{3.16}$$

3.3.1.2 The teeth deformation across the normal of contact

The normal of contact in CS_o depends on the gear configuration and is a function of the gear helix angle β_b. The convention is related to the helix direction of the gear 1: if the helix is to the right on gear 1 the helix angle is negative; if it is to the left, then the helix angle is positive. The expression for the normal of the profile of the gear 1 in CS_o are:

$$\text{Configuration 1:} \quad \vec{n}1_{R_o} = cos(\beta_b)\hat{\imath} + sin(\beta_b)\hat{\jmath} \tag{3.17}$$

$$\text{Configuration 2:} \quad \vec{n}1_{R_o} = cos(\beta_b)\hat{\imath} - sin(\beta_b)\hat{\jmath} \tag{3.18}$$

Now, $\{Q_{CS_o}\}$ is defined as the generalized gear node's displacements vector:

$$\{Q_{CS_o}\} =^T \left\{U_1 \quad V_1 \quad W_1 \quad \theta x_1 \quad \theta y_1 \quad \theta z_1 \quad U_2 \quad V_2 \quad W_2 \quad \theta x_2 \quad \theta y_2 \quad \theta z_2\right\} \tag{3.19}$$

After replacing the transmission error e_s (Equation 3.6) into Equation 3.16, the gear teeth squeezing defined by Equation 3.5 can be now expressed as:

$$\Sigma =^T \{\sigma\} \cdot \{Q\}_{CS_o} \tag{3.20}$$

With:

$$\begin{aligned}^T\{\sigma\} = \{c \quad 0 \quad s \quad -\lambda_1 \cdot s \quad \mu_1 \cdot s + d_1 \cdot c \quad \lambda_1 \cdot c \quad -c \quad 0 \quad -s ... \\ \lambda_2 \cdot s \quad -d_2 \cdot c - \mu_1 \cdot s \quad -\lambda_2 \cdot c\}\end{aligned} \tag{3.21}$$

and:

$$\begin{aligned} c = cos(\beta_b) \\ s = sin(\beta_b) \end{aligned} \tag{3.22}$$

Notice that the resulting vector $\{\sigma\}$ is the same obtained with the approach of small angular perturbations presented by Bourdon [65] in her PhD dissertation. Thus, the formulation developed above validates the use of this approach with free rigid body rotations considering the angle DOF θz_i explicit in the equations.

3.3.1.3 Equivalent stiffness matrix

The estimation of the equivalent gear stiffness matrix is obtained by substitution of Equation 3.20 into the expression of the potential energy (Equation 3.4):

$$E_p = \frac{1}{2} \cdot K_o(\theta_z) \cdot ({}^T\{\sigma\} \cdot \{Q\}_{CS_o})^2 \tag{3.23}$$

Operating, the expression of the potential energy is found:

$$E_p = \frac{1}{2} \cdot K_o(\theta_z) \cdot (\{Q\}_{CS_o} \cdot \{\sigma\} \cdot^T \{\sigma\} \cdot \{Q\}_{CS_o}) = \frac{1}{2} \cdot^T \{Q\}_{CS_o} \cdot [K_{gea}] \cdot \{Q\}_{CS_o} \tag{3.24}$$

from where it can be extracted the expression for the Equivalent stiffness for cylindrical gears, expressed in the referenced coordinate system CS_o:

$$[K_{gea}]_{CS_o} = K_o(\theta_z) \cdot \{\sigma\} \cdot^T \{\sigma\} \tag{3.25}$$

From the last equation, the gear geometric matrix $[G]$ is defined and it depends on the gear characteristics:

$$[G] = \{\sigma\} \cdot^T \{\sigma\} \tag{3.26}$$

Finally, the gear stiffness expression is:

$$[K_{gea}]_{CS_o} = K_o(\theta_z) \cdot [G] \tag{3.27}$$

where $K_o(\theta_z)$ is the gear mesh stiffness. In the current approach, the value for the teeth stiffness may be constant or variable allowing consideration of non linear stiffness which would add to the dynamics of the system the gear mesh perturbations. Working with connecting forces avoids calculation of the system stiffness matrix at each resolution step when considering non linearities due to the amount of paired teeth. The main disadvantage is that estimation of the modal properties of the system considering the gear mesh by solving the eigenvalues problem cannot be performed. If this analysis is needed, the stiffness matrix can be added to the general system's one by following the connectivity arrangement. Other solution is treating the system with an experimental approach and identifying for example the critical frequencies depending of the excitation e.g. the response of the system to unbalance.

Regarding this dissertation, to keep the signal simple for analysis of the IAS variations originated by the bearing dynamics, the choice has been made to consider the stiffness K_o as constant and equal to the teeth average stiffness. The ISO 6336 standard [68] empirical expression was used for the estimation of this parameter:

$$K_o = 20 \cdot B \cdot 10^6 \qquad [N/m] \tag{3.28}$$

where B represents the width of the paired gears.

In the next section the approach is tested in a single stage transmission under different conditions and architectures for the supports. First, rigid supports and an angle perturbation inspired by the one described in section 1.4.2 is used to show the characteristics of the IAS response. Then, with the intention to analyze the impact of coupling the gears with the non linear dynamics of the roller bearings the model presented on the last chapter is integrated in to the single gear transmission configuration. Knowing that the roller bearing model does not takes into account axial loads, the decision was made to work only with spur gears. Every mechanical system is modeled following the method described in Section 2.3.1 integrating the gearing connecting forces as shown in Equation 3.3. Also, consideration of the angular degree of freedom allowed using non stationary runs to analyze the modal behavior of the system.

3.4 Validation of the angular response of the gear coupling model

In this section, a single stage model is built considering only the angular DOF of the system (rotation in Z, Figure 3.5) with the aim of validating the response of the system in terms of the rigid rotation. The nodes N_2 and N_5 are placed at the geometrical center of the gears meaning that distances d_2 and d_5 are equal to zero. The tested operating parameters of the system are inspired in a mechanical oil pump multiplier transmission with a power of 18 kW (Part number 244513 in [69]). The geometry of the shafts and the bearings to be included later are the same of the configuration tested in section 2.4.2. The gear modules are set to 5 mm, the teeth number for the input gear is 54 and for the output is 25 teeth which leads to a transmission ratio of 2.16:1. The width of the gear is set equal to twelve modules i.e. 60 mm. The pressure angle α is 20^o and the helix angle is nil implying no axial forces. The average gear stiffness estimated with Equation 3.28 is $1.2 \cdot 10^9$ N/m. Figure 3.5 shows the configuration of the mechanical system.

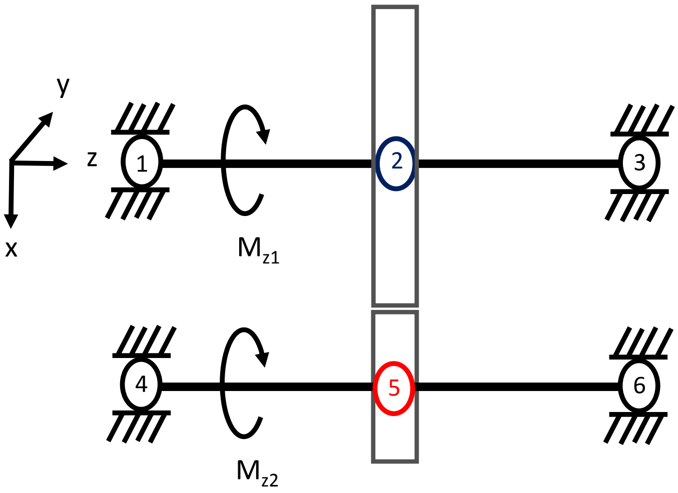

Figure 3.5: Scheme of a single-stage multiplier transmission in pure rotation

To validate the rigid body response, a mechanical analysis of the system as rigid bodies (Newton's second law) is performed in Appendix C.1. In this analysis, expressions for the steady state gear force and the angular speed of the input shaft are obtained:

$$F_{gea} = \frac{\nu_2 \cdot n \cdot M_1 + \nu_1 \cdot M_2}{\nu_2 \cdot n \cdot Rb_1 + \nu_1 \cdot Rb_2} \tag{3.29}$$

$$\omega_1 = \frac{M_1 - n \cdot M_2}{\nu_1 + n^2 \cdot \nu_2} \tag{3.30}$$

Equations 3.29 and 3.30 allowed us to perform validation of the approach. The external driving moment M_1 is 266 Nm and the resistive moment M_2 is 36 Nm. The angular damping coefficients ν_1 and ν_2 are supposed equal and set, by means of equation 3.30 to obtain an angular speed of 518 rpm. Substitution of the set and the estimated ν_i values into Equation 3.29 lead us to the expected value of the interacting gear force along the line of action which is 1835.90 N.

Integration of the equations was performed with the ODE15 Matlabs's solver. Figure 3.6 shows the response of the angular speed for nodes 2 and 5 confirming that the expected 518 rpm of the shaft 1 is obtained. It is observed that the angular speed of the Node 5 is 1119 rpm respecting the transmission ratio.

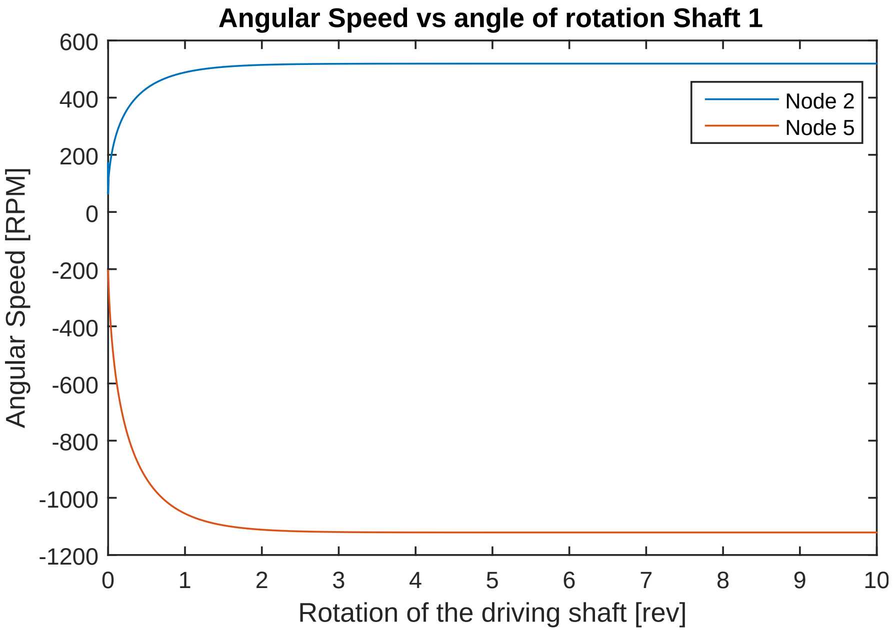

Figure 3.6: Angular Speed vs angle of rotation Nodes 2 and 5

Figure 3.7 shows the estimated gear resultant forces for the nodes 2 and 5 along the line of action which is exactly equal to the value exhibited by the rigid body analysis (Equation 3.29). The observed results for the steady state angular speeds and gear connecting forces validate the gear coupling model approach for the rigid body rotations.

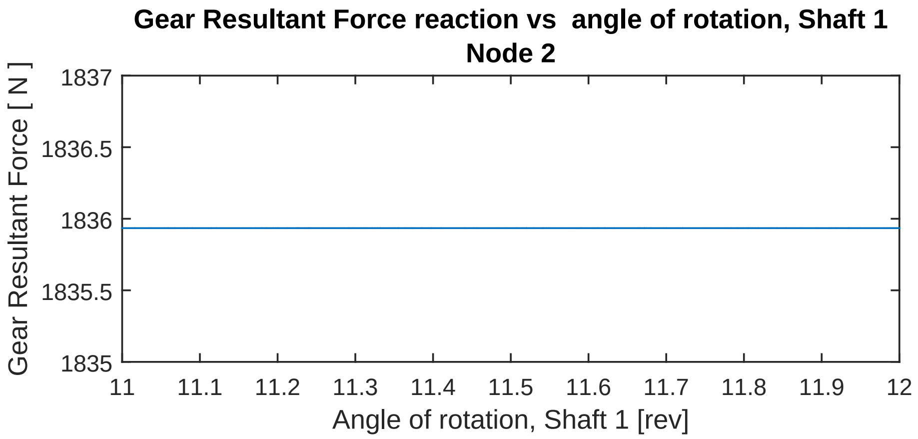

(a) Gear Interacting force Node 2

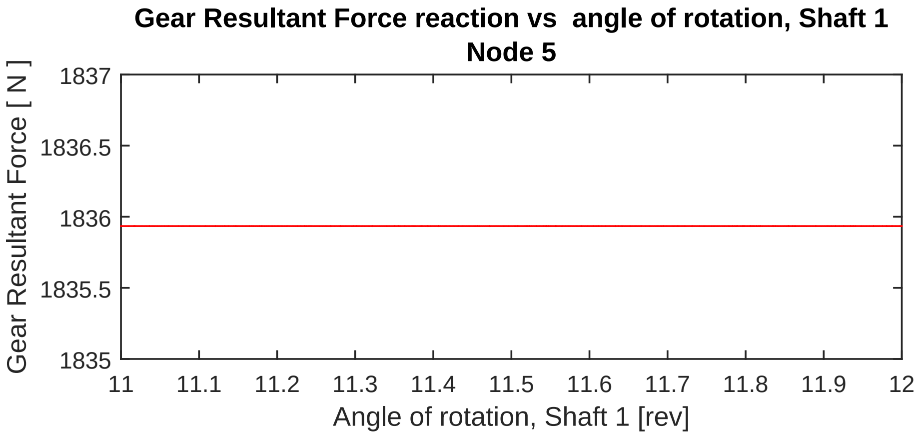

(b) Gear Interacting force Node 5

Figure 3.7: Gear connecting force along the line of action

3.5 The gear coupling and the angular torque perturbation

In an approach similar to the one used by Bourdon et al. [2], an angular torque perturbation was introduced to the system shown in Figure 3.5 at the same operating conditions. In this case a sinusoidal perturbation with an amplitude of 0.1 Nm was added to node 1 simulating a perturbation from a faulted bearing. The cyclic phenomenon corresponds to the angle BPFO of the 6214 bearing (the one tested in section 2.4.2).

Figure 3.8 shows the response of the IAS for each shaft as a response of the introduced angular perturbation. A sinusoidal angular speed variation with angular frequency equal to the perturbation torque is found not only on the input shaft but also on the output shaft proving the potential of the gear coupling model to deal with dynamic perturbations. As a constant average stiffness is considered as well as no dynamic transmission error, no other but the sinusoidal perturbation is observed in the IAS response on both shafts. Notice that the "macroscopic" angular speed has been removed to better show the amplitude of the IAS variations. The perturbation torque is transfered onto the output shaft by means of the gear force which is perturbed with the same frequency.

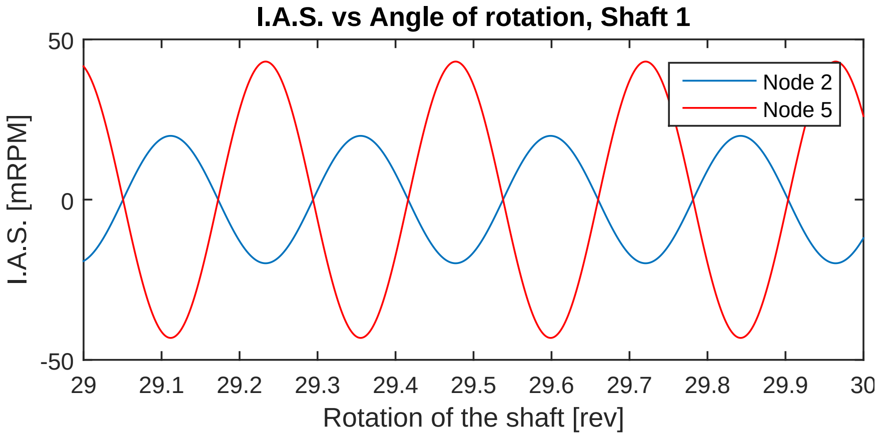

Figure 3.8: IAS variation due to angular torque perturbation

Figure 3.9 shows the perturbation around the steady state gear force along the line of action into node 5. This force, translated as a torque onto the nodes by multiplying the force by the base radius is shown in Figure 3.10. Notice that the steady state or quasi static value of the torque has been also removed with the interest of showing the amplitude of the perturbations.

It can be observed that in this conditions of pure rotation along Z, the IAS variations and the torque behave as the “macroscopic” or order zero conditions, i.e. speed variations are multiplied and the torque variations are divided by the transmission ratio.

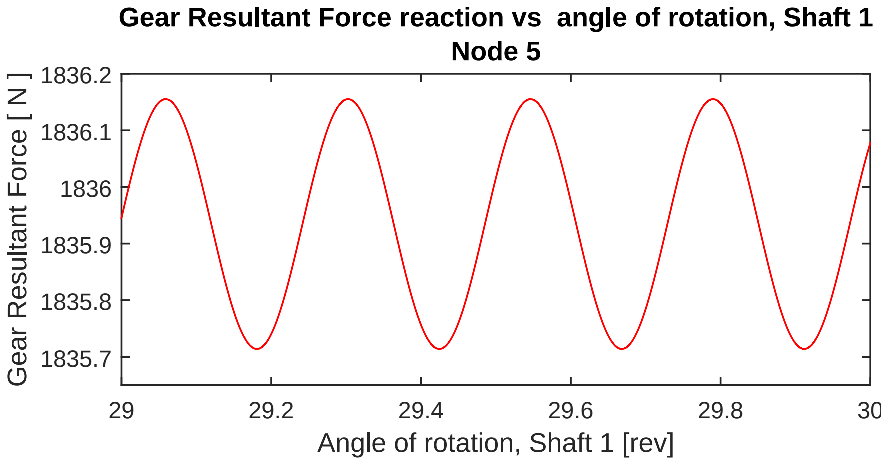

Figure 3.9: Gear Interacting force Node 5

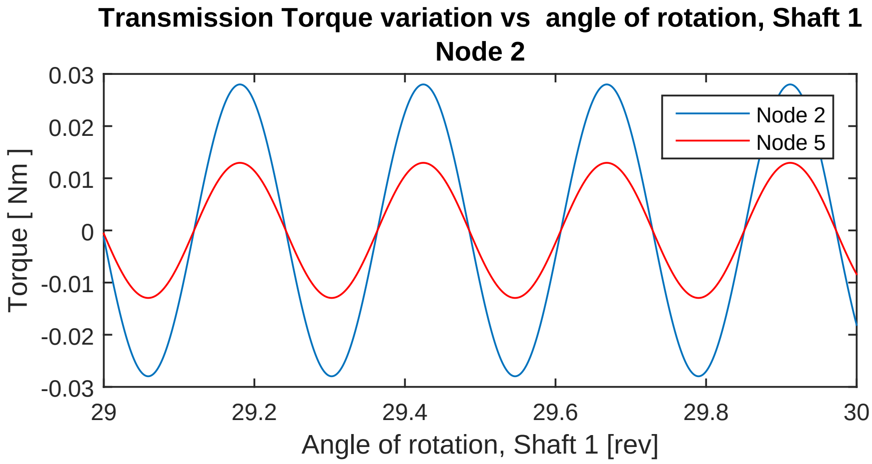

Figure 3.10: Gear torque Node 5

3.6 The gear mesh as a second source of tangential excitation due to the bearing dynamics

In the last section it has been shown that the gear mesh works as a link translating angular torque perturbations introduced on one shaft to the other producing IAS variations along the whole shaft line.

In chapter 2 it has been said that for the bearing dynamics to produce torque perturbations a phenomenon coupling the tangential and normal forces has to occur. This coupling was described by means of the rolling resistance phenomenon in which a displacement of the rolling element normal force application point occurs introducing very small torque perturbations to the inner and outer races.

In the case of gear transmissions, the nature of the gear mesh is tangential: the direction of the connecting forces is on the line of action which is the tangent to both gears' base circles. No matter which perturbation occurs, whether it is on the displacement DOF or in the angular one, the gear mesh will convert these perturbations into a torque variation which will manifest as an IAS variation of both shafts to which the gears are attached. To show this phenomenon, roller bearings are added to the transmission tested in the last sections. Figure 3.11 shows the scheme of the tested configuration.

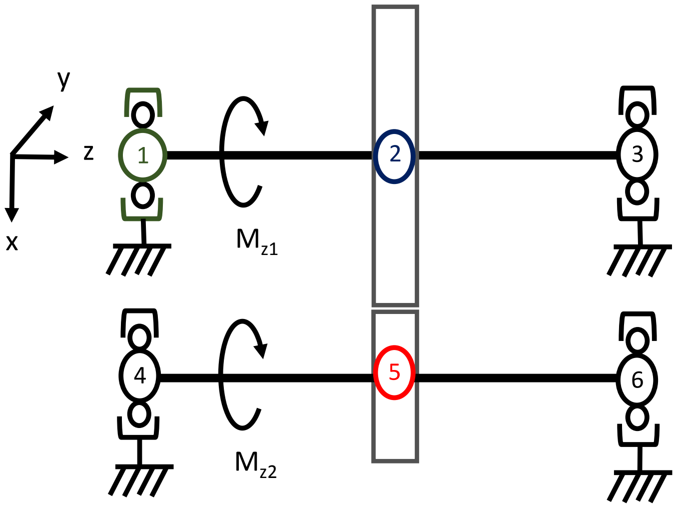

Figure 3.11: Scheme of a single-stage multiplier transmission supported by bearings

The bearing placed in node 1 denoted as "bearing 1" is modeled with the new methodology presented in Chapter 2. The other three bearings are modeled with the classic Palgrem's formulation [70] where a global average non linear stiffness is considered in which, opposed to the model presented in this dissertation, the effect of load variation over the roller bearings is not included. To match the connecting forces approach, the load applied on both the inner and the outer races are estimated and integrated to the force bearing vector $\{F_{beaN}\}$. The adapted Palgrem's formulation is described in Appendix B.3. The use of this formulation means that the only excitation in the system is originated by the bearing 1. This was decided with the intention of easing the analysis and the understanding of the phenomena. The bearing 1 is the same tested in section 2.4.2 which is a 6214 bearing with 10 rolling elements and an angle BPFO of 4.1045 ev/rev. The other three bearings, modeled with the Palgrem's formulation are 6314.

To study the interaction between the roller bearing friction torque perturbations and the gear mesh torque, simulations were performed for bearing 1 in healthy and faulted conditions, considering the rolling resistance phenomenon ($\mu = 0.0015$) and making the rolling resistance coefficient equal to zero. In the last condition, the gear mesh is the only responsible to induce torque variations due to the dynamics of bearing 1. The defect was aligned with the direction of the maximum load, set with a length of 10% of the angular distance between rolling elements with a depth provoking 75% of load loss for the rolling element passing through the defect (see figure 3.12). The same conditions of external loading of section 3.4 are considered giving an angular speed of the input shaft around 518 rpm.

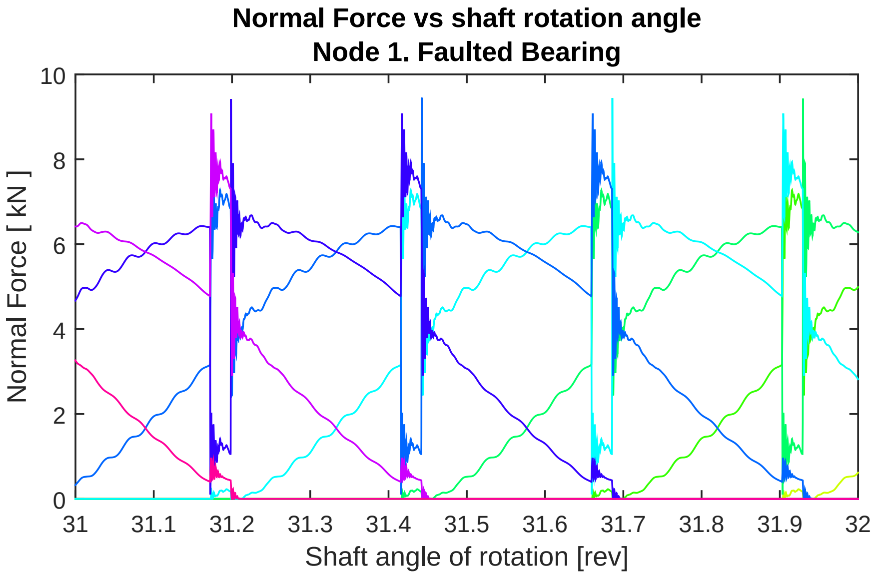

Figure 3.12: Normal force distribution with defect inducing 75% of loading loss

Figure 3.13 shows the torque perturbation for the four conditions: $\mu = 0.0015$ and $\mu =$

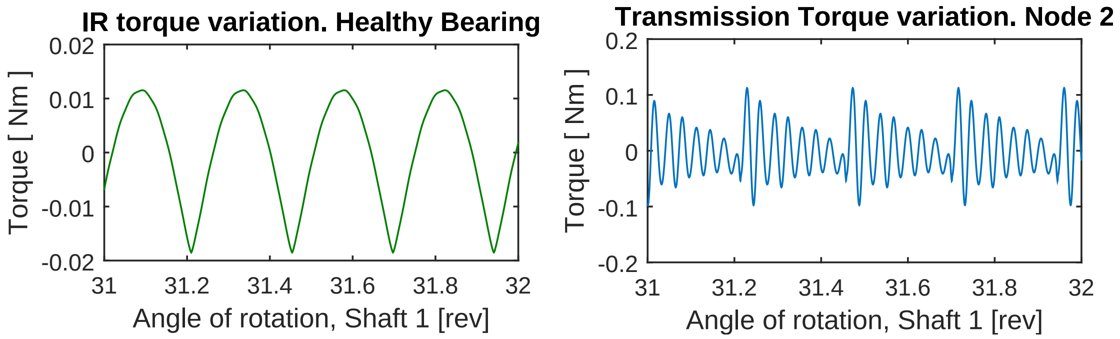

(a) IR perturbation torque variation. $\mu = 0.0015$ (b) Gear torque variation Node 2. $\mu = 0.0015$

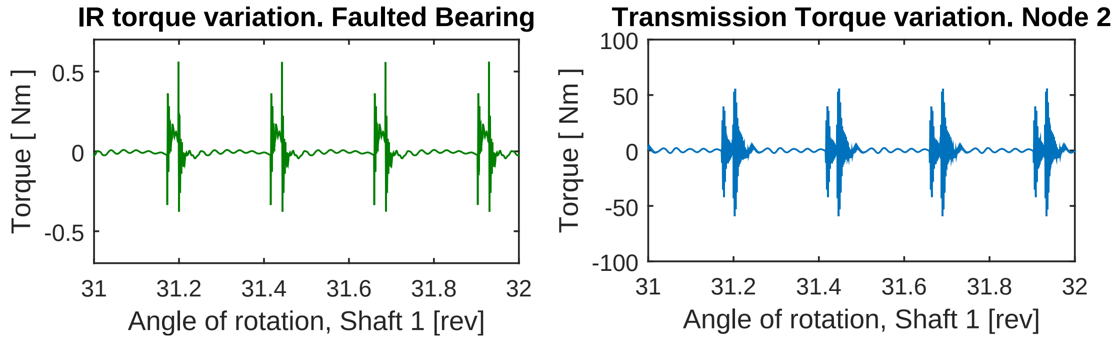

(c) IR perturbation torque variation. $\mu = 0.0015$ (d) Gear torque variation Node 2. $\mu = 0.0015$

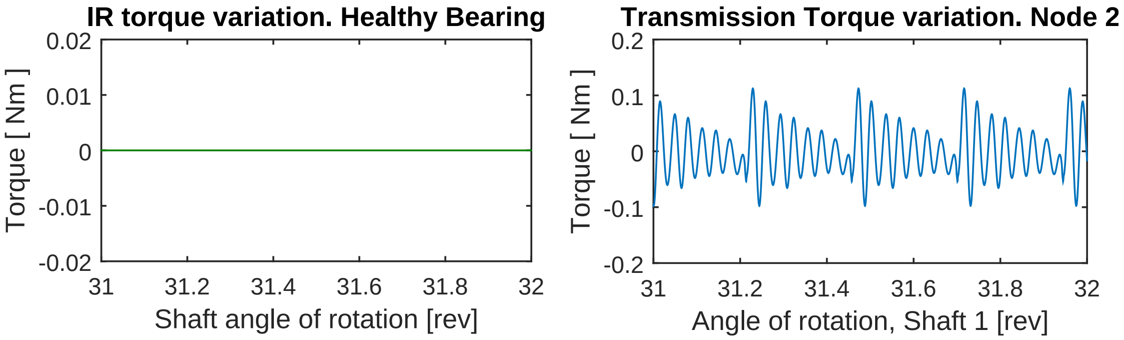

(e) IR perturbation torque variation. $\mu = 0"$ (f) Gear torque variation Node 2. $\mu = 0$

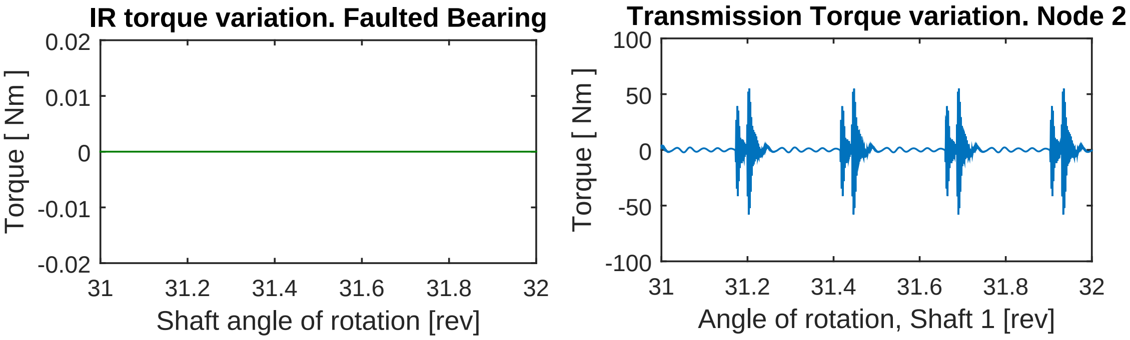

(g) IR perturbation torque variation. $\mu = 0$ (h) Gear torque variation Node 2. $\mu = 0$

Figure 3.13: Torque variation induced by the bearing dynamics. Rolling resistance vs gear mesh

0, for the healthy and faulted bearing. From Figures 3.13(a) to 3.13(d) it can be seen that in presence of the rolling resistance coefficient the effect of the radial displacements of the gearing mesh provokes a moment variation around a hundred times bigger than the one introduced by the rolling resistance phenomena, in presence or not of the bearing defect. This big difference between the two conditions makes that when the coefficient μ is equal to zero, the amplitude and shape of the gear mesh moment variation remains invariable (Figures 3.13(e) to 3.13(h)). The author can not affirm that this ratio would be the same for any configuration and dynamic parameters of the system, for example in presence of flexible bearing supports. What it can be said is that in every test performed throughout this research it was found that the tangential characteristic of the gear mesh has more influence over the moment variations than the rolling resistance phenomenon. Recall that the excitation leading to torque variations depends on the normal force variation of the races and the rolling resistance coefficient which at being very small, makes the torque variations also very small related to the normal forces. In the case of the gear mesh, the tangential forces depend on the gears' displacements and the interacting teeth stiffness which due to its magnitude leads to more important torque variations compared to the roller bearing torque excitation. In this frame, the dynamic parameters of the supports become critic due to their direct relationship to the displacements of the shafts and the gears.

The IAS variation response is shown considering the rolling resistant phenomenon in Figure 3.14. The author confirms that no difference can be noticed in the amplitude and the shape of the curves when the rolling coefficient is nil due to the big difference in the orders of magnitude of the perturbation torque variation. It is observed that the IAS is successfully transferred into the exit shaft of the transmission by means of the gear mesh. Regarding the ouput shaft, amplification of the angular speed variation occurs by means of the gear transmission ratio. However, this amplification is not directly linked to the transmission ratio as it was for the case of the pure rotation model. Actually, the looped excitation discussed in Section 2.4.2 is now coupled with the gearing dynamics which seems to contribute in the increase of the sensibility of the response to the modal parameters of the system. This phenomenon induces high frequency oscillations which are related to the bearing excitation. The shape of the IAS response as well as the amplification phenomenon varies in the presence of the bearing defect. As expected, the IAS response is a lot more energetic than in the case of the healthy bearing.

Spectra calculated over twenty revolutions of the input shaft are also shown in Figure 3.14. Notice that for the Node 5 the angle frequency is referenced to the input shaft

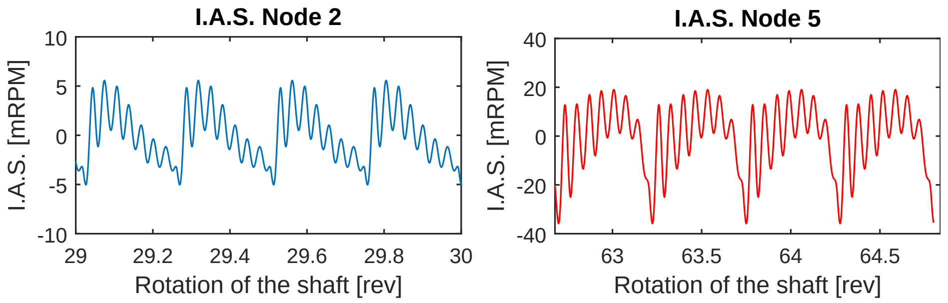

(a) IAS Node 5. Healthy bearing (b) IAS Node 5. Healthy bearing

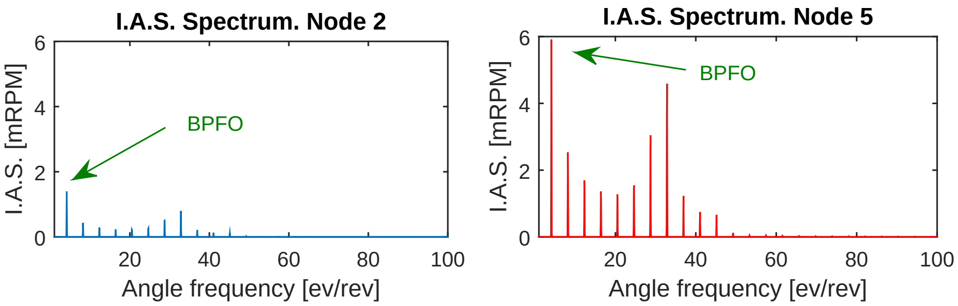

(c) IAS spectrum Node 2. Healthy bearing (d) IAS spectrum Node 5. Healthy bearing

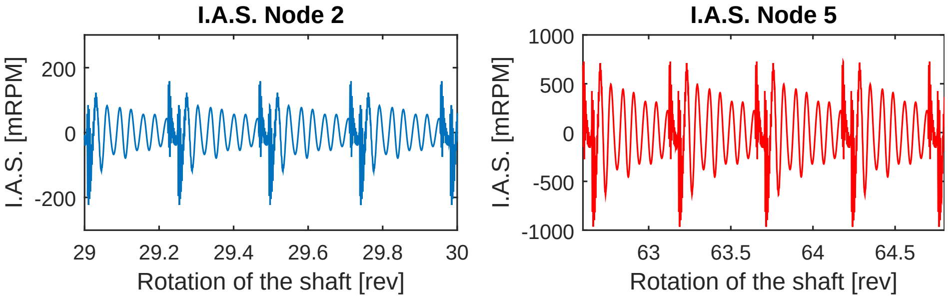

(e) IAS Node 2. Faulted bearing (f) IAS Node 5. Faulted bearing

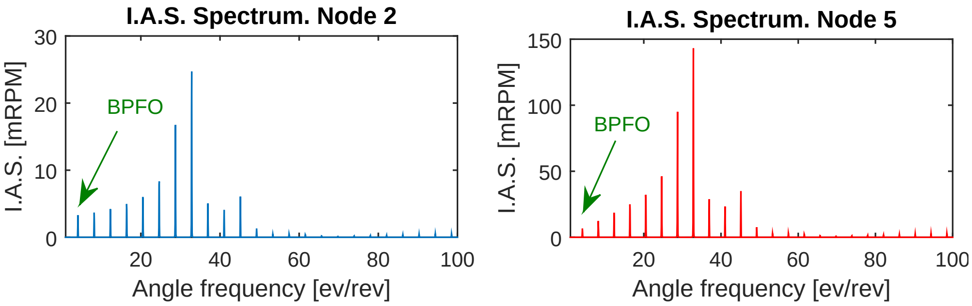

(g) IAS spectrum Node 2. Faulted bearing (h) IAS spectrum Node 5. Faulted bearing

Figure 3.14: IAS response for nodes 2 and 5. Healthy and faulted bearings

meaning that the angle BPFO does not change. It is observed on the spectra a strong harmonic behavior of the IAS. The peak at the fundamental frequency is dominant when the bearing is healthy, but there is also an outstanding peak corresponding to the eighth harmonic which predominates in the case of the faulted bearing. This behavior is verified related to the modal response of the mechanical system.

In the spectra the IAS amplification due to the transmission ratio is also observed. To explore this phenomenon experimentally, measurements performed by Fedala et al. in a gear's test rig described in [29] were analyzed. The mechanical configuration is close to the one modeled in this section but functioning in the sense of speed reduction. The gearbox ratio is 1:2.24, with a pinion of 25 teeth and a gear of 56 teeth. The measurements were taken with a missing pinion's tooth in stationary conditions at 2400 rpm by means of two encoders installed on the High Speed Shaft (HSS) and on the Low Speed Shaft (LSS) respectively. Figure 3.15 shows the spectra obtained for each measurement.

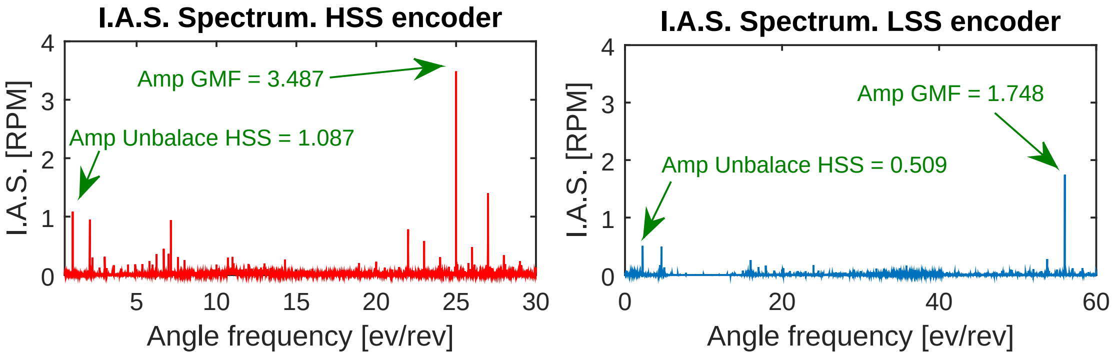

(a) IAS HSS Spectra. Gear's test Rig

(b) IAS LSS Spectra. Gear's test Rig

Figure 3.15: IAS Spectra for gear's test rig with a missing pinion's tooth

The spectral response of the gear's defect was used to analyze the IAS amplification. Observation of the spectra at the fundamental frequencies of Unbalance of the HSS and the Gear Mesh (GMF) was performed. An IAS "reduction ratio" was estimated by dividing the amplitude of the spectral peak of the HSS by the one of the LSS. Regarding the Unbalance of the HSS, a reduction ratio of 1.99 is observed which represents 89% of the transmission's ratio. In the case of the gear mesh fundamental frequency, the reduction ratio observed is 2.14 which is 95% of the transmission's ratio. When looking at the model results (Figure 3.14), the ratio of the BPFO's fundamental frequency is 4.22 for the healthy bearing and 2.00 for the faulted bearing which represent 195% and 92% of the model's transmission's ratio. From these results, it is corroborated that the gear mesh tends to “influence” the IAS variation in the same sense of the transmission ratio, as it is the case for the “macroscopic” angular speed and torque.

These results need to be carefully handled. A generalization of the amplification phenomenon can not be asserted for every cyclic excitation. The magnitude of the amplification is expected to be related to the nature of the torque perturbation which is not the same for the unbalance, the gear mesh and the bearings. Besides, it was pointed out that the dynamic parameters of the system influence the modal response of the IAS, specially in the case of the bearing defect, which makes the harmonics to respond with different amplitudes all along the frequency domain which is expected to affect the amplification phenomenon.

Summary

The exploration performed in this section led to findings outstanding the influence that the dynamic parameters of a mechanical rotating system may have on the IAS response in presence of gears.

The gear mesh tangential force variation depends on the gear displacements which translates directly into torque variations. In the case of study, the excitation is originated from the bearing dynamics and the gear displacements due to these excitations depend deeply on the flexibility of the shaft and the supports. The resulting IAS response in both shafts of the geared system has very strong harmonic behavior in which the amplitude of certain BPFO harmonics out-stand more than others. This phenomenon is supposed also to be related to the dynamic parameters of the system.

In the next section a brief exploration about the impact of the system’s flexibility on the IAS response is presented by modeling the bearing supports as discrete lumped parameters.

3.7 On the effect of a single transmission dynamic parameters on the IAS response

A brief exploration is made in this section about the effect of the the supports' flexibility on the IAS response of the mechanical configuration tested in the lasts three sections. The choice has been made to leave invariable the bearing models. The exploration was performed by adding flexible supports to the roller bearings with two degrees of freedom in each of the radial directions X and Y. The scheme in Figure 3.16 shows the representation of the supports in the X direction. The modal parameters of mass and stiffness are the same for all the supports in the X and Y directions and they were established to obtain critical frequencies of 300 and 1000 hz for the two DOF support system. The damping was set to 3%.

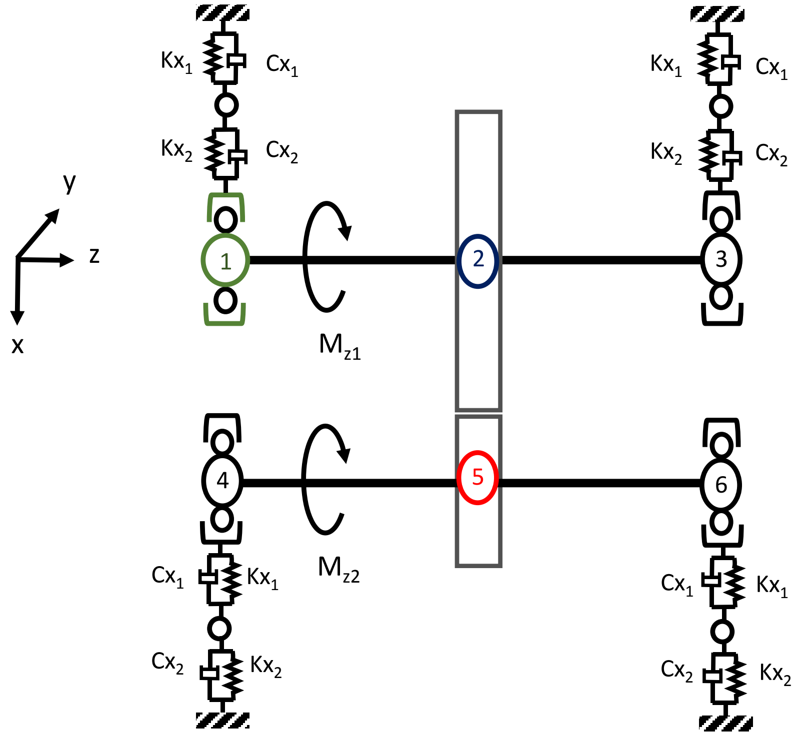

Figure 3.16: Scheme of a single-stage multiplier transmission supported by bearings

The IAS response of the system due to the healthy bearing excitation in the frequency domain was obtained by applying linear external torques M_{Z1} and M_{Z2}. The acceleration slope was the same for both torques. A radial load was applied to the Node 1 (bearing 1) equal to 20 % of the maximum dynamic charge of the bearing with the objective of having small impact on the gear loading variation due to the external linear torques. Then, a comparison was done for three mechanical configurations: rigid supports, flexible supports and dividing all support stiffnesses by 10 in the flexible configuration (Figures 3.11 and 3.16).

The angular speed response resulting from the linear external torque for the flexible support system is shown in Figure 3.17. The simulation was made for 20 revolutions of the input shaft and the speed goes from 100 to 800 rpm. As expected, the "macroscopic" angular speed response under the applied linear torque is the same for the three support configurations, knowing that it corresponds to the angular rigid body behavior of the system which is independent from the modal parameters of the supports, as it is discussed in Appendix C.1.

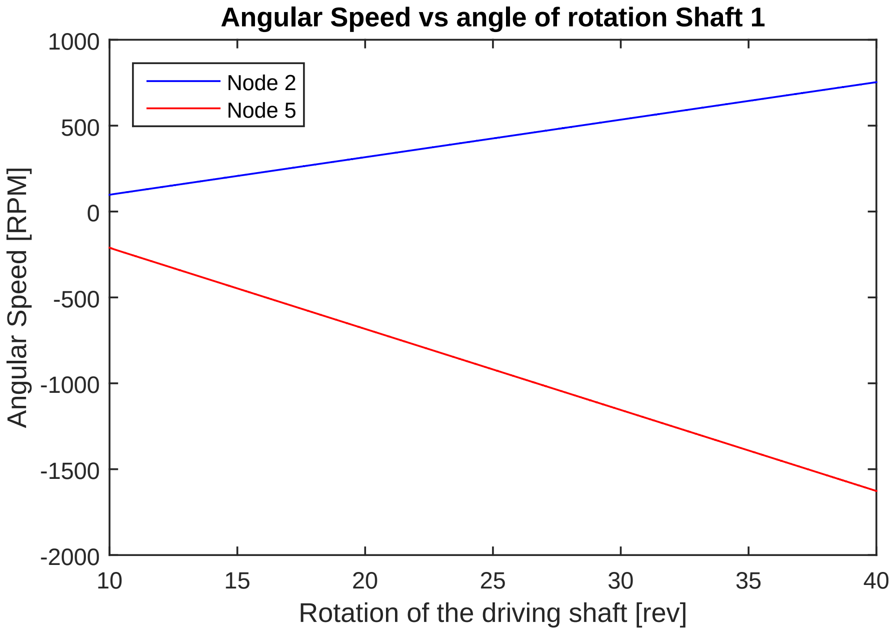

Figure 3.17: Angular Speed vs angle of rotation Nodes 2 and 5. System with flexible supports

Regarding the IAS variation, differences are clearly found between the responses of the three mechanical configurations when they are analyzed by means of the Fast Fourier Transforms shown in Figure 3.18 which, by the nature of the linear non-stationary excitation, exhibit the modal response of the system. When comparing the response between the different supports, it is found that as the system becomes more flexible the critical speeds become smaller showing the sensitivity of the IAS response to the stiffness of the supports.

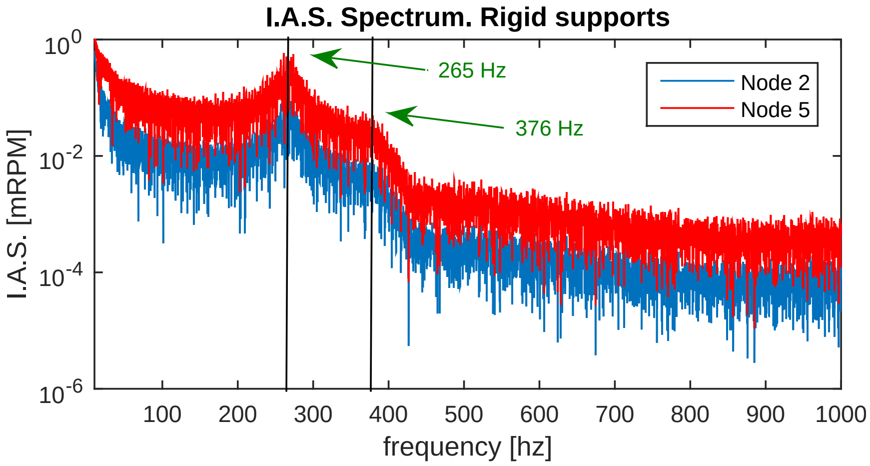

(a) IAS Spectra. Rigid supports

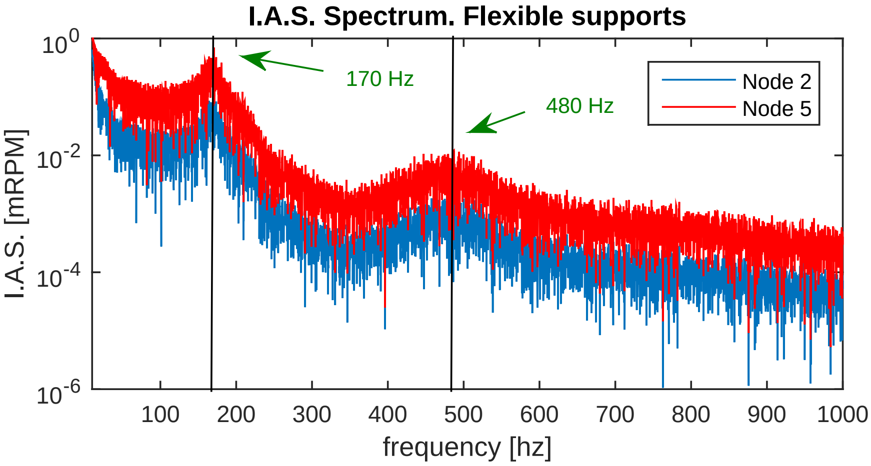

(b) IAS Spectra. Flexible supports

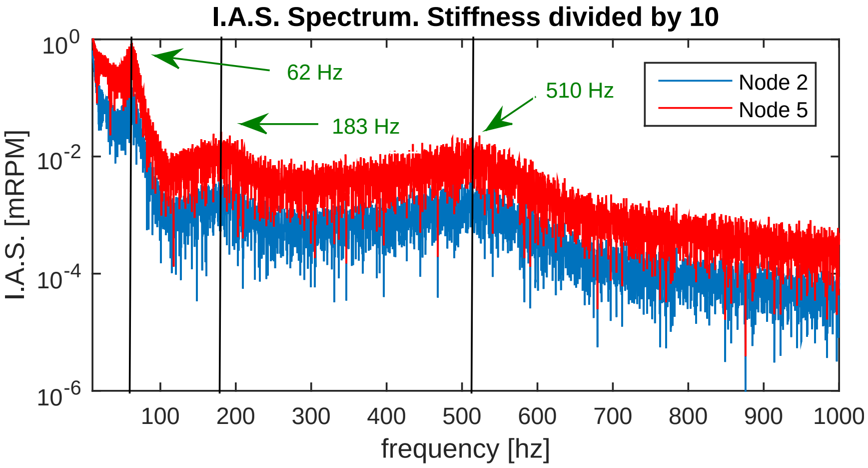

(c) IAS Spectra. Flexible supports with the stiffness divided by 10

Figure 3.18: IAS Spectra. Response to linear external torque and bearing excitation

By comparing the response between the two shafts of the same mechanical system, it is observed that they are very similar in shape. This occurs for all three support configurations and it means that the modal response of the IAS in both shafts shows the same critical frequencies.

It is important to say that the author has verified the response to the linear external torque of the system in pure rotation (Section 3.5) and no response is observed. Thus, no critical frequency is excited between the range of angular speeds of the test. This particular observation means that the modal response shown for the three bearing-support configurations belong to the radial dynamics of the mechanical system which is coupled with the angular response by the rolling coefficient phenomenon and the gear mesh. This affirmation points out special importance to the modeling of the supports and the bearings as they have major influence in the radial displacements of the entire system.

As can be inferred the modal response has an effect in the shape of the IAS in the physical domain. This influence is also noticed in the energy distribution of the phenomenon in the frequency domain as it was pointed out in the spectra shown in Figure 3.14, where certain harmonics of the BPFO of the bearing out-stand in amplitude. To explore this occurrence two stationary conditions were simulated. The external torques were adjusted to obtain angular “macroscopic” speeds of 220 rpm and 518 rpm of the input shaft for the flexible supports configuration. The simulations were performed for the healthy and the faulted bearing with the same defect tested in section 3.6. The dynamic excitation is related to the BPFO of the modeled bearing (bearing 1) which is 4.1045 epr in the angular domain, equivalent to 95 Hz and 220 Hz in the time frequency space for each of the angular speeds tested.

Figures 3.19(a) and 3.19(b) show the IAS for the case of the healthy bearing in both operating conditions. Notice the difference in the shape of each of the curves. It can be seen that in the condition of 220 rpm the oscillations corresponding to the harmonics of the BPFO are smaller in amplitude compared to the condition of 518 rpm. When looking to the spectra in the angle domain for each condition (Figures 3.19(c) and 3.19(d)), the described phenomenon is easier to observe when the peak at the BPFO’s fundamental frequency is more predominant related to the harmonics for the condition of 220 rpm. The reader is asked to recall the analysis of the modal behavior of the system shown in Figure 3.18(b). Notice that the two critical frequencies are 170 Hz and 480 Hz. This means that the BPFO excitations of 95 Hz and 220 Hz are one under and the other above the first critical speed of the system which explains the difference in the harmonic behavior and therefore the shape of the IAS response. The spectra show that in the case of the angular

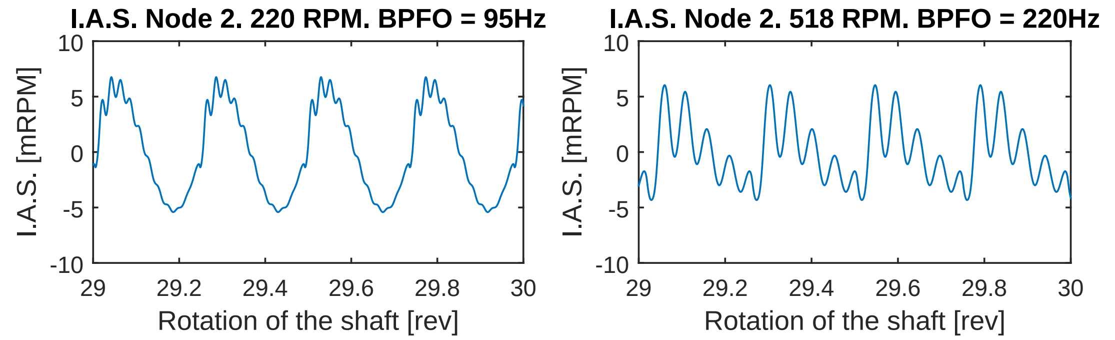

(a) IAS. Healthy bearing. 220 rpm (b) IAS. Healthy bearing. 518 rpm

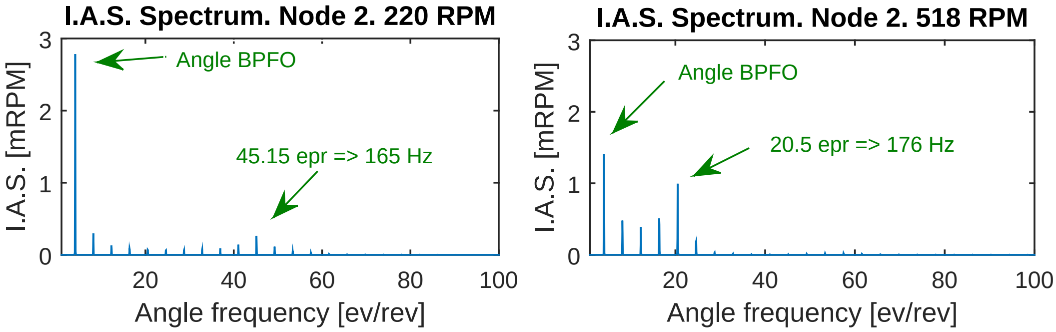

(c) IAS spectrum. Healthy bearing. 220 rpm (d) IAS Spectrum. Healthy bearing. 518 rpm

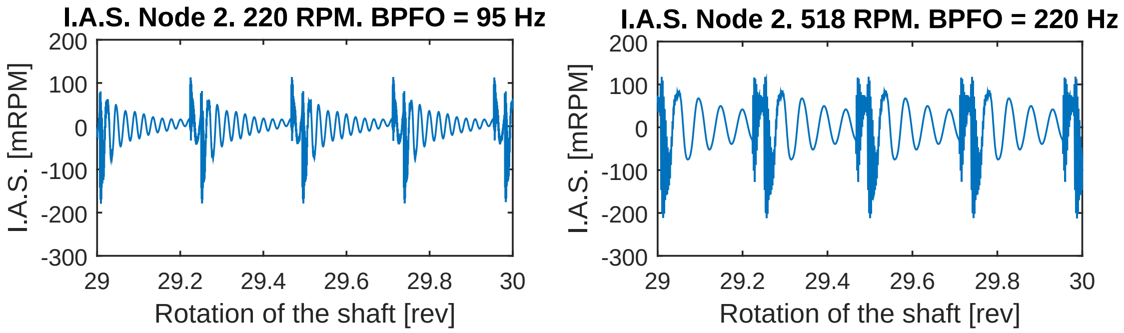

(e) IAS. Faulted bearing. 220 rpm (f) IAS. Faulted bearing. 518 RPM

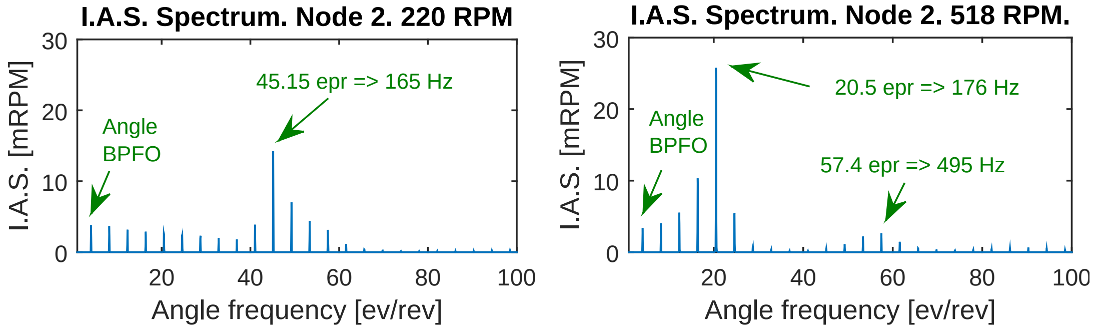

(g) IAS Spectrum. Faulted bearing. 220 rpm (h) IAS Spectrum. Faulted bearing. 518 rpm

Figure 3.19: IAS response for node 2 at 220 and 518 rpm. Healthy and faulted bearings

speed of 220 rpm, the 10th harmonic (165 Hz) stands out among the others because it excites the critical frequency of 170 Hz. Similarly, and with an order of magnitude close to the peak at the fundamental frequency, the 4th harmonic (176 Hz) stands out as a peak as it excites the same critical speed for the case of 518 rpm.

When performing an analogous observation to the cases with the bearing defect, due to the impulsive phenomenon regarding the load distribution of the rolling elements, more energy is added which contributes in the excitation of the modes. This is translated in having the predominating peak of the spectrum, in both cases, at the harmonics close to the critical frequency of 170 Hz. For the case of 518 rpm a second predominant peak is found at 495 Hz which is in the neighborhood of the second critical frequency (480 Hz).

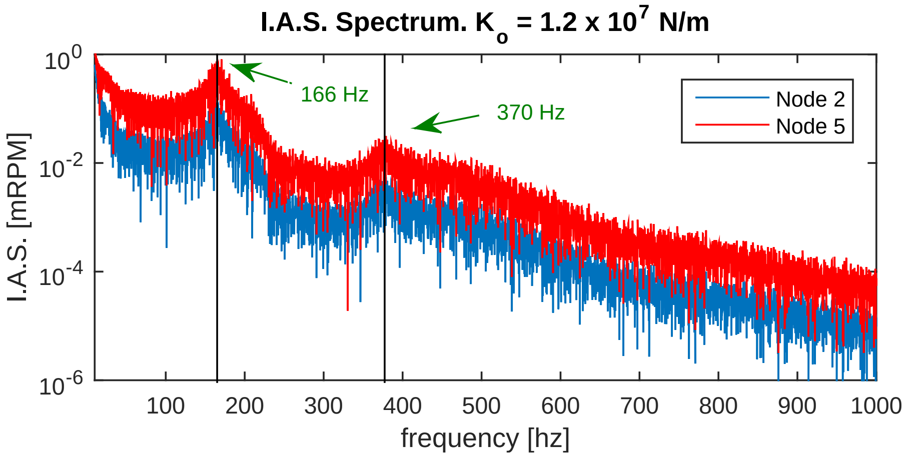

(a) IAS Spectra. Flexible Supports. $K_o = 1.2 \cdot 10^7$ N/m

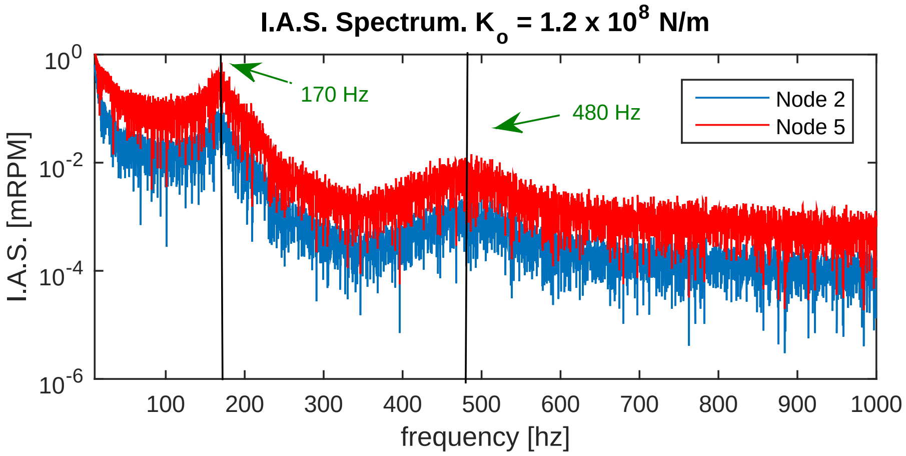

(b) IAS Spectra. Flexible Supports. $K_o = 1.2 \cdot 10^8$ N/m

Figure 3.20: IAS Spectra. Response to linear external torque and bearing excitation for two different average gear mesh stiffness

A brief analysis on the influence of the gear mesh stiffness value was performed. For the configuration of flexible supports (Figure 3.16), the response to the linear external torque and the bearing excitation was estimated for different values of the gear mesh stiffness which is equal to $1.2 \cdot 10^9 N/m$ when estimated with Equation 3.28. The simulations for different stiffnesses going between $1.2 \cdot 10^7 N/m$ to $1.2 \cdot 10^{10} N/m$ have all similar responses with exception of the one with the stiffness equal to $1.2 \cdot 10^7 N/m$. The others have responses with critical frequencies very alike to the one of $1.2 \cdot 10^9$ N/m (see Figure 3.18(b)).

Figure 4.6 presents the responses for the tested stiffness values of $1.2 \cdot 10^7$ N/m and $1.2 \cdot 10^8$ N/m. Notice that it is the second critical frequency the one having a substantial decrease in value for the lower tested average stiffness in the analyzed frequency span. When comparing these results to the ones where the support characteristics vary, it is found that the gear mesh average stiffness needs to have substantial changes in the order of magnitude to induce modal variations onto the IAS response.

3.8 Conclusions

Being the interest of this chapter the modeling of the gear mesh in presence of the bearing dynamics leading to IAS variations in non stationary conditions, a weak modification in the assumptions of a classic model was presented to make it suitable to manage rigid body angular rotations in the gear longitudinal axis. This modification based on the static transmission error was verified not changing the resulting equations for the estimation of the gear mesh stiffness. The linking gear element was presented with the approach of connecting restorative forces which would ease the introduction of non linear gear mesh stiffnesses.

The roller bearing model presented in Chapter 2 was integrated with the gear mesh approach in a single stage configuration supported by four bearings, where three of them were modeled by using the Palgrem's formulation, implying that the dynamics of the rolling element load distribution is not taken into account. This choice was made to facilitate the analysis of the IAS response of the system. In the same way, the gear mesh stiffness was considered linear which allowed to perform observations in the physical domain.

The rigid body angular rotations were validated by confronting pure rotation simulations with the analytical results of Newton's laws. It was also verified that in pure rotation a sinusoidal torque perturbation provokes an also sinusoidal IAS response in both shafts, confirming the transmissibility of the phenomenon by means of the gear mesh.

The gear mesh was shown to be a second source of coupling between tangential and normal forces meaning that the bearing radial dynamics affect the gear tangential forces contributing to the torque variations. The comparison between the response when considering or not the rolling resistance phenomenon in presence of a healthy or faulted bearing indicated for the tested configuration, that the tangential nature of the gearing connecting force has more influence in the amplitude of the IAS response than the rolling resistance.

A strong harmonic behavior of the IAS response was observed with the increasing of the amplitude in specific harmonics which led to perform an analysis of the response of the system to the bearing dynamic excitation and linear external torques to analyze the modal response of the system in three different bearing support configurations. This analysis has verified that the IAS phenomenon is sensitive to the dynamic parameters of the supports. Therefore, changing the operating conditions will impact the response in the frequency as well as in the physical domain not only as a consequence of the variation of the load in the bearing, but also due to the modal response of the system.

Variation of the gear mesh average stiffness affects the IAS response only for very flexible values which are far from reality. By seeing these results from the point of view of IAS based condition monitoring, it can be inferred that several harmonics of the spectra would respond more to the bearing dynamics. Once identified, these harmonics may be used to built surveillance indicators. Regarding the signal processing techniques, these results suggest that the use of the spectral envelope as a tool for diagnosis through the IAS signal should be further investigated. Using the correct filter in a more rich signal (excitation from gears, unbalance, multiple bearings, etc.) should be able to stand out the effect of the modal response of the structure.

The statements above make the modeling of the supports an important issue, when description of an entire transmission is intended. In non stationary machinery surveillance, having a response sensitive to the modal parameters as well as to the modal conditions complicate the development of condition monitoring indicators, which is also the case when the acceleration response of a system is measured. In the last case, accelerometers are placed on the support casing which makes this assertion more evident. However, as it was shown in Chapter 1, encoders are installed onto the shaft making one to think that supports would have little influence in the IAS response.

The amplitude of the speed variations was shown to be affected by the transmission ratio which in the case of the current study, was a speed multiplier. From measurements made in [29] it was verified for an existing single gear stage test rig that the unbalance peaks as well as the gear peaks in the spectra were affected by this phenomenon in the same sense as the model presented in this chapter. To be able to corroborate and analyze the conditions in which the speed variations are influenced by the transmission ratio, a test rig specially adapted for the IAS analysis would be needed. Such a test rig would also serve as a tool to deepen the analyses regarding the modal response of the whole system and its influence on the IAS phenomenon.

In the next chapter, as a closure to this dissertation and with the objective of testing IAS surveillance indicators under non stationary conditions, a simplified wind turbine shaft line model is build based on the architectures presented until now. The intention is to present a tool allowing tests in different bearing damaging stages and to analyze the strengths and the weaknesses of the modeling approach.

Chapter 4

The construction of a simplified wind turbine model for testing IAS surveillance indicators

Contents

4.1 Introduction

This chapter is dedicated to build an engineering application based on the modeling approaches presented in previous chapters: the construction of a mechanical model of a wind turbine shaft line with a multi stage gear transmission. The model is intended to be a demonstrative tool for analysis of surveillance indicators in non stationary operating conditions.

In the first part, the construction of the model is presented discussing the simplifications and their possible impact on the IAS response of the system. Validation of the rigid body rotation is performed and a brief analysis in stationary conditions of the frequency response of the system is presented.

Then, the system is tested under non stationary conditions simulated from experimental wind speeds and a linearized generator's torque which is a function of its angular speed.

A description of the tools used in the frequency domain as well as the analyzed surveillance indicators is performed. The protocol for testing the evolution of a simulated bearing defect and the generation of a set of healthy IAS signal measurements is presented.

Finally, the simulated healthy and faulted sets of measures are used to test the indicators which are then processed by the normalization procedure proposed by André [3]. Results are compared with experimental analysis from a wind turbine's generator roller bearing defect. A discussion is made to analyze the strengths and the weaknesses of the modeling approach and the simplifications leading to the conclusions and the perspectives of this research project.

4.2 The construction of a simplified wind turbine model

After 10 years of operations, some machines from Engie Green have already confronted several expensive maintenance issues regarding the mechanical components of the wind turbine shaft line. Several bearing defects have been detected in different machines instrumented with a self developed accelerometer based monitoring system and temperature sensors. However, in some occasions, the monitoring system have identified the defects when they were in a medium to advance stage of damage. Replacing a bearing generates costs of hundreds of thousands of euros not taking into account the time of unavailability of the machine, making it a very critic failure mode. This has led Engie Green to reinforce the IAS analysis to be used as a complementary surveillance tool.

In parallel with the IAS modeling research, a project for the construction of raw and spectral IAS indicators is being developed as part of an automated surveillance system. The construction of a wind turbine virtual demonstrator was performed to test the models developed and presented in the previous chapters in a more complex mechanical architecture. This virtual machine was then used to test a set of indicators to analyze the tendencies related to some of the experimental data collected since the time the first machine was instrumented [1]. The simplified wind turbine model is inspired in this first machine which is a Senvion MM82 of 2 MW of power generation at nominal wind speed and is centered around the dynamics of the Main Bearing.

Next, a review of the wind turbine's modeling state of the art is presented to contextualize the reader into the choices made to build the model presented in this chapter.

4.2.1 Brief review of wind turbine modeling

The majority of wind turbine models found in the literature may be divided into three groups. The first is intended to the analysis of aerodynamic loads and their effect on the whole assembly: tower, nacelle, blades and rotor. Another group is dedicated specifically to the modeling of the rotating elements: transmission, couplings and generator, always with the aim of reliability and design improvement. A third group is dedicated to the wind turbine control system.

Concerning the first group, a comprehensive work is found in the review presented by Hansel et al in [71]. This work is conformed by a wide compendium of techniques for modeling the wind in the domain of fluid dynamics. Then, it turns into the energy conversion field to deal with the rotor torque description by the wind-blade interaction. The rotor-blade and tower mechanical modeling techniques are discussed as well as the strategies for aeroelastic simulation and stability of the wind-blade-rotor interaction. In this kind of models the interest goes into improving the aerodynamic behavior of the assembly and the rotor-tower dynamics and it does not get into details regarding the transmission, bearings and the generator.

Regarding the second group dealing with the shaft line, the state of the art is highly centered on the gear transmission modeling with focus in planetary and epicyclic gears as most of the wind turbine's gearboxes have at least one stage of this kind of transmission. A very interesting remark is given in reference [72] by Cooley and Parker in a recent review of the state of the art of epicyclic transmission modeling. They point out that most of commercial codes used to model this type of transmissions are based in the multibody dynamics technique. When more precision is needed, this strategy incorporates finite element models for the housing, the planet carriers and even the gears. It is established that this kind of approach is very suitable for root cause failure analysis or reliability improvement, due to the fact that computational times are long. An example of this kind of approach applied to the wind turbine domain is the work of Hensen et al. which is developed in references [73–76]. In this extensive work, a model based on the multibody technique considering six degrees of freedom by component, is developed in a commercial software for an architecture consisting of a stage of three planets and a fixed ring and two helical stages. First, the gears, the planets, the planet carrier and the housing are considered rigid while bearings and gears contacts are modeled with discrete flexibilities. Then, the gears and the planet carrier's flexibilities are included by means of finite element models coupled with the multibody elements using classic coupling techniques. Component Mode Synthesis was used to reduce the size of the model and diminish the calculation time. First, the results were compared with those of Lin and Parker [77, 78] who modeled the same epicyclic configuration with a three degrees of freedom model with the lumped parameters method. Helsen et al. identified more vibration modes, explained by the difference in the number of considered degrees of freedom. A comparison was also made with the work of Peeters [79, 80] in which six degrees of freedom were considered. The dynamic behavior is more in agreement with the analysis of Hansel et al. for the full multibody configuration. However, the model improved with more flexibility by means of finite element analysis presented even more modes of vibration. In a second instance, a wind turbine gearbox test rig was developed and the model was adjusted and tested in several stages to achieve a modal response with good agreement related to the experiments. From the results of this compendium of works, it has been pointed out that obtaining a good correlation between model and experiments depends greatly on the modeling of supports (bearings and housing) and also the planet carrier. The configuration taking into account the components' flexibility by means of finite elements describes better the modal behavior of the real machine. Cooley and Parker [72] also added that lumped parameter models are not widely used in the industry, contrary to their large utilization in the research domain where results have shown good agreement with finite element contact models and experiments. They are similar to multibody modeling regarding modal behavior analysis and design tests but they are not suitable to accurate estimation of stresses and strains as is the case of finite element models. One example of this kind of approach is shown in the work of Abousleiman and Velex [81], where an epicyclic transmission is modeled by lumped parameter description of planets, sun and shaft coupled to a finite element modeling of the ring gear.

Finally, in the third group, the models developed have the objective of evaluating or testing generator's and blade control configuration and their impact in power generation. In this kind of studies, the mechanical models of the shaftline are highly simplified. The work of Santoso and Le [82] is a good example of this group. They present a model of wind turbine divided in four blocks: aerodynamic, mechanical, electrical and control. The drive train is modeled as a one stage gear speed multiplier, considering the inertias lumped and the transmission ratio achieved by a kinematic liaison, meaning that no gear mesh is considered. The intention of this model was not to reproduce a specific machine but to test the potential of this kind of approach to be used as a tool to perform studies in power curve generation, wind power integration, dynamic interactions between wind turbines in a farm, etc.

4.2.2 Description of the wind turbine shaft line

The wind turbine MM82, built by the German constructor Senvion, produces 2 MW of electrical power when operating with wind speeds above 12 m/s. Such a machine has a 82 meters' rotor consisting of three blades attached to a rotating Hub. The shaft line is situated at 80 meters of height inside the nacelle and is attached to a steel tower. The main components of the shaft line are the rotor, the Main Bearing, the speed multiplier gearbox and the generator. Figure 4.1 shows the disposition of these components in the wind turbine's nacelle. Notice that the shaft line axis has an inclination of 5^o.

The Main Bearing supports most of the rotor weight and, as it was mentioned already, it represents a critical asset to be surveyed by the condition monitoring program in the-

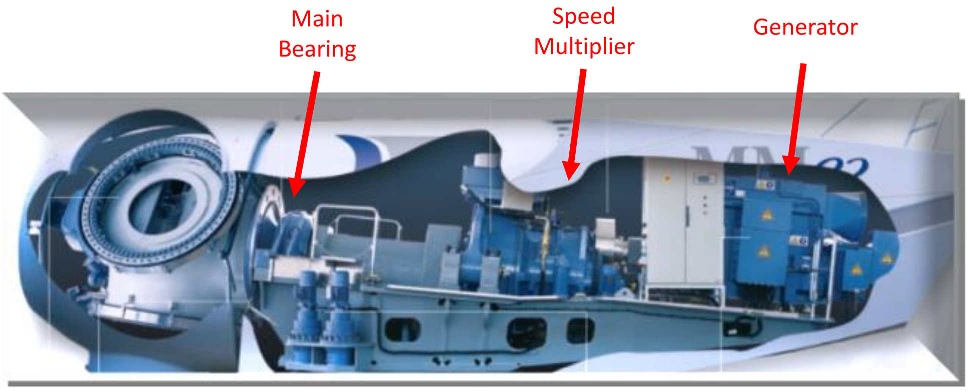

Figure 4.1: Parts of the MM82 wind turbine shaft line

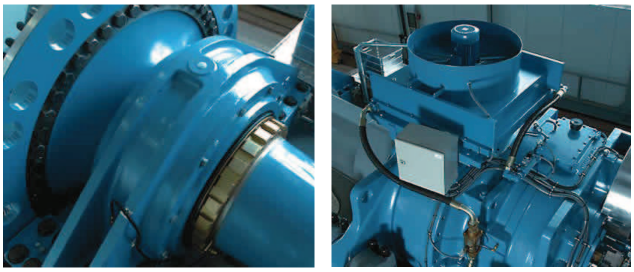

(a) Main bearing (b) Gearbox

Figure 4.2: MM82 Main Bearing and Gearbox

ses machines. For this study, a SKF 240/630 has been modeled, which is a double row spherical bearing of 630 mm of inner race diameter (see Figure 4.2(a)).

The gearbox instrumented in [1] is a RENK with three stages of combined planetary - helical gears (see Figure 4.2(b)). The nominal mechanical power is 2.225 MW and the gear ratio is 105.5. The first epicyclic stage has three planets with a fixed planetary carrier which implies no sun gear and the input is through an internal ring gear attached to the Low Speed Shaft. These planets are the input for the second epicyclic stage which has no ring gear and the output is through a sun gear connected to all three planets and to the shaft leading to the last helical gear stage. The same intermediate shaft is the one motorizing the gearbox oil pump by means of a parallel spur gear stage. Figure 4.3 shows the scheme of the kinematics of the whole wind turbine shaft line with the three stages of the gearbox. No reference to the mechanical efficiency is mentioned in the manufacturer's technical description. Table 4.1 shows the number of teeth of each gear identified with the numbering in Figure 4.3. The ratio for each increasing stage are 4.429, 4.381 and 5.438

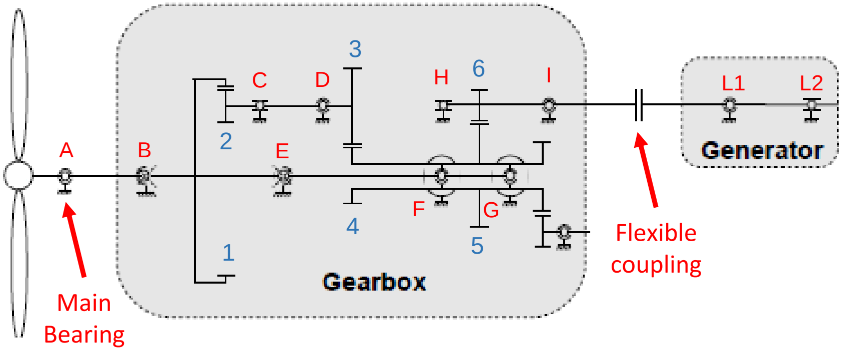

Figure 4.3: MM82 kinematics scheme

Table 4.1: Gears' teeth number for the RENK Gearbox

Gear	Z
1	93
2	21
3	92
4	21
5	174
6	32

for the total of 105.5.

The generator is asynchronous and double-fed with a nominal power of 2080 kW at 1800 rpm. It has a speed range from 900 to 1800 rpm. A frequency converter is used for the control and regulation of the active and reactive power. It also recovers the rotor power from the generator.

The machine has also blade variable pitch and a yaw system as well as an installed encoder in the shaft end of the generator. These features allow to control different system configurations to obtain maximal electrical power generation depending of the wind direction and speed.

Among the different rotating components which are surveyed by Engie Green with the IAS acquisition and analysis system, we find the complete set of bearings as well as the gears. Besides the main bearing, the machine has 9 roller bearings inside the gearbox and two more roller bearings supporting the generator's shaft. The characteristics are shown in Table 4.2 identified with the labeling of Figure 4.3.

A flexible coupling links the gearbox and the generator and its primary function is to avoid that eventual misalignment between these two components produce mechanical

Table 4.2: Bearing characteristics of the shaft line

Bearing	Characteristics
A	Double row spherical. Self-aligning
B	Single row tapered
C	Double row cylindrical
D	Double row tapered. Self-aligning
E	Single row tapered
F/G	Single row cylindrical
H	Single row tapered
I	Double row tapered
L1/L2	Deep groove ball bearings

deterioration. The main characteristic of such a coupling is its very high radial flexibility.

4.2.3 Construction of the MM82 simplified model

Modeling the shaft line of the MM82 with the approaches presented in the previous chapters demanded several simplifications. Figure 4.4 shows the resulting architecture of the mechanical system taking into account the simplifications described hereafter.

The two planetary stages of the gearbox were modeled as a cylindrical gear stage. The intermediate (or planetary and sun gear) shafts' inertia and mass were lumped into nodes 8 and 9 respectively which means that the effect of theses shafts' flexibilities are not taken into account. Another important simplification is that no axial load is considered in the system, due to the fact that the roller bearing model introduced in chapter 2 takes into account the forces only in the radial and tangential directions. The axial load comes from three different sources. The first source is the wind which introduces axial load via the rotor. The second is the 5^o shaft line inclination which makes the weight of the rotor to charge axially the Main Bearing. The third source comes from the helical gears which mesh introduces axial load onto the shafts. For this reason, all the gear teeth were considered straight teeth. Neglecting the axial forces make the distribution of the load among the bearings to be less accurate which directly affects the dynamic response of the model and in consequence the IAS variations.

Regarding the dimensions, all gears have the same pitch diameter, modulus and width of the represented gears. This choice leads to three modeled stages with the same transmission ratio of the real gearbox. The ring bearing inertia and mass was lumped into node 6 and the inertias and masses of all 6 planets were lumped into node 8.

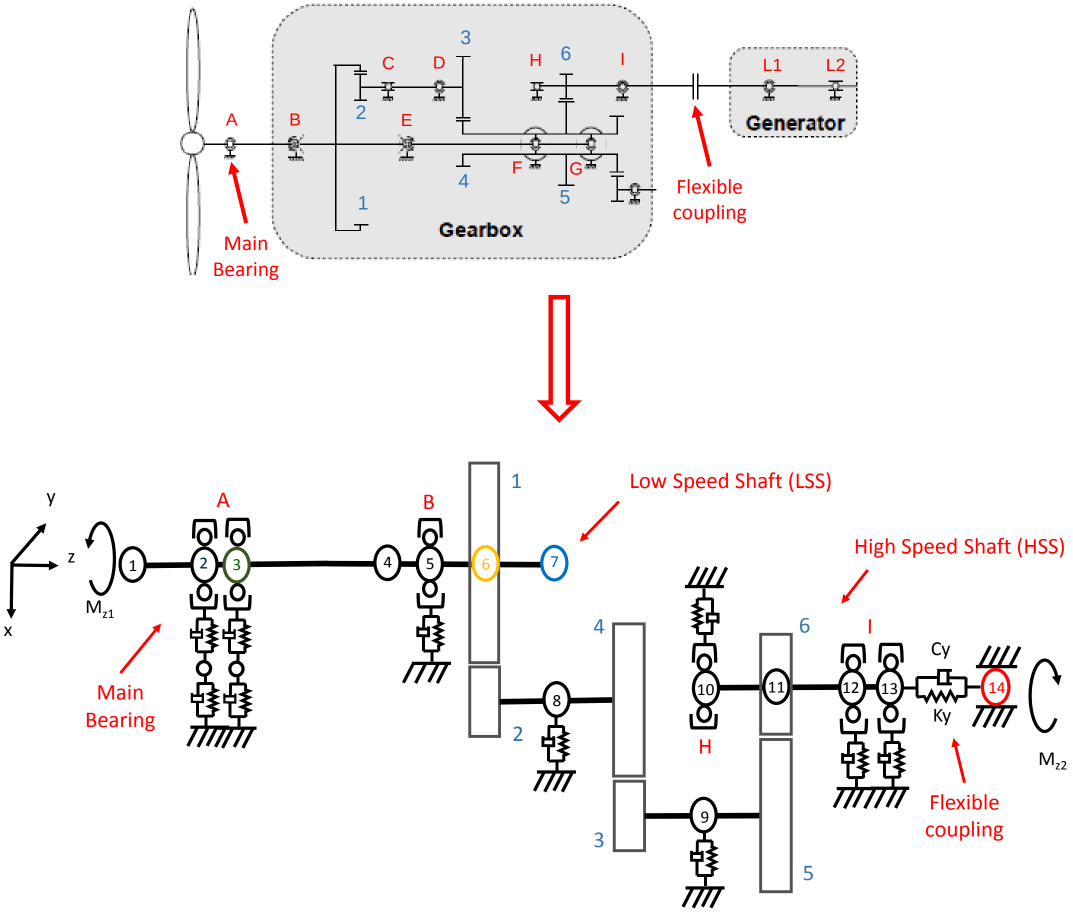

Figure 4.4: Simplified model architecture

The Low Speed Shaft (LSS), discretized into 7 nodes was geometrically truncated until node 7 which is placed spatially in the center of what would be the bearing E. The High Speed Shaft (HSS), which is the output of the gearbox, was discretized into four nodes. Only four bearings were considered. In the LSS, which has five bearings, only two were modeled including the main bearing to avoid the hyperstaticity of the real architecture. Notice that the three bladed rotor and the ring gear (gear 1) are attached to the Low Speed Shaft meaning that no flexible coupling exits in the input of the gearbox. This shaft is very slender after the third bearing from left to right (Bearing E) and the bearings are not meant to support but to be a guide to align the shaft. The other two modeled bearings were those supporting the High Speed Shaft of the gearbox. The rotor inertia and mass are lumped into the node 1 and a static load equivalent to the rotor weight is applied vertically. This load represents most of the static charge supported by the Main Bearing.

The Main Bearing (bearing A), which is a double row spherical one, is described by the model introduced in chapter 2 as a double row deep groove ball bearing. The five degrees of inclination of the shaft line, and the axial load from the wind makes the row closer to the gearbox side more loaded. To approximate this particularity, the clearance of this row was set smaller than the other one increasing the charge (see Equation 2.13). The IAS response of the system contains only the frequency characteristics of the load distribution dynamics and the geometry of this bearing. The diameter of the inner and outer races as well as the rolling element radius were considered identical to the real bearing. The other three bearings (bearings B, C and D) were modeled with the Palgrem equations presented in appendix B.3. The nodes 8 and 9 representing the intermediate shafts were allowed to rotate in the three directions and they can also have displacements along the axes X and Y of the coordinate system in Figure 4.4, allowing the radial dynamics of the gear meshes to be translated to the whole shaft line.

The shaft of the generator was concentrated onto the node 14. This node is only free to rotate in all directions and contains the inertia and mass of the generator's shaft and rotor. The flexible coupling is modeled as an external element linking nodes 13 and 14, with rotational stiffness and damping obtained from the manufacturer only in the Z direction. The choice of restraining node's 14 displacements was made to reduce the degrees of freedom of the system and to increase the stability for the convergence of the Matlab's ODE solver method.

Reduced dynamic parameters of the Main Bearing's housing were obtained by analyzing its modal behavior in Ansys. Two displacement degrees of freedom were retained for the X direction and one for the Y direction as presented in Figure 4.5.

For the rest of the bearings, only one displacement degree of freedom was considered for directions X and Y and the value was chosen with the same magnitude order of the vibrational pads in which the Gearbox rests (See Figure 4.6(a)). Regarding the supports of nodes 8 and 9 representing the intermediate shafts, one degree of freedom by radial direction stiffness and damping elements were considered. For this particular case, the stiffness was overestimated to avoid convergence issues that were identified related to lumping the whole inertia and degrees of freedom of two gears into one node (See Figure 4.6(b).)

In summary, one displacement DOF by direction was considered for all the supports except for the Main Bearing. As the Main Bearing is the focus of the model, this extra DOF was added to allow a better description of its casing which was reduced from a 3D Model in Ansys. Besides, if an eventual study in which the radial acceleration response is

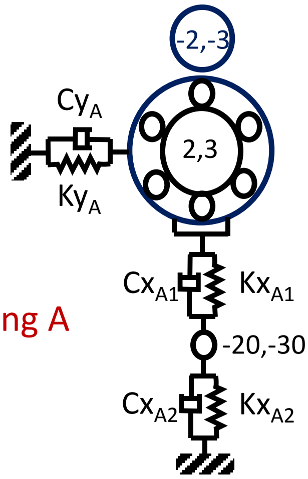

Figure 4.5: Support configuration for the Main Bearing

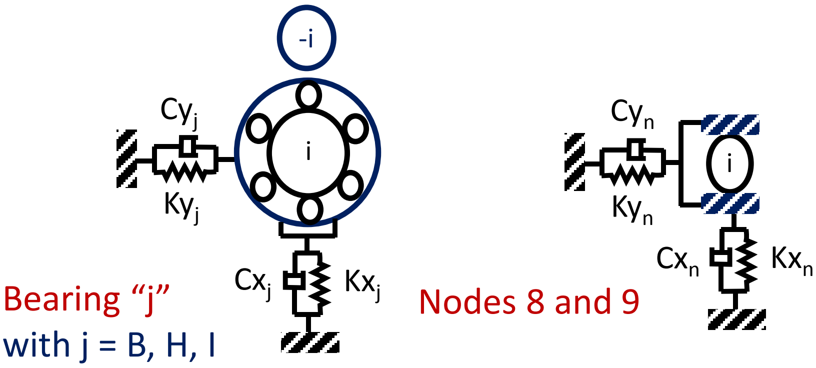

(a) Support configuration for bearings B, H and I (b) Support configuration for nodes 8 and 9

Figure 4.6: Different bearing supports

needed, the added support node would represent the place where the response is measured by an accelerometer. Appendix D.1 contains the specifications and the parameter values used for the bearings, the gears, the supports as well as the shafts described in this section.

4.3 The use of the simplified wind turbine model to test IAS spectral indicators

This section describes the protocol used to perform non stationary simulations allowing to analyze the potential of the model as a tool to build and test condition monitoring spectral indicators.

The test of the IAS indicators comprised two major stages. The former was the set up of the model for simulations taking into account the evolution of a defect in the outer race of the main bearing. The second is the estimation of such spectral indicators and their treatment related to the non stationarity conditions. The description of each of these stages follows.

4.3.1 The set up of the model

4.3.1.1 The design of non stationary simulations

The objective was to obtain non stationary realistic simulations from the point of view of the operating conditions. To perform this task, data measured by Engie Green often used to analyze machine performance and productivity has been utilized. These parameters are whether estimated or directly obtained from the wide instrumentation already installed or added by Engie Green to the machines. From the model's point of view, the inputs needed, were basically the torque induced by the blades onto the rotor by action of the wind and the resistive torque induced by the generator into the High Speed Shaft.

The rotor torque is estimated by the following aerodynamic equation [82]:

$$T_{wind} = \frac{C_e \cdot \rho \cdot V_{wind}^3 \cdot \pi \cdot R_{rotor}}{2 \cdot \Omega_{rotor}} \tag{4.1}$$

where ρ represents the air density, V_{wind} is the wind speed and R_{rotor} is the rotor radius. C_e represents the non dimensional rotor power coefficient which is usually a function of the pitch angle, the rotor angular speed Ω_{rotor} and the wind speed. The coefficient is related to the Betz's law which establishes that the maximum power recovered by a wind turbine's rotor can not be greater than 60% of the kinetic power of the wind [83].

Figure 4.7 shows the operation parameters measured by Engie Green from a MM82 wind turbine identified as M1. The range of operation chosen was limited to wind speeds between 5.5 and 8 m/s. In this range, the generator's angular speed (green curve) has approximative linear behavior related to the Wind Speed.

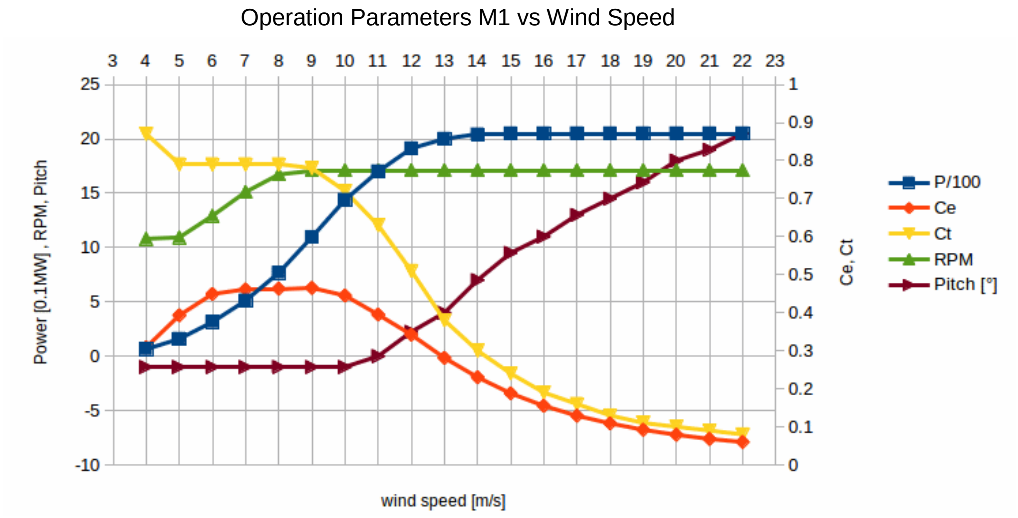

Figure 4.7: Measured operating parameters of a MM82

As an strategy to simplify the analysis, the power coefficient was considered constant and equal to its maximum which is 0.49. It can be observed from Figure 4.7 that the variation of this coefficient in the wind speed range chosen is less than 15%. This consideration overestimates the value of the input torque and in consequence the load on the gears and bearings. The wind speeds were obtained from real measured data performed by Engie Green which are registered with a sampling frequency of 1 Hz.

Regarding the generator's resistive torque, the behavior was also obtained from Engie Green's measurement data base. The torque, measured on the generator's converter, is estimated as a function of the angular speed and is shown in Figure 4.8 for two different MM82 machines. Notice that the curves are very alike. The curve from the M1 machine between 1130 and 1750 rpm was approximated to a linear function with positive slope to be used in the simulations as the generator's torque curve. The resultant generator's resistive torque function M_G, is shown in Equation 4.2 where the angular speed ω has to be expressed in rad/s and the torque is obtained in Nm.

$$M_G(\omega) = 45.66 \cdot \left(\omega - 1130 \cdot \frac{2 \cdot \pi}{60}\right) + 1100 \qquad [Nm] \tag{4.2}$$

Actually, an automated control system based on the measured parameters of wind speed and the generator's angular speed manages the operating condition response of the machine i.e resistive torque, pitch angle, etc.). In the case of the simulations, a basic control loop was built by means of the described equations to obtain the rotor and generator torques as a function of the wind speed. Figure 4.9 shows the resulting loop control for

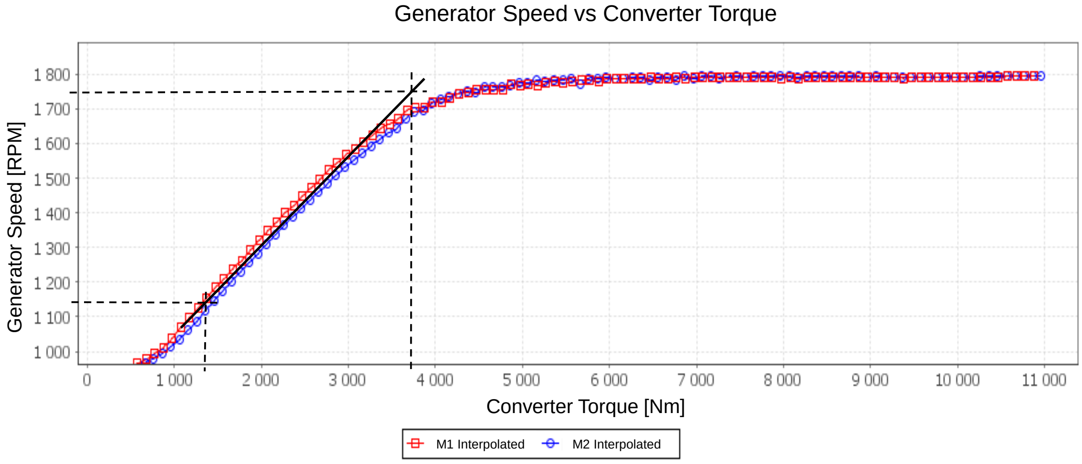

Figure 4.8: Measured converter torque of a MM82

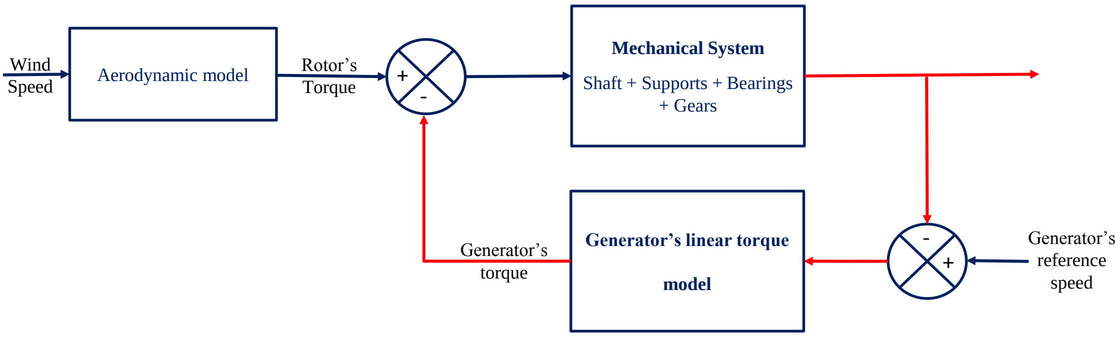

Figure 4.9: Control Loop for the Simulations

the mechanical model.

4.3.1.2 The visco-elastic angular damping coefficient and the response of the model to wind

The set up of the rigid body angular damping ν was performed by obtaining a first guess of the coefficient through the theoretical equations of the angular response of the system when applying newton's second law. This procedure is explained in Appendix D.2.1. Equation 4.3 shows the expression obtained by this analysis.

$$\nu = \frac{M_w - n_1 \cdot n_2 \cdot n_3 \cdot M_G}{\Omega_{rotor} \cdot (1 + n_1^2 + n_1^2 \cdot n_2^2 + n_1^2 \cdot n_2^2 \cdot n_3^2)} \qquad \left[\frac{Nms}{rad}\right] \tag{4.3}$$

Where ν represents the visco-equivalent angular damping coefficient for each shaft, M_w is the torque introduced by action of the wind, M_G is the resistive torque applied by the generator and n_i is the transmission ratio for the stage i which values were given in Section 4.2.2.

The equation above does not take into account the resiting torque induced by the rolling resistance coefficient, but its effect is very small related to the resulting applied torque (see section 3.6) thus, the expression gives an initial guess which is adjusted iteratively by means of simulations until obtaining a compromise between the mechanical losses and the desired angular speed.

The damping coefficient ν was estimated for an angular speed of the generator of 1450 rpm which is around the middle of the range analyzed. Equation 4.1 was used to calculate the input torque at a wind speed of 7 m/s, value obtained from the graph in Figure 4.7. Equation 4.2 was used as well to find the generator's resistive torque for this operating condition. The theoretical damping coefficient (ν) obtained with Equation 4.3 was 1 Nms/rad and the resulting value after iterations was set to 0.8 Nms/rad.

The approximated generator's resistive torque and the consideration of a constant visco-elastic damping in the analyzed wind speed range introduced an error in the response of the model in terms of the generator's angular speed for a given wind speed as is shown in Figure 4.7. The model have 1130 rpm for a wind speed of 4.50 m/s instead of 5 m/s which represents a 10% error. Analogously, the angular speed is 1750 rpm for a wind speed of 8.1 m/s instead of 8 m/s which gives a 1% error. By performing simulation tests at the operating conditions of 1130 and 1750 rpm it was verified that the mechanical losses, produced by the mixture of the inner race resistive torque of the main bearing and the visco-elastic angular damping ν, were of 4.5% and 10% respectively. Theses loses were estimated by the ratio between the power introduced by the rotor to the Low Speed Shaft and the power produced by the generator.

The impact of the deviation in the response between the model and the real machine expressed by the difference in the operating condition due to a given Wind Speed, introduced differences in the load applied to the bearings and in the dynamics of the IAS when non stationary simulations were tested. The impact of these choices and simplifications to the study performed are analyzed further in this chapter.

4.3.1.3 Modeling the encoder acquisition

The method used by Engie Green for estimating the IAS signal by means of encoders is the Elapse Time Method, which was described in Section 1.2.2.2. The following expression is used for estimating the angular speed after each encoder pulse:

$$\bar{\omega} = \frac{2\pi}{R}\frac{f_c}{N_i} \tag{4.4}$$

As it can be observed from the equation, once the resolution R and the counter clock frequency f_c of the simulated encoder are set, the estimation of the IAS is reduced to finding the elapse time signal N. The elapse time is the superior integer number of clock pulses between two consecutive encoder's rising edges. To estimate it from the simulations the following expression is used:

$$N = ceil(\Delta t \cdot f_c) \tag{4.5}$$

The function $ceil()$ calculates the immediate superior integer of the argument. Δt refers to the vector containing the time passed between two consecutive encoder's rising edges and its estimation is made from the simulation results resampled with the resolution of the encoder. Notice that the $time$ estimated when solving the differential equations (see Section 1.4.3) is sampled by the numerical method of resolution. When the emplacement of the virtual encoder is not the master DOF, the time between two encoder's rising edges Δt is reconstructed with the following expression:

$$\Delta t_i = \frac{\Delta\theta}{\omega(\theta)_i} \tag{4.6}$$

where $\omega(\theta)_i$ is the angular speed of the node where the encoder is being placed (node i) obtained from the resolution of the equations and $\Delta\theta$ is the angular distance between two samples which is defined by the resolution of the encoder as:

$$\Delta\theta = \frac{2\cdot\pi}{R} \tag{4.7}$$

4.3.2 The IAS surveillance indicators

Parallel to the current research, a project to improve IAS surveillance indicators based on longterm IAS measurement campaigns deployed in several machines is being developed in Engie Green. The author has also participated in the project in which different indicators have been proposed after preliminary analysis of the wide IAS data base. The indicator construction has two phases: the estimation based on spectral amplitudes and the normalization process allowing to make them independent of the operating conditions and to construct a model permitting the set of statistical defect thresholds.

4.3.2.1 The spectral indicators

From the indicators under test in Engie Green, five have been chosen to be tested and compared with Experimental results from the data base in a machine carrying a defective bearing in the generator (Bearing L1). These indicators based on the amplitude of the spectral response at the frequencies of interest are:

1. S_{H1}: Amplitude of the peak at the fundamental frequency of the spectrum.
2. S_{H2}: Amplitude of the peak at 2x the fundamental frequency of the spectrum.
3. S_{H4}: Amplitude of the peak at 4x the fundamental frequency of the spectrum.
4. S_{H8}: Amplitude of the peak at 8x the fundamental frequency of the spectrum.
5. S_{H12}: Amplitude of the peak at 12x the fundamental frequency of the spectrum.

The angular response from the node 7 of the model was the one foreseen to be treated by the encoder's simulation. The non-stationary simulations were set at 50 revolutions of the LSS. The simulated encoder's resolution was 20480 which is one of the resolutions found in Engie Green's sensors. The combination of length and resolution was proven sufficient to generate spectra with a clear signature of the bearing dynamics. As it will be seen afterwards, the 50 revolutions size of the signal was also verified to be enough to produce angular speed responses with similar wind-generator's torque dynamics related to the real wind turbine. An apodization window of type Hanning was used to process the broadband effect of the non stationary nature of the signal. This windowing was the same used by André et al. in reference [1] as it was described in section 1.3.2.

4.3.2.2 The parametrization and normalization procedure

With the aim of dealing with the non-stationary dependency of the indicators and the spectral response, a procedure was implemented by André et al. [3] in Engie Green as a preliminary phase of the project. The procedure is an extension of the work of Mac Bain and Timusk [84] who proposed a simple method for radial vibration surveillance from measurements performed only in linear acceleration or deceleration of the machine. The vibration signals sampled in time, are separated into fragments sufficiently short to allow the consideration of them as stationaries but long enough to allow spectral indicator's extraction depending on the resolution regarding the surveyed frequencies. The indicators obtained from the assumed stationary fragments are gathered into intervals of average angular speed. The estimated averages and variances of each fragment are then conferred to their corresponding angular speed interval. Under the assumption that the indicators behave with a parametric Gaussian law, probabilistic estimations allow the evaluation of the threshold representing a change of the statistical parameters of the law followed by the indicator.

The extension of the parametrization process proposed by André et al. [3] based on the Kernel regression, consists in modifications allowing the use of measurements sampled in the angular domain and in presence of high stationarity (non linear phenomena). The measurements analyzed were obtained from two machines of the same model where one of them is the same instrumented in [1] meaning they both have exactly the same characteristics as the one modeled in the current research. This means that the mechanical and operating parameters as well as the response related to wind are considered equivalent. The estimation of the parametric law of each indicator is performed by achieving the following tasks:

1. fragmentation of the operating parameter interval into K segments allowing a proper estimation of the Gaussian law and short enough to avoid a not desired evolution of the parametric law.
2. for each segment k the average $\hat{v}_k$ of the operating parameters related to the indicators is estimated as well as the average $\hat{\mu}_k$ and the standard deviation $\hat{\sigma}_k$ of the indicator values by means of a non linear parametric regression method.
3. by performing the linear interpolation of the pairs $(\hat{v}_k, \hat{\mu}_k)$ and $(\hat{v}_k, \hat{\sigma}_k)$ the piecewise functions $\mu(v)$ and $\sigma(v)$ composed by the $N-1$ functions each, being N the number of different operating parameters existing on the measurements.

This preliminary stage to define the model needs to be performed with the machine in a healthy condition which allows to define the threshold of the faulty state. Once the initial laws are built, the indicators to be analyzed and/or evaluated are normalized from the estimated average and standard deviation functions as shown by Equation 4.8.

$$\hat{In}_k = \frac{I_k - \hat{\mu}_k}{\hat{\sigma}_k} \tag{4.8}$$

where I_k is the estimated indicator belonging to the interval k, and $\hat{In}_k$ represents the normalized indicator. A threshold of 5 standard deviations $\hat{\sigma}_k$ was chosen as the alarm to identify the data not following the parametric model which represents the presence of a defect. Figure 4.10(a) shows the distribution of the operating parameters when the

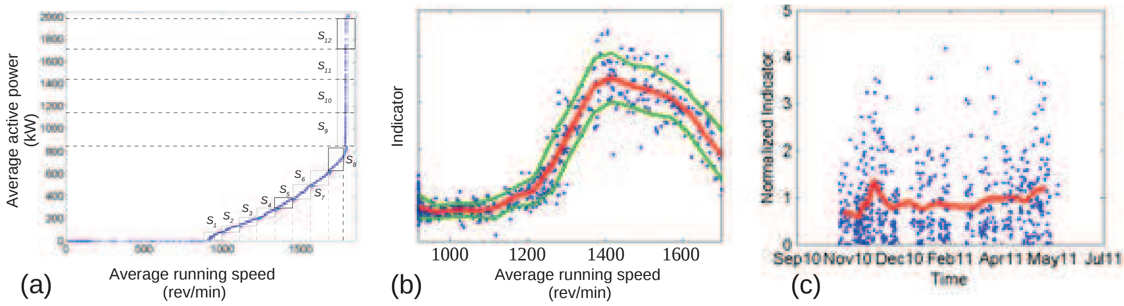

Figure 4.10: Parametrization and normalization results. André et al. [3]

indicators were estimated. To perform the parametrization and posterior normalization, André et al. divided the indicators into 12 intervals. The first eight were normalized by the angular speed as it exhibits a bijective correlation, and the last 4 were normalized by the active power of the machine. Figure 4.10(b) shows the result of the parametrization in which the red line represents the obtained average function μ and the green lines are the standard deviation function. In Figure 4.10(c) the result of the normalized indicators according to the estimated Gaussian law.

In the case of the indicators to be tested with the model, the procedure described above for the parametrization was used. The angular speed interval considered for simulations coincides with the first eight segments of the procedure meaning that the controlling parameter used was the average speed.

4.3.2.3 The evolution of the defect and the number of simulations

As a last stage to be able to build and test simulated indicators, a set of "measurements" had to be generated in healthy machine conditions to construct the parametrization law and then in faulted conditions to test the response of the indicators. To achieve this goal it was decided to run 200 non stationary simulations for a healthy machine and 200 with a defect seeded in the outer race of the Main Bearing for a total of 400 simulations. To achieve this task, 400 different wind speed measurements of 300 seconds were used in which the wind speeds are between 5.5 and 8 m/s as it was described in Section 4.3.1.1.

Regarding the faulted simulations the objective was to have an evolution of the defect with time. Ten different sizes of spall were parameterized simulating a damage evolution as shown in Table 4.3 which contains the values for the depth and the length of the defect severity. The sizes are characterized by depth and longitude regarding the percentage of normal force loss when the rolling element passes through the spall and the percentage of

Table 4.3: Defect sizes evolution

Defect Size	Depth, C_d $[\mu m]$	Angular Length, $\Delta\phi_d$ $[^\circ]$
D1	15.00	0.64
D2	33.00	0.80
D3	51.67	0.93
D4	70.00	1.07
D5	88.33	1.21
D6	107.00	1.36
D7	125.00	1.50
D8	143.00	1.64
D9	161.67	1.79
D10	180.00	1.36

angular longitude related to the angular distance between two rolling elements. Thus, the smaller defect was set to a 5% of the angular length between the balls and 5% of normal force loss. The biggest one was set to 15% of angular length and 95% of loading loss. The defect was linearly increased in length and depth to achieve the ten different sizes. Twenty different simulations were performed from 20 different wind speeds for each defect size for the total of 200 simulations with the faulted bearing.

As a demonstration, Figure 4.11 shows the normal force distribution of the Main bearing in presence of the defect sizes 1, 5 and 10 with the HSS operating at 1450 rpm. Notice the increase of the load loss which is characteristic of the defect severity.

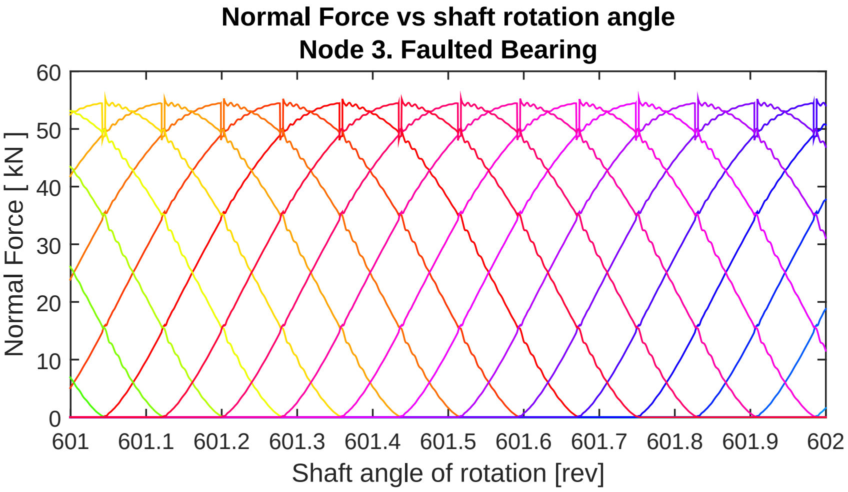

(a) Normal load distribution. Defect size 1

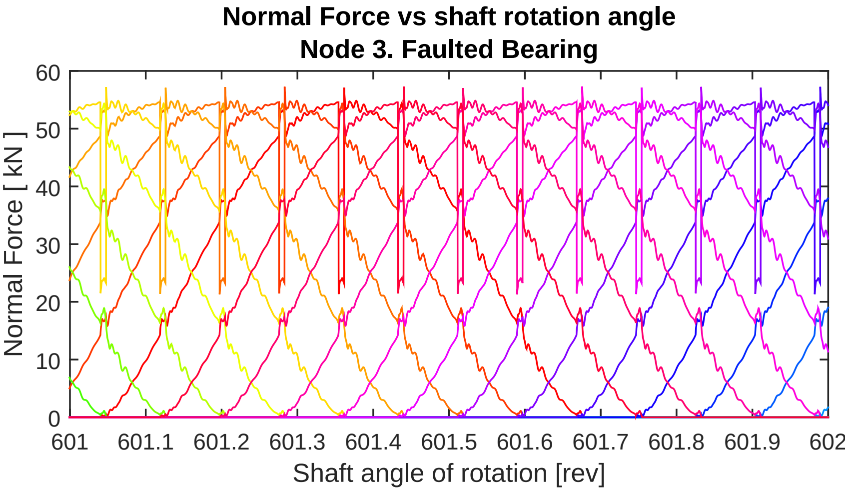

(b) Normal load distribution. Defect size 5

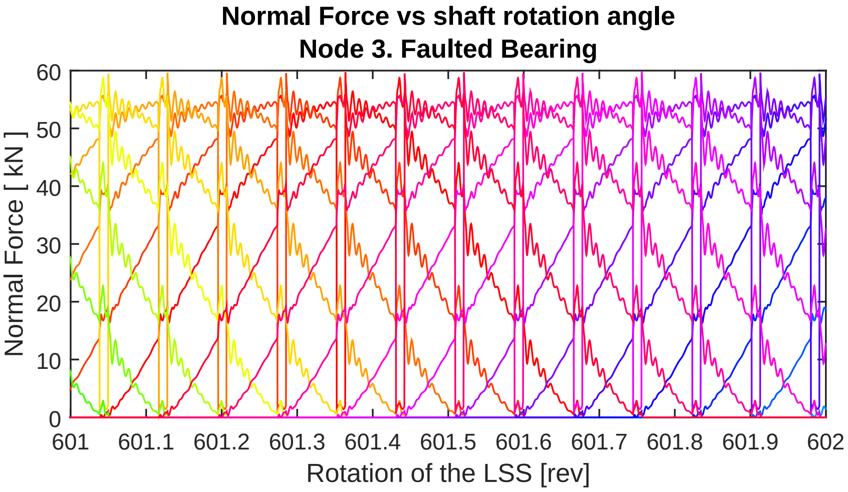

(c) Normal load distribution. Defect size 10

Figure 4.11: Normal load distribution of the Main Bearing. Node 3. Defect evolution

4.4 The simulation results. Comparison between experimental and modeled indicators

The aim of this section is to present the results of the indicators modeled and the comparison with the results obtained from the experimental data of the real wind turbines. First, simulation results under stationary conditions show the transmissibility of the angular speed variation phenomenon through several gear stages. A preliminary analysis of the indicators is also shown as an introduction to the non stationary simulations. Then, the response of the model in non stationary conditions under real wind speed (procedure described in section 4.3.1.1) is presented and analyzed. Finally, the analysis of the indicators as well as a comparison with the experimental results lead to the closure of the chapter.

4.4.1 Stationary response at 1430 rpm

As it was described, the parameters of the model were adjusted to make the High Speed Shaft to run at 1430 rpm under a constant wind speed of 7 m/s. The estimated rotor torque for this speed is 354.50 kNm and the resistive torque is 3.20 kNm for 480 kW of energy production. Figure 4.12 shows the angular speed of each shaft after achieving the steady state response. Remember that the input and output shafts were identified as LSS (Low Speed Shaft) and HSS (High Speed Shaft). The intermediate 1 and 2 corresponds to the nodes 8 and 9 respectively. The quantification procedure to simulate the encoder was not used in the results shown in this section. The IAS is shown directly from the equations resolution.

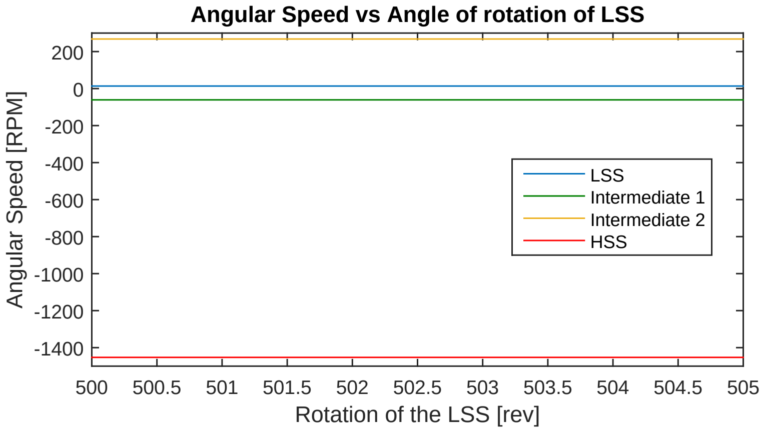

Figure 4.12: Angular speed response of all shafts vs the angle of rotation of the LSS

The resulting speeds for each shaft from the LSS to the HSS are 13.73, 60.94, 267.90 and 1453 rpm which is in agreement with the transmission ratio for each gear stage. Notice that due to the high inertia of the shaft line, related to the very small angular damping coefficient, it takes 500 revolutions of the LSS to achieve the numerical steady state condition related to the amplitude of the angular speed variation.

The response of the IAS variation is shown in presence of the defect size 10 which is the most severe as it was described in the previous section. Notice that the Main Bearing has a $BPFO_\theta$ equal to 12.75 ev/rev.

The IAS variation is shown in Figure 4.13 for the nodes 7, 13 and 14. As expected, the shape and the amplitude of the variation changes depending on the node analyzed. As it was shown in Section 3.7, the shape of the response and in consequence, the energy distribution in the frequency channels of the spectra depends strongly on the modal response of the whole mechanical architecture. In this particular case, the $9 \cdot BPFO_\theta$ is found to be in the vicinity of a critical frequency. It can be seen in both the frequency and the physical domain, that the amplitude of the phenomena tends to be amplified by the transmission ratio as it was discussed in Chapter 3. From measurements taken in the wind turbine that Engie Green has instrumented for [1], this phenomena may be observed for certain harmonics related to different mechanical cyclic events. However, no further investigation has been performed for the experimental results at the moment of writing this report. An exploratory analysis of this behavior could be performed by creating a processing tool to study the ratio between the harmonics of the same cyclic phenomenon, measured in several shafts.

Another interesting observation is the diminution of the amplitude of the IAS due to the mechanical coupling. This is easily corroborated by comparison of the IAS spectra of the nodes 13 and 14 (Figures 4.13(d) and 4.13(f)). The coupling seems to filter the phenomena and it makes the fundamental frequency's peak higher than the others reorganizing the energy distribution when compared to node 13 where the harmonics starting from the 4th have more amplitude. The results of node 14 are indicative due to the major simplification of the generator's shaft made with the intention to reduce the size of the model. Nevertheless, they show the potential of the models proposed in this dissertation to describe the IAS phenomena in complex mechanical architectures, and to perform comparison of the response between shafts, which is a valuable analysis to decide the location of the encoders in a given architecture.

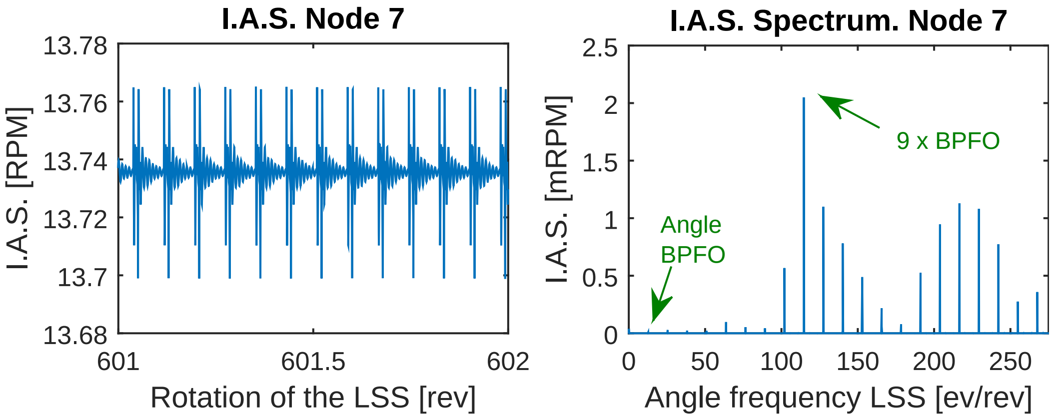

(a) IAS. Node 7. Faulted Bearing (b) IAS Spectrum. Node 7. Faulted Bearing

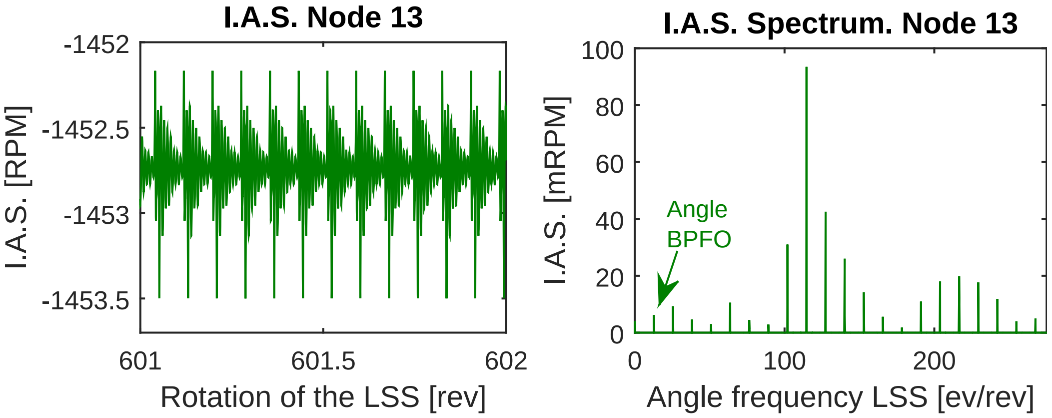

(c) IAS. Node 13. Faulted Bearing (d) IAS Spectrum. Node 13. Faulted Bearing

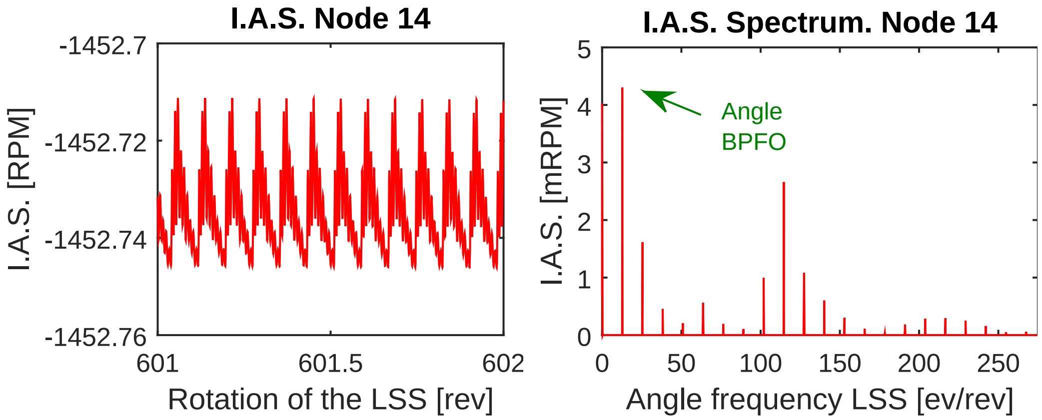

(e) IAS. Node 14. Faulted Bearing (f) IAS Spectrum. Node 14. Faulted Bearing

Figure 4.13: IAS response for nodes 7,13 and 14. Faulted bearing

4.4.2 Indicator analysis in stationary conditions

A preliminary analysis of the spectral response in healthy conditions and in presence of defect sizes 1, 5 and 10 has been done. The spectra shown in Figure 4.14 were obtained from the virtual encoder of the Low Speed Shaft placed in node 7. A logarithmic scale has been set to improve the observation of the first harmonics. As expected the amplitude of the phenomena tends to increase with the evolution of the defect size. The presence of the defect increases also the energy around the harmonics linked to the BPFO of the bearing but this phenomena was not further investigated.

An indicator extraction was performed from the spectra shown above, for the five indicators described in section 4.3.2.1. Figure 4.15 shows the results for the healthy bearing and the three defect sizes.

Regarding the H1 indicator, a phenomena that was observed in section 2.4.2 also occurs in the frame of the wind turbine model: the presence of a small defect makes the H1 indicator to decrease related to the healthy bearing. A decrease is also observed for this indicator between defect sizes 5 to 10. The obvious conclusion is that the fundamental frequency is not a good indicator for bearing surveillance. All the other chosen indicators have an increasing amplitude behavior related to the augmentation of the defect severity. The indicators H8 and H12 are more sensitive to the defect evolution. The sudden variation of the load distribution in the rolling elements due to the rotation of the shaft, highly amplified in the presence of a defect, may be the cause for the higher harmonics to respond more to the defect evolution. As the excitation behaves as successive impacts, it excites the critical frequencies of the system coupling both phenomena. In the current results, this is found for the described indicators which are in the vicinity of one critic frequency as it is observed in the spectra.

4.4.3 The non-stationary simulations

To show the model response in non stationary conditions one of the simulation runs for the indicator testing is shown in Figure 4.16. The first results presented are in presence of the Main Bearing's defect size 10 and are treated by the virtual encoders placed in nodes 7 and 14 of the model measuring LSS and HSS angular speeds respectively.

Figure 4.16(a) shows the input wind speed which transformed into rotor torque, drives the mechanical system. Notice that the linear response of the simulated generator's linear control loop makes the system to respond with an angular speed that has the same shape of the wind. The negative speed of the HSS encoder is presented as a reference of the sense

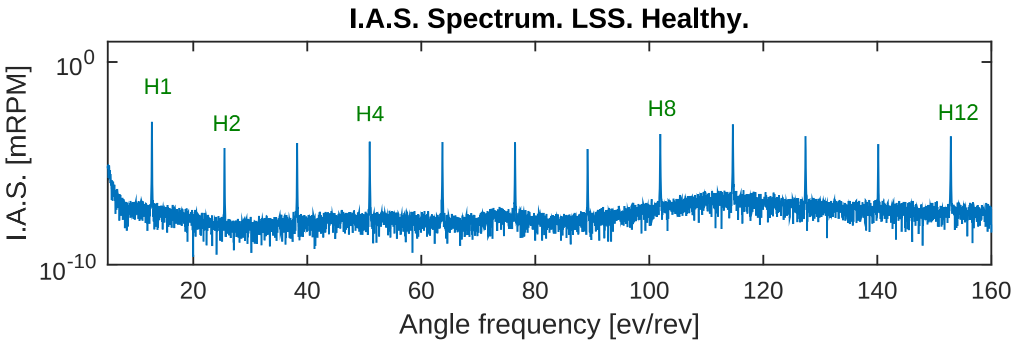

(a) IAS Spectrum. Encoder in LSS. Healthy Main Bearing.

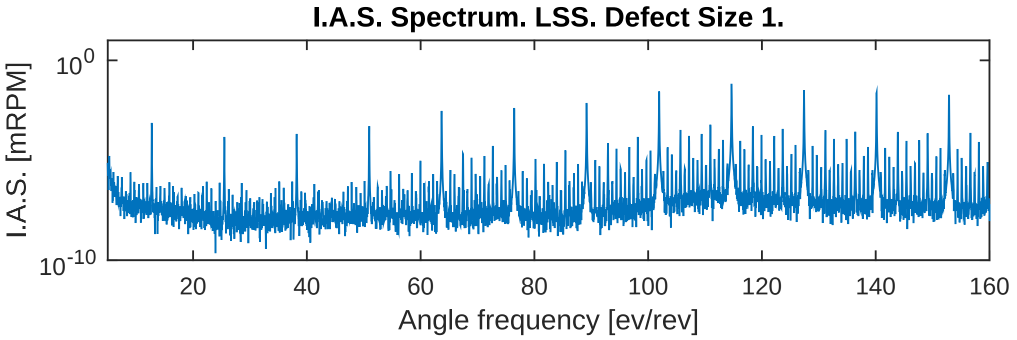

(b) IAS Spectrum. Encoder in LSS. Defect Size 1.

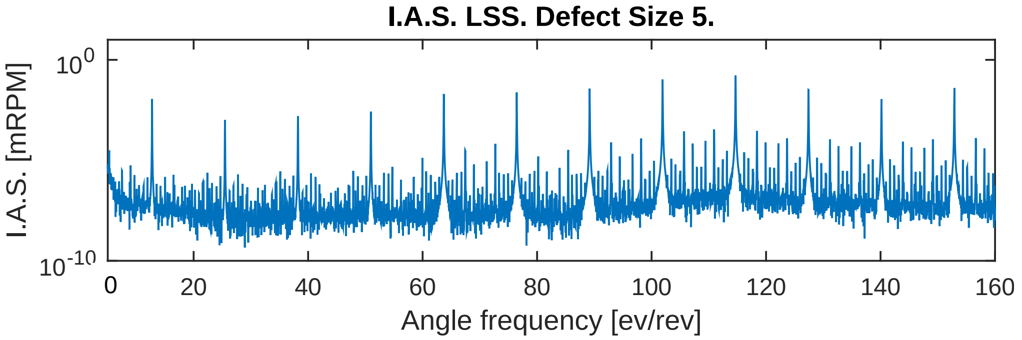

(c) IAS Spectrum. Encoder in LSS. Defect Size 5.

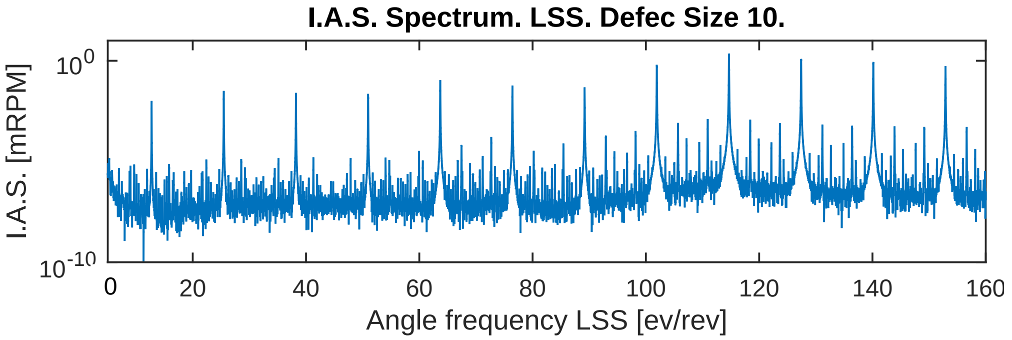

(d) IAS Spectrum. Encoder in LSS. Defect Size 10.

Figure 4.14: IAS logarithmic spectra evolution in presence of a Main Bearing defect. Stationary condition.

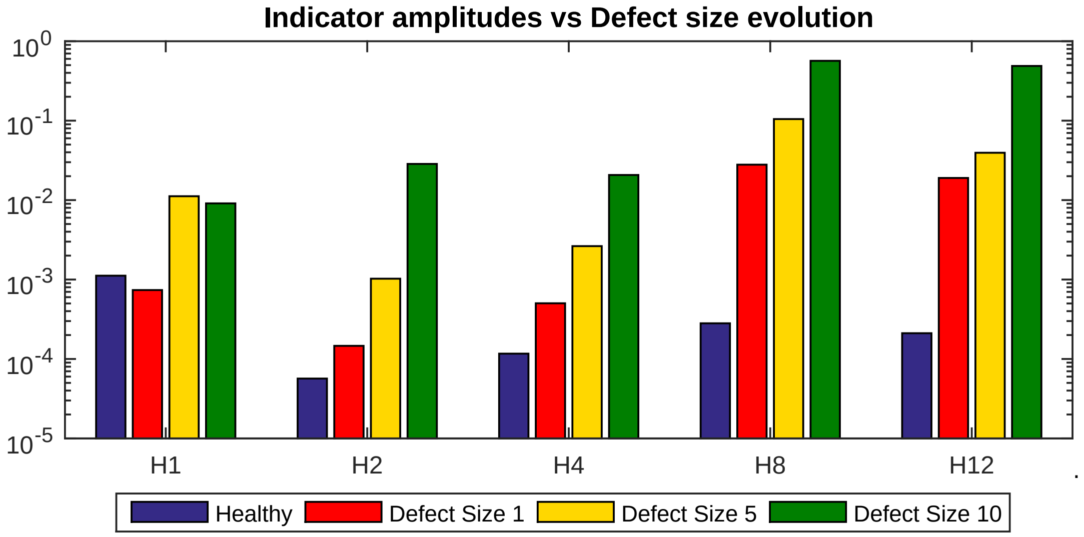

Figure 4.15: IAS indicators vs Defect evolution

of rotation knowing that the signal coming from this kind of sensor is in absolute values. In reality, the complexity of the wind turbine control makes the system to respond with less dynamics related to wind. This issue establishes differences between the simulated and the real IAS signals in terms of load variation onto the bearings and the gears. Also, more sensitivity of the system to the wind dynamics increases the noise expected in the low frequency region of the spectra coming from the non stationarity of the rotor's torque.

In general the spectra obtained from the signals do not show significant differences related to the ones estimated in stationary conditions in terms of the energy distribution between the frequency channels (See Figure 4.13). This means that the speed variation does not make the modal response to change significantly. However, a great difference in the amplitudes is observed as the non stationary spectra present smaller peaks.

To have a better observation Figure 4.17 shows the spectra in logarithmic scale for the LSS encoder of one simulation example for defect sizes 1 and 10. Even if treated with the Hanning window, the non stationary spectra show the broadband effect in the low angle frequency region originated by the transitory dynamics of the response related to wind as well as a clearer observation of the modal excitation in the region between 100 and 150 ev/rev. The critical frequency excitation moves from the H8 to the H9 in the observed spectra. The range of speeds set for normalization will make this frequency to move no more than two harmonics. It will be observed further in this chapter that having the harmonic of a defect coinciding with a critical frequency in the simple spectra observation will not necessarily make this harmonic the most sensitive to the defect evolution.

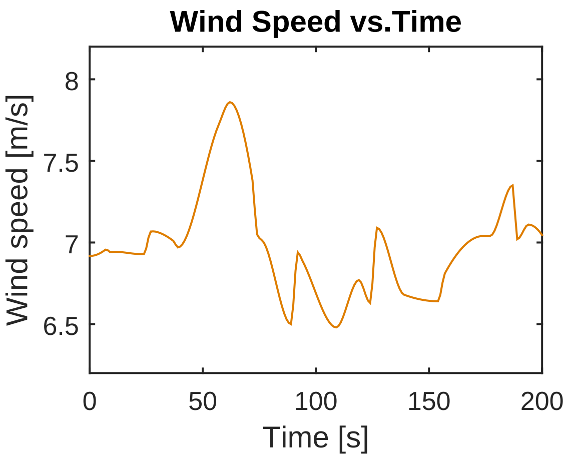

(a) Wind speed vs time

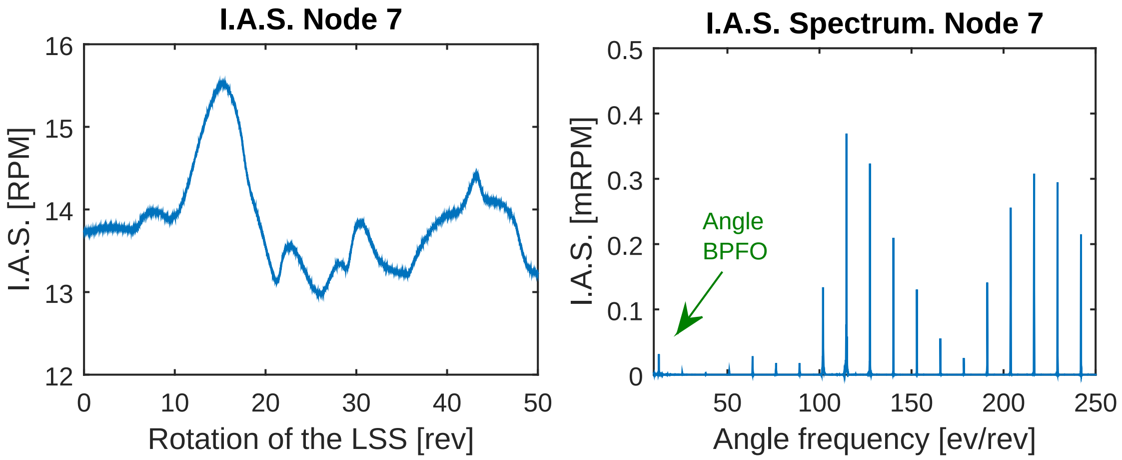

(b) IAS. Encoder in Node 7. Faulted Bearing

(c) IAS Spectrum. Encoder in node 7. Faulted Bearing

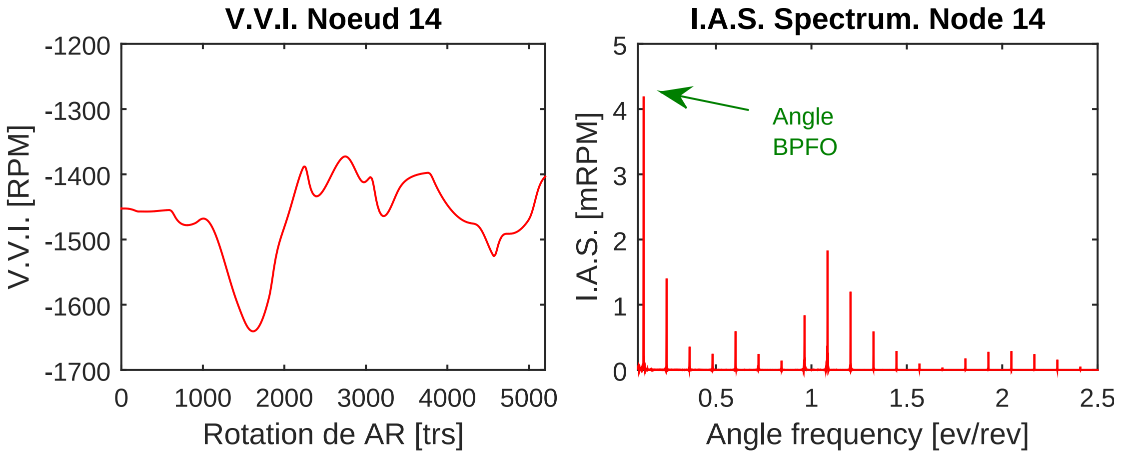

(d) IAS. Encoder in Node 14. Faulted Bearing

(e) IAS Spectrum. Encoder in Node 14. Faulted Bearing

Figure 4.16: Non stationary IAS response in presence of a Main Bearing defect. LSS and HSS modeled encoders

It can be noticed that the broadband noise hides the first three harmonics related to the bearing dynamics in the case of the defect 1. This implies that in the case of the model, using these peaks as a part or as a whole indicator in non stationary conditions would make more difficult early detection. In the case of the defect size 10, a general increase of the amplitudes is observed and the energy introduced by the big size of the bearing defect makes the first harmonics to stand out from the noise.

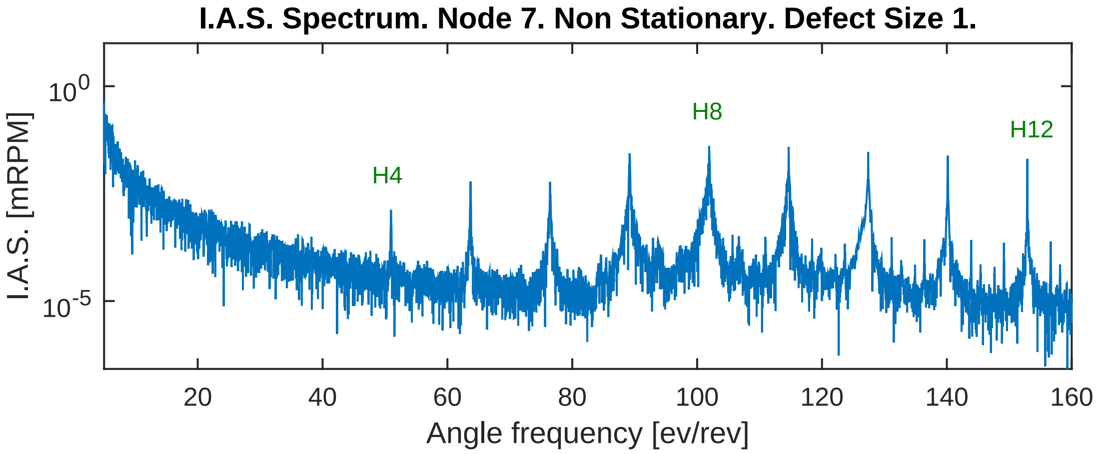

(a) IAS Spectrum. Encoder in node 7. Defect Size 1. Non stationary conditions

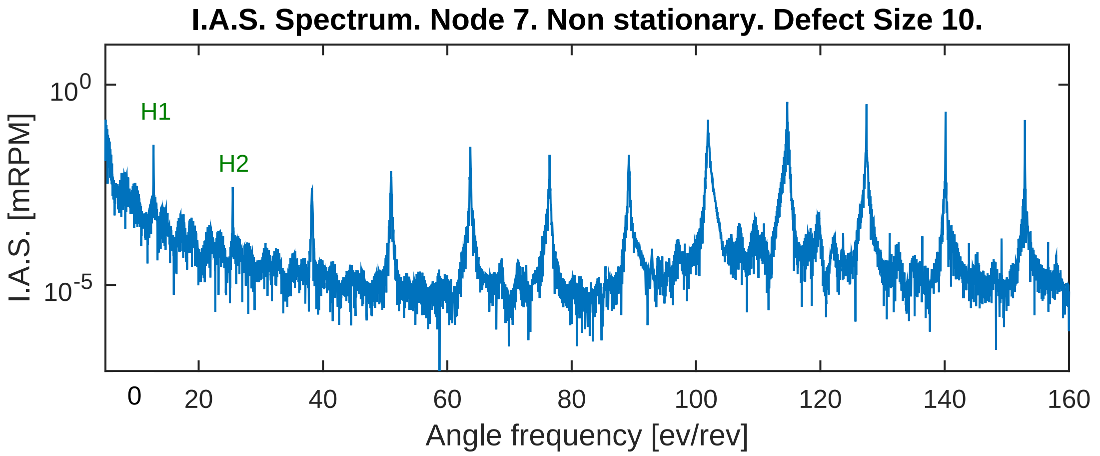

(b) IAS Spectrum. Encoder in Node 7. Defect Size 10. Non stationary conditions

Figure 4.17: IAS logarithmic spectra in presence of defect sizes 1 and 10. Non stationary conditions.

4.4.4 Indicator analysis in non stationary conditions. Comparison with experimental results

In Section 4.4.2, a preliminary analysis of the spectral indicators was presented, and it was found that H1 is not an advantageous indicator for the current study. This assertion was reinforced by the fact that at least in the case of the model, the broadband effect having its origin in the non stationary behavior of the wind hides the first harmonics of the smaller size of the defect.

The normalization procedure described in section 4.3.2.2, was applied to the 400 simulations, 200 in healthy conditions of the Main Bearing and 200 in faulted conditions following the procedure developed in Section 4.3.2.3.

With the aim of doing a comparison with experimental results, a similar analysis was made for one deep groove roller bearing outer race defect detected by the maintenance team of Engie Green, in the generator of a MM82 which happened to be equipped with encoders on the HSS and the LSS, as described by André et al in [3]. The results presented for this machine are from the HSS encoder which is installed on the same shaft of the damaged bearing at the shaft end of the generator. The normalization procedure was applied based on the angular speed with the very same parameters as it was performed for the model. However, as the analysis is made on a real bearing failure, there is no control on the defect evolution. The measurements used to build the parametric law are from the period immediately after the bearing's replacement to assure the healthy bearing condition.

The experimental measurements belong to a period of six months and they are taken at a rate of around 20 measurements per day. Nevertheless, only those satisfying the range of angular speeds between 1130 and 1750 rpm were considered to match the set up for the simulations as described in Section 4.3.2.2.

It is important to remark that the operating conditions for the simulations, induced by the wind speed measurements, are not related with the conditions of the real machine in the period of measurements. This makes the results interesting from the point of view of the aleatory selection of the conditions for the model related to the experimental data. Having common operating conditions would have been more important if the objective of the model was to accurately reproduce the machine's behavior.

Figure 4.18, presents the normalized indicators H1 and H12 for the model simulations as well as for the experimental results from the HSS encoder.

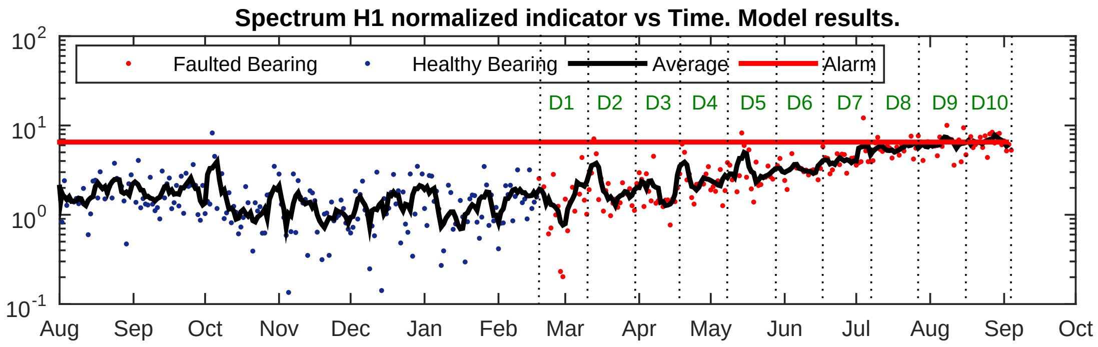

(a) IAS H1 Normalized indicator. Wind turbine model.

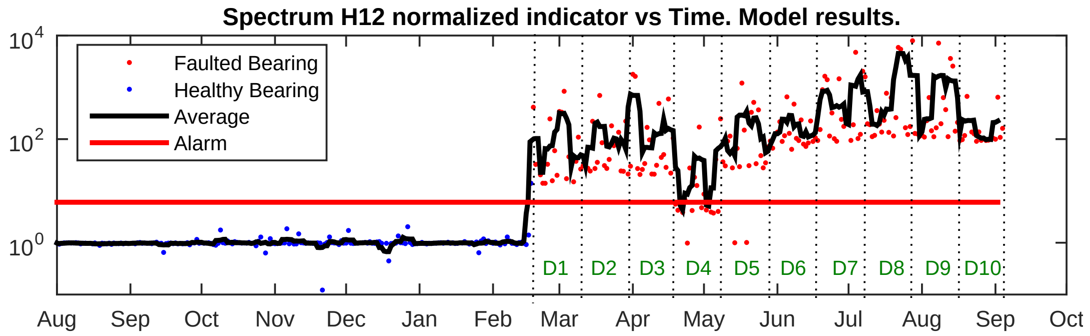

(b) IAS H12 Normalized indicator. Wind turbine model.

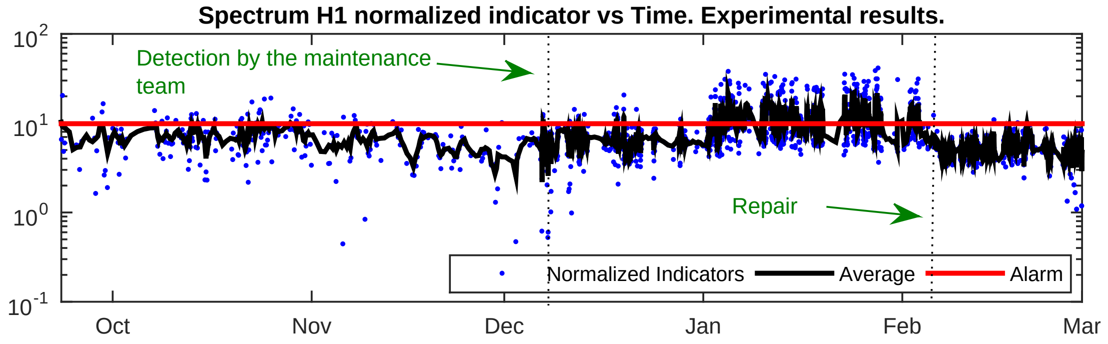

(c) IAS H1 Normalized indicator. Experimental results.

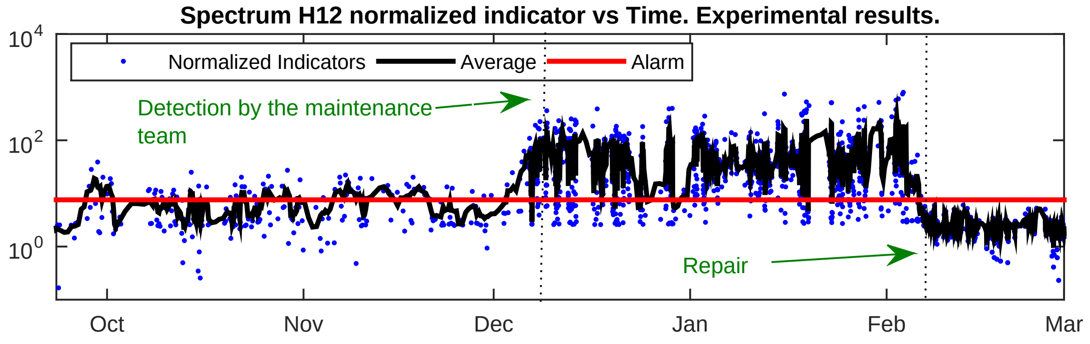

(d) IAS H12 Normalized indicator. Experimental results.

Figure 4.18: IAS normalized indicators H1 and H12. Modeled and experimental results.

Remember that the indicator alarm has been set up to 5 standard deviations. As the normalization procedure throws negative values, to be able to plot in logarithmic scale, an offset equal to the most negative value was added to each graph displacing the data into the positive range. The temporal evolution in months shown on the horizontal axes of the plots are real in the case of the experimental measurements.

Regarding the model simulations, each indicator point was labeled with a date starting from August 1st, chosen aleatory as a reference, with a frequency of one measurement per day giving a total of 400 days. The blue data corresponds to the simulations with a healthy Main Bearing and the red data corresponds to the faulted bearing at a severity rate augmentation of one defect size every twenty simulations. When looking at the results (Figures 4.18(a) and 4.18(b)), it is confirmed that the indicator H1 does not respond well to the presence of the defect. In contrast, each single estimated indicator H12 exceeds the alarm level.

In the case of the experimental results (Figures 4.18(c) and 4.18(d)), the presence of the roller bearing defect is identified by the value of the indicators related to the alarm line. Several measurements per day are taken as it can be noticed. The vertical dot line on the left of the plots points out the detection date of the defect by the maintenance team by means of vibration measurements and the dot line on the right establishes the moment of the bearing replacement. As it is the case for the results of the model, the indicator H1 “reacts” to the defect almost one month after the detection by radial vibration surveillance, but the presence of the defect is not clear as the average (black curve) is around the alarm value. Regarding the H12 indicator, the average clearly exceeds the alarm at almost the same date of the defect detection. Notice however that the average goes beyond the alarm level several times in the period between the end of September and the beginning of December, which may be interpreted as a sign of early detection of the defect.

A comparison between the whole five analyzed indicators is shown in Figure 4.19 for the model as well as for the experimental results. The colored scale has been set to turn into yellow when the alarm of five standard deviations is reached. The maximum value is established to 320, as an indicative value and it does not represent the maximum value of the analyzed indicators. The intention of these plots is to offer a way to compare the sensitivity of the indicators related to the severity of the defect.

Regarding the model results it can be observed that indicators H4, H8 and H12 are very sensitive to the defect as they “react” for the defect size 1 which represents a very small pit. It is clearly observed that the indicator H12 is more sensitive to the defect severity at is reaches the biggest amplitudes.

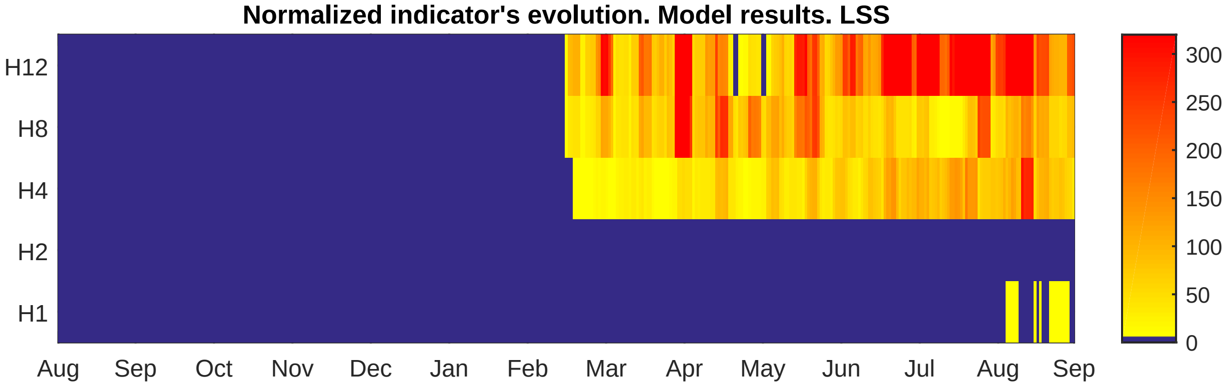

(a) IAS Normalized indicators comparison. Wind turbine model.

(b) IAS Normalized indicators comparison. Experimental results.

Figure 4.19: IAS normalized indicators comparison. Modeled and experimental results.

From the experimental results, we have a similar behavior related to indicators H8 and H12 that happens to respond much earlier than the others. When comparing the results with the model it is confirmed the already mentioned similarity in terms of the trending and defect sensitivity.

In both, model and experimental results, the indicator H2 seems not to be suitable for surveillance. For the model results, when looking at figure 4.15, showing the evolution of this indicator in stationary conditions, the not normalized amplitude seems to be smaller in general than the H1 except for the defect size 10. It was observed from the spectral observations in non stationary conditions (Figure 4.17), that in general the spectral amplitudes are smaller compared to those obtained in constant angular speed which probably causes H2 not to respond after normalization, phenomenon shown in Figure 4.19(a). For the experimental results, it can be seen from Figure 4.19(b) that it responds erratically and only at the end of the faulted condition period which could be related to high variance on the normalized indicator.

In summary, the effectiveness of the indicators to detect the defect is the same for the experimental and the modeled results. The higher harmonics indicators respond first to the defect and in the same order (H12, H8, H4, H1 and H2) for the model as well as for the experimental results. Also, the higher normalized indicator amplitudes are obtained for H12 and H8 in both cases. These similar tendencies occur even if the evolution of the simulated defect has been made only from the point of view of the size and not in the sense of the spreading into the other components i.e. inner race and rolling elements, as well as extended or multiple size defects coexisting in the same race, which is what happens in reality and it would be expected to change the indicator's response.

Besides, the major simplifications made to build the model didn't seem to affect the similarity between the experimental and the simulated results. The simplifications are expected to affect in a high degree the modal response of the system and in less degree, but still important, the load on the bearings and the gears. One would be tented to think that the better performance of the high harmonic based indicators is due to the modal excitation of the system due to the defect. This assumption could be analyzed by designing a system in which these harmonics be far from the vicinity of critical frequencies. This task is not easy, as it was shown in Chapter 3 that in a small system with only one pair of gears three modes were present in the range of angular speeds analyzed. In the case of the wind turbine's shaft-line, the complexity of the system would complicate even more this task.

Regardless the above implications which demand further research, it can be stated from the results that more complex indicators composed of several bearing harmonics (sum, multiplication, etc) would be expected to be very effective for bearing's defect detection for IAS surveillance analysis in stationary and non stationary conditions.

4.5 Conclusions

Throughout this chapter a simplified wind turbine model was presented, based on the bearing and gear modeling approaches analyzed in this dissertation. The model, inspired on a 2 MW wind turbine was built taking into account the same number of speed increasing stages of the real wind turbine. Experimental data of the wind speed and the active power generation was used to build non stationary simulations serving to test spectral indicators as a way to show the potential of the modeling approach.

The rigid body stationary response for a HSS angular speed of around 1430 rpm was confirmed validating the rigid body behavior of the system in free rotation. An indicator preliminary analysis in stationary conditions, was performed in which was observed that using the fundamental frequency amplitude as an IAS spectral indicator for roller bearings in the case of outer race defects does not seem suitable as it sometimes decrease with the increasing of the defect severity. As it was observed for the models analyzed in chapter 3, the higher harmonics tend to be more excited due to the bearing dynamics in presence of the defect which is coupled to the modal response of the whole mechanical architecture.

Regarding the non stationary response of the model, the angular speed follows exactly the same non stationary behavior of the wind, which is not what occurs in reality. The complex machine control was linearized in the model and this choice generates more dynamics in the transitory response of the model which in consequence, increases the broad band effect in in the low frequency range of the IAS spectra. This, tends to underestimate the detection of the first harmonics related to the bearing dynamics.

The indicator normalization procedure developed in the frame of the Engie Green's IAS surveillance project was used to perform the analysis of the indicators in the non stationary domain for the model results as well as for the experimental data obtained from a roller bearing defect detected in a wind turbine instrumented for IAS surveillance. From the model results as well as for the experimental indicators, it was found that higher harmonics are more sensitive to the presence of the defect, phenomenon also found in the small models analyzed in previous chapters. The difference in the modal responses between the model and the real wind turbine due to the simplifications, and the raw handling of the defect severity evolution did not seem to affect the above described similar tendencies in the indicator responses. Further studies comprising more simulations with the wind turbine model and more experimental analysis would contribute to confirm the results presented in this chapter. Engie Green has built a wide data base of IAS that is waiting to be analyzed.

As it was also suggested in Chapter 3, these results point to deepen the research in the construction of more complex indicators taking into account the higher harmonics of the defect frequency by performing mathematical combination of them. Also, deepen the exploration of techniques as the spectral envelope applied to the IAS signal stand out as one of the perspectives of the current research to take advantage of the sensitivity of the IAS signal to the mechanical parameters of the system.

General conclusions and perspectives

At the beginning of this dissertation, an introduction was presented versing about the use of the IAS variation signal as a tool for machinery surveillance whether it is in stationary or non stationary conditions. The state of the art related to modeling this phenomenon was found to be reduced and with a great potential to deepen the understanding of the experimental analysis found in the literature.

In this sense, a modeling approach was proposed to describe how the roller bearing dynamics leads to angular speed variations of the shaft. Based on the rolling resistance phenomenon, which is a representation of the friction torque originated by the rolling element-race interaction, a source of coupling was established between the normal charge of the rolling elements and the tangential forces in the bearing races. The normal load distribution between the rolling elements, in constant variation due to the rotation of the shaft and also sensitive to external load changing, has a direct impact in the tangential forces causing torsional excitations. In this way, as it may be found in the literature experimental work, angular speed variations are found in mechanical architectures consisting of single shafts supported by roller bearings. In the model proposed, the bearing is integrated to the mechanical system by means of a generalized vector of forces, allowing the use of the finite element method to model the shafts. Also, it facilitates consideration of the axial rotation degrees of freedom, permitting the construction of the angle-time function and the simulation of non stationary operating conditions.

Regarding the systems coupled by gear transmissions and supported by bearings, a gear mesh classic approach was proven to be suitable to be used considering rigid body axial angular rotations and it was also implemented by means of a generalized vector of forces applied onto the shafts. It was found that the tangential nature of the gear mesh traduces itself into a second and more important source of coupling between the normal and tangential forces. This coupling accentuates the influence of the gears displacements, mainly coming from the radial flexibility of shafts and supports, into the angular variations of the system having their origin in the bearing dynamics. Hence, the modal behavior of the whole mechanical system affects the angular speed variation response of the shafts. This finding can be extrapolated to the radial vibrations of the system, as the gear mesh is a source of coupled excitations related to the bearing dynamics. However, no further investigation in this area was made as it was out of the scope of the current work.

In general, it can be stated that both the tangential and the radial response of a rotating system are coupled by the rolling resistance phenomenon. From the local point of view in the bearing component interaction the tangential forces are affected by the radial response of the bearing generating angular excitations. From a macroscopic point of view, the friction torque of a system and therefore the steady state angular speed response depends on the normal forces magnitudes. These reflexions are important due to the fact that in the beginning, it was thought that this research would point to developing models considering only the torsional degrees of freedom of the system. Actually, accurate description of the torsional vibrations need consideration of at least one radial displacement. The advantage of such modeling feature is that the models built, allow also the analysis of radial vibrations.

The main limitation of modeling mechanical components (bearings and gears) by means of connecting forces is that no stiffness matrices are included into the equations meaning that estimation of the eigenvalues and eigenvectors of the whole system is not possible. However, taking into consideration the rigid body axial rotation degree of freedom to build the angle - time function, allows to analyze the mechanical system in non stationary conditions. This feature brings the possibility of characterizing the modal response of the modeled system with an experimental approach of parameter identification allowing for example the analysis of the response to unbalance among an infinite possibility of mechanical excitations. In Chapter 3 the identification of critical frequencies was performed by introducing linear torques to the system excited, at the same time, by the dynamics of the roller bearing.

Regarding the resolution techniques, the use of the ODE Matlab solvers was sufficient to perform resolution of the equations, in which the non linear nature of the bearing normal forces and the rigid body degree of freedom were handled without major convergence issues.

The simplified wind turbine model built as an engineering application of the models presented throughout this work, served to show the potential of the angular approach. It was possible to test data analysis techniques showing similar tendencies between the model and experimental results. This was performed by evaluating the sensitivity of different IAS spectral indicators to the presence of roller bearing outer race defects.

Perspectives

The developments and findings regarding the current work open different possibilities of going forward in the modeling approaches considering the angle-time function. The adaptation or design of a test rig with at least two gear stages in which the roller bearing defects may be seeded, would be a great opportunity to validate the findings of this research. Such a test rig would be an excellent opportunity to confront the surveillance techniques of radial vibrations and the IAS.

Another opportunity of exploration is the analysis of the origin of the mechanical unbalance which is observed experimentally on the IAS spectra. To do that, it is necessary to refer to the early analytical descriptions of the mechanical system, whether it is by the Newton's or the Lagrange's approaches applied to rotative systems where usually simplifications related to the angular degree of freedom are performed. This kind of analysis will deepen the non linearity of the equations which is the reason why the angular generalized coordinate is simplified in the classic analysis.

The findings related to the influence of mechanical parameters of the system over the IAS response opened the opportunity to deepen the analysis in the uncertain parameter domain. The uncertainty in this kind of models comes from two main sources: the non stationary operating condition and the level of accuracy in the modeling of the supports and the casing of the represented mechanical architecture. The main question would be to determine the effect of these parameters in the surveillance indicator response.

With the objective of classifying the mechanical architecture simplifications according to their influence on the wind turbine's IAS response, it is necessary to improve the description of different mechanical components. In the first place, there is the roller bearing modeling. Taking into account the angle of contact of the rolling elements is necessary to consider the axial load all along the shaft-line of the machine. Besides, the rolling resistance phenomenon should be analyzed in the frame of linear contact which is found in cylindrical and tapered roller bearings. This would allow to compare the signature of the IAS response between spherical and cylindrical rolling elements.

Regarding the gear mesh, it would be necessary to model the planetary stage. The gear mesh force approach appears to be extensible to this kind of transmission in which the forces would be changing not only in magnitude but also in direction at each step of resolution. Developing a more accurate model of the generator would allow to deeply analyze the influence of the flexible coupling to the IAS response of the High Speed Shaft which is important as one of the encoders used by Engie Green is placed on the shaft end of the generator. Finally, modeling the gearbox and the generator's casings would allow to improve the modal responses of the real machine allowing the model's tuning not only for the IAS but also for radial vibration. Regarding the response of the model to non-stationary conditions, an opportunity of improvement is also found in the description of the machine's automated control which was very much simplified in the current work.

These analyses would be oriented in evaluating the utilization of the model to contribute to the development of more complex indicator construction techniques for different surveillance tools i.e. IAS, radial vibration and current signature analysis which has been recently analyzed by means of the angular approach with promising results. Consolidating the model performance as well as having a deep knowledge of the consequence of the simplifications, would allow its utilization to generate data for artificial intelligence indicator construction techniques which represents the next stage on the state of the art of rotating machinery surveillance.

Appendix A

About the rigid body angular damping

The objective of this Appendix is to analyze the concept of the angular damping coefficient and is effect in the angular response of a rotating system by means of a simple mechanical architecture.

A.1 Effect of the rigid body angular damping into the angular response of a one DOF system

An illustrative example is used here to evoke the impact of the angular damping in a rotating system. Figure A.1 shows a scheme of a rigid body on inertia J rotating with angular speed ω by action of the external moment M applied in the direction of the angular DOF θ. The angular speed ω is defined by:

$$\dot{\theta} = \omega \tag{A.1}$$

The equation describing the rotation of the body is:

$$J \cdot \frac{d\omega}{dt} + \nu \cdot \omega = M \tag{A.2}$$

Analyzing the system in the steady state condition, which means no angular acceleration, we observe that the constant angular speed is a function of the external torque and the mechanical loses represented by the angular rigid body damping:

$$\omega = \frac{M}{\nu} \tag{A.3}$$

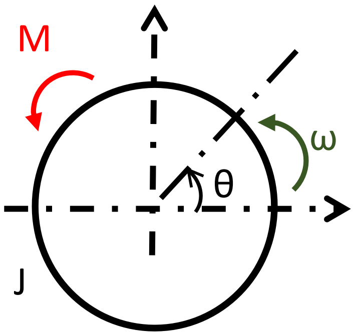

Figure A.1: General representation of single stage gear system

Logically in an ideal system with no loses, meaning ν equal to zero, the angular speed will rise linearly as a function of time by action of the moment M:

$$\int_0^t J \cdot \frac{d\omega}{dt} dt = \int_0^t M dt \tag{A.4}$$

operating:

$$\omega = \frac{M}{J} \cdot t + \omega_o \tag{A.5}$$

As an example the mass inertia of the system is set to $2.70 \cdot 10^{-4}\ kg \cdot m^2$ and the moment applied is made equal to 15 Nm. The response of the system is analyzed by being solved with Matlab's ODE15 solver with an initial condition of the speed of 10

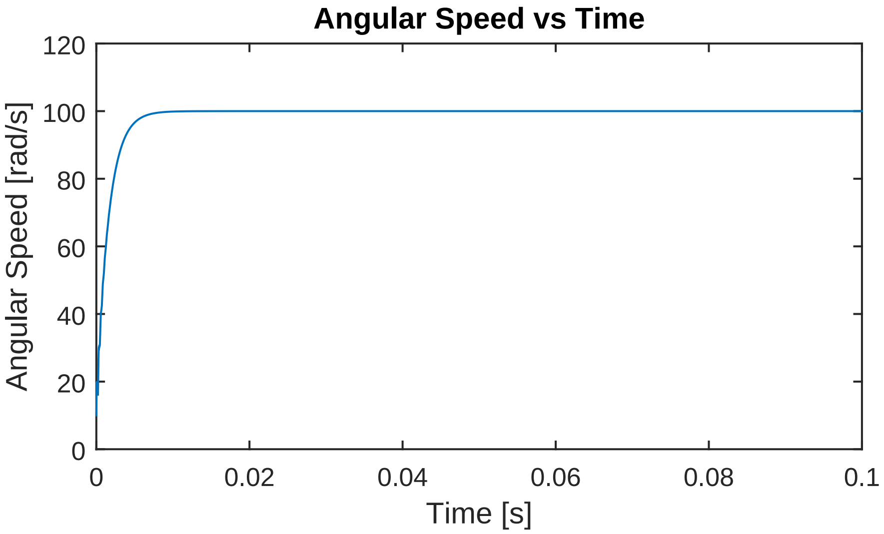

Figure A.2: Angular Speed response with rigid damping

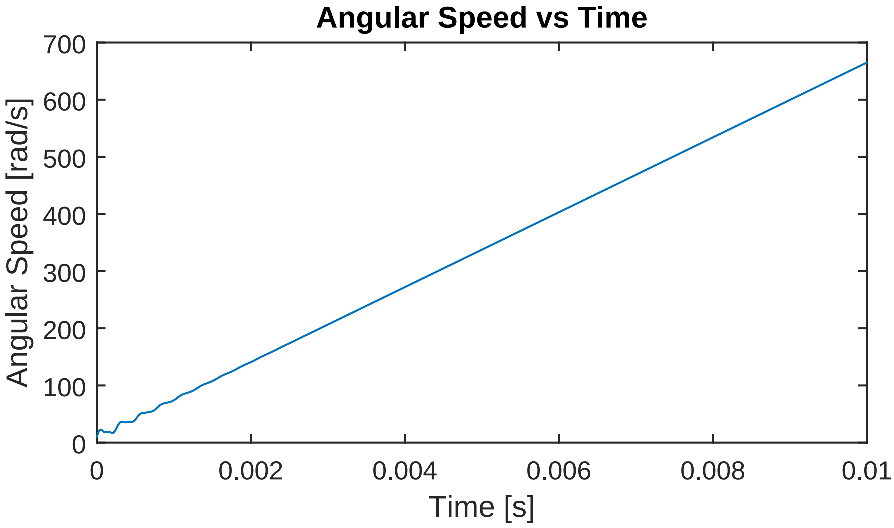

Figure A.3: Angular Speed response without angular loses

rad/s. The response is analyzed with no loses and with an angular rigid body damping of 0.15 Ns/m.

Substitution of the numerical data in Equation A.3 gives an steady state speed of 100 rad/s. Figure A.2 shows the response obtained by numerical integration and it can be observed that the system reaches, as expected, the theoretical steady state value for the angular speed.

Regarding the system with no damping, Figure A.3 shows the angular speed response after integration of the general equation. It can be observed that the linear response predicted by Equation A.5 is obtained. It can be verified, for example that the angular speed at 0.01 s is predicted to be equal to 664.50 rad/s which is exactly what is seen in the figure.

Notice that the steady state angular speed of the system is a function of this damping and it can be use to adjust the desire operating conditions of a given mechanical model.

Appendix B

Roller bearing modeling

B.1 The equivalent load deflection coefficient estimation

The contact model of Hertz considers a unique contact, which means that only one rolling element and one race interact by means of a normal force. In this work, the presence of the two races implies that the rolling element is under two different loads (N_i and N_e) applied over the two contact points. Let δ_i and δ_e be the inner and outer contact point displacements representing the crushing of the rolling element; $C_{b,i}$ and $C_{b,e}$ the load deflection coefficients. As the geometry of the races are different, we have therefore that the coefficients are different:

$$N_i = C_{b,i} \cdot \delta_i^{\frac{3}{2}} \tag{B.1}$$

$$N_e = C_{b,e} \cdot \delta_e^{\frac{3}{2}} \tag{B.2}$$

From the assumption that the rolling element is in static equilibrium on the normal plane we have

$$N_i = N_e = N \tag{B.3}$$

If we define the total crushing of the rolling element as

$$\delta = \delta_i + \delta_e \tag{B.4}$$

Substitution of equations (B.1), (B.2) and (B.3) into (B.4) gives:

$$\delta = \left(\frac{N}{C_{b,i}}\right)^{\frac{2}{3}} + \left(\frac{N}{C_{b,e}}\right)^{\frac{2}{3}} \tag{B.5}$$

which leads to:

$$N = \left(\left(\frac{1}{C_{b,i}}\right)^{\frac{2}{3}} + \left(\frac{1}{C_{b,e}}\right)^{\frac{2}{3}}\right)^{-\frac{3}{2}} \cdot \delta^{\frac{3}{2}} \tag{B.6}$$

Therefore the equivalent deflection coefficient C_b is defined by:

$$C_b = \left(\left(\frac{1}{C_{b,i}}\right)^{\frac{2}{3}} + \left(\frac{1}{C_{b,e}}\right)^{\frac{2}{3}}\right)^{-\frac{3}{2}} \tag{B.7}$$

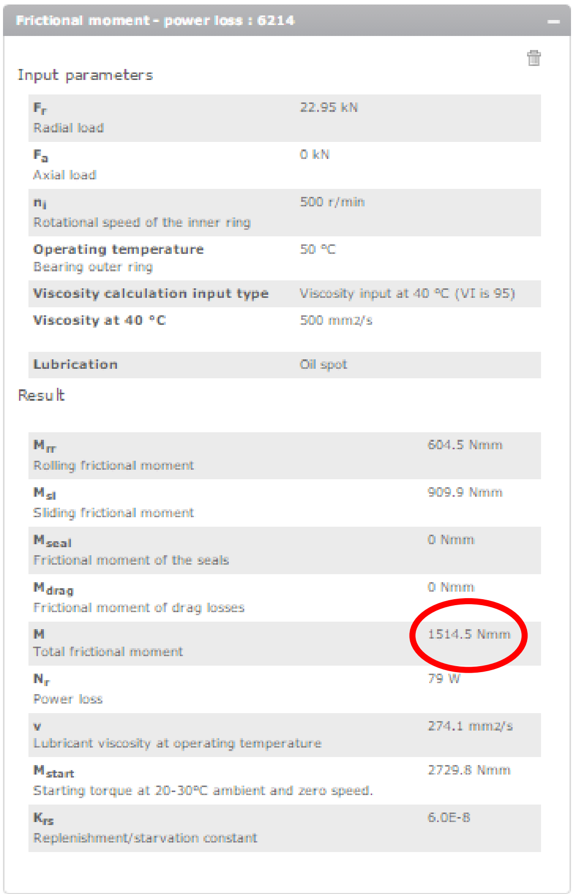

Frictional moment - power loss : 6214

Input parameters

F_r Radial load	22.95 kN
F_a Axial load	0 kN
n_i Rotational speed of the inner ring	500 r/min
Operating temperature Bearing outer ring	50 °C
Viscosity calculation input type	Viscosity input at 40 °C (VI is 95)
Viscosity at 40 °C	500 mm2/s
Lubrication	Oil spot

Result

M_{rr} Rolling frictional moment	604.5 Nmm
M_{sl} Sliding frictional moment	909.9 Nmm
M_{seal} Frictional moment of the seals	0 Nmm
M_{drag} Frictional moment of drag losses	0 Nmm
M Total frictional moment	1514.5 Nmm
N_r Power loss	79 W
v Lubricant viscosity at operating temperature	274.1 mm2/s
M_{start} Starting torque at 20-30°C ambient and zero speed.	2729.8 Nmm
K_{rs} Replenishment/starvation constant	6.0E-8

Figure B.1: Friction Torque SKF Calculation

B.2 Estimation of frictional moment with the SKF calculator

The SKF calculator [52] contains a modulus for the estimation of the frictional moment, which is an equivalent of the Torque over the inner race obtained by means of equation 2.34. The input data required by the calculator are the resultant radial and axial load over the bearing F_r, the rotational speed, the operating temperature, and the lubricant viscosity.

The SKF bearing calculator was used to estimate the frictional moment for the bearing 1 of section 2.4.2 (number 6214) with the same operating conditions: Radial load: 22.09 kN, non axial load, and rotational speed equals to 500 rpm. Temperature and viscosity are not consider by the model presented on this work, so we set logical operating values. The bearing temperature was set of 50 ^oC and the viscosity of 500 mm^2/s.

Figure B.1 shows results obtained. The Total frictional moment is equal to 1514.5 Nmm which is in the same order of magnitude as the torque estimated for the model presented on this work which is 1930 Nmm.

B.3 Adapted Palgrem formulation for roller bearings

The equations of Palgrem [70] describe a way for the estimation of the radial and axial relative displacements of the bearings' races δ_r and δ_a. In this case, we use the equations to estimate the bearing load as a function of the displacements. We present the equations for the DGBB and the cylindrical roller bearings as a function of the number of roller elements Z, effective contact length La (for cylindrical bearings) and the rolling element diameter Dw (for DGBB).

$$\text{DGBB:} \quad F_{pal} = \frac{Z}{2} \cdot \sqrt{\left(\frac{\delta}{0.002}\right)^3 \cdot Dw} \tag{B.8}$$

$$\text{Cylindrical:} \quad F_{pal} = \frac{Z}{2} \cdot \left(\frac{\delta \cdot La^{0.8}}{0.0006}\right)^{\frac{1}{0.9}} \tag{B.9}$$

In the equations above, the displacements are introduced in mm and the loads are obtained in $Newtons$. In the case of the models developed in the current research, the displacements are obtained from the FE node in X and Y so the forces are obtained in the same axes. The sense of the forces when expressed as vectors in the connectivity arrangement has to be matched with the one of the relative displacements of the bearing races.

Appendix C

Gear coupling modeling

The aim of this appendix is to analyze the rigid body rotations of a single stage gear system which is used as a way to validate the gear mesh approach introduced in the current work.

C.1 Rigid body one DOF resolution for a single stage gear coupling

The system of equations for a single stage gear couple configuration can be written to verify the rigid body angular response of the finite element model. Considering the configuration shown in Figure C.1, the rotation of the system may be described with one angular DOF.

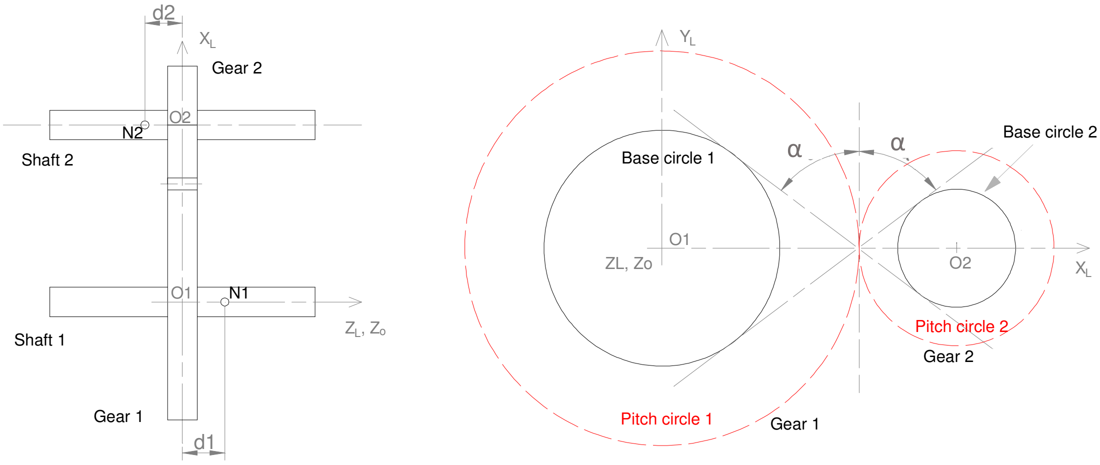

Figure C.1: General representation of single stage gear system

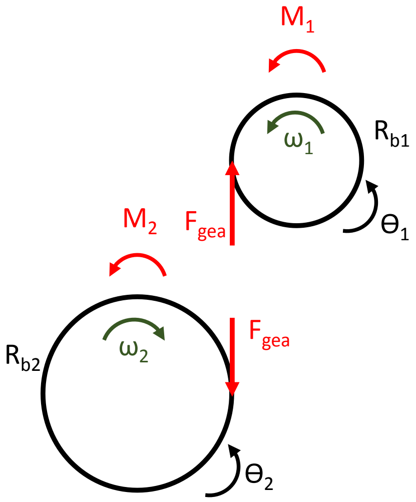

Figure C.2: General representation of single stage gear system

Figure C.2 shows the force diagram for each of the gears of the system. Defining:

$$\dot{\theta}_z = \omega \tag{C.1}$$

The system of equations describing the rotations are:

$$\begin{cases} J_1 \cdot \frac{d\omega_1}{dt} + v_1 \cdot \omega_1 = M_1 - Rb_1 \cdot Fgea \\ J_2 \cdot \frac{d\omega_2}{dt} + v_2 \cdot \omega_2 = M_2 - Rb_2 \cdot Fgea \end{cases} \tag{C.2}$$

where v_i represents the visco-equivalent damping coefficient, T_1 is the external torque moving the system and F_{gea} is the gear connecting force along the line of action with a quasi static approach. The tangential speed analysis in the point of contact between the gears describes the kinematic liaison defining the transmission ratio:

$$\omega_2 = -\frac{Rb_1}{Rb_2} \cdot \omega_1 = -n \cdot \omega_1 \tag{C.3}$$

We are interest in the system behavior on the steady state meaning that there’s no angular acceleration. The system of the equations becomes:

$$\begin{cases} v_1 \cdot \omega_1 = M_1 - Rb_1 \cdot F_{gea} \\ -v_2 \cdot n \cdot \omega_1 = M_2 - Rb_2 \cdot F_{gea} \end{cases} \tag{C.4}$$

By operating with equation C.4 we find the expressions of the gear force and operating speed as a function of the transmission ratio, the external torques, the base radius and the dissipation coefficients:

$$F_{gea} = \frac{\nu_2 \cdot n \cdot M_1 + \nu_1 \cdot M_2}{\nu_2 \cdot n \cdot Rb_1 + \nu_1 \cdot Rb_2} \tag{C.5}$$

$$\omega_1 = \frac{M_1 - n \cdot M_2}{\nu_1 + n^2 \cdot \nu_2} \tag{C.6}$$

Appendix D

The Wind turbine model construction

D.1 The simplified model parameters

Simplifications considered to construct the model of the MM82 wind turbine are easily identified in the kinematic schemes presented in Figure D.1.

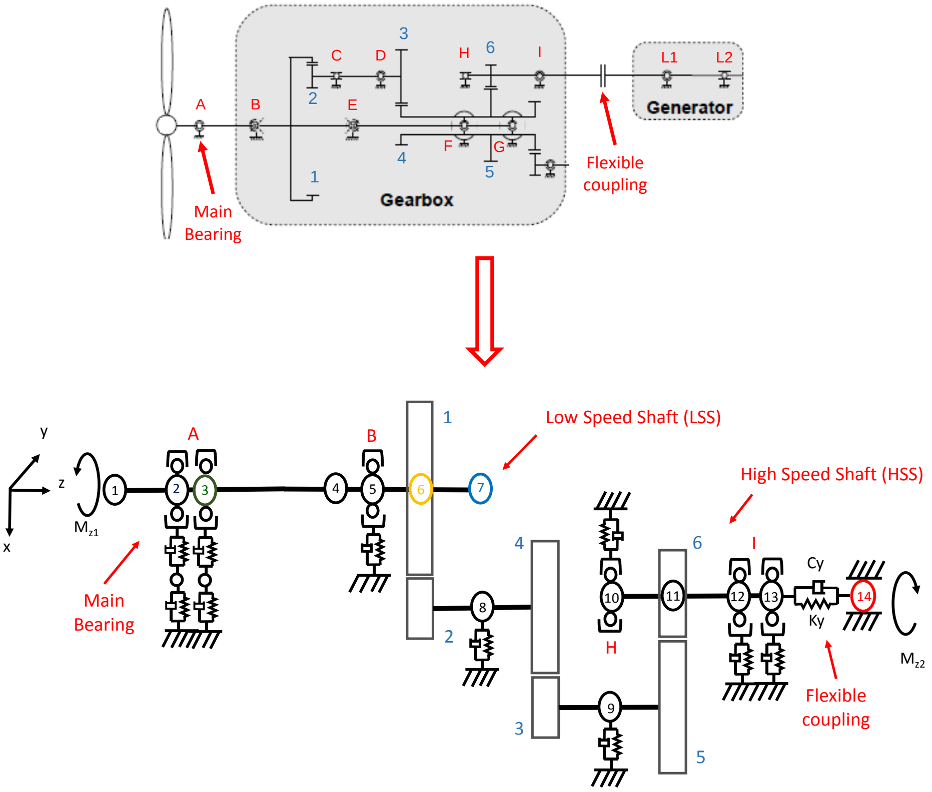

Figure D.1: Simplified model architecture

In this appendix the set values for the mechanical parameters of the model are presented. As it was described in Section 4.2.3 the gearbox has three stages of speed increasing to adapt the speed to the requirements of the generator with a total ratio of 105.5 distributed in 4.429, 4.381 and 5.438 for each stage. All gears of the model have the same number of teeth, modulus and pressure angle than the represented ones. To be in agreement to the bearing model introduced in chapter 2 the helix angles are considered nil. The rotor's inertia and mass was estimated by Engie Green in a previous project and are equal to 3.56 ton and 5 $MN \cdot m^2$ respectively. The parameters are lumped into node 1 for the dynamic response and an external load is applied vertically representing the static load of the rotor. Analogously, the estimated inertia of the generator equal to 110 $N \cdot m^2$ was lumped into node 14.

D.1.1 The shafts

The Low Speed Shaft is actually composed by three shafts which are rigidly attached by two consecutive male-female screwed unions. Figure D.2 shows an scheme provided by the manufacturer. The dimension labeled as δ is the male portion which gets into the female part of the gearbox section of the Low Speed Shaft. For confidentiality reasons the dimensions are not shown, however, to give an idea of the orders of magnitude this figure's piece of the shaft has a length of around 5000 *mm*.

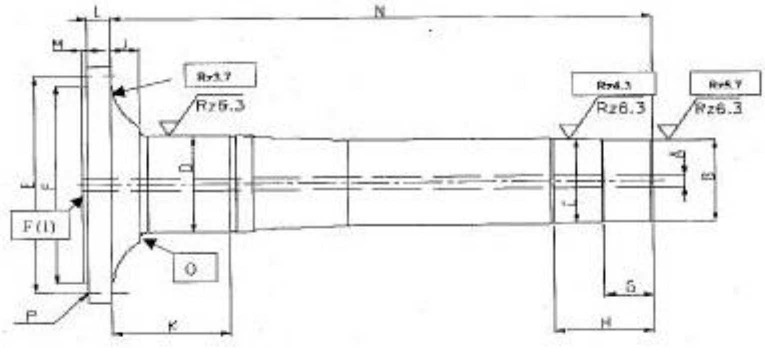

Figure D.2: Low Speed Shaft scheme. Courtesy of Senvion

The rest of the dimensions for the Low Speed Shaft and the High Speed Shaft or output shaft of the Gearbox were obtained from the plans of the assembly which is shown in Figure D.3. The values are not presented in the plan provided by the manufacturer but as Engie Green has the information of the ring gear (Gear 1) dimensions, the others were estimated using proportionality. It was said in Section 4.2.3 that in the model the Low Speed Shaft was truncated geometrically at the position of the Bearing E due to the fact that in one hand the shaft is very thin related to the rest which is also the longest part, and in the other hand because only Bearings A and B are taken into account. When seeing both Figures it can be observed that the Low Speed Shaft is hollow. This with the intention of serving as a mean to pass control and power wiring to the hub.

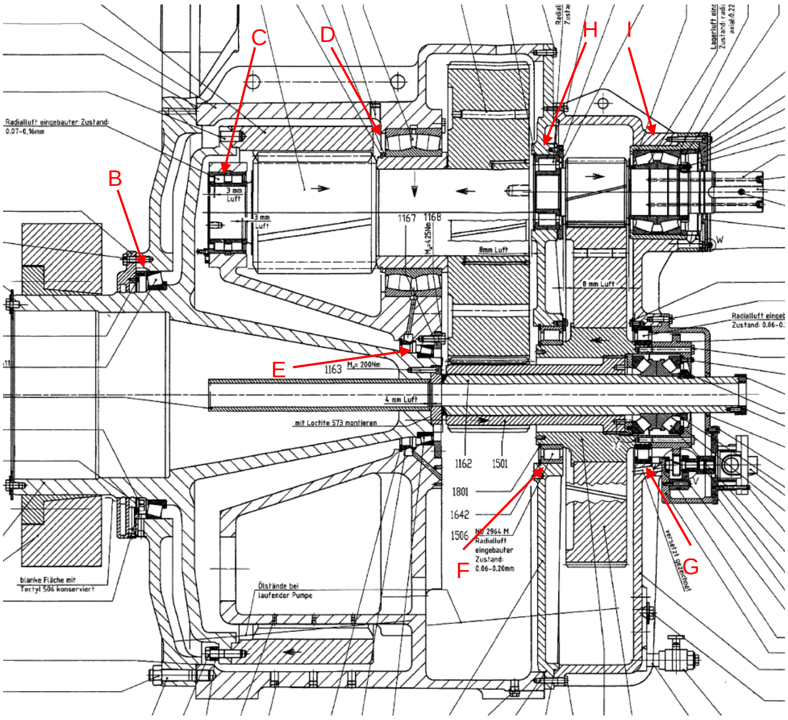

Figure D.3: Extract of the Gearbox assembly plan. Courtesy of Senvion

D.1.2 The bearings

The aim of the model is to produce dynamic IAS signals obtained due to the wind excitations and the dynamics of the Main Bearing (Bearing A) which has a double row of spherical rolling elements. The model was performed considering the bearing as a double row deep groove one allowing to use the approach presented in Chapter 2. The rolling element radius is set as the maximum radius of the spherical elements of the real bearing. In this sense, the pitch diameter was also estimated from the real bearing and in consequence the diameters for the inner and outer races.

The others bearings were modeled with the Palgrem equations presented in Appendix

Table D.1: Gear number of teeth. RENK Gearbox

Bearing	Inner Race Diameter [mm]	Pitch Diameter [mm]	Number of Rolling Elements	Rolling Element Diameter [mm]
A	630	775	28	71
B	673	741	70	29
H	110	176	13	42
I	150	210	21	21

B.3. All these bearings were considered as cylindrical from the point of view of the equations. The characteristics for all the bearings are listed in Table D.1

D.1.3 The supports

Being the Main Bearing the focus of the modeling, reduced parameters were obtained from the 3D finite element model of the casing in ANSYS. As a two degree of freedom model was desired for the vertical direction, the two first frequencies were estimated restraining all the degrees of freedom in the attaching points.

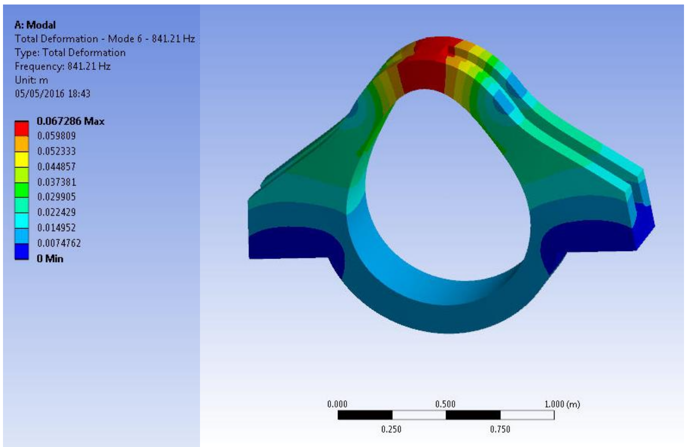

Figure D.4: Modal form of the first natural frequency

Figure D.4 shows the mode for the first natural frequency in the vertical direction. The first two natural frequencies are 840 and 1640 Hz. The reduction of the model is made by choosing a combination of parameters of mass and stiffness with natural frequencies close to the ones estimated by the finite element method analysis in the system shown in Figure D.5. The values set for stiffnesses Kx_1 and Kx_2 were $3.50 \cdot 10^{10}$ N/m and $3 \cdot 10^{10}$ N/m. The added masses m_1 and m_2 were 500 kg and 700 kg leading to natural frequencies equal to 697 and 1958 Hz respectively. By using a modal damping of 3% the values of the coefficients Cx_1 and Cx_2 were found equal to $3.30 \cdot 10^5\ Ns/m$ and $2.44 \cdot 10^5\ Ns/m$.

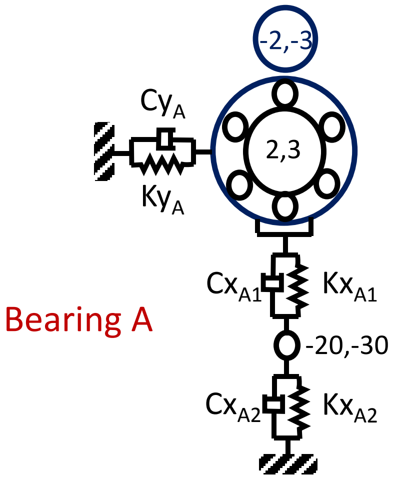

Figure D.5: Support configuration for the Main Bearing

A different approach is used for the horizontal direction. Figure D.6 shows the deformation of the casing by applying a static load of 1000 N to the geometrical center of the casing when it is restrained in the attaching points. The maximum deformation of $6.68 \cdot 10^{-8}\ m$ gives an approximated reduced stiffness of $1.5 \cdot 10^{10}\ N/m$.

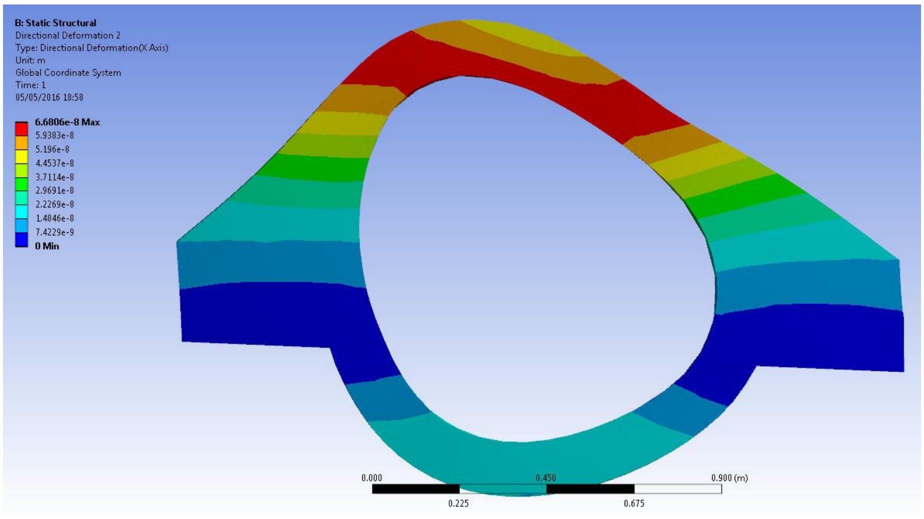

Figure D.6: Displacement of the casing under the effect of a static load

For the rest of the bearings the flexible supports were estimated by considering only two degrees of freedom, one for each radial independent direction (see Figure D.7). The

Gearbox casing rests on vibration pads. As the information for this feature was not available, several commercial pads were verified having stiffnesses with orders of magnitude between 1 to 100 MN/m. To ease convergence in the numerical method the chosen value was of 150 MN/m. Also, a 3% damping was used giving a coefficient of $1.10 \cdot 10^4$ Ns/m.

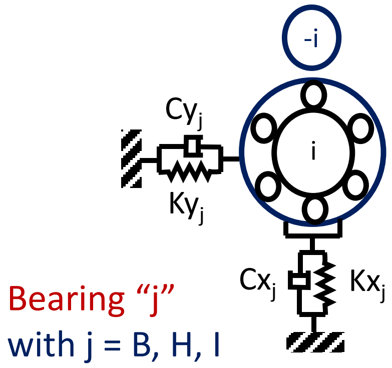

Figure D.7: Support configuration for bearings B, H and I

For the case of the nodes 8 and 9 which concentrate different elements (Gears and shafts) the value was set up to ease the convergence for the equation resolution. The configuration of the support is shown in Figure D.8. The value for the stiffness was set as 1500 MN/m and the damping set was the same than the one for bearings i.e. $1.10 \cdot 10^4$ Ns/m.

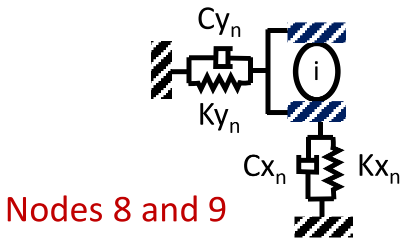

Figure D.8: Support configuration for nodes 8 and 9

Tables D.2 and D.3 show a synthesis for the whole set of parameters described above. Notice that “j” stands for bearings B, H and I in which support parameters are the same in the X and Y directions. The same consideration is applied for the supports of nodes 8 and 9 which are represented by “m” in the tables.

Table D.2: Support modeling added masses

Support	Mass [kg]
A1	500
A2	700
"j"	380
"m"	21

Table D.3: Support modeling stiffness and damping

Support	Stiffness $[N/m]$	Damping $[Ns/m]$
A1x	$3.50 \cdot 10^{10}$	$3.30 \cdot 10^{5}$
A2x	$3 \cdot 10^{10}$	$2.44 \cdot 10^{5}$
Ay	$1.50 \cdot 10^{10}$	$2.44 \cdot 10^{5}$
"j"	$1.50 \cdot 10^{8}$	$1.10 \cdot 10^{4}$
"m"	$1.50 \cdot 10^{9}$	$1.10 \cdot 10^{4}$

D.1.4 The coupling

The flexible coupling is type FLENDER and is modeled as an external element linking nodes 13 and 14. Only The rotational behavior of node 14 is taken into account. Then, the dynamic characteristic for the coupling is the rotational stiffness obtained from the manufacturer only in the Z direction. The stiffness Kz is equal to $1.44 \cdot 10^{6}$ N/m. No external damping was added. However, as the damping is estimated from the matrices of the whole system, always modal damping is added to every degree of freedom.

D.2 The setting up of the model input parameters

This section describes the tasks performed to set up the input parameters of the model for it to have a mechanical response close to the real wind turbine.

D.2.1 The rigid body equations

The rigid body angular theoretical response was obtained by means of the application of Newton's second law to the mechanical system. Figure D.9 shows the rigid body forces diagram of the gears in the simplified wind turbine model. The resulting system of equations is shown in Equation D.1.

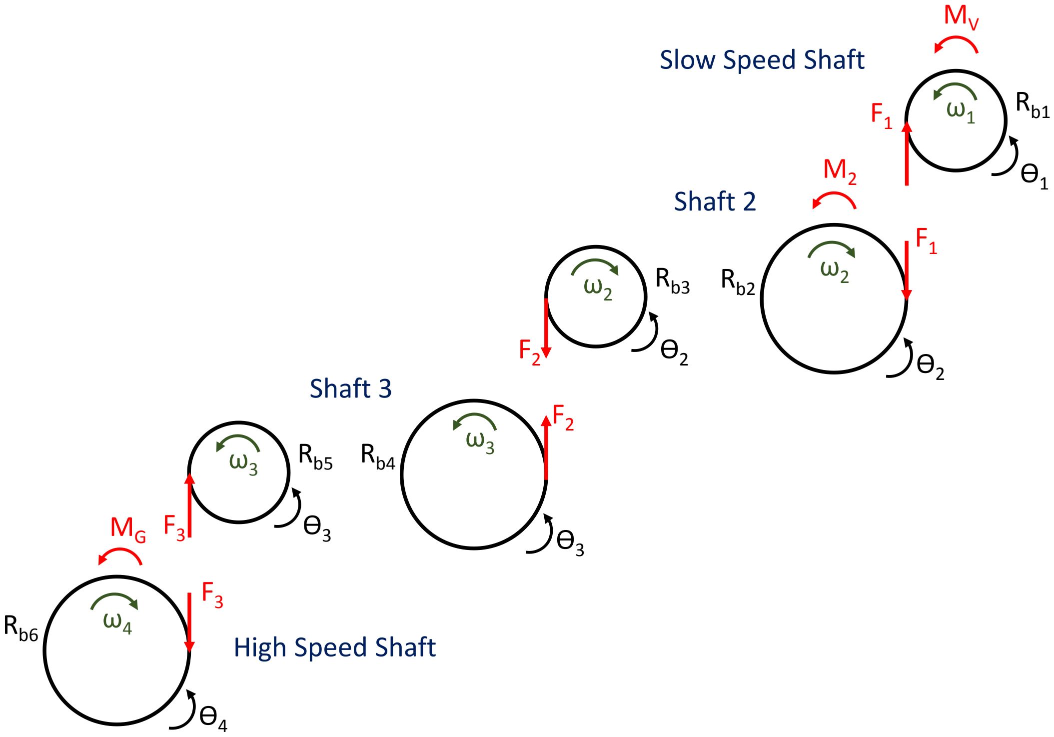

Figure D.9: Rigid body gear-shaft forces diagram. Simplified model

$$\begin{cases} J_1 \cdot \frac{d\omega_1}{dt} + \nu_1 \cdot \omega_1 = M_v - Rb_1 \cdot F_1 \\ J_2 \cdot \frac{d\omega_2}{dt} + \nu_2 \cdot \omega_2 = Rb_3 \cdot F_2 - Rb_2 \cdot F_1 \\ J_3 \cdot \frac{d\omega_3}{dt} + \nu_3 \cdot \omega_3 = Rb_4 \cdot F_2 - Rb_5 \cdot F_3 \\ J_4 \cdot \frac{d\omega_4}{dt} + \nu_4 \cdot \omega_4 = M_G - Rb_6 \cdot F_3 \end{cases} \tag{D.1}$$

where ν_i represents the visco-equivalent damping coefficient of the shaft i, M_v is the external moment introduced by action of the wind, F_i are the gear connecting forces along the line of action, M_G is the resistive moment applied by the generator and Rb_i is the base radius of the gear i. The kinematic liaisons defining the transmission ratio is obtained by analyzing the tangential speed in the points of contact between the gears:

$$\omega_2 = -\frac{Rb_1}{Rb_2} \cdot \omega_1 = -n_1 \cdot \omega_1 \tag{D.2}$$

$$\omega_3 = -\frac{Rb_3}{Rb_4} \cdot \omega_2 = n_1 \cdot n_2 \cdot \omega_1 \tag{D.3}$$

$$\omega_4 = -\frac{Rb_5}{Rb_6} \cdot \omega_3 = -n_1 \cdot n_2 \cdot n_3 \cdot \omega_1 \tag{D.4}$$

Substitution of the above equations and cancellation of the angular acceleration transform Equation D.1 into:

$$\begin{cases} \nu_1 \cdot \omega_1 = M_v - Rb_1 \cdot F_1 \\ -\nu_2 \cdot n_1 \cdot \omega_1 = Rb_3 \cdot F_2 - Rb_2 \cdot F_1 \\ \nu_3 \cdot n_1 \cdot n_2 \cdot \omega_1 = Rb_4 \cdot F_2 - Rb_5 \cdot F_3 \\ -\nu_4 \cdot n_1 \cdot n_2 \cdot n_3 \cdot \omega_1 = M_G - Rb_6 \cdot F_3 \end{cases} \tag{D.5}$$

The choice was made to set each shaft's visco-elastic damping torsional coefficient (ν_i) equal and represented by ν. This allows after operating Equations D.5 to find an expression allowing to estimate a first guess for the damping coefficient as a function of the Low Speed Shaft angular speed ω_1, the external input and resistive moments M_v and M_G, and each stage transmission ratio:

$$\nu = \frac{M_w - n_1 \cdot n_2 \cdot n_3 \cdot M_G}{\omega_1 \cdot (1 + n_1^2 + n_1^2 \cdot n_2^2 + n_1^2 \cdot n_2^2 \cdot n_3^2)} \tag{D.6}$$

Résumé étendu

Introduction générale

Dans le domaine de la maintenance, la surveillance des machines par des méthodes non intrusives représente jeu un rôle principale la pierre angulaire pour permettant la minimisation des temps d'arrêt, ce qui contribue à l'augmentation de la fiabilité et la disponibilité des parcs éoliens. Ce type de technique est basé sur la mesure et le suivi d'une ou plusieurs variables dont un seuil statistique est estimé dans des conditions normales, ceci permet alors d'établir des alarmes basées sur les variables surveillées.

Le département d'Engie Green base son CMS (Condition Monitoring System) sur les techniques suivantes : température du lubrifiant, analyse du lubrifiant, la mesure de la puissance active et les vibrations radiales. Parmi ces techniques, l'analyse des vibrations mécaniques est la seule qui permet l'identification des composantes en panne à travers des techniques avancées de traitement du signal. Cette caractéristique permet à l'équipe de maintenance la planification des interventions pour le remplacement des composantes mécaniques endommagées.

La surveillance des machines par l'analyse des vibrations radiales impose certains challenges. Un capteur (accéléromètre piézoélectrique) doit être installé près de presque tout roulement qui supporte le système en rotation pour être capable de bien surveiller l'ensemble de la ligne d'arbre de la machine. Cette particularité augmente les coûts du système. En outre, les capteurs sont fixés aux carters ce qui engendre un filtrage du signal occasionné par la voie de transfert du système. De plus, les mesures sont habituellement échantillonnées en temps, rendant quasiment impossible l'analyse des signaux dans le domaine fréquentiel dû aux variations des conditions de fonctionnement subies par les éoliennes en fonctionnement.

Dans le cadre d'une thèse CIFRE développée en partenariat entre MAIA Eolis (actuel Engie Green) et le LaMCoS de l'INSA de Lyon, un outil de surveillance original a été proposé basé sur l'analyse de la Variation de Vitesse Instantanée (VVI) mesurée avec des codeurs à travers des méthodes angulaires directes. Différentes techniques de traitement du signal ont étés analysées et adaptées basés sur les méthodes d'analyse des vibrations radiales. Une campagne de mesures de longue durée a été lancée et le développement d'une méthode de calcul d'indicateurs en conditions de non-stationnarité a été testé et amélioré après la fin des travaux de thèse au sein du département d'expertise mécanique de l'entreprise.

La réponse à cette question devient importante vis-à-vis de la définition de la complexité et de la taille du modèle exprimée par le nombre de dégrésdegrés de liberté à considérer pour modéliser correctement la réponse VVI d'un système mécanique . Une fois cette question clarifiée, la construction d'un modèle mécanique devient un outil pour le développement et le test d'indicateurs de surveillance complexes sous un environnement contrôlé dans lequel l'évolution de la sévérité du défaut peut être analysée en lien avec les conditions de fonctionnement variables de la machine.

Chapitre 1. La VVI comme outil de surveillance de machines tournantes: dès la mesure à la modélisation

Acquisition du signal VVI

La méthodologie de mesure des signaux de variations de vitesse dépend du type de capteur choisi dont le signal sera conditionné par le système d'acquisition utilisé. Il existe différents types de capteurs. Dans le cadre des projets de recherche d'Engie Green des capteurs angulaires magnétiques ou optiques sont utilisés après avoir fait des analyses techniques et économiques. La méthode de l'écart temporel a été choisie pour l'estimation de la VVI à partir du signal délivré par le capteur. Cette méthode est basée sur le comptage des pulses d'une horloge de haute fréquence entre deux fronts montants du signal provenant du codeur. L'information est récupérée par le système d'acquisition et la variation de vitesse est estimée. Chaque échantillon de vitesse estimé représente la moyenne de la vitesse réelle entre deux fronts montants du codeur ce qui engendre un filtrage passe bas du contenu du signal.

Techniques de traitement du signal pour l'observation spectrale de la VVI en condition non stationnaire

Le traitement d'un signal brut non stationnaire introduit du bruit spectral tout à long du domaine fréquentiel, cependant il est particulièrement prononcé dans le domaine des basses fréquences. L'application d'une fenêtre d'apodisation comme celle de Hanning aide à la réduction efficace de telles perturbations, permettant ainsi une meilleure observation du spectre.

Modélisation du phénomène de la VVI

La modélisation du phénomène de la variation de vitesse est basée sur la construction de la fonction angle-temps. Cette fonction est établie en considérant l'angle de rotation du système comme une des inconnues des équations. Ceci permet la simulation des conditions non stationnaires dans le système.

L'autre question importante par rapport à la modélisation du phénomène concerne l'analyse sur l'origine des perturbations mécaniques cycliques qui introduisent des variations de vitesse. Par analogie avec les vibrations radiales où la variation des forces internes est à l'origine des variations de la réponse radiale, il est supposé que des variations de couple occasionnent des perturbations angulaires. La modélisation d'un banc d'essai en considérant une perturbation de couple périodique en angle équivalent à un défaut de roulement a été réalisée par Bourdon et al [2]. Les résultats de modélisation, où seulement le dégrée de liberté angulaire a été considéré, ont été comparés avec succès aux mesures expérimentales. Ces travaux ont confirmé qu'en introduisant des variations de couple dans un système mécanique il est possible de modéliser les variations de vitesse. Ce système a comporté un arbre supporté par roulements. Un défaut a été artificiellement introduit sur la bague externe d'un roulement de test chargé radialement par un dispositif externe. Cette dernière affirmation amène à la question : Comment est-il possible que la distribution de charges internes de nature radiale dans un roulement génère des perturbations de couple? La réponse à cette question représente la thématique centrale du deuxième chapitre.

Chapitre 2. Modélisation des variations de vitesses introduites par la dynamique d'un roulement à gorges profondes

Décrire les variations des efforts normaux dans l'interaction billes-bagues des roulements est dans un premier temps passé par la définition de l'approche globale pour intégrer les modèles du roulement aux arbres qu'il supporte. De façon générale les arbres ont été décrits avec la méthode des éléments finis et les roulements comme des efforts extérieurs appliqués sur les noeuds représentants les bagues intérieur et extérieur des roulements (Figure R1).

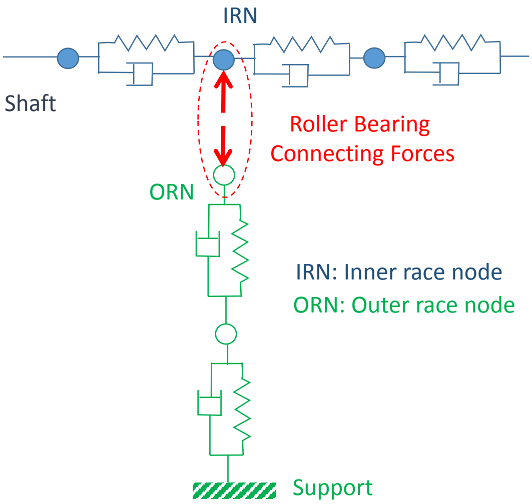

R.1 Approche générale de modélisation.

Selon la modélisation des carters le roulement est décrit avec 12 degrés de libertés dont 6 par bague. L'approche utilisée pour l'estimation des efforts externes est considéré comme une extension du modèle de Sawhali et Randall [36]. Le modèle proposé considère explicitement le degré de liberté de rotation des arbres, billes et bagues dans les équations de mouvements ayant pour but la construction de la fonction angle-temps qui permet la modélisation des conditions de fonctionnement non stationnaires ainsi que la description des phénomènes cycliques. La considération de l'ensemble des dégrées de liberté du système donne accès à l'analyse des vibrations radiales tout en ajoutant de la polyvalence à l'approche.

Origine de la perturbation angulaire

Le système des efforts décrivant l'interaction billes-bagues est purement radiale. Dans ce cadre, la question est donc de définir comment les perturbations de couple ont lieu. La réponse est basée sur l'hypothèse de l'existence d'un phénomène couplant les efforts radiaux et tangentiels de l'interaction bille-bagues. L'approche proposée est basée sur la considération du phénomène de résistance au roulement définit comme suit : dans le système représenté sur la Figure R2, la déformation des solides en contact par action des efforts externe est modélisé par le déplacement du point d'application des efforts normaux dans la direction de la vitesse du centre de masse. Ce déplacement se traduit par un couple lui même produit par le couplage des efforts radiaux et tangentiels du système. La distance de décalage des efforts normaux dépend du coefficient de résistance au roulement variable, équivalent au coefficient de friction pour ce type de roulement selon le site SKF et qui est égal à 0.0015.

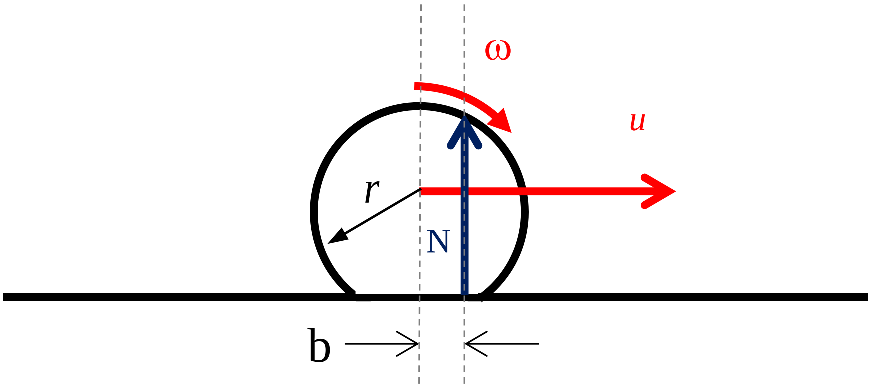

R.2 Phénomène de résistance au roulement.

Dynamique du roulement à gorges profondes en considérant le phénomène de résistance au roulement

La Figure R3 montre les diagrammes des efforts de l'interaction billes-bagues en considérant le phénomène de résistance au roulement et en conditions d'équilibre quasi statique au niveau des billes.

L'application des équations d'équilibre amène à l'expression générale du torseur d'effort des roulements présents dans le système modélisé :

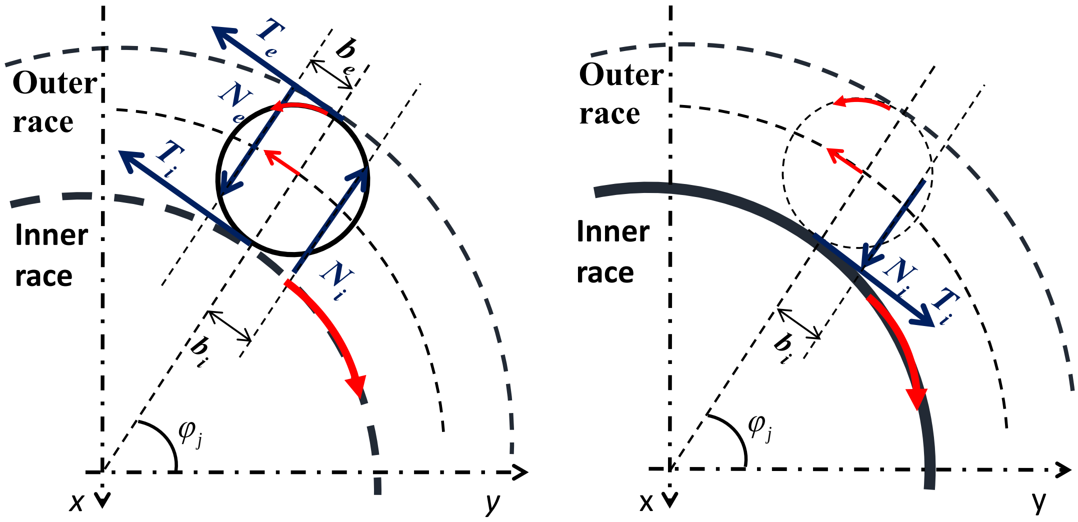

(a) Diagramme d'éfforts du j^{eme} élément roulant (b) Diagramme d'efforts. Bague intérieure

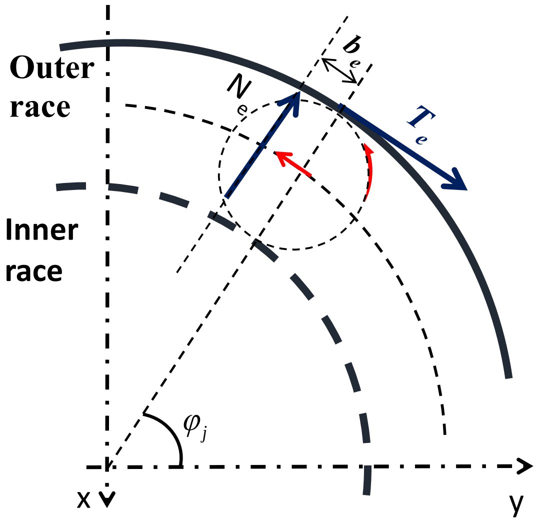

(c) Diagramme d'efforts. Bague extérieure

R3 Diagramme d'efforts interaction bille-bagues.

$$\{F_{bea}\} = \{F_{beaN}\} + \{F_{beaT}\} + \sum_{k=1}^{N_{bea}} \gamma_{IR_k} \cdot \{F_{bea\gamma}\}_k$$

Où N_{bea}, représente le nombre total des roulements. Les vecteurs $\{F_{beaN}\}$ et $\{F_{beaT}\}$ sont construits à partir des vecteurs des efforts normaux et tangentiels correspondants aux noeuds représentant des roulements et qui sont assemblés en suivant l'arrangement de connectivité des éléments finis. L'expression $\gamma_{IR_k} \cdot \{F_{bea\gamma}\}_k$ représente la composante inertielle de la bague intérieure du roulement *k*.

Test du modèle de roulement sur deux architectures mécaniques différentes.

Le modèle de roulement a été testé sur deux systèmes mécaniques. Le premier est un système composé d'un arbre supporté par un roulement à gorges profondes et une rotule. Dans ce système un défaut de roulement a été ajouté sur la bague intérieure et la réponse de la variation de vitesse a été analyse dans l'espace physique en conditions stationnaires pour le roulement sans et avec défaut. Il est observé pour le cas sain que la variation d'effort normal dû au passage des billes par la zone de chargement entraine une variation de vitesse angulaire. Ensuite, un couple externe linéaire a été appliqué sur l'arbre pour montrer la réponse du système en conditions non stationnaires.

L'approche de modélisation a été testée aussi sur un système comportant un arbre supporté par deux roulements de caractéristiques différentes (Figure R4). Dans un des roulements le coefficient de résistance à roulement a été mis à zéro pour avoir, dans la réponse de variation de vitesse la dynamique d'un seul roulement ce qui simplifie les analyses.

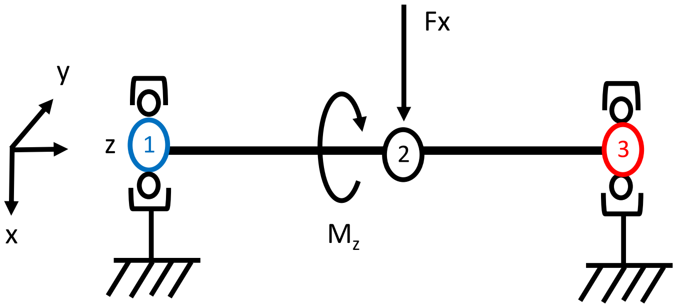

R4 Arbre supporté par deux roulements à gorges profondes

Le système a été testé en état sain et en présence d'un petit défaut de bague extérieur dans le roulement où le phénomène de résistance au roulement est considéré. Le couple perturbateur dont la moyenne représente le couple de friction dans le roulement a été estimé et comparé avec la valeur de la calculatrice du site SKF pour le même roulement avec des conditions équivalentes de fonctionnement. Les résultats obtenus sont 1530 *Nmm* et 1930 *Nmm* ce qui valide la valeur du coefficient de résistance au roulement utilisé.

Ensuite, la réponse en accélération radial du système a été analysée en présence du défaut où les impulsions correspondantes à l'écaillage sont observables. Ceci expose le potentiel du modèle pour l'analyse des vibrations radiales. Dans ce contexte, les distributions des efforts normaux ont été estimées et présentées sur la Figure R5. On peut observer dans cette figure que quand une bille passe par le défaut, une perturbation des efforts est observée dans toutes les billes qui se trouvent dans la zone de chargement. Ce phénomène est attendu car la charge de la bille passant par le défaut diminue et le système récupère l'équilibre en augmentant la charge sur les autres corps roulants.

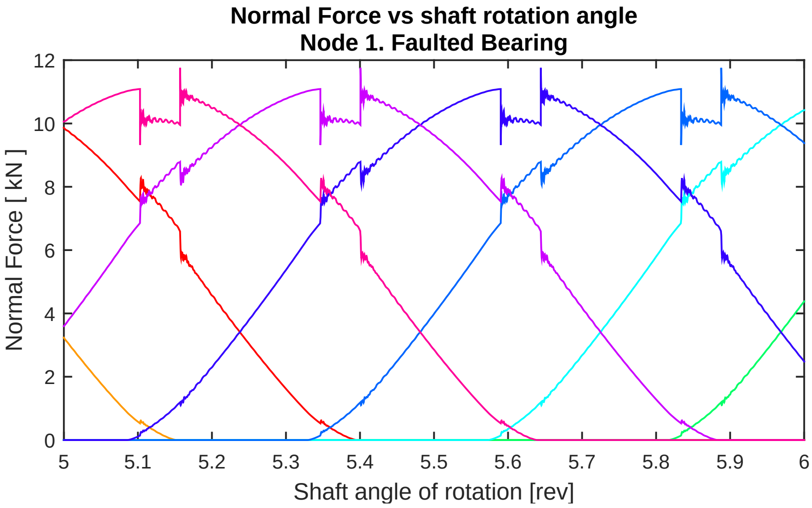

Distribution d'efforts normaux sur les éléments roulants. Node 1

Une observation intéressante peut aussi être énoncée sur la réponse de la VVI pour les deux systèmes mécaniques analysés. Pour le système avec un seul roulement, l'amplitude du phénomène augmente significativement en présence du défaut en même temps que l'amplitude diminue pour le système avec deux roulements. La différence principale entre les deux configurations est la taille du défaut par rapport à celle du roulement et le chargement statique radial. Il est difficile d'analyser les conditions de vitesse angulaire, de charge et de taille du défaut pour lesquelles la réponse VVI augmente ou diminue. Dans le chapitre 4 ce phénomène est évoqué dans le cadre de l'étude sur les indicateurs spectraux.

Une comparaison a aussi été faite entre la réponse avec et sans défaut du système avec les deux roulements (Figure R6) et des mesures expérimentales analysées par bourdon et al. [5] où deux signaux VVI ont été traités pour obtenir la réponse dans l'espace physique avec la signature d'un défaut de roulement dans la génératrice d'une éolienne.

Les réponses du modèle et ceux de l'éolienne sont similaires. Une différence est néanmoins observée : la réponse impulsive pendant l'entrée et la sortie de corps roulant

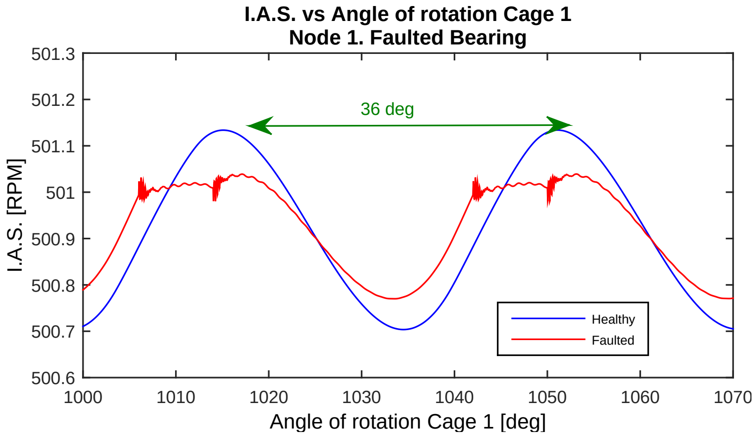

(a) VVI modèle

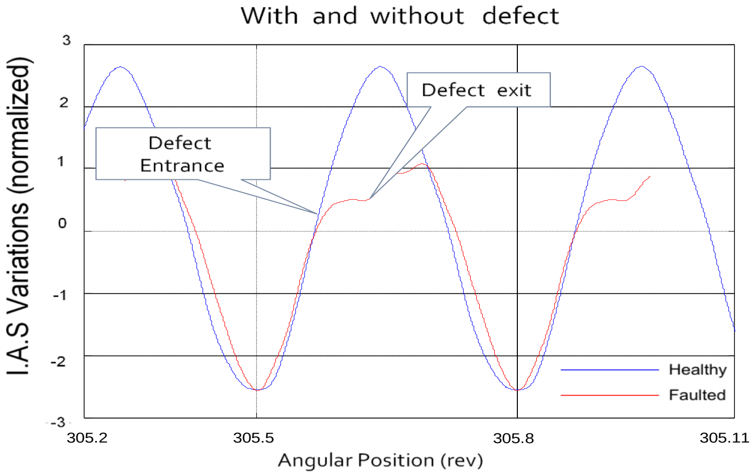

(b) VVI génératrice d'éolienne. Bourdon et al. [5]

R6 Comparaison entre la réponse VVI du modèle et d'une génératrice d'éolienne.

du défaut dans le modèle n'est pas observée dans la mesure expérimentale. Ce phénomène peut être expliqué par le fait que pour la reconstitution du signal expérimental, la méthode de traitement prend en compte un nombre spécifique d'harmoniques dans le domaine fréquentiel ce qui peut filtrer une partie de l'information.

Chapitre 3. Simuler le phénomène VVI dans les systèmes couplés par engrenages

Une approche très classique de liaison par engrenages a été utilisée avec la particularité de la considération de la variable angulaire pour la construction de la fonction angle-temps. En parallèle avec l'approche de roulement, la liaison par engrenages a été décrite comme un torseur d'efforts extérieurs appliqué sur les noeuds représentants les engrenages. Le torseur est décrit par l'expression :

$$\left\{F_{gea}\right\} = [K_{gea}] \cdot \left\{X_{gea}\right\}$$

où $\left\{F_{gea}\right\}$ est le torseur d'efforts, la matrice $[K_{gea}]$ représente la raideur de la liaison par engrenage et le vecteur $\left\{X_{gea}\right\}$ contient les déplacements généralisés des noeuds où les engrenages sont attachés. La Figure montre une représentation graphique de cette approche. Six dégrés de liberté par engrenage sont pris en compte pour un total de douze pour l'élément de liaison.

Le problème est réduit à l'estimation de la matrice de raideur $[K_{gea}]$. Cette matrice est estimée avec une approche d'énergie potentielle. La raideur de contact entre deux engrenages est modélisée comme un ressort de raideur K_o qui est fonction de l'angle de rotation et qui est placé suivant la ligne de pression des engrenages. L'énergie potentielle est fonction de la raideur K_o et de l'écrasement de la denture Σ :

$$E_p = \frac{1}{2} \cdot K_o(\theta_z) \cdot \Sigma^2$$

L'estimation de l'écrasement est basée sur l'hypothèse de petits déplacements du point de contact entre les engrenages [65]. Cependant, la considération des rotations des corps rigides des engrenages a nécessité la modification de cette hypothèse. Le déplacement du degré de liberté de rotation a été exprimé en fonction de l'erreur de transmission de corps rigide, ainsi l'expression de l'écrasement a été retrouvée. L'équation finale n'a pas été modifiée par ce changement d'hypothèse ce qui a validé l'utilisation de l'approche considérant les grandes rotations. L'expression de la raideur de liaison $[K_{gea}]$ est :

$$[K_{gea}]_{CS_o} = K_o(\theta_z) \cdot [G] \tag{D.7}$$

La matrice $[G]$ est nommée matrice géométrique car elle est composée des caractéristiques géométriques des engrenages tels que l'angle de pression et de l'hélix, les rayons, etc. La raideur K_o peut être considérée constante ou variable avec l'angle de rotation. Dans ce dernier cas, elle ajouterait des perturbations dynamiques liées aux excitations de la liaison qui peuvent être liées aux erreurs de fabrication et de montage entre autres phénomènes. Dans le cadre de ce travail de recherche, elle a été considérée constante puisque l'objectif était d'analyser les excitations provenant exclusivement des roulements dans le domaine physique. En effet, la différence entre les fréquences des phénomènes viendrait à masquer les effets du roulement sur les réponses. La valeur de K_o a été estimée avec une expression empirique suggérée par la norme ISO 6336 qui représente la valeur moyenne de la raideur de denture.

La validation de l'approche des rotations en corps rigide a été réalisée en modélisant un système avec deux arbres et une étape de transmission multiplicatrice de la vitesse de rotation. Une évaluation analytique du système en rotation a été développée. Les résultats ont ensuite été comparés avec les simulations réalisées à travers l'approche de modélisation considérant uniquement le degré de liberté de rotation. Les équations analytiques ont permis de calculer la vitesse de rotation dans l'état stationnaire et de l'effort de liaison statique entre les engrenages puis de les comparer avec la réponse du modèle. Les résultats obtenus par simulations et les résultats analytiques étant équivalents l'approche de modélisation avec la considération des grandes rotations sont validées. Dans le même système un couple perturbateur sinusoidale a été appliqué sur l'arbre d'entrée simulant une perturbation angulaire due à la dynamique d'un roulement. Une variation de la vitesse angulaire a été observée dans l'espace physique ce qui confirme la voie de transfert du phénomène VVI dans l'approche utilisée. Il a été observé dans la réponse que l'amplitude du phénomène de variation de vitesse a été affectée par le rapport de transmission du système ce qui se traduit comme une amplification de la variation de vitesse dans l'arbre de sortie.

L'engrenage comme une deuxième source de couplage normal-tangentiel

Des roulements ont été introduits dans le système analysé montré dans la Figure R7. Le modèle placé dans le noeud 1 a été modélisé avec l'approche du chapitre 2. Les autres noeuds ont été modélisés avec le modèle de Palgrem. Ceci signifie que l'excitation dynamique du système liée à la variation des efforts normaux sur les billes n'est pas considérée pour ces roulements.

Un défaut a été introduit sur la bague extérieure du roulement placée au noeud 1. Des

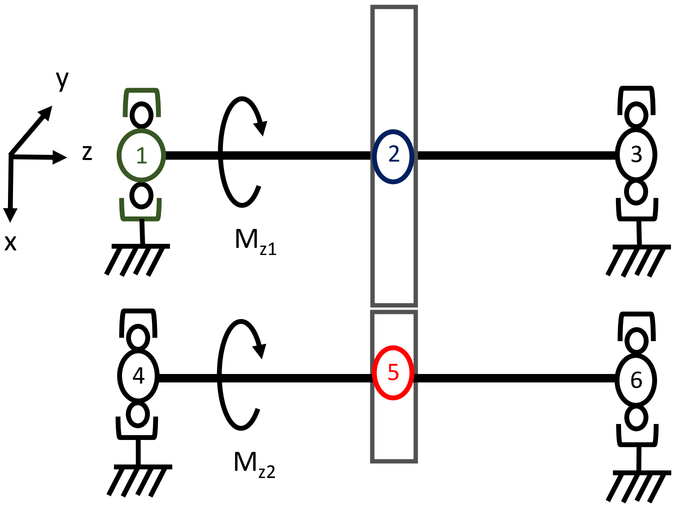

R7 Systéme multiplicateur avec un étage de transmission

simulations ont été faites avec et sans défaut de roulement où le coefficient de résistance au roulement était égal à 0.0015 et à 0. Ceci a été réalisé dans l'intérêt de démontrer que la nature tangentielle de la liaison par engrenage (efforts sur la ligne de pression) est une deuxième source de couplage des effets normaux et tangentiels. Dans le cas où des défauts sont présents, la Figure R8 montre les variations de couples introduits par la résistance au roulement ainsi que par les déplacements des engrenages produits par la dynamique du roulement.

Il est observé sur la figure que les perturbations du couple au niveau des engrenages sont près de 100 fois plus grandes que celles introduites par le phénomène de résistance au roulement. Quand le phénomène de résistance au roulement n'est pas pris en compte les perturbations de couples d'engrenages restent invariables. Il n'est pas possible d'affirmer si ce rapport serait le même pour toute configuration mécanique. Cependant, toutes les simulations faites dans le cadre de cette recherche ont montrées que les variations de couple induites par la liaison d'engrenages sont plus significatives que celles liées au coefficient de résistance au roulement. Ceci met l'accent sur l'importance des paramètres mécaniques des supports car le phénomène au niveau d'engrenages dépend des déplacements radiaux de l'ensemble arbres-engrenages.

La réponse de la variation de vitesse a aussi été observée dans le domaine physique et spectrale pour les cas avec et sans défaut en prenant en compte le phénomène de résistance au roulement. La Figure R9 montre les graphes pour le cas avec défaut. Le phénomène d'amplification de la VVI est observé. Néanmoins, cette amplification n'est

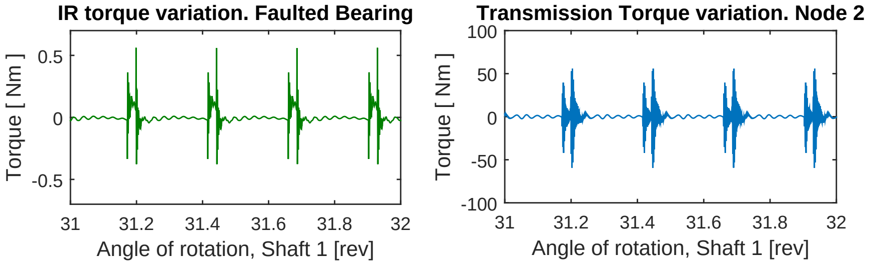

(a) Variation de couple bague intérieur. $\mu = 0.0015$

(b) Variation de couple engrenage. Noeud 2. $\mu = 0.0015$

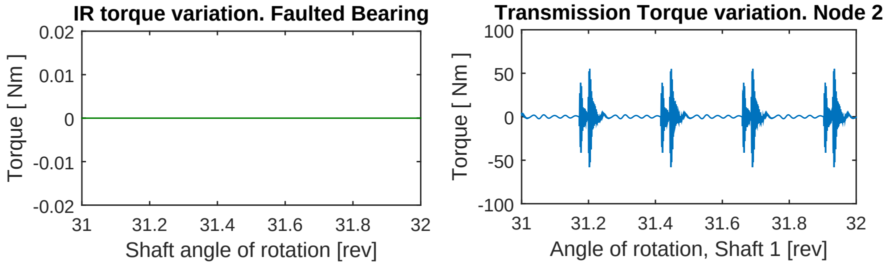

(c) Variation de couple bague intérieur. $\mu = 0$

(d) Variation de couple engrenage. Noeud 2. $\mu = 0$

R8 Torque variation induced by the bearing dynamics. Rolling resistance vs gear mesh

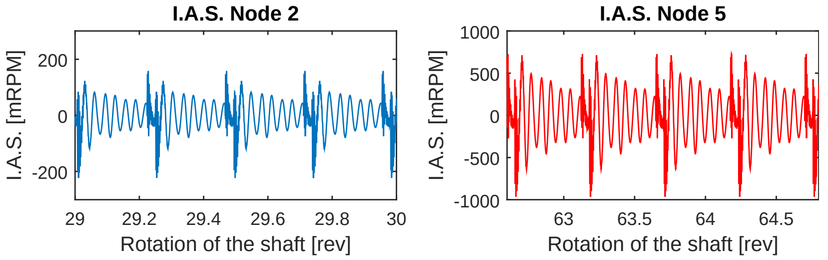

(a) VVI Noeud 2. Roulement avec défaut

(b) VVI Noeud 5. Roulement avec défaut

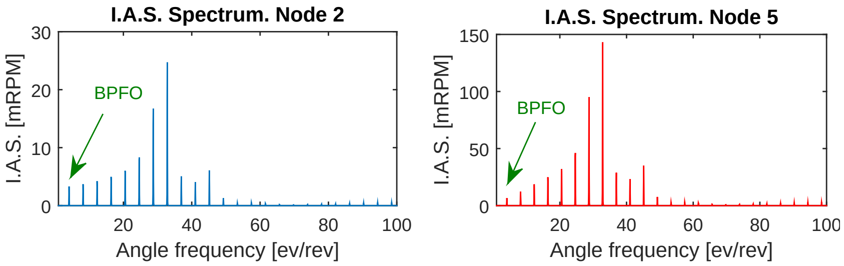

(c) Spectre VVI Noeud 2. Roulement avec défaut

(d) Spectre VVI Noeud 5. Roulement avec défaut

R9 VVI noeuds 2 et 5. Roulement avec défaut pas équivalente au rapport de transmission car le signal est plus riche au niveau fréquentiel ce qui change la distribution énergétique. Il a été vérifié avec des mesures expérimentales réalisées sur un banc d'essai que ce phénomène d'amplification arrive aussi pour des perturbations cycliques comme le déséquilibrage et l'excitation d'engrenage en présence d'une dent arrachée, ce qui valide les résultats obtenus. Cette amplification est suspectée de dépendre des paramètres mécaniques du système.

Sur ces spectres, le pic dominant pourrait indiquer une réponse modale du système. C'est pourquoi ce comportement a été étudié par la suite.

L'effet de la souplesse du système sur la réponse VVI

Pour étudier l'effet de la souplesse des supports flexibles modélisant les carters et les fondations ont été ajoutés au système analysé. Deux couples linéaires extérieurs ont étés appliqués sur les arbres de sorte à analyser la réponse du système à l'excitation des roulements. Cette étude a été réalisée pour les systèmes avec supports rigides et avec supports flexibles avec deux degrés de libertés de déplacement en X et Y. Un troisième test a été aussi réalisé en divisant la raideur des supports par dix. La figure R10 montre les graphes pour les deux premières configurations.

Les fréquences critiques deviennent plus basses quand la souplesse du système augmente. Cela a un effet sur l'espace physique où des différences dans la forme de la variation de vitesse sont visibles. Des simulations ont été réalisées avec l'excitation due au roulement égal à 95 Hz et 220 Hz pour la configuration des supports flexibles. La Figure R11 montre la réponse VVI et les spectres correspondants où il est possible d'observer le changement dans la distribution de canaux fréquentiels dû à la réponse modale du système.

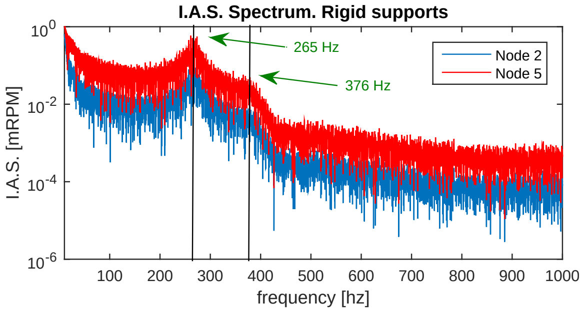

(a) Spectre VVI. Support rigides

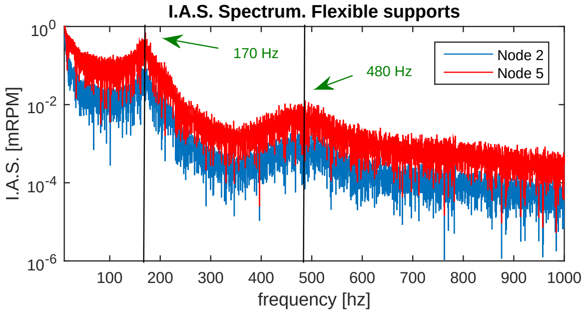

(b) Spectre VVI. Support rigides

R10 Spectre VVI. Réponse au couple linéaire et à l'excitation due au roulement

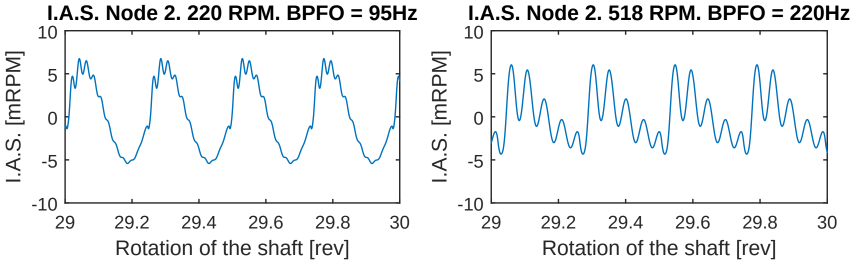

(a) VVI. Roulement sain. 220 rpm (b) VVI. Roulement sain. 518 rpm

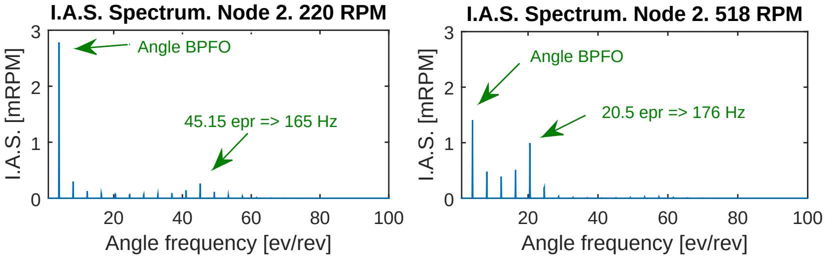

(c) Spectre VVI. Roulement sain. 220 rpm (d) Spectre VVI. Roulement sain. 518 rpm

R11 VVI pour les noeuds 2 à 220 et 518 rpm. Roulement sain et avec défaut

Chapitre 4. Construction d'un modèle simplifié d'éolienne pour le test d'indicateurs de surveillance de VVI

Dans le cadre du projet de développement de la VVI comme outil de surveillance d'éoliennes mis en place par Engie Green, une turbine a été instrumentée avec des codeurs optiques sur l'arbre du rotor et sur l'arbre de la génératrice. Ceci a été effectué pour l'exploitation des données expérimentales ayant pour but l'amélioration de la chaine d'acquisition, des outils de traitement et de l'outil informatique de calcul d'indicateurs VVI. Dans ce contexte, un modèle d'éolienne a été construit avec les approches présentées auparavant dans ce document qui ont amène à simplifications mécaniques majeures issues des hypothèses faites pour les développements présentés. Ce modèle a été créé pour être utilisé pour le test d'indicateurs en conditions de défaillance et de fonctionnement contrôlés.

L'éolienne modélisée est une Senvion MM82, qui produit en conditions de fonctionnement nominal 2 *MW* de puissance avec 12 m/s de vitesse vent. Le rayon du rotor est de 82 mètres et la ligne d'arbre est placée à l'intérieur de la nacelle à 80 mètres de haut. Les composantes principales de la ligne d'arbre sont le roulement principal, le multiplicateur et la génératrice (Figure R12). Dans son ensemble, la ligne d'arbre est inclinée de 5 degrés par rapport à l'horizontale.

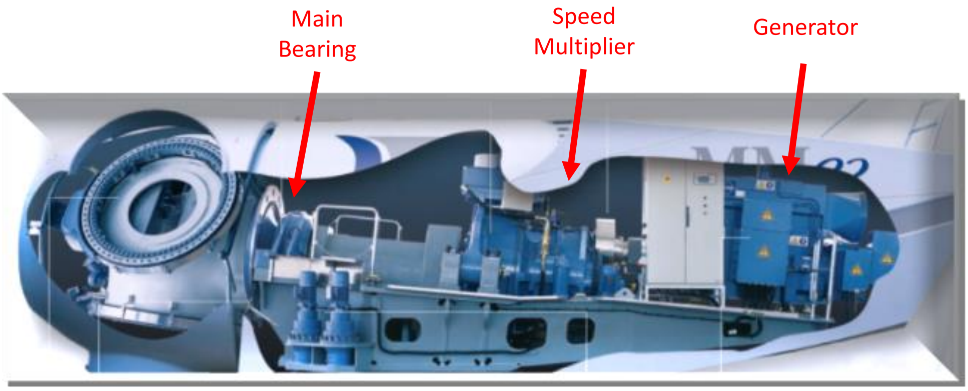

R12 Composants de la ligne d'arbre d'une éolienne MM82

Le roulement principal supporte la majorité du poids du rotor. Le multiplicateur a trois étages dont le premier est un étage épicycloidal et les autres deux correspondent à deux étages s d'engrenages hélicoidaux. La distribution des rapports de transmission par étage est de 4.429, 4.381 et 5.438 ce qui amène à un total de 105.5.

Construction du modèle de turbine

La modélisation de la ligne d'arbre d'une éolienne MM82 avec les approches présentées dans ce mémoire a demandé des simplifications majeures. La Figure R13 montre l'architecture mécanique qui en résulte.

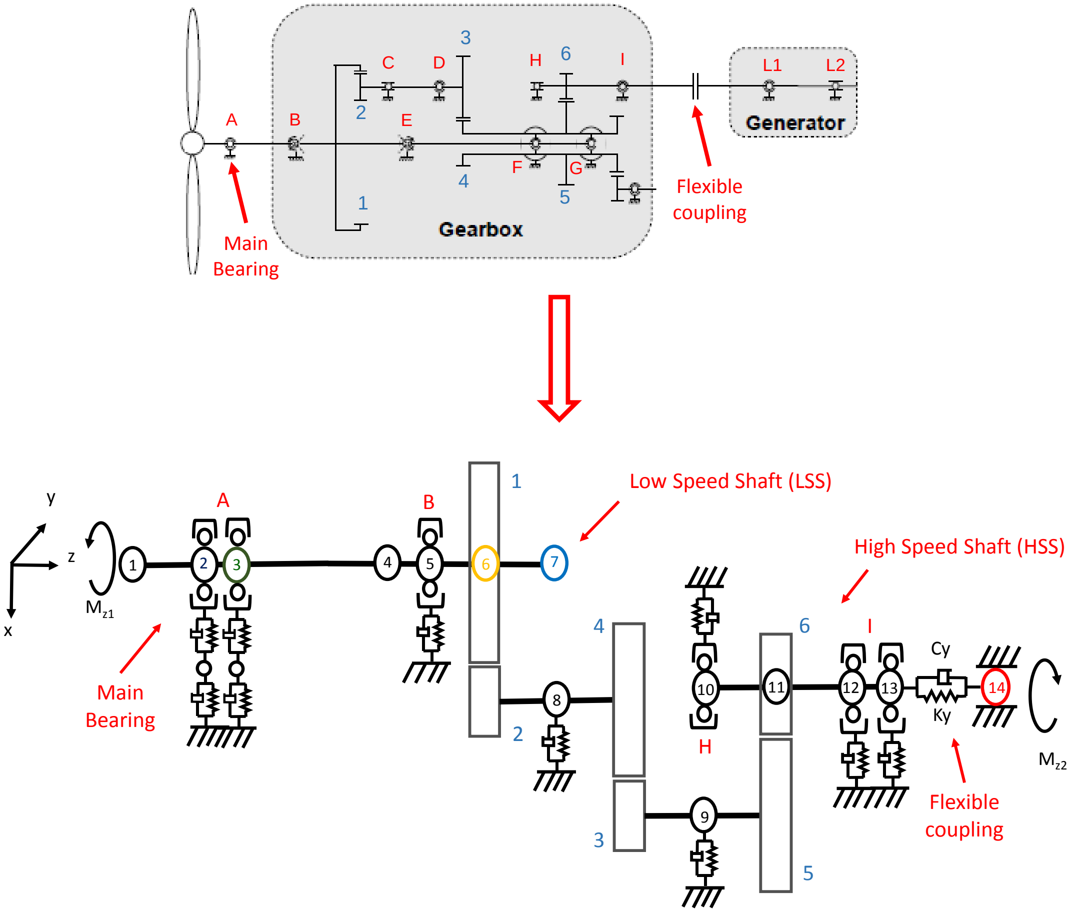

R13 Simplification de l'architecture de l'éolienne

L'étage planétaire a été modélisé avec des engrenages cylindriques extérieurs. Les arbres intermédiaires et les engrenages correspondants ont été concentrés sur les noeuds 8 et 9. L'approche de modélisation des roulements considère des efforts uniquement radiaux. Pour cela, les efforts axiaux du système n'ont pas étés considérés. Ce choix de modélisation a amené à considérer tous les engrenages avec des dentures droites, ce qui représente une simplification majeure qui affecte la distribution de charges sur l'ensemble des roulements et en conséquence la réponse dynamique du système. Par rapport aux dimensions, les engrenages ont les mêmes caractéristiques géométriques que ceux de la vraie machine. Cela permet de respecter les rapports de transmission par étage. Les arbres d'entrée et de sortie du multiplicateur, nommés arbre lent et arbre rapide, ont été modélisés avec les dimensions réelles. L'ensemble des roulements a été réduit à 2 roulements pour l'arbre lent, 2 pour l'arbre rapide et 2 supports flexibles pour les noeuds 8 et 9. Le noeud 1 concentre l'inertie et la masse du rotor et le noeud 14 a les mêmes caractéristiques que l'arbre de la génératrice. La rotation angulaire est prise en compte pour ce noeud seulement. Le couplement flexible a été modélisé par une raideur en torsion avec les paramètres donnés par le fabricant. Le roulement principal qui est composé de deux rangés de corps roulants sphériques a été modélisé comme un roulement à gorges profondes avec deux rangées de billes. Les dimensions de corps roulants et de diamètres des bagues ont été respectées. Les autres roulements ont été modélisés avec l'approche de Palgrem. Le carter du roulement principal a été modélisé sur Ansys et réduit à 3 degrés de liberté, deux dans la direction du poids du rotor et l'autre dans la direction perpendiculaire à cette dernière.

La simulation de conditions non stationnaires

Des mesures de vitesse du vent ont été utilisées pour transformer cette vitesse en un couple rotor appliqué sur l'arbre lent à travers l'équation :

$$T_{wind} = \frac{C_e \cdot \rho \cdot V_{wind}^3 \cdot \pi \cdot R_{rotor}}{2 \cdot \Omega_{rotor}} \tag{D.8}$$

où ρ est la densité de l'air, V_{wind} la vitesse du vent et R_{rotor} le rayon du rotor. Ce coefficient représente le coefficient de puissance qui est adimensionnel et a été considéré constant et égal à 0.49, valeur maximale du coefficient réel.

Par rapport au couple de la génératrice, des données expérimentales ont été utilisées pour la construction d'une courbe avec laquelle le comportement de la génératrice a été linéarisé. L'équation résultante est fonction de la vitesse de rotation de l'arbre rapide :

$$M_G(\omega) = 45.66 \cdot \left(\omega - 1130 \cdot \frac{2 \cdot \pi}{60}\right) + 1100 \qquad [Nm] \tag{D.9}$$

Le contrôle automatique de fonctionnement de la machine a été simplifié à la boucle de contrôle montrée sur la Figure R14.

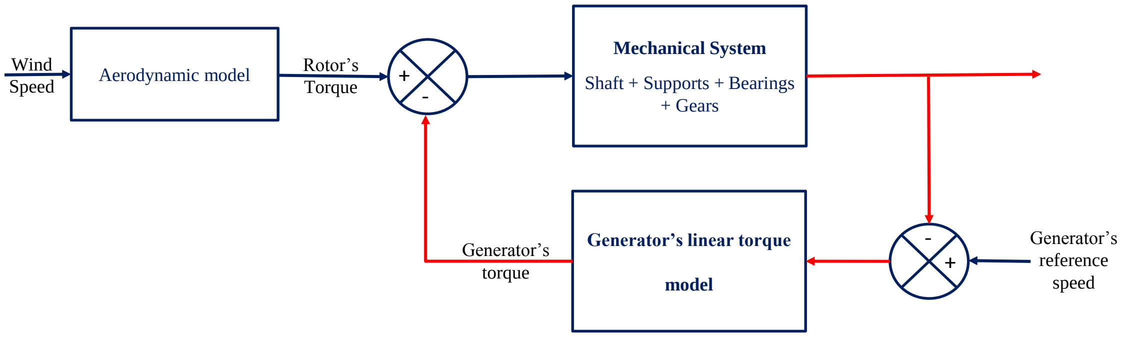

R14 Boucle de contrôle pour les simulations

Les indicateurs de surveillance VVI

Des indicateurs utilisés au sein d'Engie Green dans le cadre du projet de développement de la VVI ont étés choisis pour être testés avec le modèle d'éolienne construit. Ces indicateurs sont les suivants :

1. S_{H1}: Amplitude du pic à la fréquence fondamentale du spectre.
2. S_{H2}: Amplitude du pic à 2x la fréquence fondamentale du spectre.
3. S_{H4}: Amplitude du pic à 4x la fréquence fondamentale du spectre.
4. S_{H8}: Amplitude du pic à 8x la fréquence fondamentale du spectre.
5. S_{H12}: Amplitude du pic à 2x la fréquence fondamentale du spectre.

Ces indicateurs ont été normalisés avec la méthode présentée par André et al. en [3]. Cette normalisation permet d'analyser les indicateurs indépendants des conditions de fonctionnement pendant la mesure du signal de vitesse.

Méthodologie pour le test d'indicateurs

Pour tester les indicateurs, un ensemble de "mesures" a été généré en conditions de machine saine pour construire la loi de normalisation des indicateurs, en simulant la méthode de comptage décrite dans le chapitre 1 pour simuler un codeur installé sur l'arbre lent (noeud 7). Pour cela, 200 simulations issues d'un nombre équivalent de mesures de vent non stationnaires ont été faites. Ensuite, 200 simulations ont été réalisées en présence d'un défaut de bague extérieur du roulement principal. Ces dernières ont été aussi construites à partir de 200 mesures du vent différentes.

Pour les simulations en cas de défaut, une évolution de l'état de défaillance a été configurée à partir de dix tailles différentes du défaut. Pour chaque taille, 20 simulations ont été réalisées avec des conditions de vent différentes pour atteindre le total de 200.

Résultat des simulations et comparaison avec des résultats expérimentaux

Initialement le système a été testé en conditions de fonctionnement stationnaires à une vitesse de l'arbre rapide de 1430 rpm et en présence du plus grand défaut de roulement. Dans l'observation des spectres il a été observé sur les noeuds 7 et 13, la présence des fréquences critiques à 9x la fondamental du passage des billes par la bague extérieure (BPFO) . En regardant le noeud 14, il a été observé que l'accouplement a un effet de filtrage et de redistribution de l'énergie sur l'ensemble des canaux fréquentiels du spectre.

Ensuite, les indicateurs ont été testés en conditions stationnaires pour l'état de roulement sain et pour les tailles de défaut 1, 5 et 10. Une extraction des indicateurs a été effectuée et présentée sur la Figure R15.

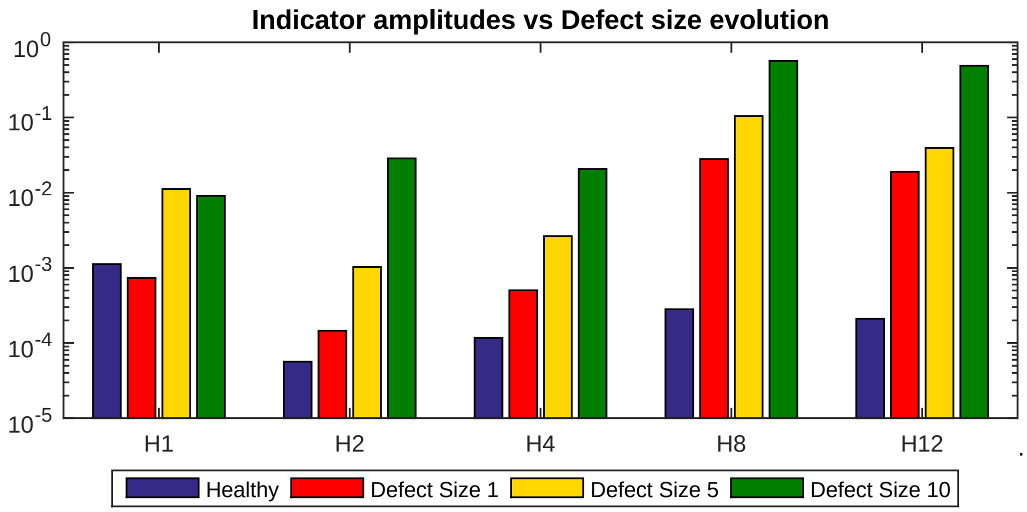

R15 Indicateurs VVI vs évolution du défaut

On observe qu'en présence du défaut l'indicateur H1 diminue par rapport au roulement sain. Aussi, une réduction de l'indicateur est observée entre les tailles de défaut 5 et 10. En conséquence, cet indicateur n'a pas une bonne performance pour la surveillance des roulements. Tous les autres indicateurs ont une tendance à incrémenter avec l'évolution de l'état de défaillance, notamment les indicateurs H8 et H12 qui sont identifiés comme les plus réactifs.

Une observation a été réalisée dans le cadre de la plus grande taille du défaut. Dans l'espace physique il a été identifié que la forme de la courbe de la VVI est très proche de celle de la vitesse du vent. Cela a été lié à la simplification du contrôle de la machine dans lequel le couple résistant de la génératrice réponds linéairement. Des observations spectrales ont été réalisées sur l'arbre lent pour les tailles du défaut 1 et 10. Il est constaté que l'effet du bruit induit dû aux conditions non stationnaires, cache les premières 3 harmoniques de la signature du défaut pour la taille du défaut 1. Pour la taille du défaut 10 un incrément généralisé des amplitudes spectrales est observé.

Avec l'objectif de réaliser une comparaison avec des résultats expérimentaux, une analyse des indicateurs VVI sur l'évolution d'un défaut de roulement de génératrice a été effectuée. La méthode de normalisation a été utilisée aussi pour les mesures expérimentales.

Une comparaison a été faite entre les indicateurs H1 et H12 pour les résultats de simulations et pour les mesures (Figure R16).

De façon générale il est observé que pour le modèle ainsi que pour les résultats expérimentaux l'indicateur H1 répond tardivement à l'évolution du défaut et il est moins réactif par rapport au H12. La Figure R17 donne une vision générale en montrant une comparaison des résultats de l'ensemble des indicateurs. L'échelle des couleurs a été configurée pour atteindre le jaune quand l'alarme issue de la loi de normalisation est dépassée.

Pour le modèle et aussi pour les résultats expérimentaux, l'indicateur H2 répond très peu à la présence du défaut indiquant que cet indicateur n'est pas pertinent dans le cadre des défauts analysés. Par rapport au H1, l'indicateur répond pour la taille de défaut la plus grande dans les simulations. Pour l'analyse expérimentale, l'indicateur a une meilleure performance par rapport au modèle mais vis-à-vis des autres indicateurs il est le moins efficace . De façon générale, les indicateurs répondent du plus au moins performant dans l'ordre H12, H8, H4, H1 et H2. Il est important de mentionner que les simplifications faites pour adapter l'architecture de la machine aux approches de modélisations présentées dans ce travail de recherche n'ont pas eu une influence majeure dans l'évaluation des indicateurs vis-à-vis des résultats expérimentaux. Même si ces résultats demandent plus de validations expérimentales, il peut être affirmé que des indicateurs combinant l'utilisation d'harmoniques supérieures de la réponse spectrale seraient très efficaces pour la détection des défauts de roulement indépendamment des conditions de fonctionnement dans lesquelles les mesures ont étés effectuées.

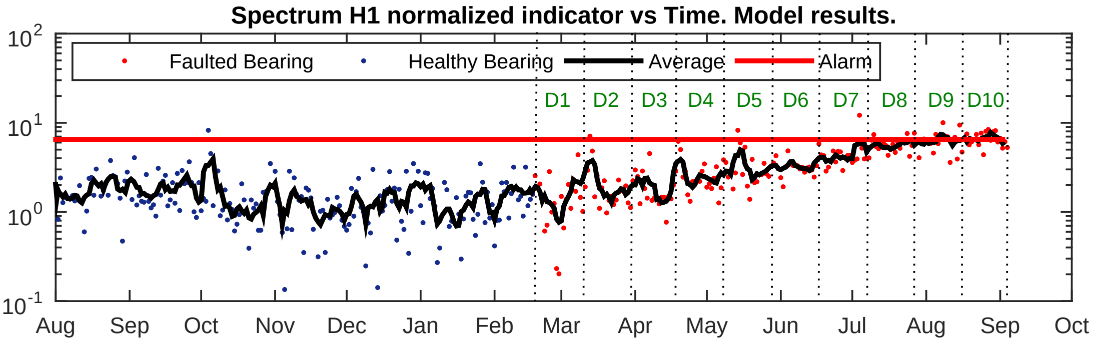

(a) Indicateur VVI H1 normalisé. Modèle.

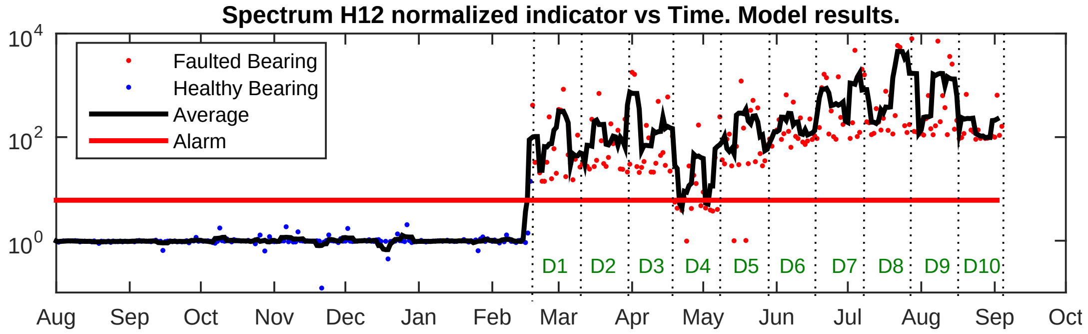

(b) Indicateur VVI H12 normalisé. Modèle

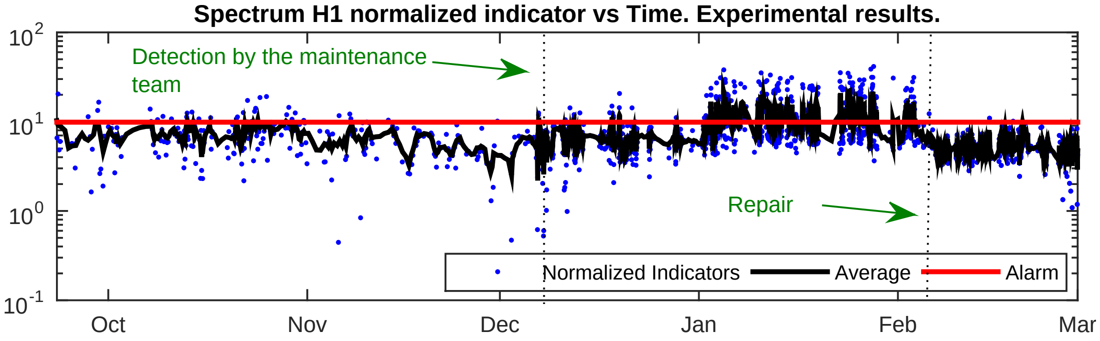

(c) Indicateur VVI H1 normalisé. Résultats expérimentaux

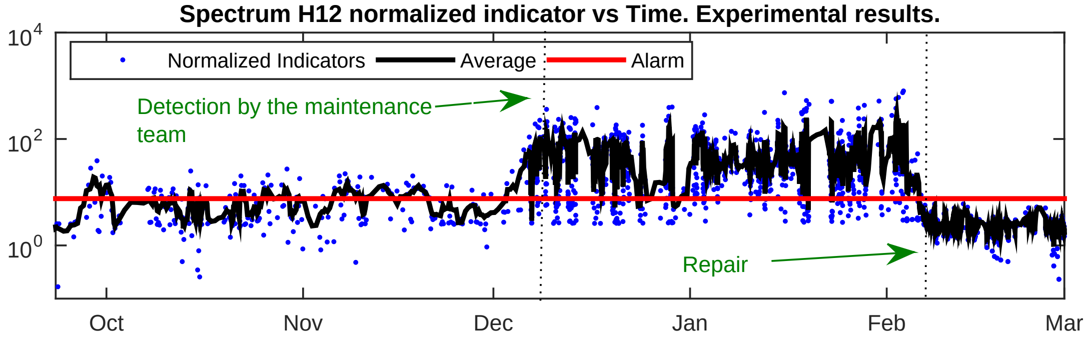

(d) Indicateur VVI H12 normalisé. Résultats expérimentaux

R16 IAS normalized indicators H1 and H12. Modeled and experimental results.

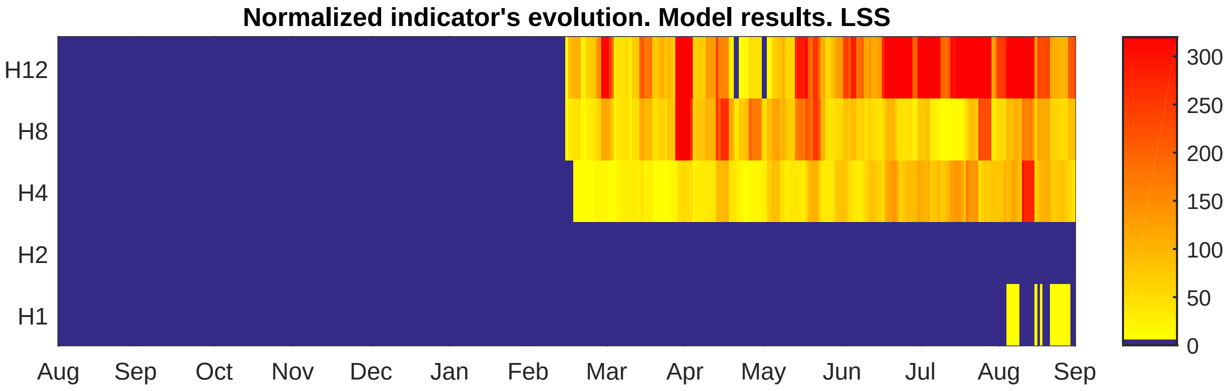

(a) Indicateurs normalisés. Modèle.

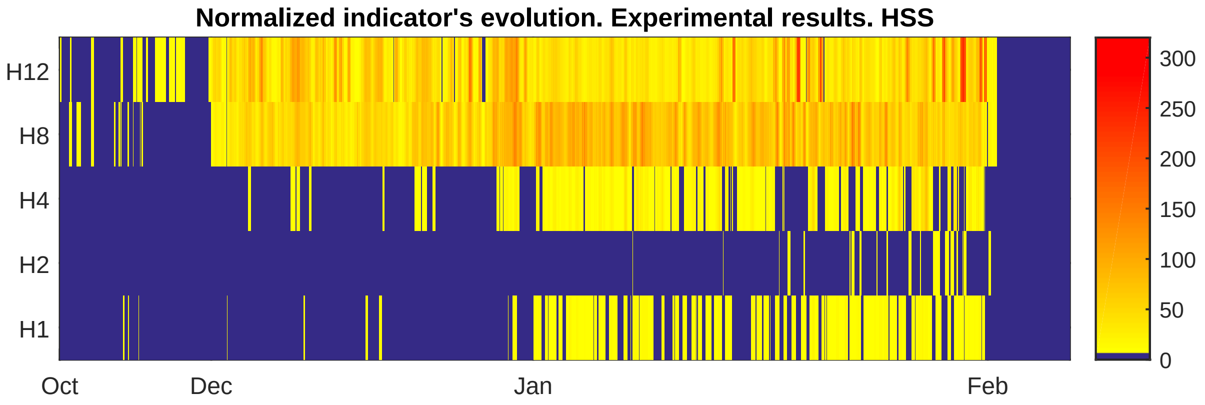

(b) Indicateurs normalisés. Résultats expérimentaux.

R17 Comparaison entre les indicateurs VVI normalisés. Modèle et résultats expérimentaux.

Conclusions générales et perspectives

Une fois l'introduction de l'analyse de la VVI comme outil de surveillance réalisée, une approche de modélisation pour le roulement a été présentée qui décrit comment la dynamique d'un roulement génère des variations de la vitesse angulaire. Basée sur le phénomène de la résistance au roulement, une source de couplage a été établie entre la charge normale et les efforts tangentiels dans l'interaction billes-bagues donnant lieu aux perturbations angulaires issues de la variation de charge normales due à la rotation du roulement. Le modèle de roulement est intégré au système général à travers un torseur d'efforts permettant l'utilisation de la méthode d'éléments finis pour la modélisation des arbres. Cette approche permet aussi la considération de la variable angulaire et la construction de la fonction angle-temps permettant le test des systèmes en conditions non stationnaires.

Une approche classique de liaison par engrenages a été couplée avec le modèle des roulements. La liaison par engrenage a été intégrée aussi comme un torseur d'efforts qui permet la considération des raideurs de denture non linéaires. Il a été trouvé que la nature tangentielle de l'effort d'engrenage devient une deuxième source de couplage entre les efforts tangentiels et normaux. Ce couplage met l'accent sur l'influence des déplacements des engrenages, dépendants de la souplesse des arbres et carters, sur les perturbations angulaires dans le système.

Le couplage entre les phénomènes radiaux et tangentiels signale l'importance d'une modélisation considérant les degrés de liberté de déplacement. Au début de cette recherche, il était suspecté que la seule considération des degrés de liberté de rotation pouvait être suffisante pour modéliser le phénomène de la variation de vitesse. Par rapport aux limitations, l'approche de couplage des composantes mécaniques aux arbres à travers d'efforts ne permet pas d'avoir la matrice de raideur du système ce qu'empêche la réalisation d'analyses modales pour trouver les fréquences critiques et les modes de vibration. Néanmoins, la construction de la fonction angle-temps donne l'opportunité de caractériser le système en profitant de l'utilisation des conditions non stationnaires pour trouver la réponse modale issue d'une excitation spécifique, par exemple, la réponse au déséquilibrage. Dans le chapitre 3, cet avantage a été exploité pour analyser la réponse modale du système par rapport à l'excitation du roulement.

Le modèle simplifié d'éolienne a servi pour montrer le potentiel de l'approche pouvant être utilisée pour le test d'outils de traitement du signal ainsi que des indicateurs de surveillance. Les résultats de l'étude d'indicateurs ont montré des tendances similaires entre les simulations et les analyses expérimentales.

Perspectives

Les travaux présentés ouvrent plusieurs possibilités d'exploration en lien avec la modélisation et la fonction angle-temps. La construction ou adaptation d'un banc d'essais avec a minima deux étages d'engrenages et ayant la possibilité d'introduction des défauts de roulements serait une très bonne opportunité pour la validation et l'approfondissement des résultats présentés dans ce mémoire. Les découvertes en lien avec l'influence des paramètres mécaniques et la réponse VVI du système offrent l'opportunité d'approfondir l'analyse avec l'utilisation des méthodes pour l'estimation des paramètres incertains.

Avec l'objectif de classifier les simplifications mécaniques des modèles vis-à-vis de leur influence sur la réponse dynamique il est nécessaire de complexifier les modèles présentés dans ces travaux. Par rapport au modèle de roulement, l'inclusion de l'angle de contact permettrait la considération des efforts axiaux tout au long de la ligne d'arbre. Aussi, le phénomène de résistance au roulement doit être analysé dans le cadre du contact linéique trouvé dans les roulements avec des corps roulants cylindriques et coniques. Par rapport à la liaison par engrenage, la modélisation du train planétaire parait réalisable avec l'approche de torseurs d'effort avec la difficulté d'avoir des efforts qui changent de magnitude mais aussi de direction. Le modèle de la génératrice peut être aussi complété pour analyser l'influence de sa dynamique sur la VVI. Aussi, il permettrait d'étudier le phénomène de filtrage du couplement flexible.

Les analyses ci-dessus seraient orientées pour l'utilisation du modèle comme outil de test d'indicateurs pour les systèmes de surveillance en VVI mais aussi vibratoire. La consolidation du modèle avec la connaissance de l'impact des simplifications permettrait son utilisation pour la génération de données qui servirait à nourrir des outils d'amélioration et de classification d'indicateurs à travers des méthodes d'intelligence artificielle.

Bibliography

[1] H. ANDRÉ, D. RÉMOND, and A. BOURDON. On the use of the instantaneous angular speed measurement in non stationary mechanism monitoring. In *ASME 2011 International Design Engineering Technical Conferences and Computers and Information in Engineering Conference*, pages 15–24. American Society of Mechanical Engineers, 2011.

[2] A. BOURDON, H. ANDRÉ, and D. RÉMOND. Introducing angularly periodic disturbances in dynamic models of rotating systems under non-stationary conditions. *Mechanical Systems and Signal Processing*, 44(1):60–71, 2014.

[3] H. ANDRÉ, A. BOURDON, and D. RÉMOND. *Instantaneous Angular Speed Monitoring of a 2MW Wind Turbine Using a Parametrization Process*, pages 415–423. Springer Berlin Heidelberg, Berlin, Heidelberg, 2012.

[4] H. ANDRÉ, F. GIRARDIN, A. BOURDON, J. ANTONI, and D. RÉMOND. Precision of the ias monitoring system based on the elapsed time method in the spectral domain. *Mechanical Systems and Signal Processing*, 44(1 - 2):14 – 30, 2014. Special Issue on Instantaneous Angular Speed (IAS) Processing and Angular Applications.

[5] A. BOURDON, S. CHESNÉ, H. ANDRÉ, and D. RÉMOND. Estimation of the size of a spall defect on a rolling bearing outer ring using instantaneous angular speed measurements. In *ISMA International conference on Noise and Vibration Engineering*, 2014.

[6] A. K. S. JARDINE, D. LIN, and D. BANJEVIC. A review on machinery diagnostics and prognostics implementing condition-based maintenance. *Mechanical Systems and Signal Processing*, 20(7):1483 – 1510, 2006.

[7] C.J. STANDER, P.S. HEYNS, and W. SCHOOMBIE. Using vibration monitoring for local fault detection on gears operating under fluctuating load conditions. *Mechanical Systems and Signal Processing*, 16(6):1005 – 1024, 2002.

[8] J. LIN and M. ZHAO. A review and strategy for the diagnosis of speed-varying machinery. In *Proceedings of IEEE Conference on Prognostics and Health Management*, 2014.

[9] J. ANTONI, F. BONNARDOT, A. RAAD, and M. El BADAOUI. Cyclostationary modelling of rotating machine vibration signals. *Mechanical Systems and Signal Processing*, 18(6):1285–1314, November 2004.

[10] D. ABBOUD, J. ANTONI, M. ELTABACH, and S. SIEG ZIEBA. Angletime cyclostationarity for the analysis of rolling element bearing vibrations. *Measurement*, 75:29–39, November 2015.

[11] Q. LECLERE, H. ANDRÉ, and J. ANTONI. A multi-order probabilistic approach for instantaneous angular speed tracking debriefing of the cmmno14 diagnosis contest. *Mechanical Systems and Signal Processing*, 81:375–386, December 2016.

[12] Y. LI, F. GU, G. HARRIS, A. BALL, N . BENNET, and K. TRAVIS. The measurement of instantaneous angular speed. *Mechanical Systems and Signal Processing*, 19(4):786–805, July 2005.

[13] F. BONNARDOT, M. EL BADAOUI, R.B. RANDALL, J. DANIERE, and F. GUILLET. Use of the acceleration signal of a gearbox in order to perform angular resampling (with limited speed fluctuation). *Mechanical Systems and Signal Processing*, 19(4):766–785, July 2005.

[14] K. C. GRYLLIAS and I. A. ANTONIADIS. Estimation of the instantaneous rotation speed using complex shifted morlet wavelets. *Mechanical Systems and Signal Processing*, 38(1):78–95, July 2013.

[15] B. BOASHASH. Estimating and interpreting the instantaneous frequency of a signal. i. fundamentals. *Proceedings of the IEEE*, 80(4):520–538, Apr 1992.

[16] K. RODOPOULOS, C. YIAKOPOULOS, and I. ANTONIADIS. A parametric approach for the estimation of the instantaneous speed of rotating machinery. *Mechanical Systems and Signal Processing*, 44(12):31 – 46, 2014. Special Issue on Instantaneous Angular Speed (IAS) Processing and Angular Applications.

[17] J. YANG, L. PU, Z. WANG, Y. ZHOU, and X. YAN. Fault detection in a diesel engine by analysing the instatanoeus angular speed. *Mechanical Systems and Signal Processing*, 15(3):549 – 564, 2001.

[18] M. DESBAZEILLE, R.B. RANDALL, F. GUILLET, M. EL BADAOUI, and C. HOISNARD. Model-based diagnosis of large diesel engines based on angular speed variations of the crankshaft. *Mechanical Systems and Signal Processing*, 24(5):1529 – 1541, 2010. Special Issue: Operational Modal Analysis.

[19] X. KONG. *Gear train monitoring by transmission error method.* PhD thesis, University of Wisconsin Madison, 1987.

[20] D. RÉMOND. Practical performances of high-speed measurement of gear transmission error or torsional vibrations with optical encoders. *Measurement Science and Technology*, 9(3):347, 1998.

[21] R. G. MUNRO. Review of the theory and measurement of gear transmission error. In *Proceedings of MechE Conference*, 1992.

[22] A. YOUSEF BEN SASI, F. GU, B. PAYNE, and A. BALL. Instantaneous angular speed monitoring of electric motors. *Journal of Quality in Maintenance Engineering*, 10(2):123–135, 2004.

[23] M. FELDMAN and S. SEIBOLD. Damage diagnosis of rotors: application of hilbert transform and multihypothesis testing. *Journal of Vibration and Control*, 5(3):421–442, 1999.

[24] M. SPAGNOL, L. BREGANT, and A. BOSCAROL. Electrical induction motor higher harmonics analysis based on instantaneous angular speed measurement. In *Proceedings of the 4th International Conference on Condition Monitoring of Machinery in Non-stationary Operations (CMMNO), Lyon, France*, 2014.

[25] C.J. SATANDER and P.S. HEYNS. Instantaneous angular speed monitoring of gearboxes under non-cyclic stationary load conditions. *Mechanical Systems and Signal Processing*, 19(4):817 – 835, 2005.

[26] L. RENAUDIN, F. BONNARDOT, O. MUSY, J.B. DORAY, and D. RÉMOND. Natural roller bearing fault detection by angular measurement of true instantaneous angular speed. *Mechanical Systems and Signal Processing*, 24(7):1998 – 2011, 2010.

[27] W. MOUSTAFA, O. COUSINARD, F. BOLAERS, K. SGHIR, and J. P. DRON. Low speed bearings fault detection and size estimation using instantaneous angular speed. *Journal of Vibration and Control*, 22(15):3413–3425, 2016.

[28] I. KHELF. *Diagnostic des machines tournantes par les techniques de l'intelligence artificielle*. PhD thesis, Université Badji Mokhtar - Annaba, 2014.

[29] S. FEDALA, D. RÉMOND, R. ZEGADI, and A. FELKAOUI. Contribution of angular measurements to intelligent gear faults diagnosis. *Journal of Intelligent Manufacturing*, pages 1–17, 2015.

[30] A. BOURDON, H. ANDRÉ, and D. RÉMOND. A new way of writing motion equation in rotating machines by translation into the angular domain. In *8th IFToMM International Conference on Rotordynamics, KIST, Seoul, Korea*, September 2010.

[31] D. RÉMOND, J. ANTONI, and R.B. RANDALL. Editorial for the special issue on instantaneous angular speed (ias) processing and angular applications. *Mechanical Systems and Signal Processing*, 44(1 - 2):1 – 4, 2014. Special Issue on Instantaneous Angular Speed (IAS) Processing and Angular Applications.

[32] J. BINDER. New generation of automotive sensors to fulfil the requirements of fuel economy and emission control. *Sensors and Actuators A : Physical*, 31(1-3):60–67, 1992.

[33] M. SPAGNOL and L. BREGANT. Instantaneous angular speed: Encoder-counter estimation compared with vibration data. In *Advances in Condition Monitoring of Machinery in Non-Stationary Operations*, pages 347–354. Springer, 2014.

[34] H. ANDRÉ. *Surveillance angulaire d'une ligne d'arbre d'éolienne sous conditions non stationnaires*. PhD thesis, Institut National des Sciences Appliqués de Lyon, 2011.

[35] R. B. RANDALL and ANTONI J. Rolling element bearing diagnostics—a tutorial. *Mechanical Systems and Signal Processing*, 25(2):485–520, 2011.

[36] N. SAWALHI and R. B. RANDALL. Simulating gear and bearing interactions in the presence of faults: Part i. the combined gear bearing dynamic model and the simulation of localised bearing faults. *Mechanical Systems and Signal Processing*, 22(8):1924 –1951, 2008.

[37] P. VELEX and M. AJMI. On the modelling of excitations in geared systems by transmission errors. *Journal of Sound and Vibration*, 290(3 - 5):882 – 909, 2006.

[38] P.D. MC FADDEN and J.D. SMITH. Model for the vibration produced by a single point defect in a rolling element bearing. *Journal of Sound and Vibration*, 96(1):69–82, 1984.

[39] D. BRIE. Modelling of the spalled rolling element bearing vibration signal: An overview. *Mechanical Systems and Signal Processing*, 14(3):353–369, 2000.

[40] A. RAFSANJANI, S. ABBASION, A. FARSHIDIANFAR, and H. MOEENFARD. Nonlinear dynamic modeling of surface defects in rolling element bearing systems. *Journal of Sound and Vibration*, 319(3):1150–1174, January 2009.

[41] P. K. GUPTA. Dynamics of rolling-element bearings-part iii: Ball bearing analysis. *Journal of Tribology*, 101(3):312–318, 1979.

[42] H. HERTZ. Über die berührung fester elastischer körper (sur le contact entre corps élastiques). *J. für reine und angewandte Mathematik*, 92:156–171, 1881.

[43] S. FUKATA, E. H. GAD, T. KONDOU, T. AYABE, and H. TAMURA. On the radial vibration of ball bearings: computer simulation. *Bulletin of JSME*, 28(239):899 – 904, 1985.

[44] N. S. FENG, E. J. HAHN, and R. RANDALL. Using transient analysis software to simulate vibration signals due to rolling element bearing defects. In *Proceedings of the Third Australasian Congress on Applied Mechanics*, volume 20, page 22. World Scientific, 2002.

[45] M. NAKHAEINEJAD and M. D. BRYANT. Dynamic modeling of rolling element bearings with surface contact defects using bond graphs. *Journal of Tribology*, 2011.

[46] Y. GUO and G. PARKER. Stiffness matrix calculation of rolling element bearings using a finite element/contact mechanics model. *Mechanism and Machine Theory*, 51:32–45, May 2012.

[47] N. BIBOULET. *Influence of indentations on rolling bearing life*. PhD thesis, Intitut National des Sciences Appliquées de Lyon, 2008.

[48] M. L. DUMONT. *Etude des endommagements de surface induits par la fatigue de roulement dans les contacts élastohydrodynamiques pour des aciers M50 et 100Cr6*. PhD thesis, Institut Nationale des Sciences Appliquées de Lyon, 1997.

[49] Frictional moment estimation, October 2016.

[50] Iso 10816-1:1995: Mechanical vibration - evaluation of machine vibration by measurements on non-rotating parts, part 1: General guidelines, 1995.

[51] N. SAWALHI and R. B. RANDALL. Vibration response of spalled rolling element bearings: Observations, simulations and signal processing techniques to track the spall size. *Mechanical Systems and Signal Processing*, 25(3):846–870, 2011.

[52] Skf bearing calculator, June 2015.

[53] P. VELEX. Advanced mechanical transmissions. lecture notes. 2007.

[54] W. A. TUPLIN. Gear tooth stresses at high speed. *Proceedings of the institution of mechanical engineers*, 16:162–167, 1950.

[55] W. A. TUPLIN. Dynamic loads on gear teeth. *Machine Design*, 25:203–211, 1953.

[56] W. A. TUPLIN. Dynamic load on gear teeth. *Proceedings of the International Conference in Gearing, Institution of Mechanical Engineers*, pages 24–30, 1958.

[57] H. NEVZAT ÖZGÜVEN and D.R. HOUSER. Mathematical models used in gear dynamics. a review. *Journal of Sound and Vibration*, 121(3):383 – 411, 1988.

[58] W. BARTELMUS. Mathematical modelling and computer simulations as an aid to gearbox diagnostics. *Mechanical Systems and Signal Processing*, 15(5):855 – 871, 2001.

[59] W. BARTELMUS, F. CHAARI, R. ZIMROZ, and HADDAR M. Modelling of gearbox dynamics under time-varying nonstationary load for distributed fault detection and diagnosis. *European Journal of Mechanics - A/Solids*, 29(4):637 – 646, 2010.

[60] W. BARTELMUS. Gearbox dynamic multi-body modelling for condition monitoring under the case of varying operating condition. *Journal of Coupled Systems and Multiscale Dynamics*, 2014.

[61] M. KUBUR, A. KAHRAMAN, D. M. ZINI, and KIENZLE K. Dynamic analysis of a multi-shaft helical gear transmission by finite elements: Model and experiment. *Journal of Vibration and Acoustics*, 126(3):398–406, July 2004.

[62] D. J. EWINS. *Model Testing, Theory and Practice*. Research Studies Press Ltd, 1984.

[63] T. ERITENEL and R. G. PARKER. An investigation of tooth mesh nonlinearity and partial contact loss in gear pairs using a lumped-parameter model. *Mechanism and Machine Theory*, 56:28 – 51, 2012.

[64] Z. WAN, H. CAO, Y. ZI, W. HE, and Y. CHEN. Mesh stiffness calculation using an accumulated integral potential energy method and dynamic analysis of helical gears. *Mechanism and Machine Theory*, 92:447 – 463, 2015.

[65] A. BOURDON. *Modelisation dynamique globale des boîtes de vitesses automobile*. PhD thesis, Institut National des Sciences Appliqués de Lyon, 1997.

[66] P. VELEX. *Contribution à l'analyse du comportement dynamique de réducteurs à axes parallèles*. PhD thesis, Institut National des Sciences Appliqués de Lyon, 1988.

[67] C. BARD. *Modélisation du comportement dynamique des ttransmission par engrenages*. PhD thesis, Institut National des Sciences Appliqués de Lyon, 1995.

[68] Iso 6336: Calculation of load capacity of spur and helical gears, 2006.

[69] Gearbox catalog, September 2016.

[70] A. PALGREM. *Les roulements: Description, théorie et applications*. S.K.F., 1967.

[71] M.O.L. HANSEN, J.N. SORENSEN, S. VOUTSINAS, N. SORENSEN, and H. A. MADSEN. State of the art in wind turbine aerodynamics and aeroelasticity. *Progress in Aerospace Sciences*, 42(4):285–330, June 2006.

[72] C. G. COOLEY and R. G. PARKER. A review of planetary and epicyclic gear dynamics and vibrations research. *Applied Mechanics Reviews*, 66(4):040804–040804–15, June 2014.

[73] J. HELSEN, G. HEIRMAN, D. VANDEPITTE, and W. DESMET. The influence of flexibility within multibody modeling of multi-megawatt wind turbine gearboxes. In

Proc. International Conference on Noise and Vibration Engineering, pages 15–17. Citeseer, 2008.

[74] J. HELSEN, F. VANHOLLEBEKE, B. MARRANT, D. VANDEPITTE, and W. DESMET. Multibody modelling of varying complexity for modal behaviour analysis of wind turbine gearboxes. *Renewable Energy*, 36(11):3098–3113, 2011.

[75] J. HELSEN, F. VANHOLLEBEKE, F. DE CONINCK, D. VANDEPITTE, and W. DESMET. Insights in wind turbine drive train dynamics gathered by validating advanced models on a newly developed 13.2 mw dynamically controlled test-rig. *Mechatronics*, 21(4):737–752, 2011.

[76] J. HELSEN, B. MARRANT, F. VANHOLLEBEKE, F. DE CONINCK, D. BERCKMANS, D. VANDEPITTE, and W. DESMET. Assessment of excitation mechanisms and structural flexibility influence in excitation propagation in multi-megawatt wind turbine gearboxes: Experiments and flexible multibody model optimization. *Mechanical Systems and Signal Processing*, 40(1):114–135, 2013.

[77] R. G. PARKER. Analytical characterization of the unique properties of planetary gear free vibration. *Journal of Vibration and Acoustics, Transactions of the ASME. v121*, (3):p316–321, 1999.

[78] R. G. PARKER and X. WU. Vibration modes of planetary gears with unequally spaced planets and an elastic ring gear. *Journal of Sound and Vibration*, 329(11):2265–2275, 2010.

[79] J. L. M. PEETERS. *Simulation of Dynamic Drive Train Loads in a Windturbine (Simulatie van de dynamische belasting in de aandrijflijn van een windturbine)*. PhD thesis, Katholieke Universiteit Leuven, 2006.

[80] J. L. M. PEETERS, D. VANDEPITTE, and P. SAS. Analysis of internal drive train dynamics in a wind turbine. *Wind Energy*, 9(1-2):141–161, 2006.

[81] V. ABOUSLEIMAN and P. VELEX. A hybrid 3d finite element/lumped parameter model for quasi-static and dynamic analyses of planetary/epicyclic gear sets. *Mechanism and Machine Theory*, 41(6):725–748, 2006.

[82] S. SANTOSO and H. T. LE. Fundamental time domain wind turbine models for wind power studies. *Renewable Energy*, 32(14):2436 – 2452, 2007.

[83] T. BURTON, D. SHARPE, N. JENKINS, and E. BOSSANYI. *Wind energy handbook.* John Wiley & Sons, 2001.

[84] J. MC BAIN and M. TIMUSK. Fault detection in variable speed machinery: Statistical parameterization. *Journal of Sound and Vibration*, 327(3):623–646, November 2009.

FOLIO ADMINISTRATIF

THESE DE L'UNIVERSITE DE LYON OPEREE AU SEIN DE L'INSA LYON

NOM : GOMEZ CHIRINOS DATE de SOUTENANCE :
(avec précision du nom de jeune fille, le cas échéant)

Prénoms : José Luis

TITRE : Angle modeling of a rotating machine. Application to Wind turbine surveillance

NATURE : Doctorat Numéro d'ordre : 2017LYSEI067

Ecole doctorale : MEGA

Spécialité : Mécanique – Génie Mécanique

RESUME :

Ce travail de recherche s'inscrit dans le cadre de la surveillance des machines tournantes en régime non stationnaire et plus particulièrement la détection des défauts de roulement. Il se focalise sur la modélisation et l'analyse des variations de la vitesse de rotation instantanée. Les modèles numériques développés s'appuient sur une approche originale dite " angulaire " qui introduit explicitement les degrés de rotation libres de la machine et permet de s'affranchir de condition de fonctionnement en régime stationnaire. Un modèle de roulement à billes à gorge profonde a été développé couplant les efforts de contact normaux et tangentiels grâce à l'introduction du phénomène de résistance au roulement. Ce couplage permet d'expliquer l'origine des fluctuations de vitesse de rotation en présence de défaut de bague extérieure, phénomènes constatés expérimentalement : la présence d'un défaut sur une bague modifie périodiquement le couple de frottement. La modélisation de la liaison par engrenages est plus classique, la problématique a été de s'assurer qu'elle était compatible avec l'approche angulaire utilisée dans ces travaux. Le couplage des éléments de roulement et d'engrenage dans un modèle simple a montré que la présence de défauts de roulement provoque des variations des efforts radiaux ce qui modifie les efforts d'engrènement et en conséquence perturbe également la vitesse de rotation. Un modèle simplifié d'une éolienne a été réalisé et utilisé pour tester et valider des indicateurs spectraux de surveillance en conditions de fonctionnement non stationnaires. La comparaison avec des mesures expérimentales issues d'une éolienne a montré la robustesse du modèle. Il peut donc être exploité comme un outil d'analyse phénoménologique et de test d'indicateurs de surveillance. Il a par exemple permis de montrer l'importance des conditions de fonctionnement (charge et vitesse) sur le niveau des indicateurs utilisés en surveillance. Si besoin, les développements proposés peuvent être étendus sans difficulté à des modèles plus complexes de roulements, d'engrènements et de structures d'accueil de ces éléments technologiques.

MOTS-CLÉS : Modélisation de roulements et engrenages, Variation de la vitesse instantanée, approche angulaire, Surveillance de machines tournantes en conditions de fonctionnement non stationnaires

Laboratoire (s) de recherche : Laboratoire de Mécanique des Contacts et des Structures
UMR CNRS 5259 – INSA de LYON
18-20 rue des Sciences
69621 Villeurbanne Cedex FRANCE

Directeur de thèse: Didier REMOND

Président de jury : Philipe VELEX

Composition du jury : Roger SERRA Jean-Luc DION
Evelyne AUBRY Philipe VELEX
Adeline BOURDON Didier REMOND
ANDRE Hugo Nicolas GIRARD